

UNIVERSITY
of
OTAGO



Te Whare Wānanga o Otāgo

**Designing oligoarginine-associated
PECA nanoparticles
for enhanced cellular uptake**

Jasper Z. S. Chiu

A thesis submitted for the degree of

Doctor of Philosophy

at the University of Otago

Dunedin, New Zealand

August 2014

Abstract

Introduction: Polymeric nanoparticles can be used as carriers to improve oral bioavailability of therapeutic peptides or proteins. These polymeric carriers can be formulated with cell-penetrating peptides such as oligoarginine to further enhance uptake. Such a combined formulation could deliver bioactive effectively, using less oligoarginine than required for effective cell permeation using oligoarginine alone. The aims of this study were to formulate poly(ethylcyanoacrylate) (PECA) nanoparticles with oligoarginine, characterize the resulting nanoparticles and investigate their *in vitro* uptake.

Methods: PECA nanoparticles were produced by *in situ* polymerization in a water-in-oil microemulsion. Various oligoarginines were dissolved in the aqueous phase of the microemulsion prior to the addition and polymerization of monomers, to produce different oligoarginine-associated nanoparticles. The resultant nanoparticles were characterized for size and zeta potential in ultra-pure water and the cell incubating medium (Hanks Balanced Salt Solution, HBSS). The nature of the association between oligoarginines and nanoparticles was investigated by MALDI-TOF mass spectrometry. The uptake of the oligoarginine-associated nanoparticles, loaded with a fluorescent probe, by Caco-2 cells was investigated using fluorescence-activated cell sorting (FACS) and confocal imaging. Uptake studies were conducted in both undifferentiated cells and fully differentiated cell monolayers. The uptake of radiolabeled oligoarginine nanoparticles by Caco-2 cells was quantified by scintillation counting and the accumulation of nanoparticles on the cell surface was evaluated with a mathematical simulation model.

Results: PECA nanoparticles formulated with di-arginine-histidine (RRH) and tetra-arginine-histidine with an aminocaproic acid spacer (R4acaH) were cationic (zeta potential of +35 and +33.5 mV, respectively) and approximately 200 nm in diameter. Mass spectrometric studies revealed that RRH was covalently tagged to the PECA nanoparticles via histidine but R4acaH was not. Because these RRH-tagged nanoparticles aggregated in HBSS, poloxamer-407 surfactant was added to stabilize the colloidal system. However, the addition of surfactant was found to neutralize the positive zeta potential of the nanoparticles. RRH-tagged nanoparticles associated with a higher proportion of undifferentiated Caco-2 cells after 2 h incubation than unmodified nanoparticles and confocal imaging showed that they were mainly located on the cell surface. Association of RRH-tagged nanoparticles in fully differentiated Caco-2 cell monolayers was not

increased compared to that of unmodified nanoparticles. The accumulation trend of PECA nanoparticles on the cell surface predicted by a mathematical simulation model was consistent with the cellular experimental data.

Conclusions: PECA nanoparticles associated covalently with RRH via histidine anchoring to produce cationic nanoparticles, which were neutralized in the presence of surfactant. These nanoparticles adhered to undifferentiated Caco-2 cells to a greater extent than unmodified PECA nanoparticles. However, scintillation counting data revealed that the greater tendency to adhere did not result in greater uptake of the RRH-tagged nanoparticles in fully differentiated Caco-2 cell monolayers, which was consistent with the findings of flow cytometry. Mathematical simulation modelling was able to predict the low accumulation of the nanoparticles at the bio-interface but did not account for the adherence tendency of the nanoparticles and the initial contact adherence that occurred during convection mixing upon introduction of the formulation to the cells. Further surface characterization of the RRH-tagged nanoparticles is required to gain deeper insight into the nature of the interaction at the cellular bio-interface. Although fluorescence analysis (such as FACS and confocal imaging) was able to quantify the proportion of cells associated with the polymeric nanoparticles and verify internalization, scintillation counting data complemented the cellular association with invaluable information on the proportion of nanoparticles associated with the cells. Therefore, these techniques should be used together to critically assess cellular association and uptake.

Acknowledgements

This PhD journey has been a long and tiring one. Though things were mostly tough along the way, there were silver linings in the cloud. I would like to take this opportunity to show my appreciation to those who aided me in this journey and made it more enjoyable and possible for me to complete.

First and foremost, I would like to thank Dr Arlene McDowell for guiding me and giving me endless encouragement as well as brilliant ideas. Without her, this PhD journey would not have been possible. I would also like to thank Prof. Ian Tucker, who has been guiding me into the right path and contributing intellectual input throughout the entire project. I would like to thank Dr Bernie McLeod for all the good times over at Invermay Possum Facility as well as allowing me to pick his brain from time to time. Though Dr Doug Eckery was unable to remain as one of my supervisors due to relocation, I would still like to thank him for his valuable input in my project.

I would also like to thank Prof. Thomas Rades for his intellectual contributions to the project, as well as all the enjoyable social nights. I would also like to thank Prof. Sarah Hook, Katie Young and Biju Balakrishnan for their contributions in my cell culture work. I would also like to acknowledge Dr Torsten Kleffmann from the Centre of Protein Research (CPR) (Department of Biochemistry, University of Otago) for the help in MALDI-TOF mass spectrometry, Andrew McNaughton from the EM unit (Department of Anatomy and Physiology, University of Otago) and Sarah Streck for the aid in fluorescent and confocal imaging and Ami Radunskaya (School of Pharmacy, University of Otago) for her guidance in mathematical modelling simulations. I would also like to extend my acknowledgement to the Teegarden group (Biological Sciences Division, Northwest, National Laboratory, WA, USA) for the provision of the ISDD code for Matlab[®] simulations and to Dr Paul Fawcett for his input with the thesis abstract.

Though I did not get to play much with the possums at the possum facility over at Invermay (Dunedin), I would like to show my gratitude to Euan Thompson for helping me with handling of the possums in the preliminary oral absorption study so that I could avoid bite marks on my hands.

I would also like to give my acknowledgment to all the technicians, Kevin Crump, Brian Young, Len Stevenson, Mike Broughton, Jo Preston and Tim Campbell

from School of Pharmacy as well as Rob Alumbaugh from Department of Pharmacology for their technical assistance with machines and instruments.

And a very special thanks to all the colleagues and friends, especially Enxin Chin, Shin Wei Chan, Lewis Lam, Sarah Streck, Sarah Bushby, Ellen Ou, Freda Feng, Himang Mujoo, Nicky Thomas, Pummy Krittaphol and Alex Kafka for their valuable time and help when I'm in need during my PhD. I would never have come this far without them. The most important thing in a PhD journey is keeping your sanity in check all the time and one could never do this alone!

Last but not least, I would like to thank my family and my fiancée for their never ending support and to put up with my absence in their lives during the completion of this long haul journey. Life for me is finally coming off pause and resuming as it should. Thanks to everyone who has made such a great impact in my PhD journey and my life.

Publications and Conferences/Presentations

Refereed journal articles

Jasper Z S Chiu, Ian G Tucker, Bernie J McLeod, Arlene McDowell. Arginine-tagging of polymeric nanoparticles via histidine to improve cellular uptake, *European Journal of Pharmaceutics and Biopharmaceutics*, 89: 48-55 (2015) .

Jasper Z S Chiu, Ian G Tucker, Bernie J McLeod, Arlene McDowell. Cellular association of polymeric nanoparticles decorated with oligoarginine in a Caco-2 cell model. (Manuscript in preparation) .

Jasper Z S Chiu, Ian G Tucker, Bernie J McLeod, Arlene McDowell. Understanding the interaction of oligoarginine-associated nanoparticles with the cell surface at the bio-interface. (Manuscript in preparation) .

Conference contributions

Oral presentations

Jasper Z S Chiu, Ian G Tucker, Bernie J McLeod, Arlene McDowell. Associating oligoarginine to polymeric nanoparticles to increase cellular penetration. *15th Annual Formulation and Delivery of Bioactives (FDB)*, Dunedin, New Zealand, February 2013.

Jasper Z S Chiu, Ian G Tucker, Bernie J McLeod, Arlene McDowell. Combining polymeric nanoparticles with oligoarginine for greater cell penetration. *Scientific Meeting of the Otago Medical School Research Society*, September 2013.

Jasper Z S Chiu, Ian G Tucker, Bernie J McLeod, Arlene McDowell. Single step arginine tagging of polymeric nanoparticles to enhance cellular uptake. *Australasian Pharmaceutical Science Association (APSA) Annual Conference*, Dunedin, New Zealand, December 2012.

Poster presentations

Arlene McDowell, Jasper Z S Chiu, Ian G Tucker. Cell-penetrating peptides – is charge important for improved uptake of nanoparticles? *41st Annual Meeting and Exposition of the Controlled Release Society*, Chicago, Illinois, USA, July 2014.

Jasper Z S Chiu, Ian G Tucker, Bernie J McLeod, Arlene McDowell. Tagging poly(ethylcyanoacrylate) nanoparticles with oligoarginine enhances their uptake by fully differentiated Caco-2 cells. *Australasian Pharmaceutical Science Association (APSA) Annual Conference*, Dunedin, New Zealand, December 2013.

Jasper Z S Chiu, Ian G Tucker, Bernie J McLeod, Arlene McDowell. Enhancing cellular uptake of poly(ethyl-cyanoacrylate) nanoparticles through arginine association. *40th Annual Meeting and Exposition of the Controlled Release Society*, Honolulu, Hawaii, USA, August 2013.

Jasper Z S Chiu, Ian G Tucker, Bernie J McLeod, Arlene McDowell. Single step arginine tagging of polymeric nanoparticles to enhance cellular uptake. *Drug Delivery Australia (DDA) Annual Conference*, Melbourne, Australia, December 2012.

Jasper Z S Chiu, Ian G Tucker, Bernie J McLeod, Arlene McDowell. Single step arginine tagging of polymeric nanoparticles to enhance cellular uptake. *Globalization of Pharmaceutics Education Network (GPEN)*, Melbourne, Australia, December 2012.

Jasper Z S Chiu, Ian G Tucker, Bernie J McLeod, Arlene McDowell. Single step arginine tagging of polymeric nanoparticles to enhance cellular uptake. *Australasian Pharmaceutical Science Association (APSA) Annual Conference*, Dunedin, New Zealand, December 2012.

Jasper Z S Chiu, Ian G Tucker, Bernie J McLeod, Doug, Eckery, Arlene McDowell. Preparation and characterization of polyarginine-associated polymeric nanoparticles. *14th Annual Formulation and Delivery of Bioactives (FDB)*, Dunedin, New Zealand, February 2012.

Table of Contents

Abstract	i
Acknowledgements	iii
Publications and Conferences/Presentations	v
List of Figures	xii
List of Tables.....	xvii
List of Equations	xix
List of Abbreviations.....	xx
1. General introduction	1
1.1. Challenges in oral drug delivery	1
1.2. Understanding the gastrointestinal absorption mechanisms	2
1.3. General mechanisms of cellular uptake	5
1.4. Oral formulations	7
1.4.1. Poly(alkylcyanoacrylate) (PACA) nanoparticles	8
1.4.2. Cell-penetrating peptides (CPPs) as penetration enhancers	11
1.4.2.1. Method of CPP association to bioactive	13
1.4.2.2. Uptake mechanisms of CPPs	15
1.4.2.3. Oligoarginine as a CPP	21
1.4.3. Incorporation of CPPs in polymeric nanoparticles.....	24
1.5. Interaction at the bio-interface	26
1.6. Aims of thesis.....	28
2. Design and characterization of oligoarginine-associated PECA nanoparticles.	30
2.1. Introduction	30
2.1.1. Conjugation methods for CPPs to colloidal carriers	30
2.1.2. Characterization of CPP-conjugated nanoparticles.....	31
2.1.3. Quantification of CPPs.....	32
2.1.4. Chapter aims.....	35

2.2. Materials.....	35
2.3. Methods.....	36
2.3.1. Preparation of PECA nanoparticles from a microemulsion template	36
2.3.2. Arginine-tagging and FITC-dextran entrapment.....	36
2.3.3. Isolation of nanoparticles from microemulsion.....	37
2.3.4. Screening for covalent association using MALDI-TOF mass spectrometry	37
2.3.5. Characterization of nanoparticles	38
2.3.5.1. Size and zeta potential	38
2.3.5.2. Entrapment efficiency.....	38
2.3.6. Quantifying oligoarginine-associated with PECA nanoparticles.....	38
2.3.6.1. HPLC assay	38
2.3.6.2. I-TRAQ™ assay	40
2.3.7. Effects of phosphates on nanoparticles	40
2.3.8. Treating PECA nanoparticles with poloxamer-407	41
2.3.9. Release of oligoarginine in HBSS.....	41
2.3.10. Statistical analysis	41
2.4. Results and discussion.....	42
2.4.1. Screening for covalent association	42
2.4.2. Characterization of oligoarginine-associated nanoparticles.....	45
2.4.3. Quantification of oligoarginine	48
2.4.3.1. HPLC/UV quantification.....	48
2.4.4. Semi-quantification of oligoarginine with i-TRAQ™ assay	50
2.4.5. Effects of phosphates on nanoparticles and treatment with poloxamer-407	54
2.4.6. Release of oligoarginine.....	60
2.4.7. Conclusion.....	62

3. Cellular association and uptake of oligoarginine-associated PECA nanoparticles	63
3.1. Introduction	63
3.1.1. Assessing cellular uptake of polymer nanoparticles in Caco-2 cells	63
3.1.2. Cellular uptake of CPP-associated polymeric nanoparticles.....	70
3.1.3. Cytotoxicity of polymeric nanoparticulate systems	71
3.1.4. Chapter aims.....	73
3.2. Materials.....	74
3.3. Methods.....	74
3.3.1. Determining dry weight of PECA nanoparticles.....	74
3.3.2. Release of FITC-dextran in HBSS	74
3.3.3. Culturing Caco-2 cells.....	75
3.3.4. Cytotoxicity assay	75
3.3.5. Determining cellular association via FACS	76
3.3.6. Statistical analysis	76
3.3.7. Confocal imaging	78
3.4. Results and discussion.....	78
3.4.1. Determining the dry weight of nanoparticles	78
3.4.2. FITC-dextran release in HBSS.....	79
3.4.3. Cytotoxicity of oligoarginine-associated nanoparticles in Caco-2 cells and in fully differentiated Caco-2 cell monolayers	84
3.4.4. Cellular association of oligoarginine-associated nanoparticles determined by FACS analysis	87
3.4.4.1. Undifferentiated Caco-2 cells	87
3.4.4.2. Fully differentiated Caco-2 cell monolayer	99
3.5. Conclusion.....	101
4. Re-evaluation of cellular association and uptake of oligoarginine-associated PECA nanoparticles	104

4.1. Introduction	104
4.1.1. Quantifying delivery based on the bioactive entrapped in nanoparticles compared to nanoparticles	104
4.1.2. Cellular uptake of nanoparticles tagged with fluorescent probe	105
4.1.3. Cellular uptake of nanoparticles tagged with radiolabels	106
4.1.4. Accumulation of nanoparticles on cell surface	106
4.1.5. Uptake kinetics	110
4.1.6. Chapter aims	111
4.2. Materials	111
4.3. Methods	112
4.3.1. Determination of the density of PECA nanoparticles	112
4.3.2. Mathematical simulation based on the ISDD model	113
4.3.3. Radiolabeling PECA nanoparticles	114
4.3.4. Release of L-Histidine [¹⁴ C] radiolabel in HBSS	115
4.3.5. Culturing Caco-2 cells and cellular association study	115
4.3.6. Liquid scintillation counting	116
4.3.7. Protein content determination	117
4.3.8. Statistics	117
4.4. Results and discussion	118
4.4.1. Determining the density of PECA nanoparticles	118
4.4.2. Characterization of radiolabeled PECA nanoparticles	119
4.4.3. L-His [¹⁴ C] radiolabel release in HBSS	120
4.4.4. Dose accumulation on cell surface	121
4.4.5. Cellular association of PECA nanoparticles	124
4.4.5.1. Cellular association with fully differentiated Caco-2 cell monolayers	124
4.4.5.2. Comparison between simulation model and experimental uptake	131
4.4.5.3. Effects of poloxamer-407 on cellular association	135

4.4.5.4. Cellular association in undifferentiated Caco-2 cells	138
4.4.6. Comparing cellular association of nanoparticles in undifferentiated Caco-2 cells and fully differentiated Caco-2 cell monolayers	141
4.5. Conclusion.....	144
5. General discussion and future directions.....	149
References	152
Appendix I.....	169
Appendix II.....	170
Appendix III	172
Appendix IV	172
Appendix V	173
Appendix VI.....	174

List of Figures

Figure 1-1. Schematic diagram of intestinal structures and translocation routes across the intestinal epithelium (modified from Woitiski <i>et al.</i> (2008)).	3
Figure 1-2. Types of endocytosis, accompanied by transmission and scanning electron microscope images in a cell (modified from (Doherty and McMahon, 2009)).	7
Figure 1-3. Types of nanoparticles and localization of bioactive molecules following encapsulation/sorption (reproduced from Krauel <i>et al.</i> (2004)).	10
Figure 1-4. Proposed models of the energy-independent membrane translocation mechanism; A. Inverted micelle model, B. Carpet and membrane thinning model, C. Pore-formation model (Wagstaff and Jans, 2006).	17
Figure 1-5. Chemical structure of octa-arginine (R8). The cationic guanidinium groups are expected to interact with negatively charged phospholipid membrane at physiological pH (Richard <i>et al.</i> , 2003).	21
Figure 1-6. Nucleophilic attack on ethylcyanoacrylate (ECA) by imidazole ring of histidine during polymerization, resulting in covalent binding to PECA (Kafka <i>et al.</i> , 2009).	25
Figure 1-7. Schematic showing the interactions of a nanoparticle at the solid-liquid interface and at the nano-bio-interface (Nel <i>et al.</i> , 2009).	27
Figure 2-1. Composition of the i-TRAQ TM reagent (Brewis and Brennan, 2010).	34
Figure 2-2. Mass spectra of PECA nanoparticles tagged with A. RH and C. RRH. CID fragmentation of selected precursor ion of B. 937 from RH-tagged nanoparticles and D. 968 from RRH-tagged nanoparticles. $[M_{RH} + H]^+ = 312.2$ and RH/ECA copolymers at m/z 812.3, 937.4, 1062.4, 1187.5; $[M_{RRH} + H]^+ = 468.3$ and RRH/ECA copolymers at m/z 718.3, 843.4, 968.4, 1093.5, 1218.5.	43
Figure 2-3. Mass spectrum of mixed RRH sample tagged with i-TRAQ 114, 115 and 116. ($M_{RRH} = 467$, $M_{i-TRAQ} = 145$).	51
Figure 2-4. CID fragmentation of m/z 612 precursor.	52
Figure 2-5. Enlarged region (m/z 110 to 118 in Figure 2-4) normalized to 100% intensity of m/z 115 peak.	53
Figure 2-6. Zeta potential of unmodified (\square) and RRH (100 μ mol)-tagged (\blacksquare) nanoparticles in ultra-pure water. Data are means \pm SD ($n = 2$).	55
Figure 2-7. Zeta potential of A. unmodified nanoparticles (open symbols) and B. RRH (100 μ mol)-tagged nanoparticles (closed symbols) titrated with phosphate buffer of	

varying pHs (\square pH 6, \diamond pH 7, \circ pH 8) and HBSS (Δ pH 7.4). Data are means \pm SD ($n = 3$).....56

Figure 2-8. A. Size of unmodified nanoparticles (unfilled) and RRH (100 μ mol)-tagged nanoparticles (filled) treated with different poloxamer-407 concentrations before re-dispersion in HBSS. **B.** Size of unmodified nanoparticles (Δ) and RRH (100 μ mol)-tagged nanoparticles (\blacktriangle) coated with poloxamer-407 at 1 : 4.2 (poloxamer : dry nanoparticles) mass ratio, incubated at 37°C over 2 h. Data are means \pm SD ($n = 3$).59

Figure 2-9. Release of oligoarginine from PECA nanoparticles (Blue = RRH, Green = R4acaH, Brown = RR, Black = R4) in HBSS at 37°C over 3 h. Data are means \pm SD ($n \geq 4$).60

Figure 3-1. Postulated non-specific, energy-dependent (endocytosis) and energy-independent (mitochondria trafficking) uptake of polymeric nanoparticles in a Caco-2 cell. Purple spheres represent nanoparticles (He *et al.*, 2013).....68

Figure 3-2. FACS analysis of Caco-2 cell populations, using FlowJo[®] analysis software. The Caco-2 cells were gated for **A.** cells, **B.** single cells, **C.** live cells and **D.** FITC (Red line representing untreated cells (negative control), and blue line representing cells incubated with 0.005% (w/v) saponin and FITC-loaded unmodified nanoparticles (positive control)). Caco-2 cells were incubated with different formulations for 2 h at 37°C.....77

Figure 3-3. Weight loss of unmodified (\circ) and RRH (10 μ mol)-tagged (\square) nanoparticles during vacuum-drying at 40°C over 5 days. Data are means \pm SD ($n = 3$).....79

Figure 3-4. Release of FITC-dextran **A.** 70 kDa, **B.** 500 kDa, and **C.** 2,000 kDa from either unmodified nanoparticles (Δ) or RRH (10 μ mol)-tagged nanoparticles (\blacktriangle) in HBSS, pH 7.4 with constant stirring at 300 rpm at 37°C. Data are means \pm SD ($n = 4$).....81

Figure 3-5. Release of FITC-dextran 2,000 kDa (5 mg) at **A.** 37°C and **B.** 4°C from either unmodified nanoparticles (\bullet), RRH (100 μ mol)-tagged nanoparticles (\blacksquare), RR (100 μ mol)-associated nanoparticles (\blacktriangle), and R4acaH (34 μ mol)-associated nanoparticles (\blacktriangledown) in HBSS with constant stirring at 300 rpm. Data are means \pm SD ($n = 3$). R4acaH (34 μ mol)-associated nanoparticles had similar release as unmodified nanoparticles at **B.** 4°C.....83

Figure 3-6. Viability of Caco-2 cells (seeded for 2 days) incubated with microemulsion (\bullet), RRH solution (\blacktriangledown), unmodified nanoparticles (\blacksquare), physical mix of unmodified

nanoparticles + RRH solution (◆) and RRH (100 μmol)-tagged nanoparticles (▲). Cells were incubated for 2 h at 37°C, determined using the one step MTS viability assay (Kumar <i>et al.</i> , 2014). Data are means ± SD ($n \geq 2$).	85
Figure 3-7. Viability of fully differentiated Caco-2 cell monolayer (grown for 21 - 28 days) incubated with unmodified nanoparticles (●), RR (100 μmol)-associated nanoparticles (■), RRH (100 μmol)-tagged nanoparticles (▲) and R4acaH (34 μmol)-associated nanoparticles (▼) for 2 h at 37°C, determined using one step MTS assay. Data are means ± SD ($n = 3$).	86
Figure 3-8. Cellular association of different nanoparticle formulations (12.5 μg/mL) in Caco-2 cells (seeded for 2 days) at 37°C. Data are means ± SD ($n = 6$).	89
Figure 3-9. Population of cells associated with different FITC-dextran formulations based on fluorescence intensity; Blank (-); FITC-dextran solution (-); Unmodified nanoparticles (-); RR (100 μmol)-associated nanoparticles (-); RRH (100 μmol)-tagged nanoparticles (-); and R4acaH (34 μmol)-associated nanoparticles (-).	90
Figure 3-10. Confocal images of an undifferentiated Caco-2 cell. Cells were treated with unmodified nanoparticles (12.5 μg/mL) loaded with FITC-dextran for 2 h at 37°C. A shows the orthogonal sections of the cell and B shows the cross-sections of the cell in descending order (from the apical to the basolateral). The unmodified nanoparticles (Green) in the Caco-2 cell labeled with membrane stain, CellMask® (red) and nucleus stain, DAPI (blue).	94
Figure 3-11. Confocal images of an undifferentiated Caco-2 cell. Cells were treated with RRH (100 μmol)-tagged nanoparticles loaded with FITC-dextran (12.5 μg/mL) for 2 h at 37°C. A shows the orthogonal sections of the cell and B shows the cross-sections of the cell in ascending order (from the basolateral to the apical). The RRH (100 μmol)-tagged nanoparticles (Green) in the Caco-2 cell labeled with membrane stain, CellMask® (red) and nucleus stain, DAPI (blue).	95
Figure 3-12. Cellular association of different nanoparticle formulations (12.5 μg/mL) in Caco-2 cells (grown for 2 days) at 37°C and 4°C. Data are means ± SD ($n = 2$).	97
Figure 3-13. Confocal images of an undifferentiated Caco-2 cell. Cells were treated with unmodified nanoparticles loaded with FITC-dextran (12.5 μg/mL) for 2 h at 4°C. The images show A . The nucleus stain, DAPI (blue); B . The unmodified nanoparticles loaded with FITC-dextran (green); C . The membrane stain, CellMask® (red); D . Merged fluorescence.	98

Figure 3-14. Cellular association of fully differentiated Caco-2 cell monolayer (grown for 21 to 28 days) incubated with different nanoparticle formulations at different conditions. Data are means \pm SD ($n = 4$, all 3 conditions were performed together).	100
Figure 4-1. Important particle transport processes influencing the accumulation of nanoparticles on the cell surface in <i>in vitro</i> systems containing a liquid medium (Hinderliter <i>et al.</i> , 2010).	108
Figure 4-2. The dimension and angle of centrifuge tube in type 60-Ti rotor.	113
Figure 4-3. Mass of unmodified nanoparticles recovered after centrifugation for different times and changes in the mass of nanoparticles after oven-drying for 3 days (■), 4 days (●) and 5 days (▲). Each data point is a single measurement and data has been adjusted for the mass of salts and poloxamer-407 content.	118
Figure 4-4. Release of L-His radiolabel from unmodified PECA nanoparticles (▲) and RRH (100 μ mol)-tagged nanoparticles (■) in HBSS over 3 h at 37°C. Data are means \pm SD ($n = 2$).	121
Figure 4-5. Predicted accumulation of nanoparticles on the cell surface for unmodified nanoparticles (blue) and RRH (100 μ mol)-tagged nanoparticles (red) over 4 h, simulated based on the ISDD model using Matlab [®]	122
Figure 4-6. Interaction plots of mean recovery (%) of unmodified PECA nanoparticles (●) and RRH (100 μ mol)-tagged PECA nanoparticles (■) A. from supernatant, B. after HBSS wash, C. after trypsinization wash and D. after cell lysis, over a 3 h incubation uptake study (fully differentiated Caco-2 cell monolayers) at 37°C. Data are means ($n = 8 - 9$).	126
Figure 4-7. Recovery of nanoparticles after cell lysis, adjusted for protein content, for unmodified PECA nanoparticles (unfilled) and RRH (100 μ mol)-tagged PECA nanoparticles (filled). The cellular association study was carried out with fully differentiated Caco-2 cells over 3 h incubation at 37°C. Data are means \pm SD ($n = 6$).	127
Figure 4-8. Association ratio between the nanoparticles recovered after the trypsinization wash and cell lysis (RATL) over the total nanoparticles associated (TA) over 3 h for unmodified nanoparticles (open bar) and RRH (100 μ mol)-tagged nanoparticles (black bar). Data are means \pm SD ($n = 8 - 9$).	131
Figure 4-9. Comparison between experimental data (filled) and predicted data using Matlab [®] simulations (unfilled) of cellular association of PECA nanoparticles for A.	

unmodified nanoparticles (■) and **B.** RRH (100 μmol)-tagged PECA nanoparticles (●). **C.** Cellular association of unmodified nanoparticles and RRH (100 μmol)-tagged PECA determined experimentally. Experimental data are means ± SD (*n* = 8 – 9).134

Figure 4-10. Interaction plots of mean recovery (%) of unmodified PECA nanoparticles (●) and RRH (100 μmol)-tagged PECA nanoparticles (■), **A.** after HBSS wash, **B.** after trypsinization wash and **C.** after cell lysis. Incubation was carried out for 1 h with fully differentiated Caco-2 cell monolayers and with different concentrations of poloxamer-407 (w/v) at 37°C. Data are means (*n* = 3). 137

Figure 4-11. Recovery of unmodified PECA nanoparticles (unfilled) and RRH (100 μmol)-tagged PECA nanoparticles (filled) after cell lysis with fully differentiated Caco-2 cell monolayer, adjusted for protein content. Incubation was carried out for 1 h with different concentrations of poloxamer-407 (w/v) at 37°C. Data are means ± SD (*n* = 3). 138

Figure 4-12. Unmodified PECA nanoparticles (unfilled) and RRH (100 μmol)-tagged PECA nanoparticles (filled) recovered from the supernatant, after HBSS wash, after trypsinization wash and after cell lysis. The cellular association was carried out with undifferentiated Caco-2 cells over 2 h at 37°C. Data are means ± SD (*n* = 6)..... 139

Figure 4-13. Recovery of nanoparticles after cell lysis, adjusted for protein content, for unmodified PECA nanoparticles (unfilled) and RRH (100 μmol)-tagged PECA nanoparticles (filled). The cellular association was carried out with undifferentiated Caco-2 cells over 2 h at 37°C. Data are means ± SD (*n* = 6). 140

Figure 4-14. **A.** Recovery of unmodified PECA nanoparticles (unfilled) and RRH (100 μmol)-tagged PECA nanoparticles (filled) after cell lysis with undifferentiated and fully differentiated Caco-2 cells after 2 h, adjusted for protein content. **B.** Interaction plot showing the cellular association (very strong association) of unmodified PECA nanoparticles (●) and RRH (100 μmol)-tagged PECA nanoparticles (■) in either undifferentiated or fully differentiated Caco-2 cells. Data are means (*n* = 6)..... 143

List of Tables

Table 1-1. Methods employed to associate CPPs with bioactives (Wagstaff and Jans, 2006).....	14
Table 1-2. Compositions of polymer-peptide conjugates and zeta potentials (Koschek <i>et al.</i> , 2013). P = Polymer, C = Cysteine, R = Arginine, T = Threonine.	23
Table 2-1. Different protein or peptide quantification assays and their detection mechanisms (Bilati <i>et al.</i> , 2005b; Hoffmann, 2000).	33
Table 2-2. Isocratic elution conditions for different oligoarginines.	39
Table 2-3. Characterization of unmodified and arginine-tagged nanoparticles, with or without entrapment of FITC-dextran of different molecular weights and their entrapment efficiencies. Data are means \pm SD (two independent batches). Values sharing the same letters are not significantly different, while values with different letters are significantly different. Unmodified-70, Unmodified-500, Unmodified-2000 are unmodified nanoparticles loaded with 70, 500 and 2000 kDa FITC-dextran, respectively and RRH-tagged-70, RRH-tagged-500 and RRH-tagged-2000 are RRH-tagged nanoparticles loaded with 70, 500 and 2000 kDa FITC-dextran, respectively.	46
Table 2-4. Characterization of unmodified and oligoarginine-associated nanoparticles. Data are means \pm SD (three independent batches). Values sharing the same letters are not significantly different, while values with different letters are significantly different.	48
Table 2-5. Validation of oligoarginine recovered from the microemulsion matrix. (y= area under the curve and x = mass of oligoarginine).....	49
Table 2-6. Association efficiency of oligoarginine with PECA nanoparticles. Data are means \pm SD.....	50
Table 2-7. Labeling efficiencies of RRH tagged with 3 different i-TRAQ labels. Data are means \pm SD ($n = 4$).....	50
Table 2-8. Validation of oligoarginine in Hanks Balanced Salt Solution. (y= area under the curve and x = mass of oligoarginine).	61
Table 3-1. Characteristics of polymeric nanoparticles and cellular uptake.	65
Table 3-2. Viability assays and their mechanisms of action (Riss and Moravec, 2004)...	72
Table 4-1. Parameters of HBSS medium in a 24-well cell culture dish.	114

Table 4-2. Characterization of the PECA nanoparticles radiolabeled with L-His, with or without RRH tagging. Data are means \pm SD ($n = 2$).....	119
Table 4-3. Mass balance of radiolabel (L-His) and radiolabeling efficiency of PECA nanoparticles.....	120
Table 4-4. Parameters of HBSS medium used to calculate the Debye length of PECA nanoparticles.....	124

List of Equations

Equation 1. Cell viability determined by the MTS assay.....	75
Equation 2. Stokes' Law.	109
Equation 3. Stokes-Einstein equation.....	109
Equation 4. The <i>In vitro</i> Sedimentation, Diffusion and Dosimetry (ISDD) model.	110
Equation 5. Radiolabeling efficiency (RE).	115
Equation 6. Accuracy of scintillation assay.	117
Equation 7. Debye length.	123
Equation 8. Sedimentation rate of nanoparticles.....	171
Equation 9. Sedimentation rate based on maximum sedimentation distance, h and Stokes' Law.	171

List of Abbreviations

In alphabetical order

a.u.	Arbitrary units
ACS	American Chemical Society
AEE	Apical early endosomes
AFM	Atomic force microscopy
ANOVA	Analysis of variance
CARS	Coherent anti-Stokes Raman scattering
CID	Collision induced dissociation
CID-MS/MS	Collision induced dissociation tandem mass spectrometry
CPPs	Cell-penetrating peptides
DAD	Diode array detector
DFO	Deferoxamine
DLS	Dynamic light scattering
DOTA	1,4,7,10-tetra-azacyclododecane-1,4,7,10-tetraacetic acid
D-R10	D-deca-arginine
D-R6	D-hexa-arginine
D-R8	D-octa-arginine
ECA	Ethylcyanoacrylate
ER	Endoplasmic reticulum
FACS	Fluorescence-assisted cell sorting
FBS	Fetal bovine serum
FITC	Fluorescein isothiocyanate
GnRH	Gonadotropin-releasing hormone
HBSS	Hanks balanced salt solution
HDCA	Hexadecylcyanoacetate
HEPES	2-[4-(2-hydroxyethyl)piperazin-1-yl] ethanesulfonic acid
His	Histidine
HPLC	High-performance liquid chromatography
HPMA	N-(2-hydroxypropyl) methacrylamide
i.d.	Internal diameter
ISDD	<i>In vitro</i> Sedimentation, Diffusion and Dosimetry
LDH	Lactate-dehydrogenase
LH	Luteinizing hormone
L-His	L-Histidine
LoD	Limit of detection
LoQ	Limit of quantitation
MALDI	Matrix-assisted laser desorption/ionization
MDR1	Multiple drug resistance protein 1
MePECA	Methxypoly(ethylene glycol) cyanoacetate
MRI	Magnetic resonance imaging
MS	Mass spectra/spectrum

MSNs	Mesoporous silica nanoparticles
NMR	Nuclear magnetic resonance
PACA	Poly(alkylcyanoacrylate)
P_{app}	Apparent permeability coefficient
PBS	Phosphate buffered saline
PECA	Poly(ethylcyanoacrylate)
PFBT	Poly [(9,9-dioctylfluorenyl-2,7-diyl)-co-(1,4-benzo-(2,1',3)-thiadazole)]
P-gp	P-glycoprotein
PIBCA	Poly(isobutylcyanoacrylate)
PLA	Poly(lactic acid)
PLGA	Poly(lactic-co-glycolic)acid
PMF	Potential of mean force
R	Arginine
R10	Deca-arginine
R4	Tetra-arginine
R4acaH	Tetra-arginine-aminocaproic acid-histidine
R6	Hexa-arginine
R7	Hepta-arginine
R8	Octa-arginine
R8H2	Octa-arginine-di-histidine
R9	Nona-arginine
RATL	Ratio between the nanoparticles recovered after the trypsinization wash and cell lysis
RCA	Rhodamine B cyanoacetate
RE	Radiolabeling efficiency
REC	Recycling endosome compartment
RH	Arginine-histidine
RP-HPLC	Reversed-phase high-performance liquid chromatography
RR	Di-arginine
RRH	Di-arginine-histidine
SD	Standard deviation
SDS	Sodium dodecyl sulfate
SIOS	Scanning ion occlusion spectroscopy
TA	Total nanoparticles associated
TATp	TAT-peptide
TCNP	Tri-block co-polymer nanoparticles
TFA	Trifluoroacetic acid
TOF	Time of flight
USA	United States of America
UV	Ultraviolet
XPS	X-ray photoelectron spectroscopy

CHAPTER ONE

General introduction

1.1. Challenges in oral drug delivery

The oral route is a safe, convenient and cost effective route of drug administration (Harvey *et al.*, 2011). Successful use of therapeutic peptides and proteins in treating diseases or contraception in pest control, has further emphasized the need for oral formulations as currently these therapeutic peptides and proteins are restricted to the parenteral route due to low oral bioavailability (Cowan, 1996; Pisal *et al.*, 2009; Rabanel *et al.*, 2012). The low oral bioavailability of therapeutic peptides and proteins, such as insulin with a bioavailability of less than 2% (Ghilzai, 2003), is due to the presence of many oral barriers that exist within the oral route (Gundogdu and Yurdasiper, 2014).

There are several chemical barriers present in the gastrointestinal tract that degrade ingested peptides or proteins. These chemical barriers include a range of pH conditions from pH 1.7 to 6.4 (Kalantzi *et al.*, 2006), proteolytic enzymes (i.e. pepsin) in the stomach (des Rieux *et al.*, 2006; Jung *et al.*, 2000), endopeptidases (such as pepsin, chymotrypsin and trypsin) at the brush border membrane in the intestines (Langguh *et al.*, 1997; Reis *et al.*, 2006; Schilling and Mitra, 1991; Tenhoor and Dressman, 1992; Wen *et al.*, 2002a; Wen *et al.*, 2002b) and intracellular enzymes (such as cathepsins) (Jung *et al.*, 2000; Reis *et al.*, 2006; Wen *et al.*, 2002b) in the lysosomal compartments of the enterocytes. In addition to the chemical barriers in the gastrointestinal tract, there are physical barriers that further hinder the absorption of proteins and peptides. The mucous layer adjacent to the epithelium, which is mainly composed of glycoproteins (mucins), along the gastrointestinal tract can reduce the absorption of peptides, proteins and particulates (Norris *et al.*, 1998) by preventing direct contact with the epithelial cells (Gruber *et al.*, 1987). The enterocytes, joined together by tight junctions, impede the passage of charged macromolecules (Gullberg, 2005; Pauletti *et al.*, 1997; Salama *et al.*, 2006; Van Itallie *et al.*, 2003).

Enterocytes can also expel internalized substrates, such as toxins or therapeutic drugs from the cell through active efflux transporters (such as P-glycoproteins) (Aungst, 2000; Aungst *et al.*, 1996; Bhattacharjee *et al.*, 2013; Hamman *et al.*, 2005; Sorensen and Dearing, 2006). However, this efflux mechanism mostly applies to lipophilic compounds and is unlikely to affect the absorption of hydrophilic peptides and protein bioactives (Aungst *et al.*, 1996).

The presence of gut microflora can also potentially cause chemical alteration to peptide or protein bioactives (Woitiski *et al.*, 2008) as the microflora are capable of several metabolic reactions, such as deglucuronidation, decarboxylation, reduction of double bonds, ester and amide hydrolysis and dehydroxylation (Drasar and Hill, 1974; Simons *et al.*, 2005). The chemical change(s) in the bioactive structure facilitated by bacteria can reduce absorption due to a change in hydrophobicity (Woitiski *et al.*, 2008) or even impair the bioactivity of the peptide or protein (Brader *et al.*, 2002).

1.2. Understanding the gastrointestinal absorption mechanisms

In order to improve oral absorption, an understanding of the absorption mechanisms in the gastrointestinal tract is required. Absorption of food and nutrients or drugs in the gastrointestinal tract occurs through several mechanisms (**Figure 1-1**); (i) paracellular transport; (ii) endocytotic uptake; (iii) passive transport and; (iv) carrier-mediated transport (Aprahamian *et al.*, 1987; Eldridge *et al.*, 1990; Gullberg, 2005; Michel *et al.*, 1991).

The paracellular route between the enterocytes is only applicable to small charged, hydrophilic molecules (Gullberg, 2005) as the pore of a tight junction is about 10 to 50 Å (Salama *et al.*, 2006) or a diameter of 0.8 to 1.6 nm (Zhou, 1994). Due to the small size of the pore, Salama *et al.* (2006) speculated that any molecule bigger than 15 Å in molecular radius (approximately 3.5 kDa) is unlikely to be able to pass through the membrane via the paracellular route. Although Mathiowitz and co-workers have reported particles in the size range of 40 to 120 nm were able to translocate across the epithelium using the paracellular route (Mathiowitz *et al.*, 1997), larger molecules generally would require the aid of permeation enhancers, such as bile salts (Raimondi *et al.*, 2008) and chelating agents (Lemmer and Hamman, 2013) to utilize the paracellular route.

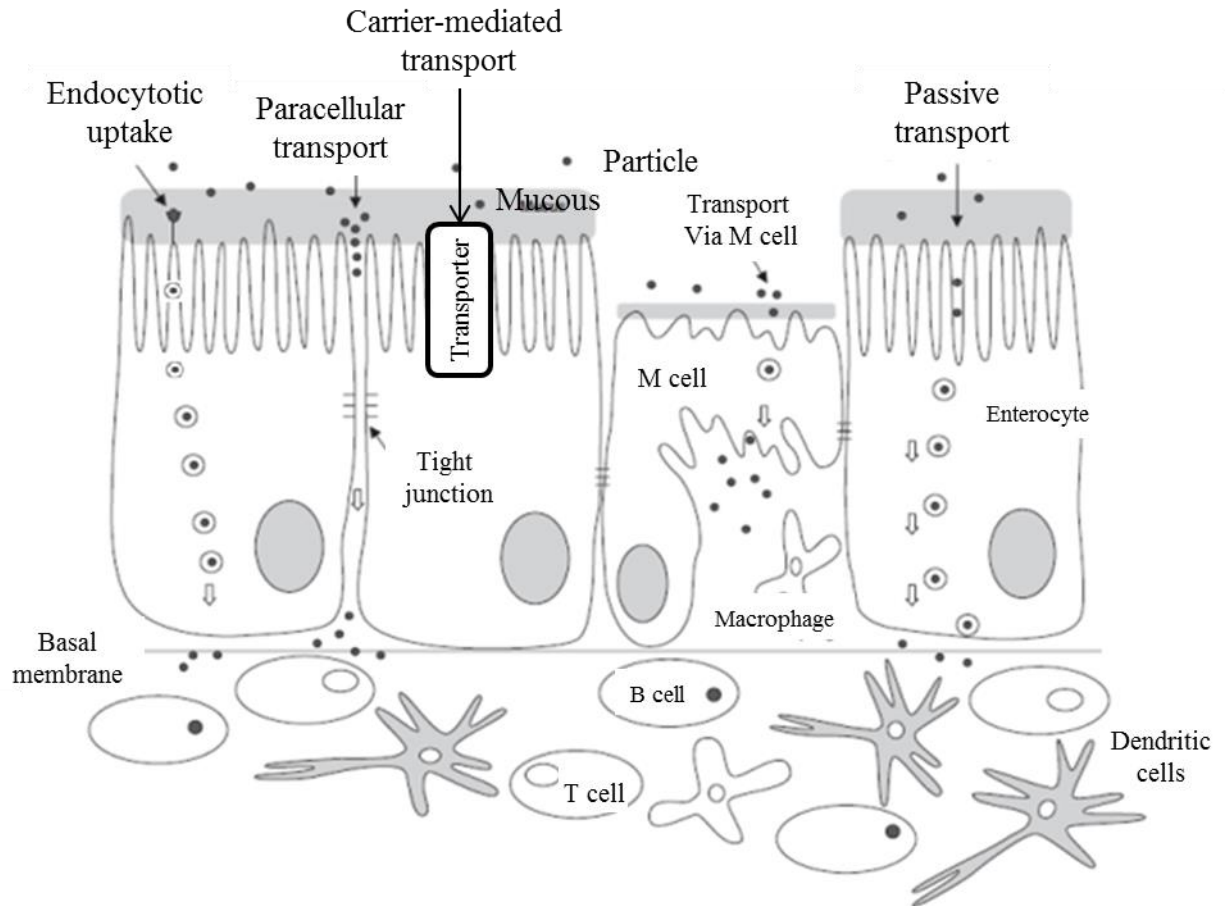


Figure 1-1. Schematic diagram of intestinal structures and translocation routes across the intestinal epithelium (modified from Woitiski *et al.* (2008)).

Endocytosis is the general mode of entry into enterocytes for large, hydrophilic macromolecules (Rejman *et al.*, 2004). Endocytosis involves the uptake of extracellular materials at the apical membrane of the cell through the formation of vesicles (endosomes) from the lipid membrane, followed by the internalized endosomes release and transport to subcellular compartments of the enterocytes (Jung *et al.*, 2000). The endocytotic process is saturable and energy-dependent (Woitiski *et al.*, 2008). Successful oral absorption via endocytosis requires the endocytosed materials to be transported to the basolateral of the enterocytes and released into the blood stream.

Other modes of therapeutic peptide or protein absorption include passive transport and carrier-mediated transport. Passive transport applies to small amphipathic molecules that are able to partition into the lipid bilayers, followed by passive diffusion through the epithelial cell layer. These amphipathic molecules have a narrow range of molecular size (less than 500 Da), a net neutral charge, less than 5-H bond donors and 10-H bond acceptors (Lipinski *et al.*, 2001). The carrier-mediated transport is facilitated by protein transporters on the membrane of enterocytes and this allows the regulation of compound-trafficking in and out of the cell (Woitiski *et al.*, 2008). Certain substrates, such as sugar, amino-acids, oligopeptides, organic acids, vitamins, co-factors and nucleosides are able to be absorbed through carrier-mediated transport, using influx transporters (Daugherty and Mrsny, 1999; Griffith and Jarvis, 1996; Tsuji and Tamai, 1996). Therapeutic peptides and proteins are very unlikely to cross the intestinal barrier through passive transport due to their hydrophilic nature of having log P-values less than 0 (Camenisch *et al.*, 1998). Therefore, peptides or proteins are more likely to be absorbed by the enterocytes via active transcellular transport using specific carriers (Fasano, 1998) or through endocytosis (Swaan, 1998).

The extent of absorption following oral administration is mainly dependent on; (i) the physicochemical properties of the therapeutic peptides or proteins (Nel *et al.*, 2009); (ii) the transit time in the gut and; (iii) the properties of the intestinal barrier (Woitiski *et al.*, 2008). The peptides or proteins absorbed by the enterocytes are subjected to first pass metabolism in the liver before the peptides or proteins are bioavailable to the site(s) of action in the body (Woitiski *et al.*, 2008). Alternatively, peptides and proteins can be absorbed through M-cells, which have a thinner mucous layer compared to enterocytes as well as bypassing the first pass metabolism in the liver (Ermak and Giannasca, 1998; Jung *et al.*, 2000) (**Figure 1-1**). However, peptides and proteins that gain entry through the M-cells would be phagocytosed and an immune response would be mounted to destroy the foreign peptides and proteins. Therefore, the absorption through the M-cells is more of a promising route for oral vaccination (Kraehenbuhl and Neutra, 2000) rather than oral delivery (des Rieux *et al.*, 2006).

1.3. General mechanisms of cellular uptake

As the enterocytes provides a potential route of entry into the blood circulation of the body via endocytosis, studies have been conducted to understand the endocytotic processes (Gullberg, 2005). The cellular uptake mechanisms of the enterocytes can be studied *in vitro* using the Caco-2 (human epithelial colorectal adenocarcinoma) cell line. When the Caco-2 cells are cultured on a cell culture insert filter, such as a Transwell[®] for 21 to 28 days, the cells form a confluent and fully differentiated monolayer. The fully differentiated Caco-2 cell monolayer resembles the enterocytes and expresses tight junctions, microvilli and a number of enzymes and transporters, including the P-gp transporter (Pinto *et al.*, 1983; Thompson *et al.*, 2012). Caco-2 cells can also be co-cultured with goblet cells to provide a better *in vitro* intestinal model with the presence of a mucous layer (Hilgendorf *et al.*, 2000). However, different culturing protocols as well as different sources of Caco-2 cells may result in variation in the morphology and characteristics of the cells, which makes the comparison between the results obtained from different laboratories challenging (Sambuy *et al.*, 2005).

Endocytotic events or processes can be divided into phagocytosis and pinocytosis (**Figure 1-2**). In the enterocytes, endocytotic events comprise only of pinocytosis, which can be sub-categorized into macropinocytosis (fluid phase endocytosis); clathrin-mediated endocytosis; caveolar-dependent endocytosis and clathrin- and caveolar-independent endocytosis (i.e. flotillin-dependent endocytosis) (Buda *et al.*, 2005; Conner and Schmid, 2003; Doherty and McMahon, 2009; Gullberg, 2005). These mechanisms are distinguished by the size of the vesicles formed upon internalization, their regulation, the intracellular trafficking route (Foged and Nielsen, 2008) and the nature of the extracellular materials taken up by the cell (Aderem and Underhill, 1999). This section explains the general background of the uptake routes available in the enterocytes, while endocytosis of nanoparticulates will be further explained in **Chapter 3 (Section 3.1.1)**.

Macropinocytosis is an active, actin-dependent endocytic pathway and involves the non-specific cellular uptake of large volumes of bulk fluid (des Rieux *et al.*, 2006; Jones, 2007). Macropinocytosis usually occurs from highly folded regions of the plasma membrane (Doherty and McMahon, 2009). Macropinocytosis differs from phagocytosis as macropinocytosis is not receptor mediated (Maniak, 2001).

Clathrin-mediated endocytosis is required for the continuous uptake of essential nutrients (i.e. cholesterol-laden low-density lipoprotein particles and iron-laden transferrin) (Rothmann, 1994). Clathrin coated vesicles are approximately 120 nm in diameter (Doherty and McMahon, 2009; Rothmann, 1994). In addition, this pathway is also crucial for intercellular communication during tissue and organ development in somatic cells (Di Fiore and De Camilli, 2001; Seto *et al.*, 2002) and internalizing membrane pumps that control the transport of small molecules and ions across the plasma membrane as well as recapturing small serum proteins after filtration through the kidney (Conner and Schmid, 2003).

Caveolar vesicles are described as caveolin-coated, flask-shaped invaginations of about 60 to 80 nm in diameter, found at the basolateral membrane of epithelial cells (Parton and Simons, 2007; Torgersen *et al.*, 2001). Caveolar-mediated endocytosis is probably less applicable for drug uptake due to the small invagination sizes of the endosomes formed (Gullberg, 2005) and because it is located at the basolateral side of the membrane, rather than on the apical side where absorption occurs.

The size of endosomes formed by clathrin- and caveolar-independent endocytosis are about 40 to 90 nm in diameter (Rothmann, 1994). Clathrin- and caveolar-independent endocytosis have been shown to internalize extracellular fluid, receptors on the membrane, glycosylphosphatidylinositol-linked proteins and other molecules (Doherty and McMahon, 2009). Types of clathrin- and caveolar-independent endocytosis identified include flotillin-dependent, clathrin-independent carrier (CLIC) / Glycosylphosphatidylinositol-anchored protein-enriched early endosomal compartment (GEEC)-type, IL2R β -dependent and Arf6-dependent endocytosis (Doherty and McMahon, 2009). Clathrin-independent endocytosis is important for cellular polarization or differentiation, motility, regulation of signaling and normal cell growth (Sandvig *et al.*, 2011). In addition, clathrin-independent endocytosis is essential for internalization and removal of damaged membrane to ensure cell survival (Sandvig *et al.*, 2011).

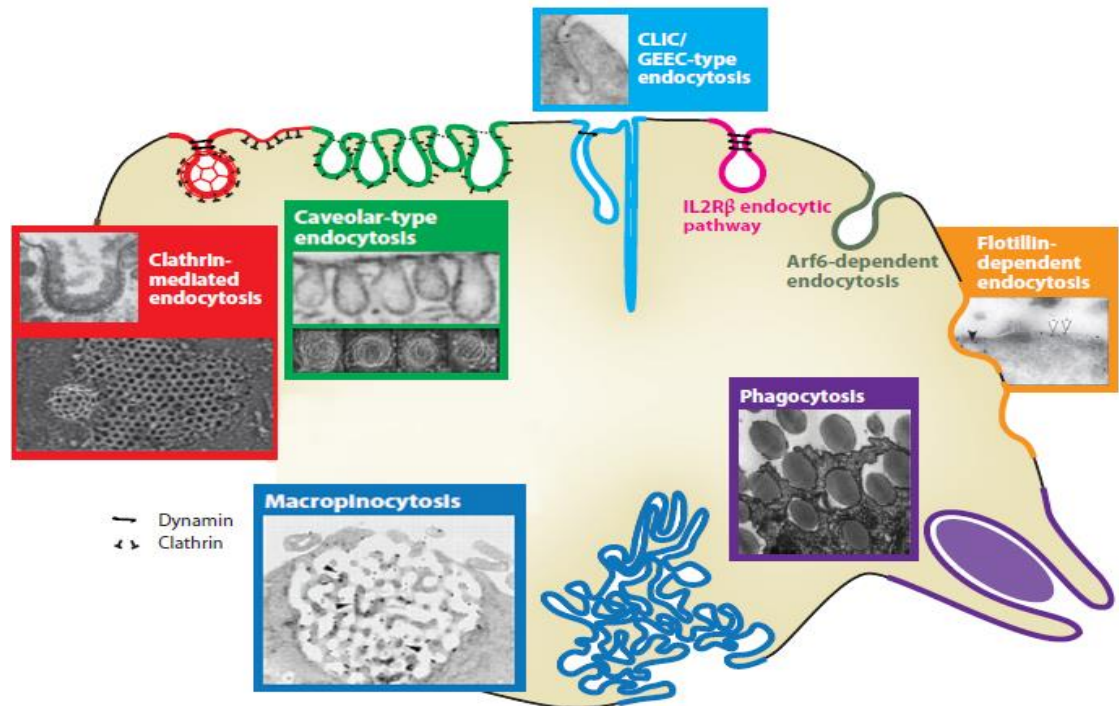


Figure 1-2. Types of endocytosis, accompanied by transmission and scanning electron microscope images in a cell (modified from (Doherty and McMahon, 2009)).

1.4. Oral formulations

Rapid degradation and the lack of cellular permeation of peptides and proteins make the oral administration of therapeutic peptides and proteins challenging (Goldberg and Gomez-Orellana, 2003; Khafagy *et al.*, 2007; Morishita and Peppas, 2006; Owens *et al.*, 2003). An oral formulation is required to; (i) protect the bioactive against the hostile acidic environment in the stomach; (ii) protect the bioactive against enzymatic degradation throughout the digestive system and intracellular enzymatic activity upon absorption and; (iii) enhance penetration of the bioactive through the mucous layer and subsequently facilitate gut uptake.

Several strategies have been adopted in attempts to overcome oral delivery barriers, including chemical modifications (Blanchfield *et al.*, 2005; Mahato *et al.*, 2003), co-administration of enzyme inhibitors (Wen *et al.*, 2002a) and permeation enhancers (Mahato *et al.*, 2003), employing particulate carrier systems (Bala *et al.*, 2004; Cartiera *et al.*, 2009; Derakhshandeh *et al.*, 2011; Graf *et al.*, 2009a) and targeting the specific

absorption site(s) in the intestines (Harush-Frenkel *et al.*, 2007; Karn *et al.*, 2011; Sawant *et al.*, 2008).

A promising formulation to improve oral absorption is to incorporate the therapeutic peptide or protein into particulate carrier systems, such as liposomes and nanoparticles. These colloidal carriers are speculated to enhance bioavailability by providing physical protection to the bioactives from degradation (Carino and Mathiowitz, 1999; Damgé *et al.*, 1988; Damgé *et al.*, 1997; Lowe and Temple, 1994; Vauthier *et al.*, 2003).

Polymeric nanoparticles have been used as drug carriers because they: (i) provide protection of bioactive and uptake enhancement (due to their submicron size) (Kafka *et al.*, 2010b; Lowe and Temple, 1994; Mathiowitz *et al.*, 1997; Tobio *et al.*, 1998); (ii) provide greater stability in the gastrointestinal tract than other colloidal carriers, such as liposomes (Galindo-Rodriguez *et al.*, 2005); (iii) have physicochemical characteristics that can be manipulated (i.e. zeta potential and hydrophobicity, bioactive release properties (i.e. delayed, prolonged, sustained or triggered) and programmed biological behaviour (i.e. targeting, bioadhesion and improved cellular uptake) via the use of various polymer materials (Galindo-Rodriguez *et al.*, 2005)); (iv) could undergo surface modification via chemical grafting such as PEGylation (Galindo-Rodriguez *et al.*, 2005) and; (v) are able to increase the solubility of poorly soluble bioactive by entrapping of the bioactive inside the nanoparticles to reduce or avoid precipitation of the bioactive (Wang and Zhang, 2012).

1.4.1. Poly(alkylcyanoacrylate) (PACA) nanoparticles

The size of polymeric nanoparticles ranges from 10 nm to 1000 nm (des Rieux *et al.*, 2006). Nanoparticles are speculated to cross gut epithelial cells through both transcellular and paracellular pathways (Graf *et al.*, 2009a). It has been reported that reduced glycaemia in diabetic rats by 50 to 60% was observed when the rats were given insulin-loaded poly(isobutyl-cyanoacrylate) (PIBCA) nanoparticles via intragastric administration, whereas administration of an insulin solution did not affect the glycaemia (Dамgé *et al.*, 1988). Administering the fertility control agent, D-Lys⁶-GnRH, loaded in poly(ethylcyanoacrylate) (PECA) nanoparticles intracaecally also significantly stimulated the release of luteinizing hormone (LH) in the common brushtail possums, compared to a D-Lys⁶-GnRH solution (Kafka *et al.*, 2011). The area under the curve of the mean plasma

LH concentration over 190 min was 367.9 ng.min/mL in the brushtail possums given D-Lys⁶-GnRH-encapsulated PECA nanoparticles, compared to 85.95 ng.min/mL in the brushtail possums given D-Lys⁶-GnRH solution (Kafka *et al.*, 2011). The increase in biological response to insulin and D-Lys⁶-GnRH demonstrated that more protein bioactive was absorbed into the systemic blood circulation when loaded in PACA nanoparticles compared to a solution. While the result of these *in vivo* studies suggests that the PACA nanoparticles may translocate across the enterocytes, the uptake and translocation of the nanoparticles themselves has yet to be shown.

Bioactives can be either; (i) entrapped in the nanoparticles (encapsulation) or; (ii) adsorbed to the surface of the nanoparticles (sorption) (Krauel *et al.*, 2004). The resulting products can be either nanospheres or nanocapsules, depending on the method of entrapment (**Figure 1-3**). Polymeric nanoparticles can be produced from the polymerization of monomers in an aqueous acidic phase (Couvreur *et al.*, 1979) and interfacial polymerization of (sub-micron) emulsions (Al Khouri Fallouh *et al.*, 1986; Couvreur *et al.*, 1979; Weiss *et al.*, 2007) or microemulsions (Watnasirichaikul *et al.*, 2002a). Although other production methods of nanoparticles, such as nanoprecipitation (Monza da Silveira *et al.*, 2004) and emulsification-solvent evaporation (Li *et al.*, 2001a; Li *et al.*, 2001b) have also been reported, nanoparticles produced using a biocompatible microemulsion may be preferred as the purification of the nanoparticles is not required (Watnasirichaikul *et al.*, 2002a) and the biocompatible microemulsion may provide additional permeation enhancement (Constantinides *et al.*, 1995; Ritschel, 1991).

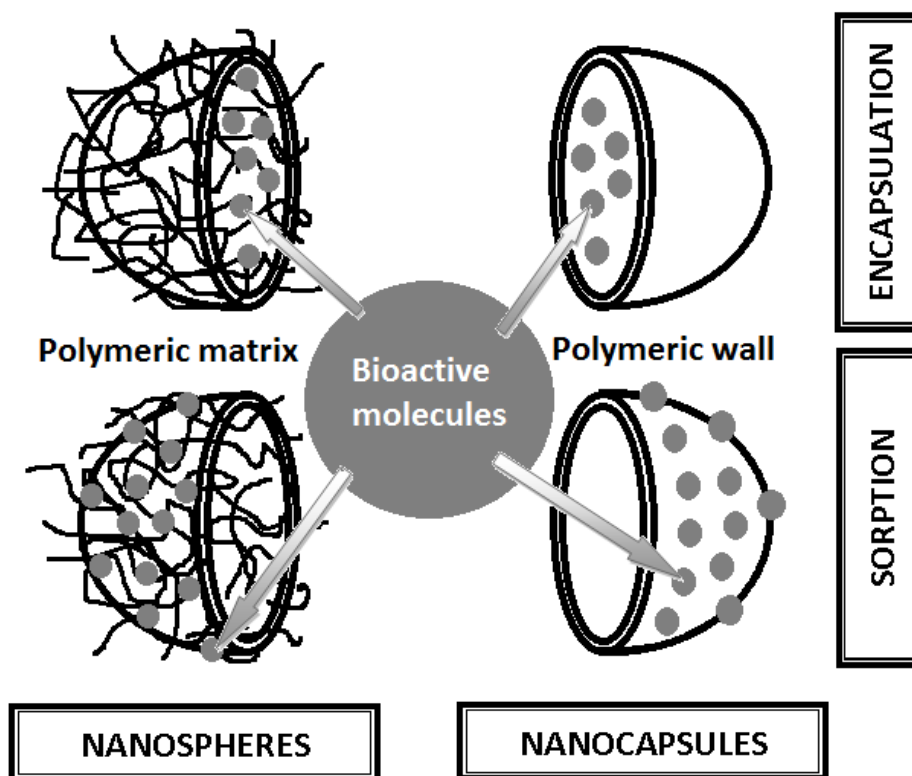


Figure 1-3. Types of nanoparticles and localization of bioactive molecules following encapsulation/sorption (reproduced from Krauel *et al.* (2004)).

Interfacial polymerization of biocompatible microemulsions was developed by Watnasirichaikul *et al.* (2002) to avoid the use of toxic organic solvents so that the separation of the particles from the templates was not necessary (Watnasirichaikul *et al.*, 2000) and the formulation may benefit from the permeability enhancing effects of the microemulsion (Constantinides *et al.*, 1995; Ritschel, 1991). The microemulsion templates can be flexible because the type of microemulsion template does not appear to influence the properties of the resulting nanoparticles (Graf *et al.*, 2008). Therefore, the microemulsion template can be formulated according to the solubility of the bioactive to be entrapped. However, the type of microemulsion template (together with the monomer concentration) does change the entrapment efficiency of the bioactives (Graf *et al.*, 2009b; Krauel *et al.*, 2005). The type of microemulsion template also influences the distribution of the bioactive within the nanocarriers (Graf *et al.*, 2009b), whereas the monomer concentration influences the wall thickness (Watnasirichaikul *et al.*, 2002a) or the number of the particles formed (Graf *et al.*, 2009b). For example, a high entrapment efficiency can

be achieved by utilizing a high monomer concentration and a small aqueous volume to concentrate the hydrophilic bioactive (Graf *et al.*, 2009b).

PACA nanoparticles have a low surface charge, with a negative zeta potential of between -6 to -20 mV in distilled water due to the acrylic acid head groups (Müller *et al.*, 1992; Pitaksuteepong *et al.*, 2002). These PACA nanoparticles are considered to be biocompatible (Vauthier *et al.*, 2003). The major *in vivo* degradation pathway is through the ester hydrolysis of the polymer back bone, catalysed by esterases (Grislain *et al.*, 1983; Schere *et al.*, 1994). The degraded by-products, such as alkylalcohol and poly(cyanoacrylic-acid) are then excreted from the body via the kidneys (Vauthier *et al.*, 2003). The *in vivo* stability of the PACA nanoparticles is dependent on the alkyl side chain with the longer chain having a slower degradation rate (Grislain *et al.*, 1983; Leonard *et al.*, 1966).

1.4.2. Cell-penetrating peptides (CPPs) as penetration enhancers

The discovery of cell-penetrating peptides (CPPs) has opened up a new chapter in oral delivery methodology to gain intracellular access by endocytosis (Fonseca *et al.*, 2009) and translocation across cell membranes (Fischer *et al.*, 2005; Frankel and Pabo, 1988; Green and Loewenstein, 1988). CPPs are short cationic sequences of 10 to 30 amino acids (rich in basic residues such as arginine and lysine) that can be derived from natural sources (e.g. TAT, the HIV trans-activator of transcription protein or penetratin from *Drosophila*) or constructed synthetically (Foged and Nielsen, 2008; Kersemans *et al.*, 2008). They are also known as protein transduction domains, Trojan peptides, peptide delivery vectors, membrane permeating motifs, cell permeable motifs, amphipathic model peptides (e.g. transportan (Pooga *et al.*, 2001)) or delivery peptides (Kersemans *et al.*, 2008). CPPs can be divided into three classes; (i) protein-derived peptides (short chains of protein domain, e.g. TAT peptide); (ii) model peptides (model peptides that mimic the translocation properties of known CPPs, e.g. the model amphipathic peptide) and; (iii) designed CPPs (chimeric peptides that are produced by the fusion of hydrophilic and hydrophobic domains from different sources, e.g. transportan) (Torchilin, 2007). Further understanding of the nature of CPPs led to more synthetically designed CPPs, increasing the range of CPPs currently available for drug delivery applications (Fonseca *et al.*, 2009) such as the shortening of TAT to a few amino acids (TAT-peptide (TATp)) without the loss of its penetrating ability (Vives *et al.*, 1997).

CPPs have been investigated in the delivery of proteins (Fawell *et al.*, 1994), nucleic acids (Chiu *et al.*, 2004), small molecule therapeutics (Rothbard *et al.*, 2000), quantum dots (Santra *et al.*, 2005) and magnetic resonance imaging (MRI) contrast agents (Lewin *et al.*, 2000) to their targeted sites, such as the brain. CPPs have also been shown to be able to increase the oral bioavailability of proteins or peptides, by enhancing penetration through the intestinal barrier in rats (Kamei *et al.*, 2008a; Morishita *et al.*, 2007) and in intestinal Caco-2 cell models (Liang and Yang, 2005). In an *in situ* loop study, a significantly increased bioavailability was observed with insulin when the protein was physically mixed with CPPs such as D-R8 (D-octa-arginine) and L-penetratin (Kamei *et al.*, 2008a). The insulin administered enterally gave a bioavailability of 3.0% with the D-R8 mixture and 5.5 with the L-penetratin mixture compared to 0.2 with insulin alone (Kamei *et al.*, 2008a). In a similar *in situ* loop rat study, Morishita *et al.* (2007) demonstrated that insulin delivery was significantly enhanced when the insulin was covalently conjugated with oligoarginine, with a bioavailability of 4.1 for D-R6 (D-hexa-arginine), 14.1 for D-R8 and 10.9 for D-R10 (D-deca-arginine) compared to 0.4 for insulin alone. Therefore, it is speculated that oligoarginine association with insulin via covalent conjugation is more efficient at enhancing insulin permeability through the gut compared to a physical mixture of insulin and oligoarginine. An insulin-TAT conjugate was also shown to significantly improve permeability of insulin across Caco-2 monolayer, with apparent permeability coefficient (P_{app}) of $1.6 \times 10^{-5} \text{ cm.s}^{-1}$ compared to $0.2 \times 10^{-5} \text{ cm.s}^{-1}$ with insulin without TAT conjugation (Liang and Yang, 2005). Conjugating R8 to poly(lactic-co-glycolic acid) (PLGA) nanoparticles significantly enhanced intestinal insulin absorption by at 3 times, with insulin-loaded PLGA nanoparticles and insulin-loaded R8-conjugated PLGA nanoparticles having a bioavailability of 3.1% and 10.2%, respectively (Liu *et al.*, 2013). The increased absorption of insulin with R8-conjugated PLGA nanoparticles also led to significant decrease in blood glucose concentration than unmodified PLGA nanoparticles, with a reduction in blood glucose of 40% and 20%, respectively (Liu *et al.*, 2013).

CPPs are also known for their low toxicity (Foged and Nielsen, 2008; Nagahara *et al.*, 1998), which is determined by the type of CPP used, the bioactive cargo the CPP is coupled to, the length of the bioactive peptide and the dose applied (Cardozo *et al.*, 2007; Jones *et al.*, 2005). Cardozo *et al.* (2007) reported TAT is better tolerated by cells compared to penetratin, with 30 μM penetratin showing marked toxicity while TAT up to

100 μM showed negligible toxicity. The authors attributed the toxicity of penetratin to elevated lipid-binding (due to penetratin's amphipathicity) causing membrane destabilisation and permeabilisation (Cardozo *et al.*, 2007). Toxicity was also significantly increased with conjugation of a bioactive peptide to TAT compared to TAT alone, with longer TAT-bioactive conjugates resulting in more cell death (Cardozo *et al.*, 2007). The authors postulated smaller TAT-bioactive conjugates (less than 50 amino acids) would rapidly translocate into the cells, while larger TAT-bioactive conjugates were internalized via cytoplasmic vesicles (Cardozo *et al.*, 2007). Therefore, larger TAT-bioactive conjugates would induce a greater stress on the cells, thus triggering apoptosis (Cardozo *et al.*, 2007). It is also worth noting that CPPs may be tolerated differently between different cell lines and the species of subjects (such as difference in susceptibility to pancreatic beta-cell injury between humans and rodents) due to different composition of the cellular membrane (Cardozo *et al.*, 2007).

1.4.2.1. Method of CPP association to bioactive

There are two strategies to attach CPPs (**Table 1-1**) to the bioactive; (i) covalent attachment of the CPP and bioactive through fusion proteins generated from bacteria or via various types of linker molecules (Wagstaff and Jans, 2006) or; (ii) non-covalent self-assembly through ionic and/or hydrophobic interactions (Kamei *et al.*, 2008a; Kamei *et al.*, 2008b; Morishita *et al.*, 2007; Pujals *et al.*, 2006). Each type of association carries its own advantages and disadvantages (**Table 1-1**). Although covalent attachment is stable, it can be difficult to achieve (Foged and Nielsen, 2008) and could potentially decrease the efficacy or even cause a total loss of activity of the bioactive (Fonseca *et al.*, 2009). Disulfide bonds between the CPP and bioactive can be utilized to allow rapid bond degradation in the cells to release the bioactive intracellularly (Pooga *et al.*, 1998).

Although non-covalent association between CPP and bioactive can be achieved by physically mixing both compounds together, successful non-covalent association would require high binding affinity of the CPPs to the bioactive through electrostatic and/or hydrophobic interactions. As electrostatic binding is much weaker than covalent binding, the CPP-bioactive physical mixture would require a higher amount of CPP than in covalent association to increase the likelihood of bioactive associating with CPP in order to achieve effective penetration (Kamei *et al.*, 2008a; Kamei *et al.*, 2008b; Morishita *et al.*, 2007).

Table 1-1. Methods employed to associate CPPs with bioactives (Wagstaff and Jans, 2006).

	Covalent linkages	Non-covalent linkages
Association methods	<p>A</p>  <p>Fusion protein (bioactive and CPP as a single peptide/protein) generated from bacteria</p>	<p>C</p>  <p>Electrostatic interactions (and/or hydrophobic interactions)</p>
	<p>B</p>  <p>Side-chain linkages, such as peptide bonds, disulfide bridge, thiazoline ring and bifunctional linker molecule</p>	<p>D</p>  <p>“Piggy-back” attachment, where a linker group attaches covalently with CPP and non-covalently with bioactive</p>
Advantages	<p>(i) Equal ratio of CPP to bioactive required for effective penetration</p> <p>(ii) Stable covalent bonding</p>	<p>(i) Easy to achieve</p> <p>(ii) Does not modify bioactive molecule</p>
Disadvantages	<p>(i) Labour intensive</p> <p>(ii) Direct modification to bioactive molecule</p>	<p>(i) Generally requires a higher ratio of CPP to bioactive for effective penetration</p>

In addition to the possibility of covalent CPP attachment causing alteration to the bioactivity of the bioactive, the bioactive attachment can also affect the cell-penetrating properties of CPPs in various ways. These alterations could affect the internalization

mechanism, intracellular trafficking and membrane destabilizing properties of the CPPs (Zorko and Langel, 2005). Therefore, covalent coupling could potentially affect the cellular penetration ability of the CPP-bioactive conjugate and in the worst case, completely inactivates the CPP (Zorko and Langel, 2005).

Most CPP studies are presently performed in serum-free conditions, which might give misleading results due to the instability of CPP-bioactive complexes in the presence of serum components (Foged and Nielsen, 2008). As CPPs are peptides, they can be degraded by enzymes (Christiaens *et al.*, 2004; Kamei *et al.*, 2008b). Current published studies investigating the translocation of CPPs across gut epithelial cells were conducted *in situ* (in the ileum) (Morishita *et al.*, 2007) or in an *in vitro* setting (Cardozo *et al.*, 2007; Kamei *et al.*, 2013), which bypasses the degradation in the stomach. Therefore, the use of CPPs for improved gut uptake may require a formulation that shields the CPPs from acidic conditions in the stomach and high enzymatic activity in the intestine. However, some CPPs, such as penetratin, may not require such a formulation as they retain their translocation capacity even after degradation (Christiaens *et al.*, 2004; Kamei *et al.*, 2008a).

1.4.2.2. Uptake mechanisms of CPPs

The proposed mechanism for CPP uptake is that the positively charged CPPs interact with the negatively charged phosphate groups of membrane lipids by specific bidentate interactions, which then leads to uptake (Kaznessis *et al.*, 2002; Richard *et al.*, 2003). It was also demonstrated that the guanidinium head group is superior to other cationic groups in improving cellular penetration (Mitchell *et al.*, 2000; Wender *et al.* (2000)). Mitchell *et al.* (2000) postulated that the superior cellular penetration is due to the highly basic nature of the guanidinium head group ($pK_a \approx 12$), which is charged at normal physiological pH of 7.4 and able to form a stable bidentate hydrogen bond with anions such as phosphate or sulfate on the cell membrane. The exact type of uptake, either energy-dependent or energy-independent, is debatable as conflicting results have been acquired by different research groups (Derossi *et al.*, 1996; Ferrari *et al.*, 2003; Fittipaldi *et al.*, 2003; Kaplan *et al.*, 2005; Madani *et al.*, 2011; Matsuzaki *et al.*, 1997; Pouny *et al.*, 1992; Richard *et al.*, 2005; Säälük *et al.*, 2004; Wadia *et al.*, 2004; Wagstaff and Jans, 2006).

For the energy-independent uptake pathway, several mechanisms have been hypothesized (**Figure 1-4**) including inverted micelle formation (Derossi *et al.*, 1996), pore formation (Matsuzaki *et al.*, 1997), the carpet-like model (Pouny *et al.*, 1992) and the membrane thinning model (Lee *et al.*, 2005). All of the postulated models are more likely to be applicable to amphipathic CPPs, such as transportan. This is because the postulated uptake mechanisms would require the CPP with both hydrophilic and hydrophobic residues to interact with the cell membrane (Madani *et al.*, 2011).

In the inverted micelle model (**Figure 1-4 A**), the positively charged head groups and the hydrophobic residues of the CPPs are hypothesized to interact with the cell membrane, which then induces the formation of an inverted micelle that entraps the CPPs in the hydrophilic core of the inverted micelle. This is followed by the subsequent release of the CPPs from the micelle into the cell cytoplasm.

In the carpet and the membrane thinning model (**Figure 1-4 B**), it is suggested that the membrane thins as a result of cationic CPPs disrupting the integrity of the negatively charged phospholipids (Lee *et al.*, 2005; Pouny *et al.*, 1992) as well as hydrophobic residues of the CPPs interacting with the hydrophobic tails of the lipid membrane. Upon successful translocation of the CPPs across the membrane, the membrane is expected to return to its normal state.

In the pore formation model (**Figure 1-4 C**), it is postulated that the CPPs would form bundles on the membrane surface. The hydrophilic residues of the CPPs would form the pore within the bundles, while the hydrophobic residues of the CPPs would interact with the cell membrane. The formed hydrophilic pore would allow other CPPs or bioactive to pass into the cytoplasm. The pore formations are expected to be transient, as permanent or long lasting pore formations would lead to a leakage of intracellular contents and cell death.

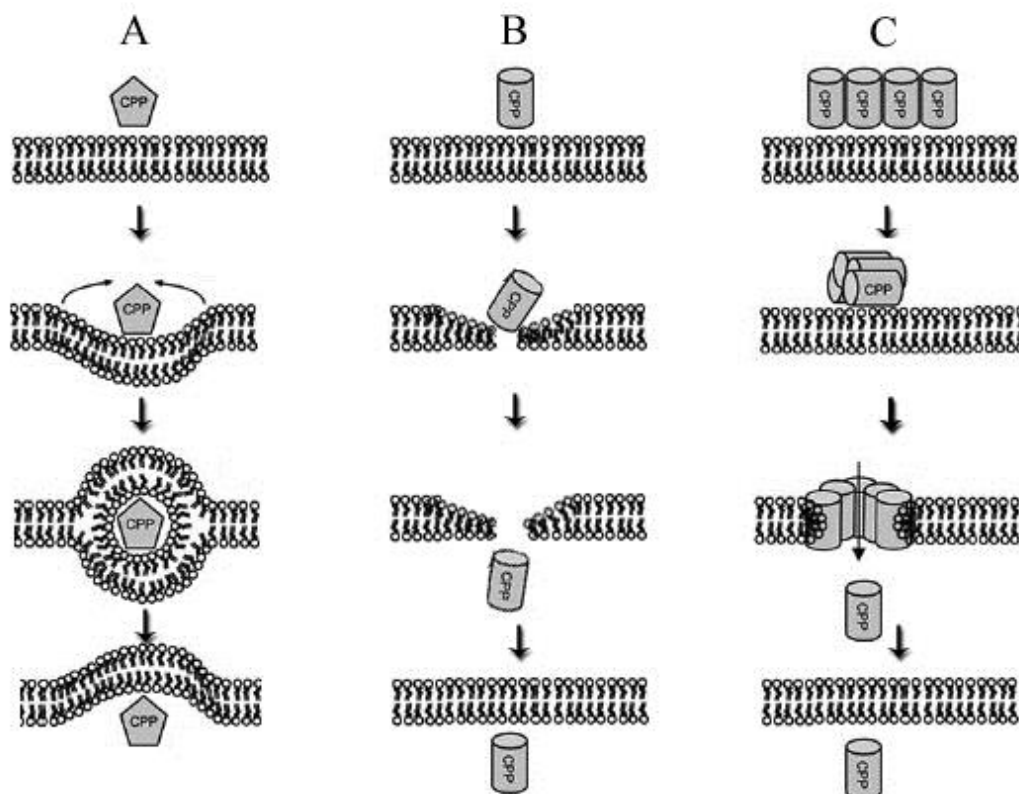


Figure 1-4. Proposed models of the energy-independent membrane translocation mechanism; A. Inverted micelle model, B. Carpet and membrane thinning model, C. Pore-formation model (Wagstaff and Jans, 2006).

Recently, Li *et al.* (2013) hypothesized another translocation mechanism for polyarginine and polyarginine-associated nanoparticles across membranes, based on the potential of mean force (PMF) modelling (Li *et al.*, 2013). The PMF generated from molecular dynamics simulation is able to determine the energy change in a lipid bilayer membrane system. Therefore, the interaction of the polyarginine with the lipid bilayer can be postulated based on the favourable energy state of the system. The PMF of a single nona-arginine (R9) peptide interacting with the bilayer suggested that the R9 peptide can adsorb onto the outer leaflet surface of the bilayer, leading to a favourable low free energy (Li *et al.*, 2013). Although the R9 peptide would prefer to stay in the inner leaflet of the bilayer to maintain an even more favourable lower energy in the PMF, this phenomenon does not occur due to the high energy barrier generated by the hydrophilic R9 peptide and lipid tails of the bilayer (Li *et al.*, 2013). Li *et al.* (2013) suggested translocation across the

membrane would require multiple nona-arginine (R9) of more than 5 peptides to suppress the high energy barrier as the energy barrier is too much for a single peptide to overcome by thermal motion (Li *et al.*, 2013). For R9-conjugated nanoparticles, several R9-conjugated particles would be required to be adsorbed onto the outer leaflet surface of the bilayer to overcome the high energy barrier for effective penetration across the membrane. However, the amount of particles, adsorbed onto the outer leaflet surface of the membrane, required for effective membrane penetration would be proportional on the size of the particles (Li *et al.*, 2013).

Contrary to energy-independent uptake pathways, CPPs have also been shown to be internalized into cells through energy-dependent uptake pathways, such as macropinocytosis (Kaplan *et al.*, 2005; Wadia *et al.*, 2004), caveolin-dependent endocytosis (Ferrari *et al.*, 2003; Fittipaldi *et al.*, 2003) and clathrin-mediated endocytosis (Richard *et al.*, 2005; Säälük *et al.*, 2004). Foged and Nielsen (2008) postulated that larger CPP conjugates are taken up by macropinocytosis due to the larger vesicles formed (1 to 5 μm), instead of other types of endocytosis that form vesicles of less than 150 nm.

The uptake mechanism for octa-arginine (R8) conjugated to a fluorescent probe has been investigated in Chinese hamster ovary (CHO) cells using confocal microscopy (Lee *et al.*, 2008). By focusing the confocal microscope on the cell surface, the time the fluorescent R8 conjugate was observed associated with the cell surface can be measured. The fluorescent R8-conjugate can either be internalized into the cells or dissociate from the cell surface or stop fluorescing due to photobleaching, which in all cases would lead to a reduced fluorescence intensity of the fluorescent-R8 conjugate associated with the cell surface (Lee *et al.*, 2008). Lee *et al.* (2008) demonstrated in a control experiment without cells that a 50% reduction in fluorescence intensity was observed within 6.9 seconds due to photobleaching. As a 50% reduction in fluorescence intensity in the cell experiments occurred significantly faster (1.1 second) than the control experiment, the reduction in fluorescence intensity was therefore attributed to the movement of the fluorescent-R8 conjugate away from the focused area of the microscope (cell surface), which could either be internalization of the fluorescent R8-conjugate into the cell or dissociation of the fluorescent-R8 conjugate from the cell surface. The authors then postulated that the reduction in the fluorescence intensity of the fluorescent-R8 conjugate observed in the cell experiment (1.1 second) was due to cellular internalization as the reduction in fluorescent

intensity due to dissociation would be expected to occur at a much faster rate (Lee *et al.*, 2008). The group then compared the fluorescent intensity reduction pattern for the R8-fluorescent conjugate to the patterns observed for a fluorescent lipid analogue-conjugate and a fluorescent transferrin-conjugate. The fluorescent lipid analogue-conjugate was expected to passively diffuse into the cells, while the fluorescent transferrin-conjugate was expected to be internalized via endocytosis. As the fluorescence movement of R8 fluorescent-conjugate was similar to the pattern observed with fluorescent transferrin-conjugate and did not match the movement of fluorescent lipid analogue-conjugate, Lee *et al.* (2008) postulated the R8-conjugate to be internalized into the cells via endocytic uptake processes. However, it is also possible for the R8 fluorescent-conjugate to gain entry into the cell via other energy-independent pathways, such as via membrane disruption, which may generate a similar fluorescent movement as fluorescent transferrin-conjugate. Therefore, it is only appropriate for Lee *et al.* (2008) to conclude that the R8-fluorescent conjugate did not passively diffuse into the cells. Lee *et al.* (2008) also demonstrated that further addition of excess free R8 to the treatment of fluorescent R8-conjugate increased the rate and extent of internalization. Therefore, a high concentration of R8 may augment the uptake of fluorescent R8-conjugate.

The conflicting results in uptake mechanisms suggested in different studies could be explained by the use of different cell models and varying culturing conditions, such as the incubating medium. The uptake mechanism is also highly dependent on the type of CPP and the concentration of CPP used (Duchardt *et al.*, 2007; Kamei *et al.*, 2013; Tünnemann *et al.*, 2006). For example, although D-penetratin can bind strongly to insulin through electrostatic and hydrophobic interactions leading to increased cellular uptake, its permeation across the Caco-2 monolayer was poor as the D-penetratin/insulin complex remained in the intracellular compartment (Kamei *et al.*, 2013). This was not the case for L-penetratin, which underwent rapid degradation intracellularly and was able to release its insulin load for translocation (Kamei *et al.*, 2013). The group also demonstrated that the proportion of CPP that associated non-covalently with the bioactive is also dependent on the CPP concentration applied (Kamei *et al.*, 2013). Kamei *et al.* (2013) then further showed that a high concentration of D-octa-arginine (D-R8) ($\geq 20 \mu\text{M}$) was internalized in Caco-2 cells utilizing multiple pathways, both energy-dependent as well as energy-independent pathways. They also studied the uptake kinetics of different D-R8 concentrations in the absence of insulin, in a fully differentiated Caco-2 cell monolayer

model and calculated the maximum transport velocity (V_{\max}) to be 137 pmol per mg protein per 30 min and the Michaelis constant (K_m), or the substrate concentration at which the transport velocity is half of V_{\max} , to be 3.82 μM (Kamei *et al.*, 2013). They then attributed the observation of 5-fold increase in insulin uptake by the Caco-2 cell monolayer when the insulin was associated non-covalently with 60 μM D-R8 (D-R8/insulin complex), to an unsaturable uptake rather than a saturable uptake. This is because the concentration of D-R8 used (60 μM) with the insulin was well above the K_m of the D-R8 in the saturable phase (3.82 μM) (Kamei *et al.*, 2013). This conclusion is likely to be flawed as their results also showed that the D-R8 uptake was time-dependent whereas the D-R8/insulin complex uptake was not, which suggested that the D-R8 could have utilized multiple uptake pathways that might not be all applicable to the D-R8/insulin complex. Nevertheless, this study clearly demonstrated that the uptake of CPP is concentration dependent and is able to utilize multiple pathways. It is also plausible that CPPs utilize multiple uptake pathways, and inhibition of one pathway may cause the CPP to use an alternative pathway.

Another explanation for the observation of conflicting uptake results lies in the methodologies employed to assess the uptake study. Richard *et al.* (2003) pointed out the importance of a trypsinization step in *in vitro* studies of CPP uptake to remove cell surface bound CPPs or quenching the fluorescence of surface bound fluorophores, while Madani *et al.* (2011) suggested the use of multiple techniques to study the uptake of CPPs. For example, fluorescence-assisted cell sorting (FACS) is able to quantify the uptake of CPPs by measuring the number of cells that have taken up the fluorescent-labeled CPPs. However, the FACS technique lacks discrimination between the fluorescent-labeled CPPs bound to the cell and the internalized fluorescent-labeled CPPs. To resolve this limitation, live cell confocal microscopy imaging can be employed to monitor intracellular localization of CPPs to distinguish between extracellular and internalized peptides (Madani *et al.*, 2011).

1.4.2.3. Oligoarginine as a CPP

Polycations, such as polyarginine and poly(ethylenimine)s, have been shown to penetrate cells and the interactions between the polycations and the polyanionic structures on the outer cell membrane, such as negatively charged glycoproteins and phosphate groups, are considered vital to trigger subsequent cellular uptake (Morille *et al.*, 2008; Richard *et al.*, 2003). Oligoarginine was found to be superior in uptake efficiency compared to oligomers of other cationic amino acids, such as oligohistidine and oligolysine (Mitchell *et al.*, 2000). The uptake efficiency of oligoarginine is dependent on the number of arginines; Wender and colleagues only observed enhanced uptake with arginine residues of between 6 to 20 (Wender *et al.*, 2008). Although oligoarginine with 15 arginine residue was found to give the most effective cellular penetration, octa-arginine (R8) (**Figure 1-5**) is more commonly studied due to the high cost involved in oligoarginine synthesis (Wender *et al.*, 2008).

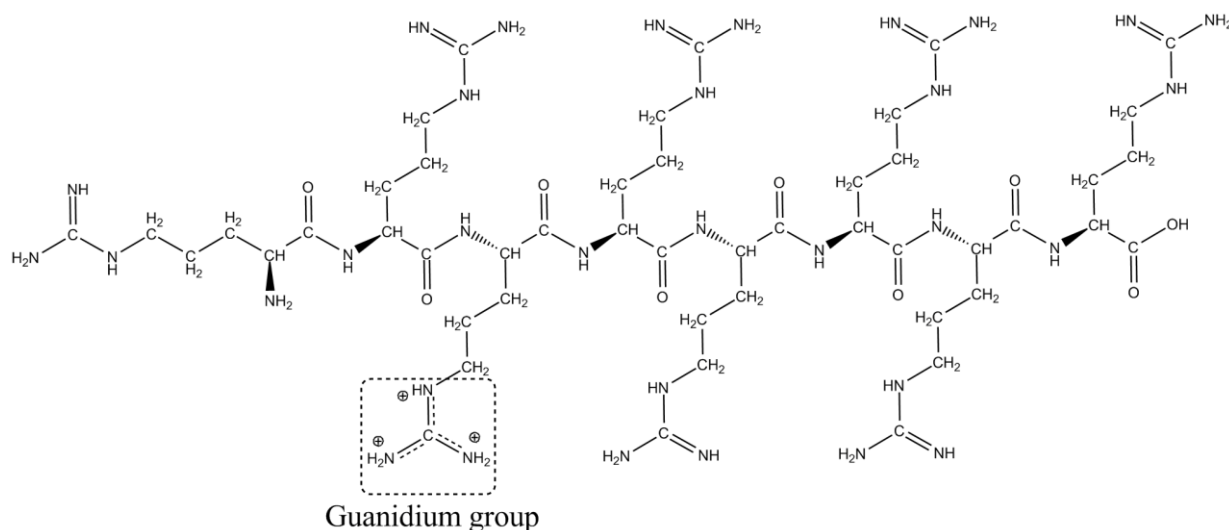


Figure 1-5. Chemical structure of octa-arginine (R8). The cationic guanidinium groups are expected to interact with negatively charged phospholipid membrane at physiological pH (Richard *et al.*, 2003).

In comparison to other CPPs, oligoarginine is more effective than TAT and penetratin at facilitating cellular uptake of proteins (Rothbard *et al.*, 2000; Thorén *et al.*, 2003). Hepta-arginine (R7) has shown internalization through both energy-dependent and

energy-independent uptake pathways, but greater uptake was observed with the latter pathways (Thorén *et al.*, 2003).

The importance of the spacing of the arginine backbone in relation to penetration efficiency of oligoarginine has also been investigated (Rothbard *et al.*, 2002). The cellular uptake is enhanced with increasing spacing between the arginine residues (Rothbard *et al.*, 2002). However, the optimal spacing between the arginine residues was obtained with an oligoarginine analogue with an aminocaproic acid spacer, while an oligoarginine analogue with 8-aminocaprylic acid spacer had reduced penetration potency compared to the oligoarginine analogue with an aminocaproic acid spacer (Rothbard *et al.*, 2002).

Koschek *et al.* (2013) investigated the effects of cationic charge and charge distribution on uptake of N-(2-hydroxypropyl) methacrylamide (HPMA) polymer conjugated with multiple arginine residues. They conjugated arginine residues to HPMA polymers by either positioning the arginine residues haphazardly or arranging the residues sequentially or continuously along the polymer conjugate. The estimated zeta potential per arginine in the polymer-peptide conjugates was similar for a conjugate with non-continuous 19 arginine residues (P-(CR)₁₉) (0.9 mV per arginine) and a conjugate with continuous 9 arginine residues (P-(CT)₂₂(CR)₉)₁ (1.15 mV per arginine). However, the estimated zeta potential per arginine value decreased significantly for P-(CR)₉)₁₅ with a non-continuous 15 arginine residues (0.17 mV per arginine) (**Table 1-2**). The low zeta potential per arginine value in P-(CR)₉)₁₅ was due to the lack of protonation of guanidinium groups in the polymer-peptide conjugate at pH 7.

Koschek *et al.* (2013) then evaluated the uptake in HeLa cells incubated with different polymer-peptide conjugates using confocal microscopy. Although the zeta potential of P-(CR)₁₉ (17.8 mV) was almost twice the zeta potential of P-(CT)₂₂(CR)₉)₁ (10.4 mV), the uptake was similar between both polymer-peptide conjugates with an fluorescence a.u. (arbitrary units) of 64.5 and 79.1 for P-(CR)₁₉ and P-(CT)₂₂(CR)₉)₁, respectively. P-(CR)₉)₁₅ was excluded from the uptake study due to cytotoxicity. Although the group did not find any linear correlation between zeta potential and uptake efficiency, they concluded that cationic zeta potential was a prerequisite for enhanced uptake.

Table 1-2. Compositions of polymer-peptide conjugates and zeta potentials (Koschek *et al.*, 2013). P = Polymer, C = Cysteine, R = Arginine, T = Threonine.

Polymer-peptide conjugate	Number of arginine residues	Zeta potential (mV)	Estimated zeta potential per arginine (mV/arginine)
P-(CR) ₁₉	9	17.8 ± 1.6	0.9
P-(CR ₉) ₁₅	35	3.5 ± 5.1	0.17
P-(CT) ₂₂ (CR ₉) ₁	9	10.4 ± 1.2	1.15

Haphazard multivalent peptide presentation (P-(CR)₁₉) was also observed to have similar uptake as P-(CT)₂₂(CR₉)₁ (Koschek *et al.*, 2013). Although the zeta potential of P-(CR)₁₉ suggested incomplete guanidinium protonation, there is also the possibility of the guanidinium groups ionizing upon binding with the cellular membrane and thus aiding the adherence and uptake of the polymer-peptide conjugate. Kamei *et al.* (2008b) suggested that the electrostatic interaction between oligoarginines (fluorescent-D-hexa-arginine (R6) conjugate) is essential for effective permeation through the rat intestinal membrane in an *in situ* loop absorption study. The addition of heparin significantly reduced the absorption of fluorescent-D-R6 conjugate, with an P_{app} of $1.6 \times 10^{-8} \text{ cm.s}^{-1}$ compared to $7.3 \times 10^{-8} \text{ cm.s}^{-1}$ in the control treatment without heparin (Kamei *et al.*, 2008b). The negatively charged heparin was speculated to bind to the fluorescent-D-R6 conjugate, therefore reducing the electrostatic adsorption on the surface of the enterocytes (Kamei *et al.*, 2008b). Although the negation of the fluorescent-D-R6 with heparin was a possibility, characterization of the compound should have been done to confirm this phenomenon.

Cell penetration enhancement with oligoarginine was hypothesized to be due to the interaction of the guanidinium group of arginine with the cell membrane (Bonduelle and Gillies, 2010), this then led to the synthesis of guanidinium functionalized dendrimers. Dendrimers can be synthesized with versatile backbones (Medina and El-Sayed, 2009; Tomalia, 2005) that are able to resist rapid biodegradation (Cheng and Xu, 2008; Dutta, 2007; Pini *et al.*, 2008; Wang, 1999). However, their use is limited by cell toxicity as polycationic dendrimers can induce the formation of nano-holes in model lipid membranes and is highly concentration dependent (Fischer *et al.*, 2003; Hong *et al.*, 2004; Hong *et al.*, 2006; Leroueil *et al.*, 2008; Leroueil *et al.*, 2007; Malik *et al.*, 2000). Dendrimers are generally spherical or ellipsoid-shaped and consist of a central core surrounded by

repeated branches and surface functional groups (Aulenta *et al.*, 2003). “Generations” are the repeated branches in series of radially concentric layers (Caminade *et al.*, 2005). Nam and co-workers evaluated the permeation of 4th generation dendrimers across Caco-2 cell monolayer and suggested that the particles translocated across the monolayer paracellularly (Nam *et al.*, 2008). Guanidinium functionalized dendrimers has also been postulated to cross the cell membrane via a passive diffusion mechanism (Pantos *et al.*, 2008).

Therefore, oligoarginine is an effective CPP and has potential to be coupled to polymeric backbones (Rothbard *et al.*, 2002) or co-formulated into a nanoparticulate system, such as guanidinium functionalized dendrimers, to enhance the uptake of nanoparticles.

1.4.3. Incorporation of CPPs in polymeric nanoparticles

As CPPs have been shown to increase cellular uptake as well as improve oral bioavailability of CPP-bioactive conjugates (as discussed previously in **Section 1.4.2**), a number of efforts have been made to incorporate CPPs into colloidal carrier systems. Suggested advantages over CPP-bioactive conjugate are; (i) targeted delivery as other ligands can be coupled to the colloidal carriers (Zhang *et al.*, 2013); (ii) greater enhancement in payload delivery as colloidal carriers can be loaded with bioactive; (iii) reduced amount of CPPs required for effective penetration as CPP are associated with colloidal carriers (loaded with bioactive) rather than individual bioactive molecule; (iv) delivering the bioactive in its native form (Liu *et al.*, 2013), and; (v) providing physical protection of the bioactive from the biological environment. Examples of CPPs incorporated into colloidal carriers systems are discussed in detail in **Chapter 3 (Section 3.1.1)**.

PECA nanoparticles can potentially be covalently coupled with oligoarginine in a convenient single step polymerization process. Kafka *et al.* (2009; 2010a) discovered that the histidine residue in the gonadotropin-releasing hormone analogue D-Lys⁶-GnRH covalently conjugated to PECA nanoparticles both during and after nanoparticle formation. These authors suggested that the unprotonated histidine side chain (pK_a 6.04) in D-Lys⁶-GnRH acts as a nucleophile (Kafka *et al.*, 2009) instead of hydroxyl ions, to initiate the anionic interfacial polymerization of ethylcyanoacrylate (ECA) subunits (Vauthier *et al.*,

2003) (**Figure 1-6**). Thus, it may be possible to exploit histidine as a linker for deliberate covalent attachment of functional peptides such as oligoarginine to PECA nanoparticles in a single step polymerization process.

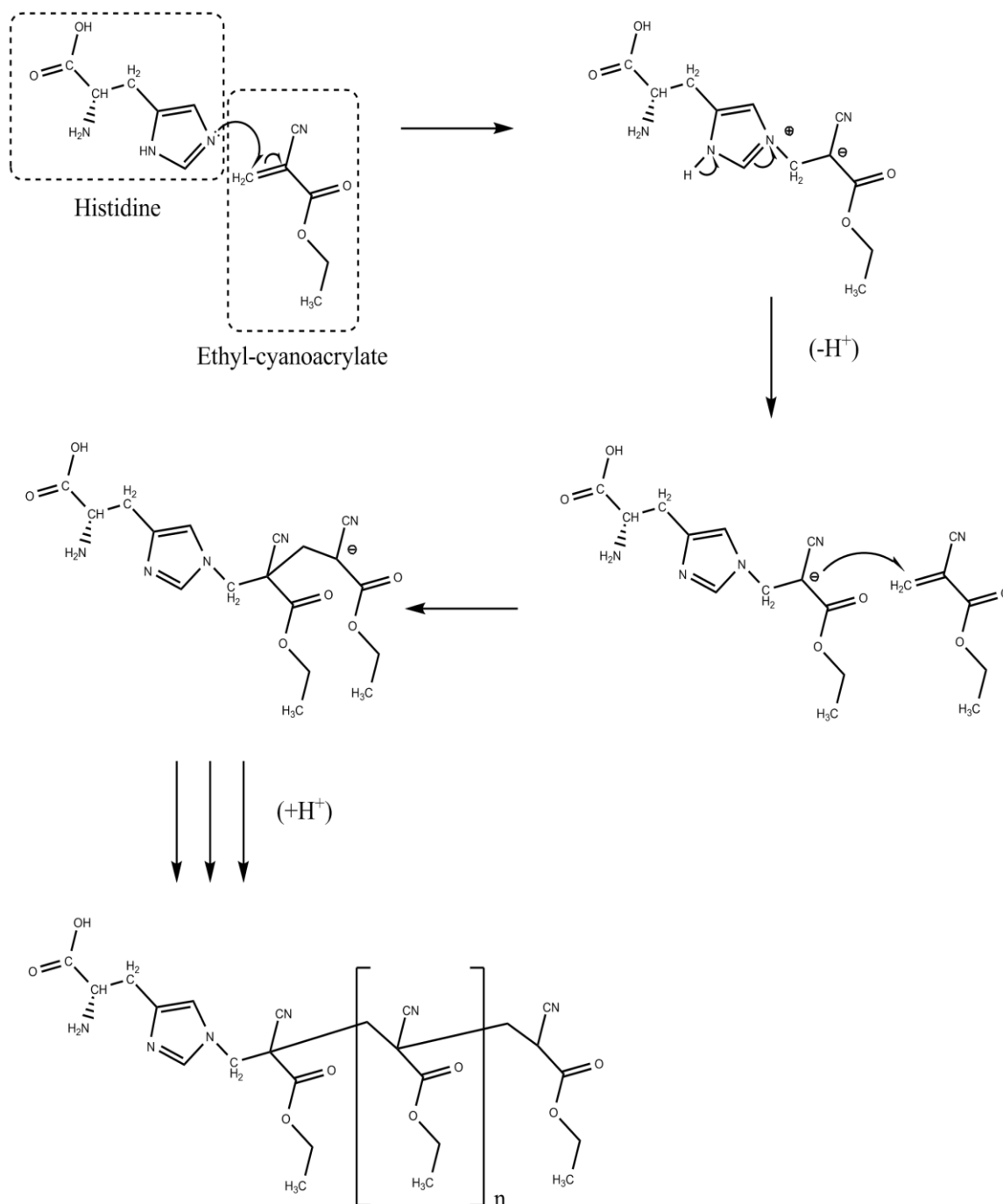


Figure 1-6. Nucleophilic attack on ethylcyanoacrylate (ECA) by imidazole ring of histidine during polymerization, resulting in covalent binding to PECA (Kafka *et al.*, 2009).

1.5. Interaction at the bio-interface

One of the critical factors affecting oral absorption as previously mentioned is the physicochemical properties of the peptide or protein bioactive. The surface properties of the bioactive presented to the surface of the cells (the bio-interface) will dictate the subsequent cellular processes (Nel *et al.*, 2009).

In a nanoparticulate system, the surface properties of the nanoparticles can change when the particles interact with other components in the surrounding medium, such as binding with other proteins in chyme (Nel *et al.*, 2009). The aggregation or clustering of nanoparticles can affect the site and mode of entry into the cell (Doherty and McMahon, 2009). It is important to take the interaction at the bio-interface into consideration when formulating nano-materials for oral delivery. Considering specifically polymeric nanoparticles, variables such as size, shape, surface area, surface charge of the nanoparticles and the suspending media could influence the response of the epithelial cells (Nel *et al.*, 2009) and so the degree of uptake.

Schulze *et al.* (2008) found that Ca^{2+} ions in Krebs-Ringer-Buffer caused carboxylated polystyrene nanoparticles (50 nm) to agglomerate, while the addition of bovine serum albumin resulted in complete de-agglomeration. They attributed the de-agglomeration to the surface adsorption of the albumin on the nanoparticles. The adsorption of albumin occurred due to the formation of hydrogen bonds with the carboxyl groups of the nanoparticles and the hydrophobic interactions with the styrene backbone of the nanoparticles (Schulze *et al.*, 2008). The group also noticed changes in zeta potential of the polystyrene nanoparticles in different media (Schulze *et al.*, 2008). As cells would only be presented with the final “interacted” product (**Figure 1-7**), it is important to characterize the particles in the final form, rather than the clean precursor, to draw appropriate uptake correlations and predictions on the absorption behaviour.

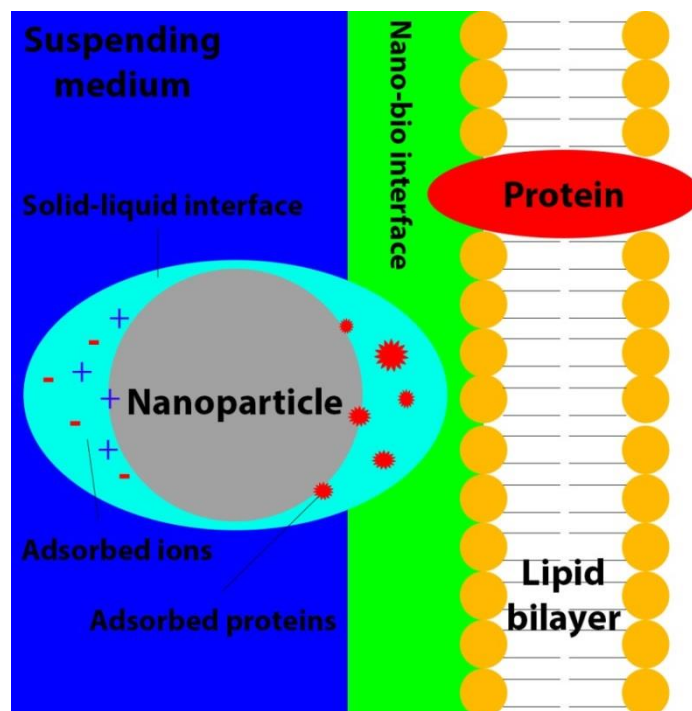


Figure 1-7. Schematic showing the interactions of a nanoparticle at the solid-liquid interface and at the nano-bio-interface (Nel *et al.*, 2009).

As the characteristics of nanoparticles are dependent on the suspending medium, extra considerations are required when assessing the cellular uptake of the nanoparticles as proteins and/or ions in the incubating medium may potentially be adsorbed onto the surface of the nanoparticles. This phenomenon may impair the functionality of the CPPs on the surface of the nanoparticles or affect the interactions between the CPPs and cell surface. Therefore, CPP-associated nanoparticles should be characterized in the cell incubating medium in *in vitro* studies to draw appropriate uptake correlations.

1.6. Aims of thesis

Although therapeutic peptides and proteins can potentially be administered via the oral route, an oral formulation is required to ensure a high oral bioavailability is achieved. Instead of formulating each peptide or protein bioactive individually, it would be desirable to design an oral formulation that could cater for a vast range of peptide or protein bioactives. Polymeric nanoparticles have been shown to be carriers for a range of different bioactives and have been reported to increase oral absorption of protein bioactives, such as D-Lys⁶-GnRH and insulin (Damgé *et al.*, 1988; Kafka *et al.*, 2011). PECA nanoparticles are a good colloidal carrier candidate to be coupled with CPPs, such as oligoarginine, to enhance cell uptake of nanoparticles into the enterocytes and ultimately increase the oral bioavailability via subsequent translocation across the enterocytes into the blood stream. This is because the CPPs can potentially be associated covalently with the PECA nanoparticles in a single polymerization step, in a water-in-oil microemulsion. These CPP associated nanoparticles can also be administered orally without needing to be purified as the microemulsion template is biocompatible (Watanasirichaikul *et al.*, 2002b) and may provide additional permeation enhancing effects (Constantinides *et al.*, 1995).

The overall aim of this thesis was to design and characterize oligoarginine-associated PECA nanoparticles via histidine anchoring and to investigate the cellular association and uptake in a Caco-2 cell model. This was achieved in a number of stages.

Initially, PECA nanoparticles associated with different oligoarginine constructs were designed and characterized. The nanoparticles were characterized in uncontaminated water and also in the cell incubating medium to determine the effect of the medium on the characteristics of the nanoparticles, such as aggregation. The nanoparticles were characterized in the cell incubating medium to help understand the interactions at the bio-interface. This section of the research is discussed in **Chapter 2**.

The interaction of the oligoarginine-associated PECA nanoparticles with Caco-2 cells was investigated using flow cytometry in order to understand how the load and type of oligoarginine affects the interaction at the bio-interface (**Chapter 3**). The effects of temperature (37°C and 4°C) on the interaction at the bio-interface was also investigated (**Chapter 3**).

To understand the rate of contact of the oligoarginine-associated nanoparticles with the cell surface, a mathematical modelling simulation was employed to predict the accumulation of the nanoparticles at the cell surface (**Chapter 4**). The predicted accumulation of the nanoparticles generated by the mathematical model was correlated with cellular association determined experimentally (**Chapter 4**).

Overall discussions and contributions from the work described in this thesis towards improving the understanding of the interaction of nanoparticles with the cell surface at the bio-interface are discussed in **Chapter 5**. This final chapter also discusses the potential use of oligoarginine-associated PECA nanoparticles in oral delivery of therapeutic peptide and protein as well as further studies required to further strengthen the knowledge in the field of bio-interface.

CHAPTER TWO

Design and characterization
of oligoarginine-associated
PECA nanoparticles

2.1. Introduction

Polymeric nanoparticles can improve the poor oral bioavailability of therapeutic peptides or proteins and could potentially be associated with cell-penetration peptides (CPPs) to enhance the cellular uptake. CPPs, such as oligoarginine, have been shown to improve cellular permeation of bioactive compounds (Rothbard *et al.*, 2002; Wender *et al.*, 2008). Such a delivery system could offer the advantage of delivering the bioactive in its unaltered form, while minimizing the amount of oligoarginine required for effective cell permeation. This chapter aims to design and characterize oligoarginine-associated nanoparticles.

2.1.1. Conjugation methods for CPPs to colloidal carriers

In order to harness the cell-penetrating ability of CPPs to improve cellular uptake and enhance permeation of bioactives (Fischer *et al.*, 2005), CPPs have been coupled to the bioactives. Common conjugation methods such as synthetic production in bacteria or utilizing covalent side-chain linkages, were discussed in **Section 1.4.2.1**. To overcome the limitation of covalent linkages to bioactive affecting the activity and/or efficacy of the bioactive (Fonseca *et al.*, 2009), CPPs can be conjugated to the colloidal carriers containing the bioactive. However, current methods of conjugating CPPs to colloidal carriers are often complex and require multiple steps (Liu *et al.*, 2013; Rao *et al.*, 2008; Sawant *et al.*, 2008; Sharma *et al.*, 2013). CPPs have been associated covalently to phospholipids to produce CPP-tagged liposomes (Sawant *et al.*, 2008; Sharma *et al.*, 2013) while Rao *et al.* and Liu *et al.* have successfully conjugated CPPs to PLGA nanoparticles using epoxy conjugation (Rao *et al.*, 2008) and PEGylation (Liu *et al.*, 2013). However, these conjugation techniques are difficult to apply to polymeric PECA nanoparticles as the only reactive carbonyl group on ECA is required for polymerization of the monomers. Non-covalent association via the addition of amphiphilic CPPs to the lipid mixture during the liposome production (Sardan *et al.*, 2013) also may not be applicable to PECA nanoparticles as the addition of amphiphilic CPPs may impair the polymerization of the monomers, thus disrupting the formation of particles. A physical mixture of nanoparticles with CPPs is possible, but this would require substantially higher amounts of CPP to associate the CPPs with the surface of the nanoparticles via electrostatic interactions (Kamei *et al.*, 2008b). An alternative method to covalently conjugate CPP to PECA

nanoparticles is by synthesizing an additional histidine residue in the CPP to be used as a covalent linker (**Section 1.4.3**).

Using poly(ethyl-cyanoacrylate) (PECA) nanoparticles as the colloidal carrier for CPP conjugation can offer additional advantages such as; (i) achieving conjugation in a single step polymerization using histidine anchoring (Kafka *et al.*, 2009); (ii) direct oral administration of the nanoparticles prepared in a biodegradable and biocompatible, water-in-oil microemulsion template (Watanasirichaikul *et al.*, 2002a) without the need for purification and; (iv) additional permeation enhancing effects from the microemulsion template (Constantinides *et al.*, 1995).

2.1.2. Characterization of CPP-conjugated nanoparticles

As mentioned in **Section 1.5**, it is important to characterize the CPP-conjugated nanoparticles as the physicochemical properties of the particles would influence the subsequent cellular uptake. Although particles are generally characterized for their size and surface charge, it is also important to take elasticity and the shape of the particles into considerations (Agarwal and Roy, 2013). Traditional techniques utilized for size characterization of nanoparticles include dynamic light scattering (DLS) (Bootz *et al.*, 2004), electron microscopy (Krauel *et al.*, 2007), size exclusion chromatography (Husain *et al.*, 1980), gel electrophoresis (Xu *et al.*, 2007), ultrasound spectroscopy (Liu, 2009) and nanoparticle tracking analysis (Filipe *et al.*, 2010). Newer techniques in particle sizing include scanning ion occlusion spectroscopy (SIOS) (Yang *et al.*, 2012) and imaging with atomic force microscopy (Rao *et al.*, 2007). Although these newer techniques are able to provide measurements for individual particles, measuring various sized populations in a mixed sample is both tedious and time consuming. Yang *et al.* (2012) showed that filtering mixed particles may aid in particle analysis (Yang *et al.*, 2012), but the particles may also interact with filter membranes, thus affecting the concentration measurements.

Zeta potential, which is associated with the surface charge of the nanoparticles, can be determined using DLS (Bootz *et al.*, 2004), gel electrophoresis (Allison *et al.*, 2007) and scanning ion occlusion spectroscopy (Weatherall *et al.*, 2013). Although both X-ray photoelectron spectroscopy (XPS) and zeta potential measurements could provide an indirect insight to the presence of the CPP on the surface of the nanoparticles (Liu *et al.*,

2013; Rao *et al.*, 2008), information regarding the CPP distribution on the surface would require the aid of atomic force microscopy imaging (AFM) (Moribe *et al.*, 2008).

It is also vital to determine the type of association between the CPP and polymeric nanoparticles in order to understand the nature and stability of the particles. Liu *et al.* indirectly confirmed covalent association between oligoarginine and PLGA nanoparticles through the loss of maleimide peak in the nuclear magnetic resonance (NMR) spectrum (Liu *et al.*, 2013). Compared to NMR analysis, Kafka *et al.* determined covalent binding of D-Lys⁶-GnRH to PECA nanoparticles via histidine using matrix-assisted laser desorption/ionization coupled to time-of-flight (MALDI-TOF) mass spectrometry without the need of a pure sample (Kafka *et al.*, 2009).

2.1.3. Quantification of CPPs

The amount of CPP associated with the colloidal carrier as well as the release rate of the CPP from the nanoparticles should also be determined. This can be achieved using various methodologies (**Table 2-1**). High performance liquid chromatography (HPLC) is commonly used to separate specific peptides and proteins from impure samples for quantification. This technique is able to distinguish monomeric protein forms, aggregates and chemically modified species (Bilati *et al.*, 2005a; Hoffmann, 2000). Depending on the targeted analyte, various types of chromatography with columns made of different materials, can be utilized. Commonly used chromatographies include normal-phase (Yoshida, 1997), reversed-phase (Cameron *et al.*, 2000), ion-exchange (Andrews, 1988) and size exclusion (Irvine, 2003). As most peptides have chromophores, HPLC can be coupled to UV-spectrometry for quantification. The use of diode array detector (DAD) enables the discrimination of different degraded forms of analyte (Hoffmann, 2000) and di-peptide with different aromatic residues that could not be resolved with a single wavelength UV detector (Nyberg *et al.*, 1986). Alternatively, colorimetric assays can be used (Hoffmann, 2000). An example of colorimetric assays is Coomassie brilliant blue (Bradford's assay) that reacts with protein analyte to produce a product that has an absorption wavelength of 595 nm (Hoffmann, 2000). However, these colorimetric methods often lack specificity and sensitivity as they can only provide relative concentrations between the sample and a reference protein, such as bovine serum albumin (BSA) that may have different responsiveness. MALDI-TOF mass spectrometry can also potentially be used to quantify protein bioactive in polymeric carrier systems (Bilati *et al.*,

2005b; Na *et al.*, 2004). This soft ionization method allows the direct analysis of large intact bioactive, without the need for bioactive separation prior to analysis (El-Aneed *et al.*, 2009). It is also important be aware that the amount of CPP quantified may not have a direct correlation to bioactivity, as bioactivity itself would require further bioassay testing (Bilati *et al.*, 2005a).

Table 2-1. Different protein or peptide quantification assays and their detection mechanisms (Bilati *et al.*, 2005b; Hoffmann, 2000).

Quantification assays	Mechanisms	Advantages	Disadvantages
HPLC	Separates compound(s) of interest from sample based on hydrophilicity/hydrophobicity or charge and size to be analysed using UV-spectrometry or mass spectrometry	<ul style="list-style-type: none"> • High sensitivity assays • Able to distinguish different degraded products using DAD 	Requires successful separation of compound(s) of interest from sample
Colorimetry	Reacts with compound of interest to produce coloured assays for quantification	<ul style="list-style-type: none"> • Simple assays 	Lack specificity and sensitivity
MALDI-TOF	Uses a laser beam to ionize the sample and then analyses compound(s) of interest using mass spectrometry	<ul style="list-style-type: none"> • Very high sensitivity assays • Does not require separation of compound(s) of interest from sample 	Quantification difficult to be achieved

Although HPLC coupled to UV-spectrometry is able to be used to quantify CPP, this method requires CPP isolation from other contaminants in the sample. CPP associated with PECA nanoparticles can be indirectly quantified by determining the amount of CPP unassociated with the nanoparticles in the microemulsion supernatant. The unrecovered portion of CPP is assumed to be associated with the nanoparticles, either non-covalently entrapped in the nanoparticles or covalently tagged with the nanoparticles. However, HPLC is unable to analyse the CPP associated with the nanoparticles as the dissolved nanoparticles may precipitate in the column. This limitation can perhaps be overcome

with the use of isobaric tagging with MALDI-TOF mass spectrometry that is able to directly detect and quantify the CPP in the dissolved CPP-associated nanoparticles. MALDI-TOF mass spectrometry shows the amount of the most abundant protein or peptide (signal intensity) in relative to all ions present in the sample, including other contaminant ions. Peptide quantification with MALDI-TOF mass spectrometry is difficult to achieve as the amount of contaminants in the sample is unknown and is highly variable between sample preparations. I-TRAQTM (Isobaric Tags for Relative and Absolute Quantification) resolves this issue by tagging the peptide or protein of interest to provide an internal standard (Brewis and Brennan, 2010). The i-TRAQTM reagent consists of a charged reporter group, a peptide reactive group (PRG) to covalently tag with the N-terminus group of a peptide and a neutral balance group to maintain an overall mass of 145 (**Figure 2-1**). The CPP can be tagged with two different i-TRAQTM reagents (with two different reporter mass), to be used for CPP-tagging and as an internal standard (of known concentration) in the sample for quantification. Upon fragmentation in the MALDI-TOF mass spectrometry, reporter groups with different mass would be generated. Therefore, semi-quantification can be carried out by comparing the signal intensities between the report groups. As the i-TRAQ reagent tags the CPP via the N-terminus of the CPP peptide, this covalent tagging should not interfere with the tagging of CPP to PECA nanoparticles that occurs via the imidazole ring of the histidine.

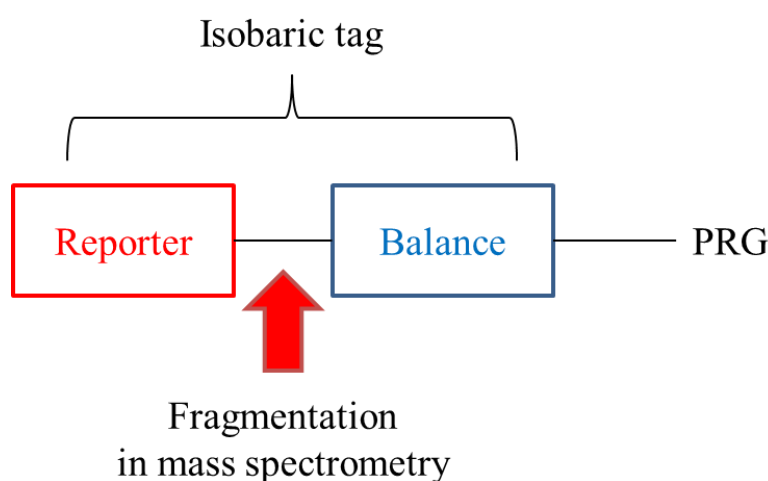


Figure 2-1. Composition of the i-TRAQTM reagent (Brewis and Brennan, 2010).

2.1.4. Chapter aims

To design oligoarginine-associated nanoparticles, various oligoarginine peptides are synthesized with a histidine residue. The type of association between the oligoarginine and PECA nanoparticles is to be determined using MALDI-TOF mass spectrometry. As this chapter aims to investigate the influence of incubating medium on the oligoarginine-associated nanoparticles, the nanoparticles are characterized for size and zeta potential in different media, relevant to cell culture studies. In order to gain information regarding the surface of nanoparticles, which is important for understanding the interactions at the cellular bio-interface, the amount of oligoarginine associated with PECA nanoparticles is quantified using a combination of HPLC/UV and MALDI-TOF mass spectrometry.

2.2. Materials

Arginine-histidine (RH), di-arginine-histidine (RRH), tetra-arginine-aminocaproic acid-histidine (R4acaH), octa-arginine-histidine (R8H), octa-arginine-di-histidine (R8H2) and octa-arginine (R8) (all $\geq 95\%$ purity) from GLS (Shanghai, China) were used as supplied. For preparation of the microemulsion, ethyloleate (GPRTM) was supplied by BDH Laboratory Supplies (Poole, England), while the surfactants sorbitan monolaurate (Crill 1) and ethoxy 20 sorbitan mono-oleate (Crillet 4) were kindly provided by BTB chemicals (Auckland, New Zealand). The monomer ethyl-2-cyanoacrylate (ECA), fluorescein isothiocyanate (FITC)-dextran (MW = 70 kDa, 500 kDa and 2,000 kDa), 2-[4-(2-hydroxyethyl)piperazin-1-yl] ethanesulfonic acid (HEPES) ($\geq 99.5\%$ purity), sodium bicarbonate ($\geq 99.5\%$ purity), Hanks Balanced Salt Solution (HBSS; without sodium bicarbonate and phenol) and trifluoroacetic acid (TFA) were purchased from Sigma-Aldrich (St. Louis, MO, USA). Poloxamer-407 (Lutrol-F127[®]) was purchased from BASF (Ludwigshafen, Germany). Methanol (HPLC grade), acetonitrile (HPLC grade), chloroform were supplied by BDH Laboratory Supplies (Poole, England) and hydrochloric acid (fuming 37%, ACS grade) and D(+)-glucose were sourced from Merck (Darmstadt, Germany, cell culture grade). Sodium chloride (NaCl, ACS grade), di-sodium-hydrogen phosphate (Na₂HPO₄, ACS grade) and sodium-di-hydrogen phosphate (NaH₂PO₄, ACS grade) were purchased from Univar, Asia Pacific Specialty Chemicals Limited (Sydney, Australia) and absolute ethanol was supplied by Anchor Ethanol (Auckland, New Zealand, HPLC grade). Distilled, ultra-pure water was produced using a Milli-Q[®] water Millipore

Purification SystemTM (Billerica, USA). I-TRAQTM reagents multiplex (4-plex) kit was purchased from Sciex (Massachusetts, USA).

2.3. Methods

2.3.1. Preparation of PECA nanoparticles from a microemulsion template

The microemulsion was prepared based on the method described by Watnasirichaikul *et al.* (2000). Briefly, a mixture of Crill 1 and Crillet 4 was prepared in a mass ratio of 4 : 6. Then the surfactant mix, ethylolate oil and water were mixed together at a weight ratio of 5.4 : 3.6 : 1, respectively, to produce the microemulsion template. ECA monomer (200 μ L ECA (1.6 μ mol) dissolved in 600 μ L of chloroform) was added drop-wise to 10 g microemulsion template under constant stirring at 700 rpm at 4°C. The polymerization process was allowed to progress for a minimum of 4 h. To produce a smaller batch of nanoparticles from 1 g microemulsion, all components (including ECA monomer, oligoarginine and FITC-dextran) were scaled down by a factor of 10.

2.3.2. Arginine-tagging and FITC-dextran entrapment

To produce R-tagged nanoparticles, either RH, RRH, R4, R4acaH, R8H, R8H2 or R8 was dissolved in the aqueous phase (water) of the microemulsion, prior to making up the microemulsion. To load the nanoparticles with FITC-dextran, 1 mg of FITC-dextran of either MW 70 kDa, 500 kDa and 2,000 kDa was dissolved in the aqueous phase (water) of the microemulsion, prior to making up the microemulsion. Then polymerization was carried out as described in **Section 2.3.1**.

To screen for covalent association and to investigate the effects of phosphate on nanoparticles, nanoparticles (in 10 g microemulsion) were produced with RH (10 μ mol), RRH (10 μ mol), R4 (5.6 μ mol), R4acaH (5.6 μ mol), R8H (4 μ mol), R8H2 (5.2 μ mol) or R8 (4 μ mol), while nanoparticles produced with RRH (100 μ mol), R4 (34 μ mol), R4acaH (34 μ mol) were used for all other experiments unless otherwise specified. The concentrations of the oligoarginines were selected based on the difference in zeta potential of the resultant nanoparticles.

2.3.3. Isolation of nanoparticles from microemulsion

Microemulsion (0.1 or 0.2 g) containing nanoparticles was gently mixed with 600 μL of dilute HCl (pH 2.5) and 600 μL of methanol 80% (v/v). The sample was centrifuged at 20,800 g (Eppendorf Centrifuge 5417C) for 30 min to sediment the nanoparticles from the microemulsion. After decanting the microemulsion, the pellet was re-suspended with brief sonication in absolute ethanol to wash the isolated nanoparticles and then spun at 20,800 g for 30 min. This purification step was repeated twice in total. The same process was used for bulk isolation (1 or 2 g microemulsion). The bulk sample was centrifuged at 40,100 g at 25°C for 35 min in Beckman Optima™ L-80 Ultracentrifuge.

2.3.4. Screening for covalent association using MALDI-TOF mass spectrometry

Detailed sample preparation and operation protocols used were as described by Kafka *et al.* (2009). Briefly, the nanoparticles were isolated from 0.1 g microemulsion and dissolved with sonication in 20 to 30 μL acetonitrile. An aliquot (0.5 μL) of the dissolved nanoparticle suspension was added to 9.5 μL matrix (10 mg/mL α -cyano-4-hydroxycinnamic acid dissolved in aqueous acetonitrile 60% (v/v) with TFA 0.1% (v/v)). An aliquot (0.8 μL) was then spotted onto the MALDI-plate (Opti-TOF 384 well plate, Applied Biosystems, Framingham, MA, USA) and air-dried prior to analysis. All mass spectrometry (MS) spectra were obtained in positive-ion reflector mode with 1000 laser pulses per sample spot. Relevant precursor ions were chosen for collision induced dissociation tandem mass spectrometry (CID-MS/MS). Laser pulses were then set at 2000 to 4000 per selected precursor using 2 kV mode and air as the collision gas at a pressure of 1×10^{-6} Torr. Nanoparticles with oligoarginine covalently bound to the PECA polymer were selected for further characterization.

2.3.5. Characterization of nanoparticles

2.3.5.1. Size and zeta potential

Isolated nanoparticles from 0.1 g microemulsion were either re-suspended in absolute ethanol (containing 0.2% polysorbate 80) for size measurements, or 1 mM NaCl solution for zeta potential measurements (Zetasizer ZEN3600, Malvern instruments Ltd, UK).

2.3.5.2. Entrapment efficiency

Isolated nanoparticles from 0.1 g microemulsion were dissolved in 1 mL aqueous acetonitrile 80% (v/v) and analysed for fluorescence of FITC-dextran using spectrofluorometry (excitation 485 nm and emission 516 nm). Entrapment efficiency was calculated as the percentage FITC-dextran recovered upon dissolving the nanoparticles as a proportion of the total FITC-dextran added to the microemulsion. A standard curve was prepared with each batch of FITC-dextran loaded nanoparticles produced to quantify the FITC-dextran entrapment. The standard curve was prepared by spiking the isolated empty unmodified or oligoarginine-associated nanoparticles in 1 mL aqueous acetonitrile 80% (v/v) with a known concentration of FITC-dextran.

2.3.6. Quantifying oligoarginine-associated with PECA nanoparticles

2.3.6.1. HPLC assay

Reversed-phase high-performance liquid chromatography (RP-HPLC) was used to detect and quantify the amount of associated oligoarginine in the microemulsion through an indirect method. Nanoparticles were isolated from 0.2 g microemulsion and the supernatant of the spun microemulsion (1 mL) was drawn for HPLC analysis. RP-HPLC analysis was carried out using an AgilentTM series 1200 HPLC system (CA, USA) with a micro-vacuum degasser (G1379B), a quaternary pump, a temperature-controlled auto-sampler (G1329A with G1330B thermostat) and a temperature-controlled column compartment (G1316A) coupled to a variable wavelength UV detector (G1314B). Samples in the auto-sampler were kept at 4°C and the column (HiChrom ultrasphere 5 ODS, 250 x 4.6 mm i.d. 5µm particle size, 80 Å pore size, Berkshire, UK) was heated to 40°C. The column was protected by a widepore C18 Phenomenex Analytical Guard

cartridge column (KJ0-4282, 4.0 x 3.0 mm i.d.). The injection volume for all samples was 100 μ L with detection wavelength set at 198 nm for RR, RRH, R4acaH and R4. The mobile phase consisted of solvent A: TFA 0.1% (v/v) in ultra-pure water and solvent B: Ultra-pure water 10% in acetonitrile. Isocratic elution conditions employed are summarized in **Table 2-2** for each oligoarginine.

Table 2-2. Isocratic elution conditions for different oligoarginines.

Oligoarginine	Elution conditions
RR and RRH	1% Solvent B : 99% Solvent A Flow rate of 1 mL/min over 10 min
R4 and R4acaH	7.5% Solvent B : 92.5% Solvent A Flow rate of 1 mL/min over 10 min

A washing step was added to flush residual formulation components from the column, such as oil and surfactants, by increasing the concentration of solvent B to 80% over an additional 3 min at a flow rate of 1.1 mL/min. Then the system was re-equilibrated by reducing the concentration of solvent B to the appropriate concentration and the flow rate to 1 mL/min. The system was allowed to re-equilibrate for 5 min prior to the next sample.

For the validation of the RP-HPLC assay to measure the oligoarginine concentration recovered from the microemulsion matrix, the microemulsion matrix (0.1g) was spiked with 5 different concentrations of the oligoarginine (**Table 2-5**). The spiked microemulsion was then mixed with 600 μ L of dilute HCl (pH 2.5) and 600 μ L of methanol 80% (v/v). The standard sample was centrifuged at 20,800 g (Eppendorf Centrifuge 5417C) for 30 min to separate the oil and water phase. Then the aqueous phase was subjected to RP-HPLC analysis to determine the concentration of the oligoarginine.

The validation of the RP-HPLC assay to measure the oligoarginine concentration in HBSS medium was performed by spiking the HBSS medium with 5 different concentrations of oligoarginine (**Table 2-8**).

Three independent sets of standard samples were prepared in total for all RP-HPLC validations. The interday and intraday variability were determined by injecting the same samples for multiple injections within one day and on 3 subsequent days. All RP-HPLC assays were validated according to the according to ICH guidelines (ICH, 1996)

2.3.6.2. I-TRAQ™ assay

Oligoarginine sample (0.1 μmol), dissolved in 20 μL of 0.5 M triethylammonium bicarbonate buffer, was mixed with the contents of one i-TRAQ™ Reagent vial that had been reconstituted in 70 μL ethanol. The sample was left at room temperature for 1 h to allow labeling reactions to complete. The same procedure was repeated for a second batch of oligoarginine sample (50 μg) with different i-TRAQ™ tag to be used as the internal standard. An aliquot of sample (0.1 μL) from each batch was spotted on the MALDI-plate for MALDI-TOF analysis to determine labeling efficiency (**Section 2.3.4**).

The remaining labeled peptides were then freeze-dried. One batch of the i-TRAQ™ labeled oligoarginine was then re-dissolved in the aqueous phase (0.1 mL) of 1 g microemulsion (**Section 2.3.2**). ECA monomer was added drop-wise and the polymerization was allowed to progress overnight (**Section 2.3.1**).

Oligoarginine (labeled with i-TRAQ) covalently tagged with PECA nanoparticles was extracted from 0.1 g microemulsion by centrifugation (**Section 2.3.3**). After centrifugation, the supernatant (40 μL) was mixed with 40 μL of acetonitrile for analysis of unassociated oligoarginine, while the pellet was dissolved in 40 μL acetonitrile for quantification of oligoarginine physically associated with the nanoparticles. The samples (0.5 μL) were then mixed with MALDI matrix spiked with the internal standard (oligoarginine labeled with a different i-TRAQ label) (0.5 μL) and blank MALDI matrix (9.0 μL), before spotting an aliquot (0.8 μL) onto MALDI-plate for analysis (**Section 2.3.4**).

2.3.7. Effects of phosphates on nanoparticles

Oligoarginine-tagged and unmodified nanoparticles, both without FITC-dextran, were extracted from 2 g microemulsions (**Section 2.3.3**). The nanoparticles were dispersed in 10 mL ultra-pure water and then titrated incrementally with phosphate buffer (5 mM; pH 6, 7 or 8) at room temperature under constant stirring (1,000 rpm) with a

magnetic flea. A sample aliquot (0.5 to 1 mL) was withdrawn for zeta potential determination after each volume addition. The variation in sample volume is to ensure sufficient nanoparticles was obtained for size and zeta potential analysis after each buffer addition.

2.3.8. Treating PECA nanoparticles with poloxamer-407

Oligoarginine-tagged and unmodified nanoparticles were isolated from 0.1 g microemulsion and then re-dispersed in ultra-pure water containing poloxamer-407, in mass ratios (poloxamer-407 : dry nanoparticles) of 1 : 8.3, 1 : 4.2, 1 : 1.4, 1 : 0.8, prior to adding equal amounts of HBSS (2X concentrated, pH 7.1). The zeta potential and size of the nanoparticles were measured. The dispersion stability of poloxamer-407 treated nanoparticles in HBSS at 37°C was investigated over 2 h.

2.3.9. Release of oligoarginine in HBSS

Oligoarginine-associated PECA nanoparticles were isolated from 2 g microemulsions (**Section 2.3.3**) and then first suspended in 10 mL 0.12% (w/v) poloxamer-407. Then an equal volume of 2X-concentrated HBSS (pH 7.1) (10 mL) was added to the nanoparticle suspension. The suspension was stirred at 300 rpm at 37°C and samples (1 mL) were drawn at 10, 40, 70, 120, 180 and 240 min. Samples were spun at 20,800 g for 30 min and the supernatant (0.9 mL) was concentrated under vacuum before HPLC/UV analysis (**Section 2.3.6.1**).

2.3.10. Statistical analysis

Comparisons of size, zeta potential and oligoarginine release between the different nanoparticle formulations were analyzed with General Linear Model ANOVA using Minitab[®] ver. 16.1.0.0. Post ANOVA pair-wise comparisons were assessed using the Bonferroni method. $P < 0.05$ was considered significantly different.

2.4. Results and discussion

2.4.1. Screening for covalent association

Using MALDI-TOF spectrometry, covalent association of oligoarginine to the PECA nanoparticles can be determined by the presence of prominent peaks of the parent peptide mass (M_{peptide}) plus 125 mass unit increments due to sequential addition of ECA monomer units (n), resulting in a mass pattern of $[M_{\text{peptide}} + (125)_n + H]^+$ in the mass spectrum. By selection of a prominent peak in the mass spectrum, collision-induced-dissociation (CID) fragmentation can be used to identify the location of covalent association. The mass spectrum is expressed as m/z (mass-to-charge ratio) and all compounds analysed by MALDI-TOF was assumed to have a charge of 1, which is attributed to the H^+ gained during the ionization.

The mass spectrum of unmodified PECA nanoparticles had characteristic peaks in 125 mass unit increments that represent sequential ECA monomer subunit additions. The mass spectrum of RH-tagged nanoparticles had prominent peaks at parent RH mass with 125 mass unit increments $[M_{\text{RH}} (311) + (125)_n + H]^+$ at m/z 812, 937, 1062, 1187 and 1312 corresponding to parent RH conjugated to 4, 5, 6, 7 and 8 monomer units respectively (**Figure 2-2 A**). Subsequent fragmentation of parent ion 937 (**Figure 2-2 B**) resulted in peaks of parent mass $[M_{\text{RH}} + H]^+$ at m/z 312 with subsequent ECA additions at m/z 436, 562, 687 and 812. Similarly, the mass spectrum of RRH-tagged nanoparticles showed peaks, $[M_{\text{RRH}} (467) + (125)_n + H]^+$, at m/z 718, 843, 968, 1093 and 1218 corresponding to parent RRH conjugated to 2, 3, 4, 5 and 6 monomer units (**Figure 2-2 C**) with fragmentation of precursor 968 bearing RRH mass peak $[M_{\text{RRH}} + H]^+$ at m/z 468 and subsequent ECA additions at m/z 718 and 843 (**Figure 2-2 D**).

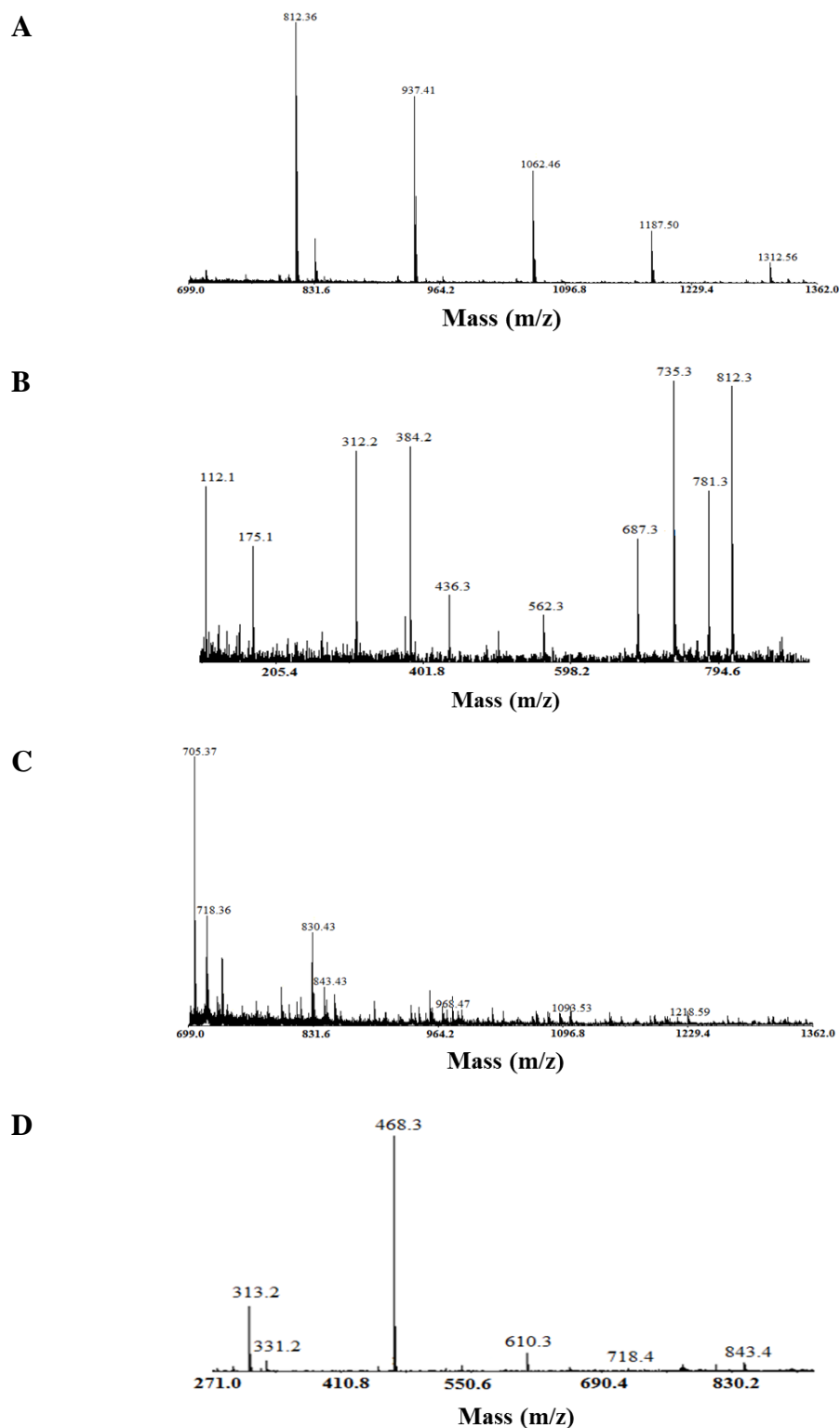


Figure 2-2. Mass spectra of PECA nanoparticles tagged with **A.** RH and **C.** RRH. CID fragmentation of selected precursor ion of **B.** 937 from RH-tagged nanoparticles and **D.** 968 from RRH-tagged nanoparticles. $[M_{RH} + H]^+ = 312.2$ and RH/ECA copolymers at m/z 812.3, 937.4, 1062.4, 1187.5; $[M_{RRH} + H]^+ = 468.3$ and RRH/ECA copolymers at m/z 718.3, 843.4, 968.4, 1093.5, 1218.5.

Low mass immonium ions (*i*) are generated through multiple fragmentation of a precursor and can be used to confirm the presence of certain amino acids (Biemann, 1990). Fragmentation of RH and RRH-tagged nanoparticles generated *i*Histidine ions ($M_{\text{histidine}} = 110$) conjugated to 5 ECA subunits (m/z 735 in **Figure 2-2 B**) and 4 ECA subunits (m/z 610 in **Figure 2-2 D**), respectively. The mass spectra of RH-tagged nanoparticles (**Figure 2-2 A**) and RRH-tagged nanoparticles (**Figure 2-2 B**) with their respective fragmented precursors of 937 and 968 is evidence that oligoarginine covalently bound to the PECA polymer, consistent with the findings of Kafka *et al.* (2009). Fragmentation of these parent precursors generated *i*[histidine] peak at m/z 110, with the $-\text{COOH}$ group cleaved. Therefore, the presence of *i*[histidine] attached to 5-ECA and 4-ECA subunits (m/z 735 in **Figure 2-2 C** and 610 in **Figure 2-2 D**), indicated that the histidine residue was the side chain that associated covalently with the PECA polymer.

MALDI-TOF spectra did not reveal any evidence of covalent association of longer oligoarginine (R8H, R8H2 and R4acaH) or oligoarginine without histidine (RR, R4 and R8) to PECA nanoparticles. As the covalent association with PECA nanoparticles was expected to occur through histidine, oligoarginine without histidine was expected not to associate covalently with PECA nanoparticles. Although RRH was found to be covalently bound to the PECA, the occurrence of this binding as seen with the peak intensity in the mass spectrum was less evident compared to the peak intensity for RH. Furthermore, longer oligoarginines (R8H2, R8H and R4acaH) did not covalently associate with the PECA nanoparticles. These observations are suggestive of a trend in reducing capability of histidine to act as a nucleophile with increasing arginine residues. The fact that the larger arginine oligomers did not covalently bind is not likely to be due to an electron inductive effect of the arginine since inclusion of a spacer in R4acaH oligoarginine did not result in covalent binding. The lack of covalent attachment of longer oligoarginines may be due to the flexibility of the peptide backbone. Rothbard *et al.*(2002) discussed the importance of spacing and rigidity of arginine residues in CPPs to allow interaction between the guanidinium headgroup of arginine and the cell surface. Therefore, increasing arginine residues in oligoarginine could decrease the rigidity of the peptide backbone and allow the peptide to fold and shield the imidazole ring of histidine, thus preventing histidine from participating in the nucleophilic reaction during the polymer polymerization.

2.4.2. Characterization of oligoarginine-associated nanoparticles

R-tagged and unmodified nanoparticles had a similar size of approximately 200 nm ($P > 0.05$) with polydispersity index less than 0.3, which indicates a mono-dispersed particle suspension (**Table 2-3**) (Thapa *et al.*, 2013). However, there were significant differences ($P < 0.001$) in zeta potential of nanoparticle formulations, being -12.5 mV for unmodified nanoparticles, -3.5 mV for RH-tagged nanoparticles and +18 mV for RRH (10 μ mol)-tagged nanoparticles. The surface of PECA nanoparticles would have negative charge (zeta potential of -12.5 mV) due to the presence of acrylic acid head groups (Pitaksuteepong *et al.*, 2002), however the zeta potential was shifted to +18 mV and -3.5 mV with RRH and RH-tagging, respectively. This alteration in zeta potential could be explained by covalent association of cationic arginine residues on the surface of the nanoparticles. Although RH appeared to bind more readily to the PECA nanoparticles compared to RRH (**Figure 2-2**), nanoparticles tagged with RH were less cationic (-3.5 mV) than particles tagged with RRH (+18 mV). This finding suggests that less arginine residues are present on the surface of the RH-tagged nanoparticles compared to RRH-tagged nanoparticles despite the increased covalent binding. The lack of arginine residues on the surface of the RH-tagged nanoparticles could be due to RH peptide having a single arginine residue compared to RRH peptide having two arginine residues or most of the RH peptide is covalently bound to the interior of the nanoparticles, rather than the external surface. The longer RRH peptide could also protrude its terminal arginine through the meshwork of the polymer, allowing it to be presented closer to the surface of nanoparticles, giving the particles a more cationic zeta potential. As RH-tagging did not result in a positive zeta potential, RH was excluded from the nanoparticle formulations for all subsequent experiments.

Table 2-3. Characterization of unmodified and arginine-tagged nanoparticles, with or without entrapment of FITC-dextran of different molecular weights and their entrapment efficiencies. Data are means \pm SD (two independent batches). Values sharing the same letters are not significantly different, while values with different letters are significantly different. Unmodified-70, Unmodified-500, Unmodified-2000 are unmodified nanoparticles loaded with 70, 500 and 2000 kDa FITC-dextran, respectively and RRH-tagged-70, RRH-tagged-500 and RRH-tagged-2000 are RRH-tagged nanoparticles loaded with 70, 500 and 2000 kDa FITC-dextran, respectively.

Nanoparticles	Oligoarginine amount (μ mol)	Size (d.nm)	Polydispersity index	Zeta potential (mV)	FITC-dextran loaded (kDa)	Entrapment efficiency (%)
Unmodified	-	186 \pm 6 ^a	0.02 \pm 0.03	-13.7 \pm 2.9 ^a	Nil	-
RH-tagged	10	206 \pm 24 ^a	0.08 \pm 0.07	-3.5 \pm 0.2 ^b	Nil	-
RRH-tagged	10	196 \pm 26 ^a	0.02 \pm 0.00	+18.4 \pm 1.9 ^c	Nil	-
Unmodified-70	-	198 \pm 8 ^a	0.17 \pm 0.12	-12.4 \pm 1.0 ^a	70	42.9 \pm 3.3
RRH-tagged-70	10	195 \pm 15 ^a	0.09 \pm 0.01	+18.2 \pm 0.4 ^c	70	52.4 \pm 4.4
Unmodified-500	-	188 \pm 5 ^a	0.07 \pm 0.02	-11.9 \pm 0.2 ^a	500	80.5 \pm 11.7
RRH-tagged-500	10	208 \pm 15 ^a	0.04 \pm 0.02	+18.4 \pm 1.9 ^c	500	77.7 \pm 4.6
Unmodified-2000	-	204 \pm 2 ^a	0.10 \pm 0.08	-11.9 \pm 2.0 ^a	2,000	89.1 \pm 0.8
RRH-tagged-2000	10	186 \pm 5 ^a	0.03 \pm 0.03	+18.1 \pm 1.6 ^c	2,000	92.9 \pm 1.3

FITC-dextran loading did not affect the size ($P > 0.05$) or zeta potential ($P > 0.05$) of the nanoparticles. FITC-dextran entrapment efficiency was higher with higher molecular weight FITC-dextran ($P < 0.05$), with similar entrapment in both unmodified and RRH (10 μmol)-tagged nanoparticles ($P > 0.05$) (**Table 2-3**). This is explained by the reduced Brownian motion of higher molecular weight molecules and increased difficulty of higher molecular weight molecules to diffuse out of the meshwork of PECA polymer wall.

Oligoarginine without histidine (RR and R4), which did not covalently associate with PECA nanoparticles, did not alter the size ($P > 0.05$) nor the zeta potential ($P > 0.05$) of PECA nanoparticles (**Table 2-4**). However, R4acaH, which did not covalently associate with PECA nanoparticles, significantly increased the zeta potential of the particles ($P < 0.01$), suggesting the presence of the oligoarginine on the surface (**Table 2-4**). It is possible that the amphiphilic R4acaH molecules concentrate at the water-oil interface of the microemulsion during the polymerization and thereby the amphiphilic oligoarginine was indirectly trapped between the interlinked polymer on the surface of the nanoparticles during polymerization. When the amount of RRH used to tag the PECA nanoparticles was increased to 100 μmol (**Table 2-4**) from 10 μmol (**Table 2-3**), the zeta potential of the RRH-tagged nanoparticles increased, indicating the increased presence of RRH on the surface of the nanoparticles.

Table 2-4. Characterization of unmodified and oligoarginine-associated nanoparticles. Data are means \pm SD (three independent batches). Values sharing the same letters are not significantly different, while values with different letters are significantly different.

Nanoparticles	Oligoarginine amount (μ mol)	Size (d.nm)	Polydispersity index	Zeta potential (mV)
Unmodified	-	230 \pm 31 ^a	0.06 \pm 0.07	-12.6 \pm 1.1 ^a
RR-associated	100	266 \pm 10 ^a	0.06 \pm 0.03	-12.0 \pm 1.4 ^a
RRH-tagged	100	224 \pm 7 ^a	0.12 \pm 0.07	+35.0 \pm 2.0 ^b
R4-associated	34	270 \pm 53 ^a	0.08 \pm 0.06	-8.5 \pm 1.6 ^a
R4acaH-associated	34	193 \pm 16 ^a	0.07 \pm 0.10	+33.5 \pm 4.5 ^b

2.4.3. Quantification of oligoarginine

2.4.3.1. HPLC/UV quantification

All assays were validated according to ICH guidelines (ICH, 1996) and **Table 2-5** shows the summary of validation of each oligoarginine recovered from the microemulsion matrix. There are several ways the oligoarginine can associate with PECA nanoparticles, which include adsorption on the surface, covalent binding with PECA polymer and entrapment within the nanoparticles. As the oligoarginine peptide chain increased, the associated amount of oligoarginine to the PECA nanoparticles increased (**Table 2-6**). Longer chain oligoarginine had higher association efficiency possibly due to its increased difficulty to diffuse out of the meshwork of PECA polymer wall. Although having fewer residues, RRH had similar entrapment as R4 probably due to RRH associating covalently with PECA nanoparticles.

HPLC/UV assay was able to indirectly quantify the total amount of oligoarginine associated with the PECA nanoparticles. However, this technique was unable to separate the physically associated oligoarginine from the covalently associated oligoarginine in the nanoparticles due to likelihood of the dissolved polymer precipitating in the column. This limitation can be resolved by MALDI-TOF mass spectrometry technique as this ionization technique does not require the separation of the oligoarginine from the polymer matrix (discussed in **Section 2.1.3**).

Table 2-5. Validation of oligoarginine recovered from the microemulsion matrix. (y= area under the curve and x = mass of oligoarginine).

Oligoarginine	Retention time (min) (n =18)	Standard curve equation, Linearity (R ²), LoD and LoQ	Concentration (mg/1.2 mL)	Accuracy (%) (n = 3)	Intraday Coefficient Variation (%) (n = 3)	Interday Coefficient Variation (%) (n = 3)
RR	4.9 ± 0.2	y = 17145.7x – 337605 R ² = 99.61% LoQ = 21.0 µg/mL LoD = 6.9 µg/mL	100	100.0	0.7	0.9
			120	100.5	-	-
			140	100.2	-	-
			160	99.4	1.4	0.6
			200	99.8	-	-
			240	100.2	2.3	1.9
RRH	6.4 ± 0.5	y = 18213.6x – 21617.7 R ² = 99.72 LoQ = 12.5 µg/mL LoD = 4.1 µg/mL	20	103.5	5.9	5.3
			35	99.7	-	-
			50	100.0	3.3	2.2
			75	98.3	-	-
			90	99.9	2.4	2.0
			120	100.7	-	-
R4	5.2 ± 0.1	y = 33153.4x – 542010 R ² = 99.34% LoQ = 22.9 µg/mL LoD = 7.5 µg/mL	80	96.5	2.9	1.6
			100	102.1	-	-
			120	100.8	-	-
			140	100.5	3.5	1.7
			160	100.0	-	-
			200	99.5	2.7	2.3
R4acaH	7.0 ± 0.5	y = 48680.2x – 221974 R ² = 99.89% LoQ = 4.9 µg/mL LoD = 1.6 µg/mL	20	96.8	5.9	1.8
			35	98.6	-	-
			50	102.6	0.9	4.5
			75	100.9	-	-
			90	99.5	1.9	0.7
			120	99.7	-	-

*LoD = Limit of detection, LoQ = Limit of quantitation

Table 2-6. Association efficiency of oligoarginine with PECA nanoparticles. Data are means \pm SD.

Oligoarginine	RR	RRH	R4	R4acaH
Association efficiency with PECA nanoparticles (%)	65.5 \pm 8.0 (<i>n</i> = 4)	73.9 \pm 6.9 (<i>n</i> = 6)	72.5 \pm 4.1 (<i>n</i> = 4)	88.8 \pm 1.8 (<i>n</i> = 6)

2.4.4. Semi-quantification of oligoarginine with i-TRAQ™ assay

The MALDI-TOF mass spectrometry technique is able to analyze peptide or protein of interest in a matrix sample without the need of separation. The mass spectrum obtained from MALDI-analysis of i-TRAQ™-labeled peptide or protein allows the quantification of the specific peptide or protein by providing an internal standard upon fragmentation (MS/MS) analysis. As the mass spectrum is relative to the highest peak, the closer the concentration of the standard (peptide tagged with i-TRAQ) to the unknown concentration of the peptide in the sample, the more accurate the calculated concentration will be. Labeling efficiencies (**Table 2-7**) were determined by first obtaining a mass spectrum (**Figure 2-3**), then performing a CID fragmentation on the RRH-labeled peak, *m/z* 612 (**Figure 2-4** and **Figure 2-5**). The total amount of labeled peptide with each i-TRAQ label can be determined using the peak ratios between the i-TRAQ labels.

Table 2-7. Labeling efficiencies of RRH tagged with 3 different i-TRAQ labels. Data are means \pm SD (*n* = 4).

i-TRAQ label	Labeling efficiency (%)
114	34.7 \pm 3.6
115	84.1 \pm 28.4
116	67.1 \pm 6.6

As RRH labeled with i-TRAQ 115 and i-TRAQ 116 had higher labeling efficiencies than i-TRAQ 114, RRH-labeled with i-TRAQ 115 was used for arginine tagging with PECA nanoparticles, while RRH labeled with i-TRAQ 116 was used as the internal standard to spike the MALDI matrix.

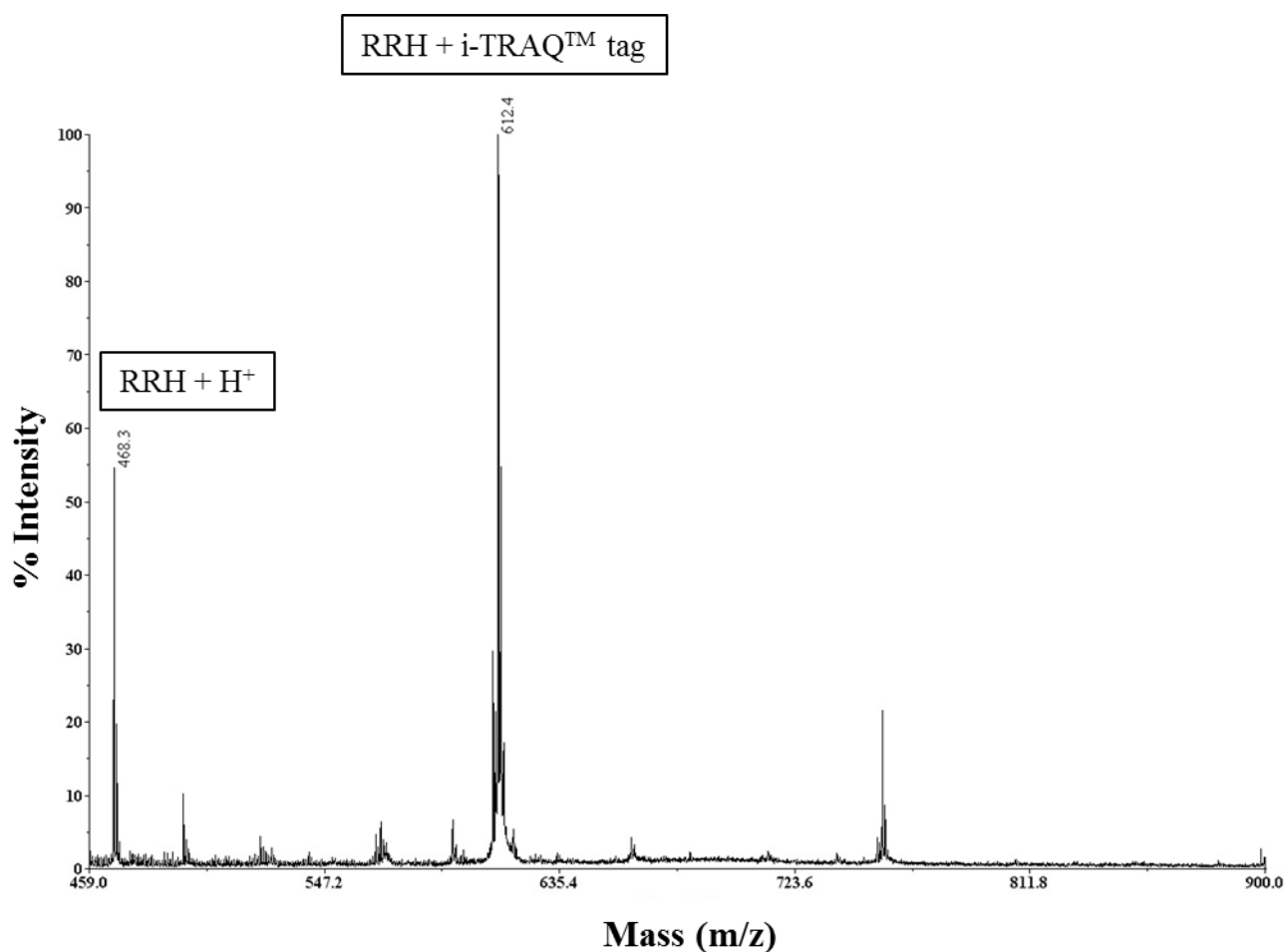


Figure 2-3. Mass spectrum of mixed RRH sample tagged with i-TRAQ 114, 115 and 116. ($M_{\text{RRH}} = 467$, $M_{\text{i-TRAQ}} = 145$).

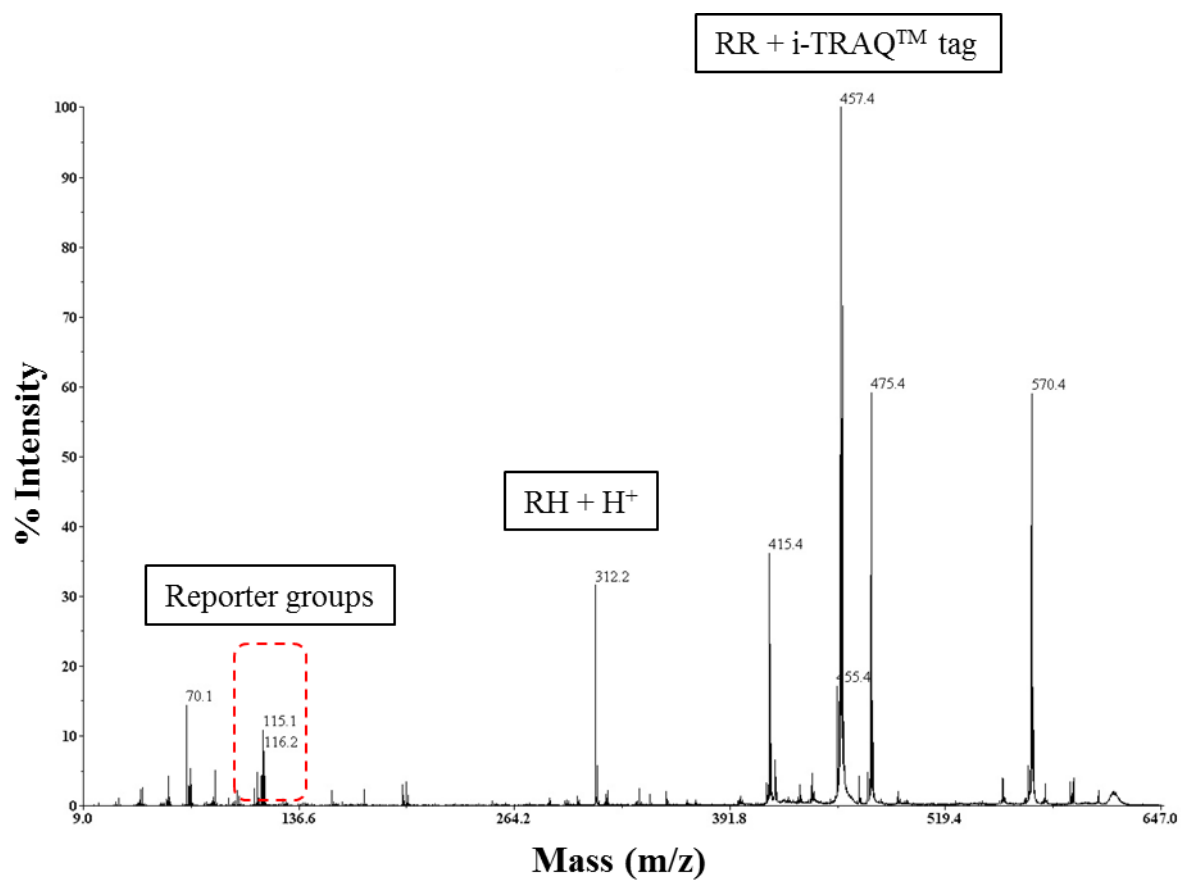


Figure 2-4. CID fragmentation of m/z 612 precursor.

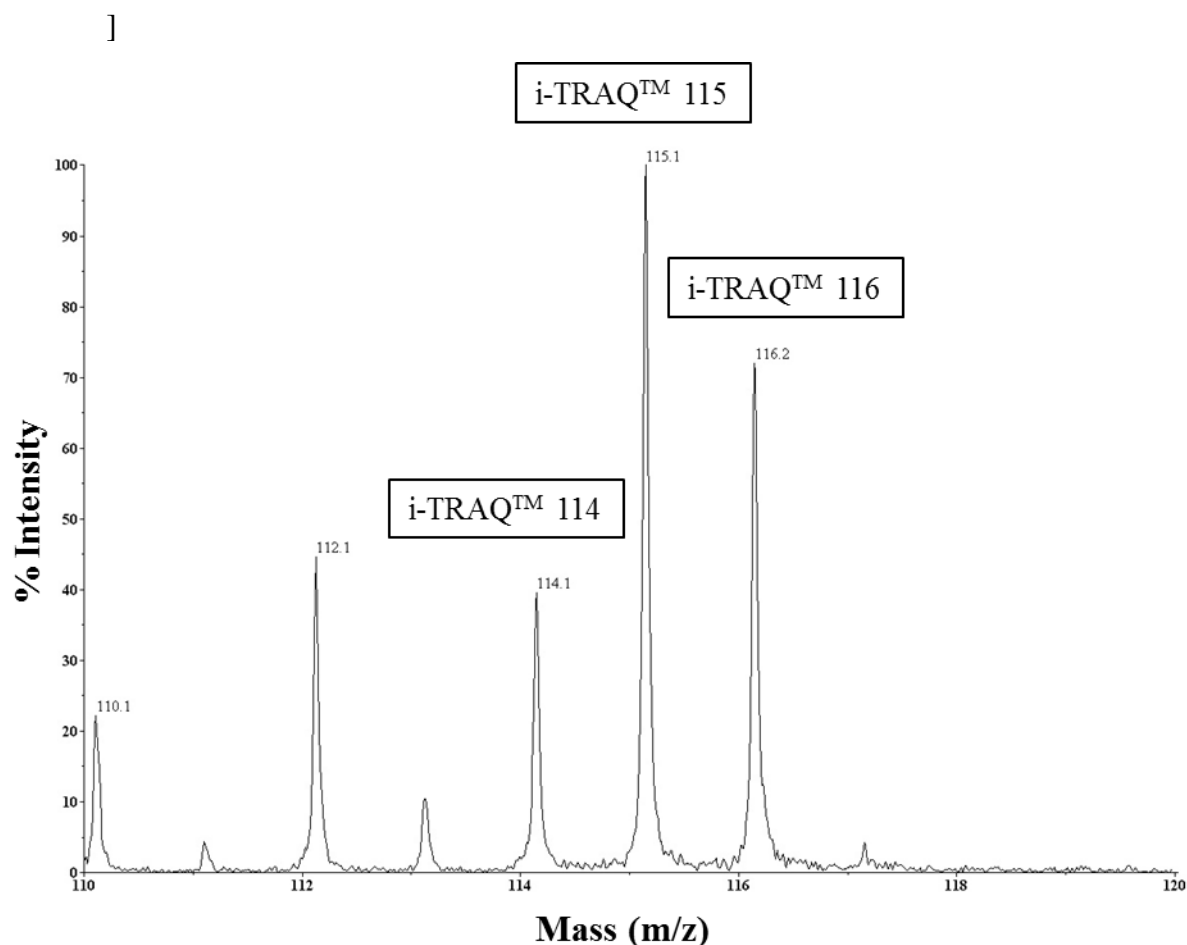


Figure 2-5. Enlarged region (m/z 110 to 118 in **Figure 2-4**) normalized to 100% intensity of m/z 115 peak.

Unassociated RRH in the microemulsion matrix for RRH-tagged nanoparticles with 0.1 μmol RRH loading was quantified by MALDI-TOF mass spectrometry. Unassociated RRH was determined to be $9.8\% \pm 1.4$ ($n = 2$, one batch) and was in agreement with unassociated RRH in the microemulsion matrix for RRH-tagged nanoparticles with 10 μmol RRH loading as determined with HPLC/UV assay, $11.9\% \pm 3.5$ ($n = 7$, two independent batches).

The amount of RRH (tagged with i-TRAQ 115) recovered from the supernatant of the microemulsion matrix and dissolved RRH-tagged nanoparticles sample was determined by the peak ratio of the reporter groups (i-TRAQ 115 to i-TRAQ 116) obtained from CID fragmentation of m/z 612 precursor. The amount of RRH recovered the

supernatant of the microemulsion matrix ($9.8\% \pm 1.4$, $n = 2$) was considered as unassociated RRH with the nanoparticles, while the amount of RRH recovered from the dissolved RRH-tagged nanoparticles sample ($65.2\% \pm 8.8$, $n = 2$) was considered to be RRH physically associated with the nanoparticles. The unrecovered portion of the RRH (~25%) was assumed to be covalently conjugated to PECA nanoparticles.

2.4.5. Effects of phosphates on nanoparticles and treatment with poloxamer-407

Both unmodified and RRH-tagged nanoparticles formed aggregates upon re-dispersion in HBSS; therefore the effect of phosphate on aggregation of nanoparticles was explored to better understand the behavior of these polymeric nanoparticles in an *in vitro* system. Unmodified and RRH (100 μmol)-tagged nanoparticles were stable in ultra-pure water and maintained their respective zeta potentials of -29 mV and +18 mV over 4 h under constant stirring at room temperature (25°C) (**Figure 2-6**). Upon titration with phosphate buffer (containing phosphates; dihydrogen phosphate and hydrogen phosphate) the zeta potential of unmodified nanoparticles increased, eventually reaching a plateau at 3 mM phosphates (**Figure 2-7A**). Conversely, the zeta potential of RRH (100 μmol)-tagged nanoparticles decreased with increasing concentration of phosphates, ultimately reaching a stable zeta potential at +2 mV, -9 mV and -19 mV for pH 6, 7 and 8 respectively (**Figure 2-7 B**). When titrated with HBSS (pH 7.4), the zeta potential of unmodified nanoparticles increased to -23 mV (**Figure 2-7 A**), while RRH (100 μmol)-tagged nanoparticles decreased to -7 mV and further addition of HBSS resulted a plateau at approximately -12 mV for both unmodified nanoparticles and RRH (100 μmol)-tagged nanoparticles (**Figure 2-7 B**).

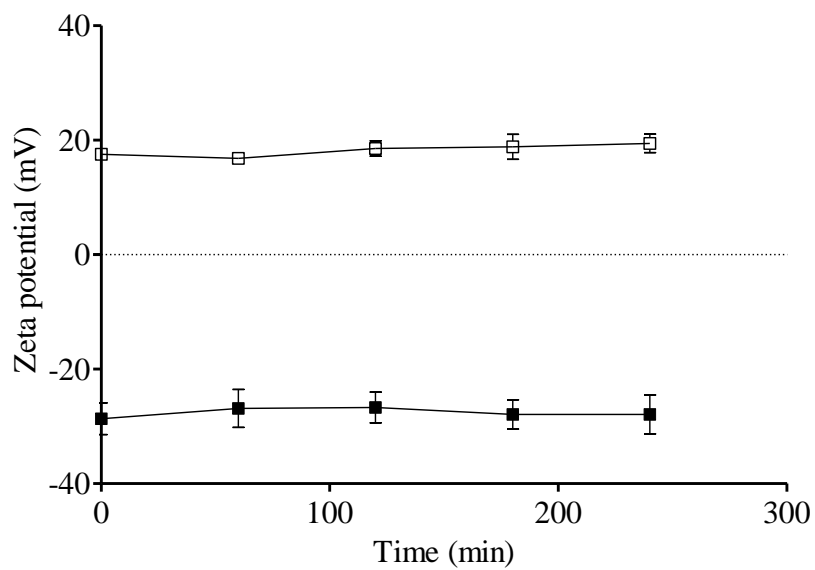
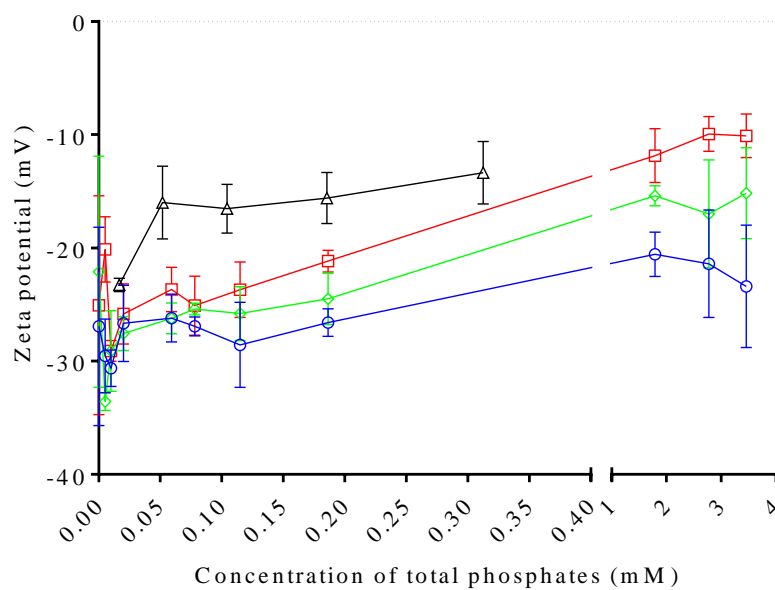


Figure 2-6. Zeta potential of unmodified (□) and RRH (100 μmol)-tagged (■) nanoparticles in ultra-pure water. Data are means ± SD ($n = 2$).

A



B

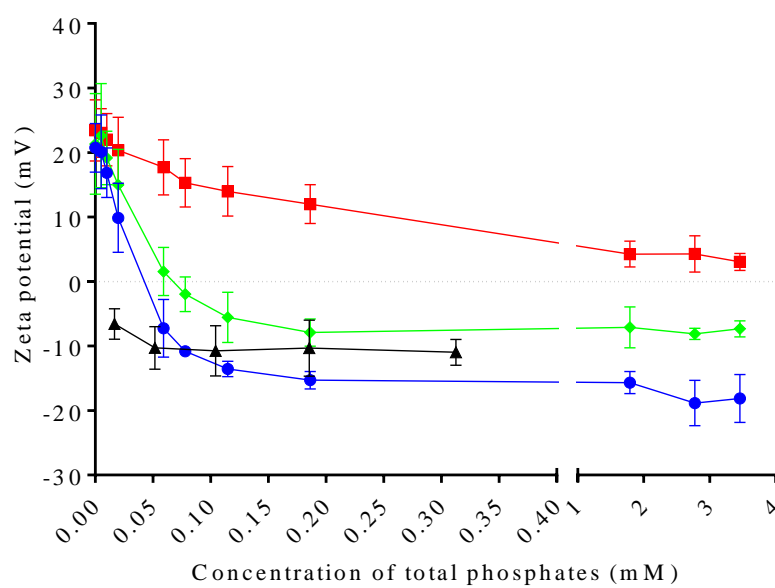


Figure 2-7. Zeta potential of **A.** unmodified nanoparticles (open symbols) and **B.** RRH (100 μmol)-tagged nanoparticles (closed symbols) titrated with phosphate buffer of varying pHs (\square pH 6, \diamond pH 7, \circ pH 8) and HBSS (Δ pH 7.4). Data are means \pm SD ($n = 3$).

Interaction of cationic chitosan particulates with electrolytes and proteins in media has been previously reported (Loh *et al.*, 2010). A rise in pH from 6 to 7.4 in HBSS increased the size of chitosan nanoparticles from 25 nm to 333 nm and slightly shifted the zeta potential from +5.3 mV to +3.3 mV (Loh *et al.*, 2010). An increase in pH of HBSS buffer reduces the ionization of the amine group of chitosan ($pK_a = 6.31 - 6.51$) (Wang *et al.*, 2006) and alters the composition of phosphate species in the buffer. Both decreased ionization of chitosan and increased surface adsorption of HPO_4^{2-} lead to a reduction in zeta potential, forming a less stable particle suspension that is prone to aggregation. In contrast to chitosan particles, where a pH rise decreases ionization, the rise in pH from 6 to 8 caused a drop in zeta potential for RRH (100 μmol)-tagged PECA nanoparticles (**Figure 2-7 B**), presumably due to the ionization of the acrylic acid head groups ($pK_a = 4.35$) in PECA nanoparticles as discussed by Müller *et al.* (1992) and surface adsorption of HPO_4^{2-} . At pH 8, HPO_4^{2-} would be the major ion present and therefore, would displace $H_2PO_4^-$ adsorbed on the surface of the RRH (100 μmol)-tagged nanoparticles, resulting in a more negative zeta potential. For unmodified PECA nanoparticles, the increase in ionic strength of buffer is the likely explanation for the less negative zeta potential (**Figure 2-7 A**) (Carneiro-da-Cunha *et al.*, 2011).

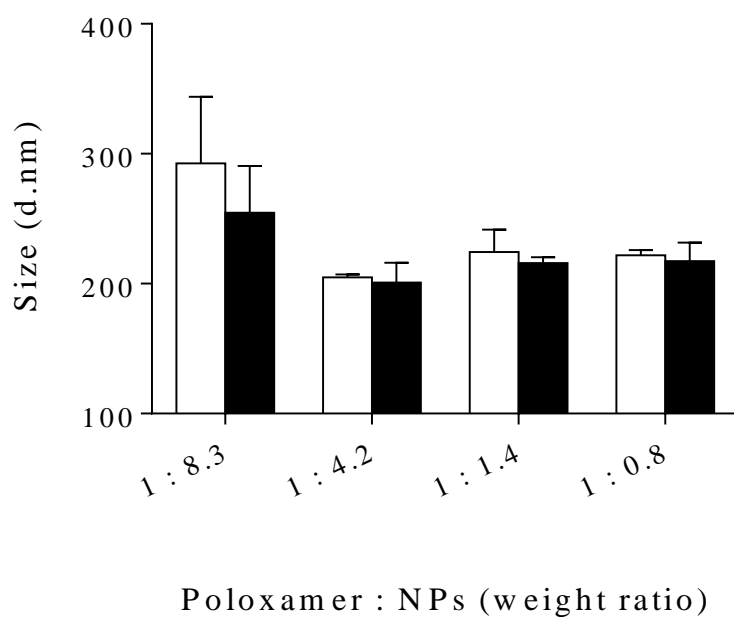
When the titration was performed with HBSS, the unexpected drop in zeta potential with the initial addition of 200 μL HBSS (containing 0.015mM phosphate) could be attributed to the presence of 2-[4-(2-hydroxyethyl)piperazin-1-yl] ethanesulfonic acid (HEPES), a zwitterionic buffering agent, in HBSS (25 mM HEPES). Addition of 0.3 mM HEPES (pH 7.4) was sufficient to negate the cationic zeta potential of RRH (100 μmol)-tagged nanoparticles, giving a zeta potential of $-5.0 \text{ mV} \pm 0.6$ ($n = 2$). The negative charge from HEPES carboxy groups could aid in the neutralization of the cationic charge on the surface of the RRH-tagged nanoparticles. Although phosphate and HEPES were found to be contributing factors in charge alteration in RRH-tagged nanoparticles, the impact of other components in HBSS has yet to be identified.

Treating the nanoparticles with poloxamer-407 at a mass ratio of at least 1 : 4.2 (poloxamer : dry nanoparticles) prevented the nanoparticles from aggregating upon re-suspension of particles in HBSS (**Figure 2-8** **Figure 2-8 A**). However, size variability of the particles was increased with decreasing concentrations of poloxamer-407. Treating the nanoparticles with poloxamer at 1 : 4.2 mass ratios maintained the size of unmodified and

RRH (100 μmol)-tagged nanoparticles at approximately 200 nm over 2 h at 37°C (**Figure 2-8 B**).

Stabilizing agent such as poloxamer has been used to prevent aggregation of particulates (White *et al.*, 2012). Although treating both the unmodified and RRH (100 μmol)-tagged nanoparticles with poloxamer-407 of at least 1 : 4.2 (poloxamer : dry nanoparticles) mass ratio prevented aggregation upon re-dispersion in HBSS, poloxamer-407 treatment altered the zeta potential of both unmodified and RRH (100 μmol)-tagged nanoparticles to 0 mV (**Appendix I**). All the nanoparticle formulations for the following experiments in the thesis were treated with poloxamer-407 of 1 : 4.2 (poloxamer : dry nanoparticles) mass ratio. Though the concentration of poloxamer-407 used was low (0.06% or 47.6 μM), the critical micelle concentration (CMC) of the poloxamer-407 may have been reached (8 to 600 μM (Cafaggi *et al.*, 2008)). Therefore, the poloxamer-407 may have formed micelles around the nanoparticles, preventing the aggregation from occurring at the expense of negating the zeta potential of the nanoparticles.

A



B

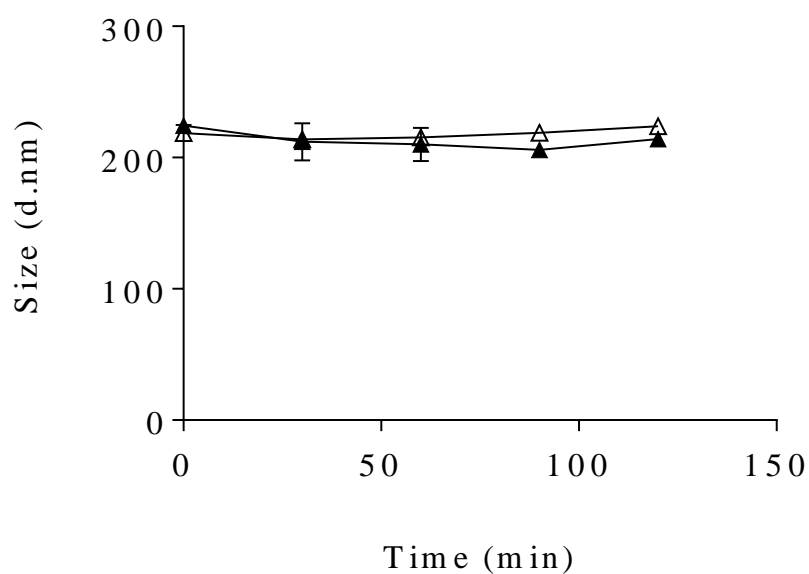


Figure 2-8. **A.** Size of unmodified nanoparticles (unfilled) and RRH (100 μmol)-tagged nanoparticles (filled) treated with different poloxamer-407 concentrations before re-dispersion in HBSS. **B.** Size of unmodified nanoparticles (Δ) and RRH (100 μmol)-tagged nanoparticles (\blacktriangle) coated with poloxamer-407 at 1 : 4.2 (poloxamer : dry nanoparticles) mass ratio, incubated at 37°C over 2 h. Data are means \pm SD ($n = 3$).

2.4.6. Release of oligoarginine

A fully validated RP-HPLC assay (**Table 2-8**) was employed to determine the release of oligoarginine from PECA nanoparticles in HBSS over 3 h (**Figure 2-9**). All nanoparticle formulations had an initial rapid release within the first 25 min, with RRH, R4acaH, RR, R4 releasing about 10%, 8%, 3% and 3% of the oligoarginine load respectively. RRH and R4acaH nanoparticles further released oligoarginine for a further 30 min. All nanoparticles formulations showed incomplete release over 3 h, with RRH, R4acaH, RR and R4 releasing 20%, 16%, 4%, 4% of their oligoarginine load, respectively. The continuing release of RRH and R4acaH could be explained by a leakier polymer particle due to RRH covalently associating with the PECA polymer and interfering with polymer network formation, while amphiphilic R4acaH would concentrate at the water-oil interface where the polymerization occurs. Therefore, covalent tagging of RRH and the presence of R4acaH at the water-oil interface may interfere with the polymerization of the polymer network as well as being entrapped closer to the surface, which was in agreement with the positive zeta potential observations (**Table 2-4**). RR and R4 would be mainly associated inside the nanoparticles and not present on the surface as indicated by the anionic zeta potential of the nanoparticles. The slow release of RR and R4 could be due to the electrostatic interaction of the cationic oligoarginine with the anionic polymer inside the nanoparticles.

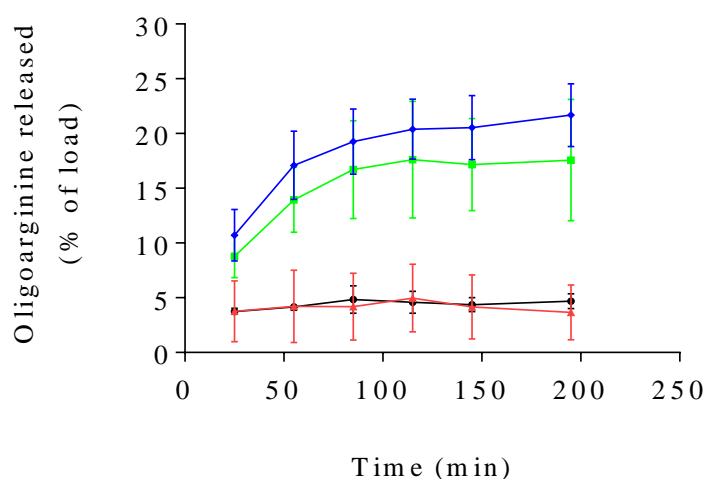


Figure 2-9. Release of oligoarginine from PECA nanoparticles (Blue = RRH, Green = R4acaH, Brown = RR, Black = R4) in HBSS at 37°C over 3 h. Data are means \pm SD ($n \geq 4$).

Table 2-8. Validation of oligoarginine in Hanks Balanced Salt Solution. (y= area under the curve and x = mass of oligoarginine).

Oligoarginine	Retention time (min) (n =18)	Standard curve equation, Linearity (R ²), LoD and LoQ	Concentrations (mg/0.2 mL)	Accuracy (%) (n = 3)	Intraday Coefficient Variation (%) (n = 3)	Interday Coefficient Variation (%) (n = 3)
RR	5.0 ± 0.1	y = 566580x + 19058.4 R ² = 99.87% LoQ = 6.6 µg/mL LoD = 2.2 µg/mL	1	107.4	2.7	3.8
			5	102.8	-	-
			10	98.3	-	-
			15	97.8	1.3	1.0
			20	101.3	-	-
			25	100.1	0.8	1.4
RRH	6.2 ± 0.2	y = 620463x – 324583 R ² = 99.93 LoQ = 23.2 µg/mL LoD = 7.7 µg/mL	10	105.0	0.5	0.8
			25	103.5	-	-
			50	101.1	1.9	0.8
			75	101.0	-	-
			100	100.3	0.9	0.3
			125	98.2	-	-
R4	5.5 ± 0.2	y = 613382x – 229693 R ² = 99.64 LoQ = 11.1 µg/mL LoD = 3.6 µg/mL	1	101.6	7.3	0.2
			5	102.6	-	-
			10	97.9	-	-
			15	100.9	0.4	3.4
			20	98.8	-	-
			25	100.7	5.2	4.1
R4acaH	6.6 ± 0.2	y = 810178x – 3315930 R ² = 99.95% LoQ = 19.5 µg/mL LoD = 6.4 µg/mL	10	102.3	5.8	6.6
			25	98.5	-	-
			50	97.5	2.4	1.3
			75	100.5	-	-
			100	100.1	0.8	0.1
			125	99.6	-	-

*LoD = Limit of detection, LoQ = Limit of quantitation

2.4.7. Conclusion

PECA nanoparticles covalently tagged with RRH via histidine anchoring in a single step polymerization using a water-in-oil microemulsion template were prepared and characterized. MALDI-TOF mass spectrometry was used to determine the type of association between RRH and PECA nanoparticles, as well as semi-quantifying the amount of RRH covalently associated with PECA nanoparticles. The size of RRH (10 μmol)-tagged nanoparticles did not alter with oligoarginine tagging, however the zeta potential of the particles shifted from -13 mV to +18 mV and + 35 mV for 10 μmol and 100 μmol RRH respectively, suggesting the presence of RRH on the surface of the nanoparticles. A similar trend was observed with R4acaH association even though the peptide did not covalently associate with the PECA nanoparticles. The presence of phosphates was shown to have a significant impact on the size and zeta potential of RRH (100 μmol)-tagged PECA nanoparticles. As size is a critical factor in determining the particulate uptake in cells, poloxamer-407 is a potential candidate to prevent aggregation of PECA nanoparticles in HBSS and will be used for all other further experiments in the thesis, but at the expense of negating the positive zeta potential of the nanoparticles. Approximately 20% of the RRH and the R4acaH were released from the PECA nanoparticles after 3 h incubation in HBSS, whereas majority of the RR and the R4 (> 95%) remained associated with the PECA nanoparticles. It is important to consider the influence of the cell incubating media on the nanoparticles when performing *in vitro* experiments as cellular response would depend on the surface characteristics of the particulates presented at the bio-interface.

CHAPTER THREE

Cellular association and uptake of
oligoarginine-associated PECA nanoparticles

3.1. Introduction

Characterization of nanoparticles should be conducted in the cell incubating media to gain information on the characteristics of the nanoparticles presented at the bio-interface, as particle aggregation and neutralization of the zeta potential may occur (Section 2.4.5). Apart from characterization of the nanoparticles, it is also important to critically evaluate the technique used to assess the uptake of the nanoparticles to draw the correct conclusion from each study. A common technique used to assess cellular uptake is the fluorescent activated cell sorting (FACS). This technique quantifies the uptake based on the intensity of fluorescent probe associated with the cells. However, this technique is unable to distinguish between cell surface association and internalization (Madani *et al.*, 2011). Therefore, it is inappropriate to associate cellular uptake with results obtained solely from FACS. To resolve this limitation, confocal imaging with appropriate cellular staining can be employed. Another important factor to consider in designing cellular uptake experiments is the characteristics of the cell-line used. Although the majority of cellular uptake studies are carried out with undifferentiated Caco-2 cells, the result obtained with undifferentiated Caco-2 cells may not be extrapolated to fully differentiated Caco-2 cell monolayers. Caco-2 cell monolayers resemble more closely to the gut and have very different characteristics to undifferentiated cells (Section 1.3). This chapter aims to critically assess the cellular association of the oligoarginine nanoparticles using FACS and verify the cellular uptake with confocal imaging.

3.1.1. Assessing cellular uptake of polymer nanoparticles in Caco-2 cells

Uptake of polymeric nanoparticles in Caco-2 cell monolayers has been extensively studied to understand the behaviour and fate of different nanoparticles in the human gut (Bhattacharjee *et al.*, 2013; Derakhshandeh *et al.*, 2011; He *et al.*, 2013; Reix *et al.*, 2012; Yin Win and Feng, 2005). The size of nanoparticles has been a focus of many studies and it has been documented that the cellular uptake of nanoparticles is inversely proportional to size, but the trend did not hold true for 50 nm polystyrene particles (Table 3-1). However, conflicting results were reported by Lu *et al.* (2009), where particles smaller than 50 nm had higher cellular uptake compared to larger particles. The reporting of lower cellular uptake of 50 nm particles could possibly be due to particle aggregation in the incubation medium, resulting in cells being exposed to larger aggregates rather than

individual 50 nm particles that the authors presumed they had applied to the cells. Lu *et al.* (2009) showed that 30 nm particles, which formed aggregates of approximately 130 nm in serum-free medium, had a similar uptake to particles of 110 nm (**Table 3-1**). This finding emphasizes the importance of particle characterization in the intended incubation medium (as discussed in **Section 2.4.5**) as this would be an accurate representation of the nanoparticles presented to the cellular bio-interface.

Table 3-1. Characteristics of polymeric nanoparticles and cellular uptake.

Particulate type	Characterization (Size and zeta potential)	Medium	Cell-line	Cellular uptake (Highest to lowest)	Reference
Polystyrene	50 – 1000 nm -31 ± 5 mV	Deionized water	Caco-2 (Intestinal model)	100 nm > 200 nm > 500 nm > 1000 nm > 50 nm	Yin Win and Feng (2005)
Polystyrene	25 – 500 nm -39 – -49 mV	Deionized water	Caco-2 (Intestinal model)	100 nm > 200 nm > 50nm > 500 nm > 25 nm Note: Statistical analysis was not performed	Kulkarni and Feng (2013)
			MDCK (Kidney epithelial model)	100 nm > 25 nm ≈ 50 nm > 200 nm ≈ 500 nm Note: Statistical analysis was not performed	
Mesoporous silica	30 – 280 nm 0 mV (at pH 7)	Serum free medium	HeLa (Cervical cancer cell model)	50 nm > 30 nm* > 110 nm > 280 nm > 170 nm	Lu <i>et al.</i> (2009)
Carboxymethyl chitosan	150 – 457 nm -13 – -38 mV	Water	L02 (Hepatic cell model)	150 nm (-15mV) > 150 nm (-25 mV) > 150 nm (-40 mV) > 500 nm (-25 mV)	He <i>et al.</i> (2010)
Chitosan hydrochloride	150 – 457 nm + 15 – +35 mV	Water	L02 (Hepatic cell model)	150nm (+35 mV) > 150 nm (+25 mV) > 150 nm (+15 mV) ≈ 300 nm (+25 mV)	He <i>et al.</i> (2010)

Apart from particulate size, other critical nanoparticulate parameters influencing uptake include surface charge and hydrophobicity (He *et al.*, 2010; Verma and Stellacci, 2010). Cationic nanoparticles have been reported to have greater cellular uptake compared to nanoparticles with an anionic charge (He *et al.*, 2010) or neutral charge (Jiang *et al.*, 2011; Thorek and Tsourkas, 2008; Villanueva *et al.*, 2009). Cho *et al.* (2009), using inductively coupled plasma mass spectroscopy that is able to detect and quantify the metal ion of the nanoparticles in the cells, have also observed that more cationic gold nanoparticles (zeta potential of +20 mV in deionized water) accumulated at the surface of SK-BR-3 cells compared to anionic (zeta potential of -10 mV in deionized water) and neutral (zeta potential of -4 mV in deionized water) gold particles. In the same study, the cationic particles were absorbed into cells to a greater extent (4 times greater) than the anionic or neutral particles (Cho *et al.*, 2009).

Mathematical modelling and simulations have been used to understand the influence of hydrophobicity of the nanoparticles on the cell surface and the interaction of the nanoparticles with the lipid bilayer (Li *et al.*, 2008). The hydrophobic nanoparticles were predicted by the simulations to be able to partition across the membrane and translocate into the cells, while semi-hydrophobic nanoparticles would remain adsorbed on the cellular surface (Li *et al.*, 2008). As the simulations did not predict passive translocation of hydrophilic nanoparticles across the membrane, Li *et al.* (2008) postulated that the hydrophilic particles have to be taken up via endocytosis. However, it may still be possible for the hydrophilic particles to enter the cells passively via membrane disruption, which the simulation model excluded.

Polymeric nanoparticles have been postulated to be taken up into Caco-2 cells using multiple, active pathways as well as through passive translocation (**Figure 3-1**) (He *et al.*, 2013). PLGA nanoparticles could internalize into the cells through energy-independent trafficking (unknown mechanism) and endocytosis (caveolin-mediated, clathrin-mediated, and macropinocytosis) (**Section 1.3**) (He *et al.*, 2013). The internalized nanoparticles form apical early endosomes (AEE) that are then either transported to the endoplasmic reticulum (ER); or to the lysosome via late endosome (LE); or exocytosed back out of the cell via the recycling endosome compartment (REC) (He *et al.*, 2013). The accumulated PLGA nanoparticles in the ER can either be transported to the Golgi complex and later exocytosed back out of the apical side of the cell via REC (He *et al.*, 2013); or

exported to the basolateral side for successful translocation (Butowt and Von Bartheld, 2001; Taberner *et al.*, 2002).

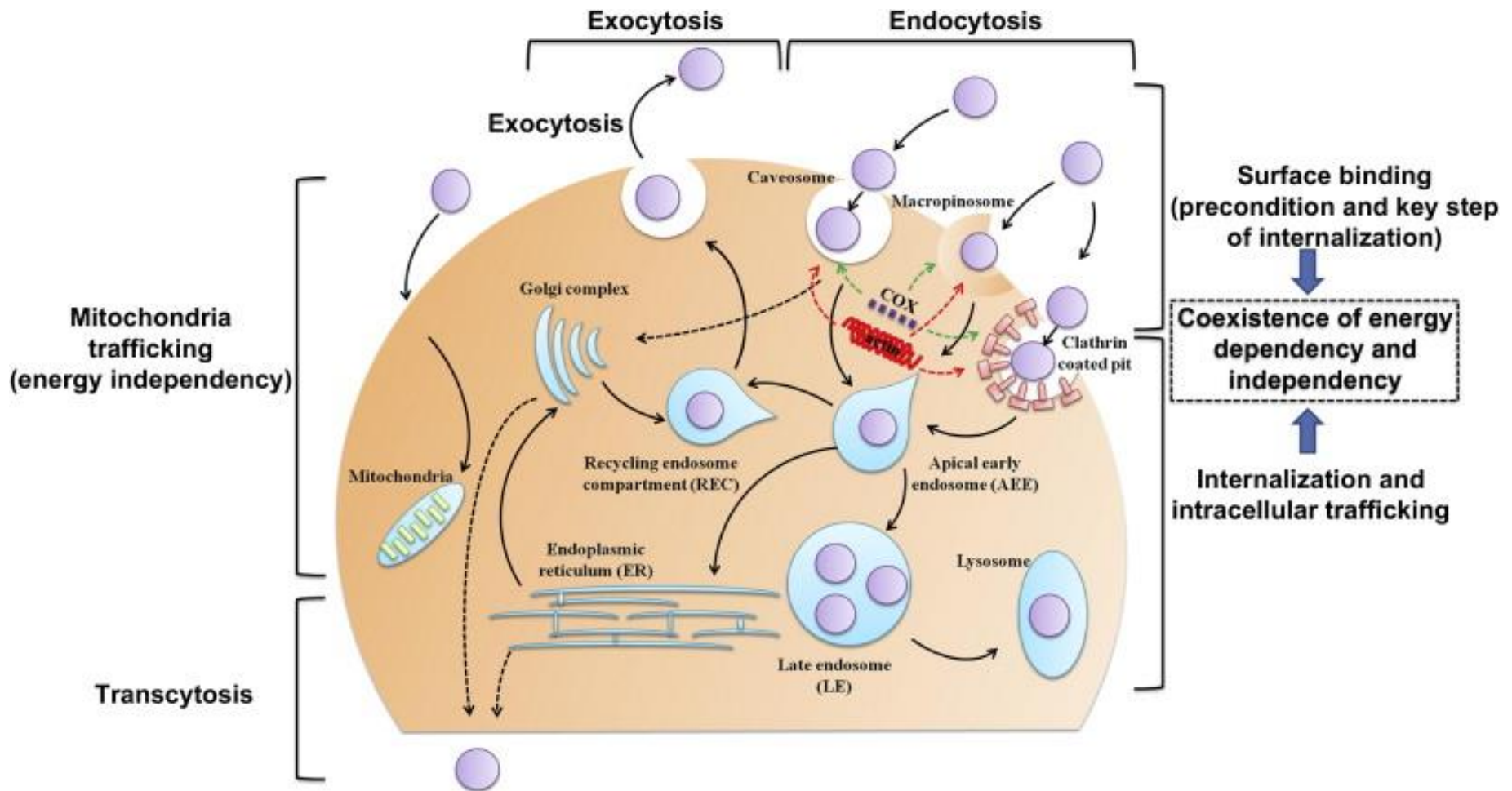


Figure 3-1. Postulated non-specific, energy-dependent (endocytosis) and energy-independent (mitochondria trafficking) uptake of polymeric nanoparticles in a Caco-2 cell. Purple spheres represent nanoparticles (He *et al.*, 2013).

The type of uptake mechanism involved in the cellular uptake of nanoparticles, such as endocytosis can be investigated by varying the incubation conditions. For example, uptake inhibitors (i.e. sodium azide, nystatin, 5-(N-ethyl-N-isopropyl)-amiloride)) can be used to selectively block active uptake pathways to investigate energy-independent uptake (He *et al.*, 2013). Uptake studies can also be conducted at 4°C to identify whether the nanoparticles can passively translocate into the cells (Langel, 2006). However, it is important to note that a temperature change can also alter other variables, such as the release of fluorescent marker from the nanoparticles (Zhou *et al.*, 2009), rate of contact of nanoparticles with the cell membrane (Hinderliter *et al.*, 2010) and ligand-receptor interactions (He *et al.*, 2013; Hulme and Trevethick, 2010). The release rate of fluorescent marker from nanoparticles at different temperatures can be important if the fluorescence detection of the payload is used as a proxy for particle uptake. Therefore, a fast release of fluorescent marker from the nanoparticles at a higher temperature may lead to an underestimate of the particle uptake if the free fluorescent marker is not taken up by the cells. At a lower temperature, the contact rate of nanoparticles with cell membrane decreases as random Brownian motion of the particles in the incubation medium decreases. Hulme and Trevethick (2010) showed that the frequency of ligand-receptor interactions also decreases at lower temperatures. According to Stokes-Einstein Equation, transport of nanoparticles due to diffusion is less prominent in particles larger than 200 nm compared transport due to sedimentation (Hinderliter *et al.*, 2010).

The presence of efflux transporters can also affect the accumulation of nanoparticles in the cells. Bhattacharjee *et al.* (2013) postulated that multidrug resistance/P-glycoprotein (MDR1/P-gp) in Caco-2 cells is able to efflux cationic, polymeric nanoparticles from cells while multiple drug resistance protein 1 (MRP1) would be mainly responsible for the efflux of anionic polymeric nanoparticles in fully differentiated Caco-2 cell monolayers. Cationic, fluorescent, tri-block co-polymer nanoparticles (TCNP) with terminal amines showed significant intracellular accumulation upon MDR1/P-gp inhibition with verapamil (Bhattacharjee *et al.*, 2013). Upon MRP1 inhibition with MK571, the accumulation of anionic TCNP (with terminal carboxylic acids) in the basolateral compartment was significantly decreased, which suggested that the MRP1 aided with the anionic nanoparticles transport out of the Caco-2 cells (Bhattacharjee *et al.*, 2013).

It is also important to emphasize that all uptake studies performed using FACS should be accompanied by other techniques such as confocal imaging as the FACS technique lacks discrimination between surface bound and translocated fluorescent-labeled CPPs (Section 1.5.1.1).

3.1.2. Cellular uptake of CPP-associated polymeric nanoparticles

Pan *et al.* (2012) showed that conjugating TAT to mesoporous silica nanoparticles (MSNs) enhanced intracellular delivery of MSNs into HeLa cells. Confocal laser scanning microscope imaging showed that 50 nm particles conjugated with TAT had greater uptake compared to 105 nm particles conjugated with TAT after 4 hours, based on fluorescence intensity (Pan *et al.*, 2012). This observation was consistent with the discussion above for plain polymeric nanoparticles, where smaller sized nanoparticles showed higher cellular uptake than larger nanoparticles. However, a limitation with this study is that confocal imaging lacks the ability to quantify the nanoparticles taken up into the cells.

Kar *et al.* (2013) conjugated polyarginine to MSNs (unmodified MSNs having a zeta potential of -47 mV in water), producing 80 nm cationic particles with zeta potentials of +20 mV and +32 mV for MSNs conjugated with 10 and 20 arginine residues, respectively. Kar and co-workers utilized fluorescence-activated cell sorting (FACS) and showed cellular uptake enhancement (greater than 90%) of polyarginine conjugated MSNs in both HeLa cells and A549 cells, while unmodified MSNs was not taken up (Kar *et al.*, 2013). They then further showed that MSNs conjugated with 20 arginine residues were more efficient at transfecting A549 cells compared to MSNs conjugated with 10 arginine residues, with transfection efficiencies of 60% and 18%, respectively (Kar *et al.*, 2013). However, associating uptake efficiency with transfection efficiency may be misleading as the transfection efficiency is strongly influenced by additional factors, such as the binding strength of pDNA to MSNs and endosomal escape of MSNs to infect the nucleus.

Another polymeric nanoparticle system used with CPPs to enhance cellular uptake is poly(lactic-co-glycolic acid) (PLGA) nanoparticles. Liu *et al.* (2013) conjugated octa-arginine (R8) to PLGA nanoparticles through pegylation and these R8-conjugated nanoparticles were cationic, bearing a zeta potential of +15 mV compared to -34 mV with unmodified PLGA nanoparticles (Liu *et al.*, 2013). R8-conjugated nanoparticles enhanced cellular internalization of the particles into undifferentiated Caco-2 cell monolayers

approximately 1.5 times compared to unmodified PLGA nanoparticles (Liu *et al.*, 2013). Liu *et al.* (2013) concluded that the cellular uptake of the nanoparticles was mainly through an energy-dependent process because the cellular uptake of the nanoparticles was reduced by 5 to 7-fold at 4°C compared to 37°C. However, this conclusion should not be drawn without an ATP-depletion study as reduced diffusion of the nanoparticles at lower temperature decreases the number of particles coming in contact with cell surface as well. Uptake enhancement of PLGA nanoparticles (4.5 times higher compared to unmodified particles) in Caco-2 cells was also shown by coupling TAT to PLGA nanoparticles (approximately 200 nm with a zeta potential of +11.3 mV) (Yan *et al.*, 2013).

The physical properties of nanoparticles, such as size and zeta potential, are vital in determining the cellular uptake, but the nanoparticles should be characterized in the cell incubating media. Although cationic nanoparticles have been shown to increase cellular uptake, more studies are required to strengthen the correlation between the surface charge of the nanoparticles and cell uptake. RRH-tagged PECA nanoparticles could be used to study the cellular interaction of arginine and cationic charge of nanoparticles at the bio-interface.

3.1.3. Cytotoxicity of polymeric nanoparticulate systems

Another critical factor to consider in formulating nanoparticulate drug delivery systems is cytotoxicity. Ideally, nanoparticulate formulations should have no or minimal effect on the cells. However, this can be difficult to achieve.

Although most studies are concerned with viability of the cells that have been incubated with the particulate formulations, the definition of viability can be rather vague, depending on the nature of the study. The classical definition of cell viability includes the ability of cells to continue proliferating (Riss and Moravec, 2004). There are a number of assays that could be used to assess viability (**Table 3-2**). However, one should be aware of the limitation of each assay and viability assessment should only be drawn from studies done using more than one type of assay.

Table 3-2. Viability assays and their mechanisms of action (Riss and Moravec, 2004).

Assay	Mechanism	Limitation(s)
Trypan blue	Indicator of membrane integrity	Unable to detect cytostatic effect
Propidium iodide		
Lactate dehydrogenase (LDH) leakage		
MTT or MTS tetrazolium reduction	Measurement of NAD(P)H-dependent oxidoreductase enzymes activities	Underestimates viability of metabolically quiet cells, such as splenocytes.
ATP quantification	Measurement of total ATP released from lysed live cells	Highly dependent on the total number of cells

Maassen *et al.* (1993) reported that the cytotoxicity of nanoparticulates can be attributed to factors such as degradation products of the polymers, the stimulation of cells and subsequent release of inflammatory mediators, and membrane adhesion of the polymers that interfere with cellular functions. The toxicity of PACA is thought to be dependent on the length of the alkyl side chain with lower toxicity for longer alkyl side chains due to decreased hydrolytic degradation of the polymer chain (Vauthier *et al.*, 2003). Membrane perforation due to the dilation of endoplasmic reticula of the cells, was observed with poly(methylcyanoacrylate) nanoparticles (Kante *et al.*, 1982) and poly(isobutylcyanoacrylate) nanoparticles (Gipps *et al.*, 1987). Cell growth inhibition, rather than cell death, was also reported in Swiss 3T3 fibroblasts, with shorter molecular weight of PACA causing greater cell growth inhibition (Tseng *et al.*, 1990). Therefore, it is more appropriate to evaluate the viability of nanoparticles using MTS reduction or ATP quantification assays, which detects cellular activities rather than LDH leakage assay, which detects the integrity of the cell membrane.

CPPs are claimed to have low toxicity (Foged and Nielsen, 2008; Nagahara *et al.*, 1998). In general, their cytotoxicity is determined by the type of CPP used and the dose applied (Cardozo *et al.*, 2007; El-Andaloussi *et al.*, 2007; Jones *et al.*, 2005) (details in **Section 1.4.2**). Most CPP cytotoxicity studies are performed using assays evaluating the cell membrane integrity, such as propidium iodide viability assay and LDH leakage,

because CPPs are hypothesized to cause perturbation and disruption of the cellular membrane (Cardozo *et al.*, 2007; El-Andaloussi *et al.*, 2007; Saar *et al.*, 2005).

For cytotoxicity of polymeric nanoparticles associated with CPPs, Kar *et al.* (2013) demonstrated that HeLa and A549 cells retained 80 to 85% viability with treatment up to 100 µg of either MSNs conjugated with 10 or 20 arginine residues, using the MTT assay. Liu *et al.* (2013) showed that PLGA nanoparticles conjugated with L-R8 (at 10 mg/mL) significantly reduced the viability of Caco-2 cells (about 60% viability), compared to unmodified nanoparticles and nanoparticles conjugated with D-R8 (both having about 80% viability) using the MTT assay. They speculated that the increased toxicity of nanoparticles due to L-R8 conjugation might be caused by charged byproduct fragments from the rapid degradation of L-R8 in the cytoplasm (Liu *et al.*, 2013). Liu and co-workers also showed that although all PLGA nanoparticle formulations (unmodified, L-R8 and D-R8 conjugated) enhanced LDH leakage from the intestinal lumen of the rat compared to Krebs-Ringers buffer solution, the elevation was not significant (Liu *et al.*, 2013). As LDH leakage measures the integrity of the cell membrane, the increased LDH leakage may indicate disruption of the membrane caused by the nanoparticles.

As PECA nanoparticles associated with oligoarginine have the potential to disrupt the cellular membrane as well as interfere with cellular functions, it is important to perform more than one type of viability assays for cytotoxicity evaluation of polymeric nanoparticles associated with CPPs as cell proliferation effect(s) caused by nanoparticles would not be able to be detected by assays such as LDH leakage and propidium iodide viability assay alone.

3.1.4. Chapter aims

To understand how the load and type of oligoarginine affects the interaction at the cellular bio-interface, FACS was used to investigate the cellular association between oligoarginine-associated nanoparticles and Caco-2 cells. As cytotoxicity is a potential issue with nanoparticles, the cytotoxicity of the oligoarginine-associated nanoparticles is evaluated by two types of viability assays. This chapter also aims to investigate the effects of temperature (37°C and 4°C) on the interaction at the bio-interface.

3.2. Materials

A description of the general materials used in the following experiments can be found in **Section 2.2**. Dulbecco's Phosphate Buffered Saline powder (DPBS, cell culture grade), Dulbecco's Modified Eagle Medium, high glucose with phenol red solution (DMEM, sterile, cell culture grade), trypsin-EDTA with phenol red solution (0.05%, sterile, cell culture grade), penicillin (10,000 units/mL)-streptomycin (10,000 µg/mL)-L-glutamine (29.2 mg/mL) solution (100X, sterile, cell culture grade) were sourced from Gibco[®] Life Technologies Corporation (Grand Island, NY, USA) Fetal Bovine Serum (FBS) (New Zealand origin, sterile, cell culture grade) was purchased from Moregate[®] Australia and New Zealand (Queensland, Australia) and sodium azide was purchased from Sigma Aldrich (St Louis, MO, USA, ACS grade). Propidium iodide solution, BD Pharmigen[™] was purchased from BD Biosciences (NJ, USA, cell culture grade).

3.3. Methods

3.3.1. Determining dry weight of PECA nanoparticles

The dry weight of nanoparticles is critical in determining the dose for uptake experiments and also the cytotoxicity of the particles. Unmodified and RRH (10 µmol)-tagged PECA nanoparticles were prepared as described previously (**Sections 2.3.1** and **2.3.2**), isolated and washed (**Section 2.3.3**) from 2.0 g of microemulsion. Then the nanoparticles were weighed prior to vacuum-drying at 40°C. The weight measurements were repeated daily until a constant weight was achieved.

3.3.2. Release of FITC-dextran in HBSS

Oligoarginine-associated PECA nanoparticles were isolated from 2.0 g of microemulsion by centrifugation (**Section 2.3.3**) and then re-suspended in 10 mL 0.12% (w/v) poloxamer-407 via sonication to prevent aggregation. The 10 mL particle suspension was later mixed with 10 mL 2X-concentrated HBSS (supplemented with 4.2 mmol sodium bicarbonate, 25 mmol D(+)-glucose and 25 mmol HEPES, pH 7.1) to make 20 mL particle suspension in 1X-concentrated HBSS with 0.06% (w/v) poloxamer-407. The suspension was stirred with a magnetic flea at 300 rpm at 37°C or 4°C and samples (1 mL) were drawn at 10, 40, 70, 120, 180 and 240 min. Immediately after sampling, the samples were spun at 20,800 g for 30 min and the supernatant (0.9 mL) was collected and

the fluorescence was measured (excitation 485 nm and emission 516 nm). A standard curve of FITC-dextran (2,000 kDa) in HBSS was prepared daily together with the samples to quantify the FITC-dextran (2,000 kDa) released from the nanoparticles.

3.3.3. Culturing Caco-2 cells

Caco-2 cells were cultured in culture flasks (surface area of 75 cm²) following standard protocols (Gao *et al.*, 2000). Cells were fed on alternate days with 15 mL Dulbecco's Modified Eagle Medium (supplemented with 10% FBS, 1% non-essential amino acid and 1% penicillin-streptomycin). Upon 70% cell confluency, cells were trypsinized and seeded on 12-well plates at 100,000 cells/well for 2 days (undifferentiated cells) or 24-well plates at 25,000 cells/well for 21 to 28 days (to obtain fully differentiated monolayer) for uptake studies.

3.3.4. Cytotoxicity assay

Caco-2 cells were seeded in 96-well plates (10,000 cells/well) for 2 days or 21 days. For the assessment of cytotoxicity, the cells were washed twice with HBSS (1X) and then incubated with nanoparticles formulations (dispersed in HBSS(1X) with 0.06% poloxamer-407) for 2 h at 37°C. Then the cells were washed with HBSS (1X) thrice, before incubating the cells with MTS reagent (CellTiter 96[®] Aqueous One Solution Cell Proliferation Assay, WI, USA) for 2 to 4 h at 37°C. The plate was then read using a spectrophotometer (Molecular Devices Spectramax 340 microplate reader, CA, USA) at 490 nm. To adjust for background absorbance, the absorbance value of each well (with cells) was subtracted from the average absorbance value of wells without cells ($n = 3$). The total viability of the cells (%) is calculated using **Equation 1**.

Equation 1. Cell viability determined by the MTS assay.

$$Viability (\%) = \frac{Absorbance_{(cells\ treated\ with\ formulation)} - Absorbance_{(background)}}{Absorbance_{(untreated\ cells)} - Absorbance_{(background)}} \times 100$$

The cytotoxicity was also determined using propidium iodide assay, assessed using FACS (**Section 3.3.5**). Each cell samples were spiked with 50 ng propidium iodide and analysed with flow cytometry.

3.3.5. Determining cellular association via FACS

Prior to incubation with formulations (nanoparticles dispersed in HBSS(1X) with 0.06% poloxamer-407), the undifferentiated Caco-2 cells or fully differentiated Caco-2 cell monolayers were washed twice with HBSS (1X) before replacing with 2 mL (12-well plate) or 1 mL (24-well plate) of FITC-dextran loaded nanoparticle formulations (12.5 µg dry weight/mL for undifferentiated Caco-2 cells and 125 µg dry weight/mL for fully differentiated Caco-2 cell monolayers) for incubation at 37°C. The difference in particle dosing was due to the different particle tolerance of undifferentiated Caco-2 cells and fully differentiated Caco-2 cell monolayers. For energy inhibition studies, cells were either pre-treated at 4°C or 37°C with HBSS without glucose (supplemented with 4.2 mM sodium bicarbonate, 10 mM sodium azide and 25 mM HEPES) for 1 h before incubating the cells with the formulations to block energy-dependent uptake.

After 2 h incubation, the formulations were discarded and cells were washed twice with ice cold HBSS (1X). Then the cells were trypsinized (with 0.2 mL 0.05% trypsin for 10 mins) and FACS (fluorescence-activated cell sorting) buffer (1% w/v bovine serum albumin and 0.01% w/v sodium azide in phosphate buffered saline) (0.8 mL) was added to stop the trypsinization process. The cells were centrifuged at 210 g for 5 min and washed again with FACS buffer (1 mL), before re-suspending each sample in 100 µL FACS buffer with 50 ng propidium iodide. Samples were placed on ice in the dark until analysis.

Cells (10,000 cells) were counted with FACSCanto™ II flow cytometer (BD Biosciences, California, USA) and data were analyzed using FlowJo® 7.6 analysis software (Tree Star, Oregon, USA). The flow cytometry data were gated for Caco-2 cells, single cells, viable cells and FITC fluorescence (**Figure 3-2**).

3.3.6. Statistical analysis

Comparison of cellular uptake between the different nanoparticle formulations were analyzed with General Linear Model ANOVA using Minitab® ver. 16.1.0.0. Post ANOVA pair wise comparisons were assessed using the Bonferroni method. $P < 0.05$ was considered to be significantly different. The weight loss of the nanoparticles due to vacuum dry and the FITC release (based on AUC) were compared between the different types of nanoparticles using the same statistical analysis as previously mentioned.

Additional F2-similar factor tests were also performed on the FITC release profiles from the nanoparticles.

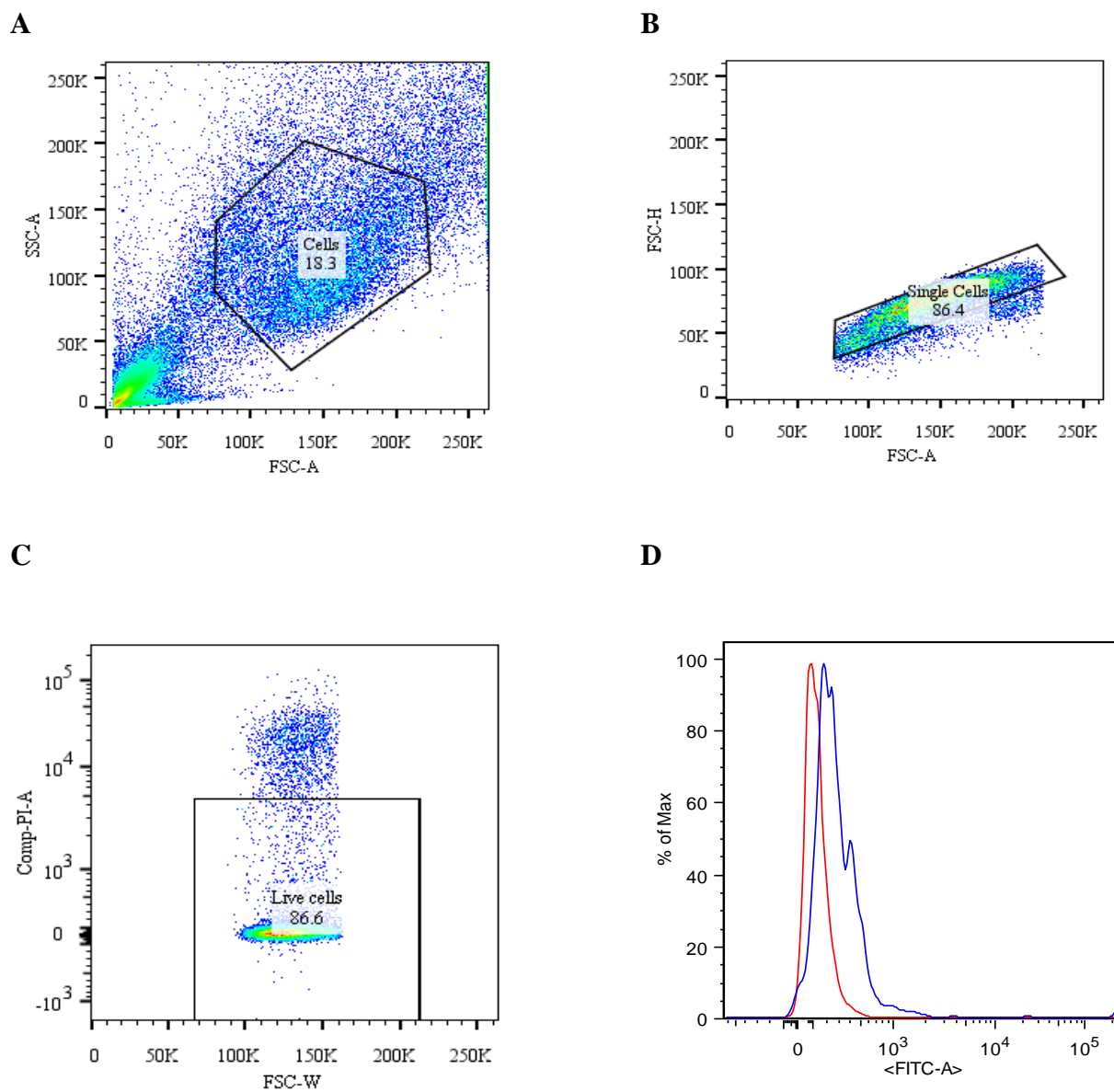


Figure 3-2. FACS analysis of Caco-2 cell populations, using FlowJo[®] analysis software. The Caco-2 cells were gated for **A.** cells, **B.** single cells, **C.** live cells and **D.** FITC (Red line representing untreated cells (negative control), and blue line representing cells incubated with 0.005% (w/v) saponin and FITC-loaded unmodified nanoparticles (positive control)). Caco-2 cells were incubated with different formulations for 2 h at 37°C.

3.3.7. Confocal imaging

Caco-2 cells were seeded at a cell density of 100,000 cells/mL or 50,000 cells/mL on a microscope cover slip (22 mm x 22 mm) in a 3.7 cm glass petri dish and grown for 2 days or 21 to 28 days, respectively. As with the FACS experiments (**Section 3.3.5**), Caco-2 cells were incubated with different nanoparticle formulations at 37°C or 4°C for 2 h. Cells were then washed with HBSS twice and FACS buffer twice before imaging. The samples were imaged using a confocal laser scanning microscope on Axioplan 2 (Zeiss LSM 510, Carl Zeiss Jenna GmbH, Jena, Germany), equipped with argon lasers (458, 477, 488 and 514 nm) and helium-neon lasers (543 and 633 nm) for excitation as well as phase objectives and a mercury burner. Nanoparticles (FITC-dextran loaded) were excited at 488 nm; the emission was collected through a band-pass filter at 505-530 nm. The nucleus stain, 4',6-diamidino-2-phenylindole (DAPI), was excited by the mercury burner (365 nm) and the membrane stain, CellMask[®] was excited at 633 nm and the emission was collected through a band-pass filter at 650 nm.

3.4. Results and discussion

3.4.1. Determining the dry weight of nanoparticles

As 200 mg monomer ECA was used for polymerization in a 10 g microemulsion, the maximum amount of nanoparticles that could be recovered from 2 g microemulsion was 40 mg. The 2 g microemulsion yielded 35 mg \pm 0.6 ($n = 3$) and 38 mg \pm 0.3 ($n = 3$) dry nanoparticles, for unmodified and RRH (10 μ mol)-tagged nanoparticles, respectively. Therefore, the majority (greater than 85%) of the nanoparticles were extracted and recovered from the microemulsion. Nanoparticles extracted from the microemulsion lost approximately 76% of their weight after 1 day when dried at 40°C and no further change in weight was observed over the next 4 days. There was no difference in weight loss between the unmodified and (10 μ mol)-tagged nanoparticles ($P > 0.05$) (**Figure 3-3**).

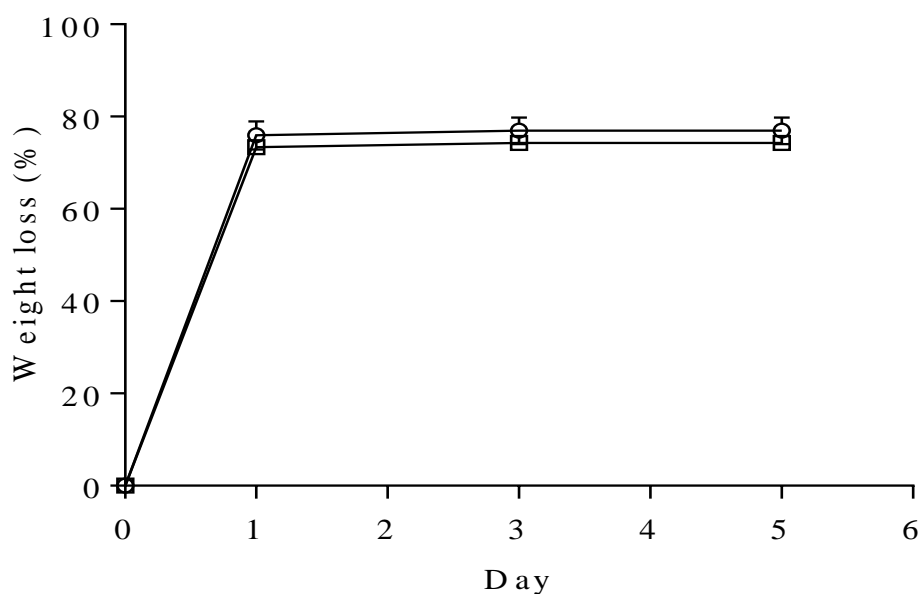


Figure 3-3. Weight loss of unmodified (○) and RRH (10 μmol)-tagged (□) nanoparticles during vacuum-drying at 40°C over 5 days. Data are means ± SD ($n = 3$).

3.4.2. FITC-dextran release in HBSS

Both unmodified and RRH-tagged nanoparticles showed a rapid release of FITC-dextran over the first 10 min, followed by a slower, incomplete release over 4 h. The amount of the rapid release decreased with increasing molecular weight of FITC-dextran entrapped in the nanoparticles ($P < 0.001$) (**Figure 3-4**). The release was the greatest (based on AUC) with FITC-dextran 70 kDa, followed by FITC-dextran 500 kDa and the smallest was with FITC-dextran 2,000 kDa. F2 similar factors tests also showed that all FITC-dextran release profiles were different between unmodified and RRH-tagged nanoparticles for all three sizes of dextran (with all F2 values lesser than 50). The fact that release of fluorescent material from the nanoparticles was slower with higher molecular weight FITC-dextran could be due to reduced Brownian motion and increased difficulty for the macromolecules to diffuse out of the meshwork of polymer network that comprises the nanoparticle wall. FITC-dextran (2,000 kDa) was able to diffuse from the RRH-tagged nanoparticles more quickly and to a greater extent than from unmodified nanoparticles ($P < 0.001$), suggesting that RRH-tagging the nanoparticles may have interfered with the

polymerization of PECA, affecting the integrity of the polymer wall formed (Graf *et al.*, 2009a). However, the magnitude of the difference was small (~5%).

It has also been postulated that the release from polymeric nanoparticles is influenced by the swelling of the polymer in the incubation medium (Vlachou *et al.*, 2001). The swelling magnitude of the polymer is dependent on the characteristics of the polymer, such as porosity and ionizable groups. Increased porosity of the polymer would allow faster penetration of medium into the nanoparticles, thus leading to faster and more extensive swelling of the polymer. The presence of charged, ionizable groups within the polymer would determine the repulsion or attraction between the polymer chains, thus influencing the swelling of nanoparticles. Swelled polymer would then lead to increased diffusion of the associated bioactive out of the nanoparticles. However, the quick release from the RRH-tagged nanoparticles could not be explained by the increased swelling of the oligoarginine-associated polymer, as the size of RRH-tagged nanoparticles in HBSS was slightly smaller ($P > 0.05$) than the unmodified nanoparticles (**Appendix I**).

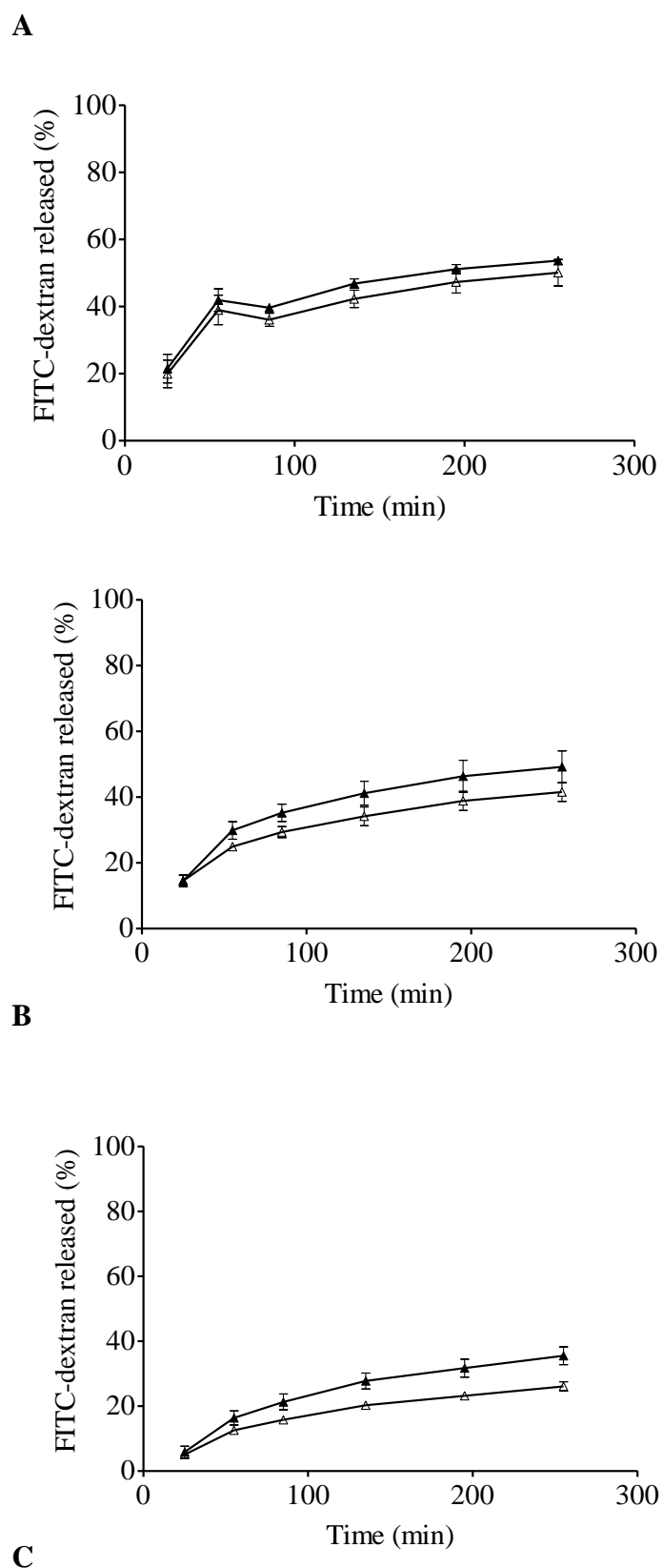


Figure 3-4. Release of FITC-dextran **A.** 70 kDa, **B.** 500 kDa, and **C.** 2,000 kDa from either unmodified nanoparticles (Δ) or RRH (10 μmol)-tagged nanoparticles (\blacktriangle) in HBSS, pH 7.4 with constant stirring at 300 rpm at 37°C. Data are means \pm SD ($n = 4$).

The release profile of FITC-dextran 2,000 kDa was further investigated comparing unmodified PECA nanoparticles and PECA nanoparticles associated with different residues of oligoarginine (**Figure 3-5**). Different incubation temperatures were also used to investigate the effect of temperature on the release of FITC-dextran from the nanoparticle formulations. For the RRH-tagged nanoparticles, 100 μmol was used to investigate the effect of RRH-tagging on the release of FITC-dextran from the PECA nanoparticles. At 37°C, all nanoparticles showed an immediate release of FITC-dextran over the first 30 min and the magnitude of the burst release differed between the formulations (**Figure 3-5 A**). Unmodified nanoparticles had an incomplete release over 3 h with 27% of the contents released, while RRH (100 μmol)-tagged, RR (100 μmol)-associated, R4acaH (34 μmol)-associated nanoparticles released 91%, 79% and 62% of their contents within 3 h, respectively (**Figure 3-5 A**). The faster FITC-dextran release from all three oligoarginine-associated nanoparticles (RRH, RR and R4acaH) compared to the unmodified nanoparticles provides evidence that the addition of oligoarginine, regardless of covalent association, may have interfered with the polymerization process of the ECA and affected the integrity of the polymer wall formed as discussed by Graf and co-workers (Graf *et al.*, 2009a). At 4°C, all nanoparticles, except unmodified nanoparticles, showed a lower immediate release of FITC-dextran compared to at 37°C and no further release of the FITC-dextran content observed for all nanoparticle formulations over 3 h (**Figure 3-5 B**).

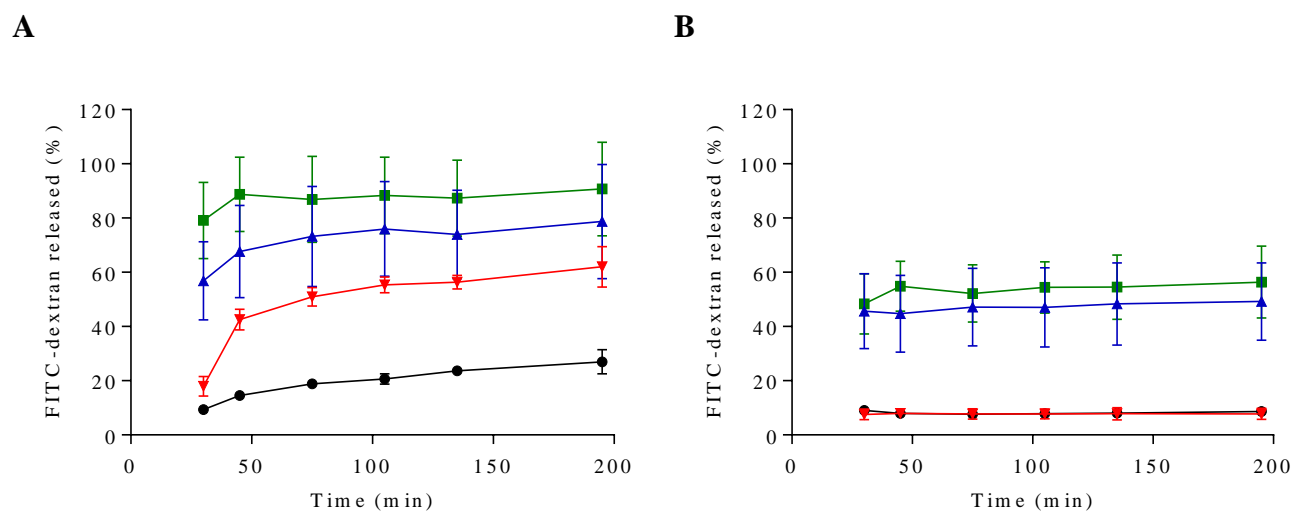


Figure 3-5. Release of FITC-dextran 2,000 kDa (5 mg) at **A.** 37°C and **B.** 4°C from either unmodified nanoparticles (●), RRH (100 μmol)-tagged nanoparticles (■), RR (100 μmol)-associated nanoparticles (▲), and R4acaH (34 μmol)-associated nanoparticles (▼) in HBSS with constant stirring at 300 rpm. Data are means ± SD ($n = 3$). R4acaH (34 μmol)-associated nanoparticles had similar release as unmodified nanoparticles at **B.** 4°C.

Polyalkylcyanoacrylate is known to degrade through a first order kinetics process and the rate of degradation is also strongly influenced by the environmental temperature (Cicek *et al.*, 1994; Leonard *et al.*, 1966). PECA nanoparticles were shown to fully degrade within 15 h at pH 7.4 at 37°C, whereas 90% degradation was observed after 800 h at 4°C (Cicek *et al.*, 1994). At lower temperature, the rate of ester hydrolysis is decreased, thus leading to a slower degradation rate of PECA and so a slower release rate of entrapped compounds (Cicek *et al.*, 1994). Therefore, the faster FITC-dextran release from the PECA nanoparticles at 37°C compared to 4°C observed (**Figure 3-5**) could be explained by the significantly faster degradation of PECA nanoparticles at a higher temperature. Cicek and co-workers observed a similar burst release (20%) with 2,4-dinitrophenylhydrazine (198 g/mol)-loaded PECA microparticles at 37°C and they attributed the release to surface erosion of PECA particles, thus allowing the instantaneous release of bioactive associated closer to the surface of particles (Cicek *et al.*, 1994). It is also possible that the slow release rate could be due to the slower diffusion rate of associated compounds out of the particles at 4°C compared to at 37°C.

Interestingly, the R4acaH (34 μmol)-associated nanoparticles had faster FITC-dextran release than unmodified nanoparticles at 37°C, but they had a similar release (almost identical) as the unmodified nanoparticles at 4°C. As discussed in **Section 2.4.2**, R4acaH did not covalently bind to the PECA polymer, but was associated non-covalently. Due to the amphiphilic nature of R4acaH, it was expected to be associated close to the surface of the nanoparticles during polymerization. Therefore, the release of R4acaH associated close to the surface of the nanoparticles, within the polymer, at 37°C (**Section 2.3.9**) could result in formation of pores in the nanoparticles. The highly porous R4acaH associated nanoparticles would therefore lead to a fast diffusion of FITC-dextran out of the nanoparticles at 37°C. In contrast, the non-covalently associated R4acaH release is slower at 4°C (**Section 2.3.9**), thus leading to a slower pore formation and a slower FITC-dextran release. It is also important to note that the diffusion of FITC-dextran out of the nanoparticles is also slower at the lower temperature of 4°C, compared to 37°C.

3.4.3. Cytotoxicity of oligoarginine-associated nanoparticles in Caco-2 cells and in fully differentiated Caco-2 cell monolayers

Caco-2 cells seeded for 2 days were able to tolerate the PECA nanoparticles up to $10^{4.1}$ ng/mL (or 12.5 $\mu\text{g/mL}$), with a viability of approximately 80%, regardless of RRH association, either through tagging or in a physical mixture (**Figure 3-6**). RRH solution (up to $10^{5.7}$ ng/mL (501 $\mu\text{g/mL}$ or 1 $\mu\text{mol/mL}$)) and microemulsion template (up to 10^7 ng/mL (or 10,000 $\mu\text{g/mL}$)) were tolerated well by the Caco-2 cells (**Figure 3-6**). The highly variable result of RRH solution could be due to the increased NAD(P)H-dependent oxidoreductase enzymes activities (measured by MTS assay) as a result of higher cell proliferation (Riss and Moravec, 2004). The cytotoxicity result from the MTS assay suggests that the addition of RRH (either through tagging or in a physical mixture) does not increase the toxicity of the PECA nanoparticles over that of untagged PECA nanoparticles. The amount of RRH associated with the PECA nanoparticles is far less than the highest amount of RRH solution tested (1 $\mu\text{mol/mL}$). For example, 12.5 μg (dry weight) of RRH (100 μmol)-tagged PECA nanoparticles would only be associated to 0.01 μmol RRH (assuming 100% of the RRH added was associated to the PECA nanoparticles).

PECA nanoparticles are known to degrade to toxic ethyl(cyanoacrylic acid) and formaldehyde in the incubating medium. The PECA nanoparticle dose that does not result in cytotoxicity was determined to be 12.5 $\mu\text{g/mL}$ with MTS assay. This observation

concur with the findings of Lherm *et al.* (1992), where concentrations above 25 $\mu\text{g}/\text{mL}$ of PECA nanoparticles were reported to kill the majority of L929 fibroblast cells after 72 h. Lherm *et al.* (1992) attributed the observed toxicity to the degradation of the particles, both in the incubation medium and associated on the cell wall.

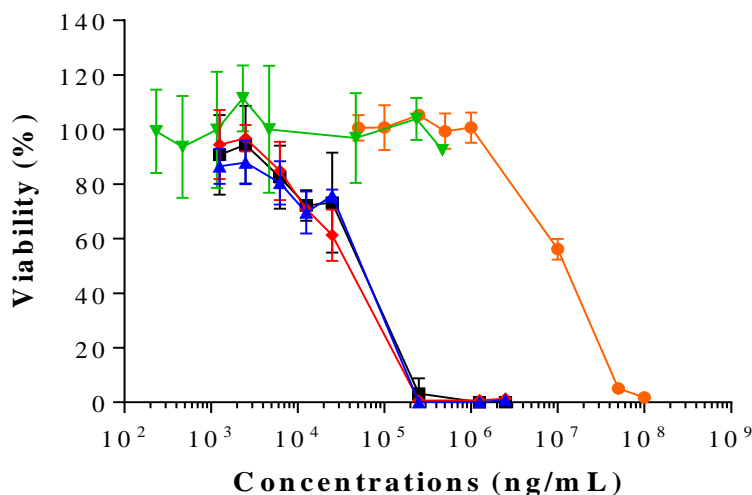


Figure 3-6. Viability of Caco-2 cells (seeded for 2 days) incubated with microemulsion (●), RRH solution (▼), unmodified nanoparticles (■), physical mix of unmodified nanoparticles + RRH solution (◆) and RRH (100 μmol)-tagged nanoparticles (▲). Cells were incubated for 2 h at 37°C, determined using the one step MTS viability assay (Kumar *et al.*, 2014). Data are means \pm SD ($n \geq 2$).

Fully differentiated Caco-2 cell monolayers grown for 21 to 28 days were more tolerant of PECA nanoparticles, up to a $10^{5.1}$ ng/mL (or 125 $\mu\text{g}/\text{mL}$), with a viability of approximately 80% after 2 h. Associating PECA nanoparticles with RR, RRH and R4acaH did not increase the toxicity of the PECA nanoparticles (Figure 3-7), which was expected as oligoarginine (RRH) solution was not toxic to Caco-2 cells grown for 2 days. The higher tolerance to the PECA nanoparticles of fully differentiated Caco-2 cell monolayers compared to 2 day old Caco-2 cells may be due to the lower ratio of nanoparticles to number of cells (Vauthier *et al.*, 2003). In the situation where a full monolayer is formed, each cell is exposed to fewer particles as there would be more cells in Caco-2 cells grown for 21 to 28 days (monolayer) than cells grown for 2 days. This is because an individual cell would be able to interact with the nanoparticles from all sides of its membrane, except from the basolateral side as the cells are adhered to the bottom of the

cell culture dish. However, a confluent cell monolayer would only be able to absorb the nanoparticles presented on the apical side. As the particles would move randomly in a diffusion manner, the collective contact or absorptive area of individual undifferentiated cells would be much greater than a fully differentiated monolayer. It is also possible that the presence of efflux transporters and a less permeable membrane in fully differentiated Caco-2 cells may contribute to the higher tolerance (He *et al.*, 2013; Hubatsch *et al.*, 2007). Efflux transporters such as MDR1/P-gp and MRP1 in Caco-2 cells are speculated to efflux cationic polymeric nanoparticles and anionic polymeric nanoparticles, respectively (Bhattacharjee *et al.*, 2013). The efflux transporters would reduce the accumulation of nanoparticles in the cells, therefore reducing the stress on cellular functions and increasing the survivability of the cells.

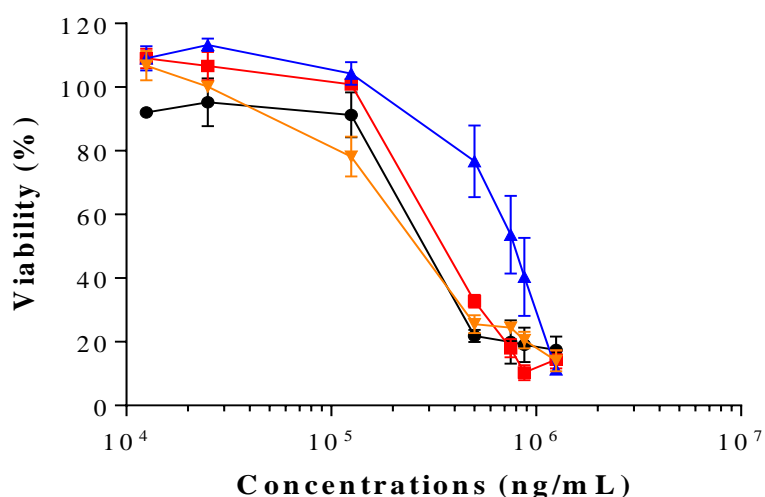


Figure 3-7. Viability of fully differentiated Caco-2 cell monolayer (grown for 21 - 28 days) incubated with unmodified nanoparticles (●), RR (100 μmol)-associated nanoparticles (■), RRH (100 μmol)-tagged nanoparticles (▲) and R4acaH (34 μmol)-associated nanoparticles (▼) for 2 h at 37°C, determined using one step MTS assay. Data are means ± SD ($n = 3$).

However, contradictory results were obtained with the propidium iodide viability assay using flow cytometry. The propidium iodide viability assay indicated a viability of greater than 80% ($n = 6$) for fully differentiated Caco-2 cell monolayers incubated with PECA nanoparticles with a concentration of $10^{5.6}$ ng/mL (or 398 μ g/mL) for 2 h at 37°C whereas the MTS assay showed that the fully differentiated Caco-2 cell could tolerate significantly less PECA nanoparticles (a concentration $10^{5.1}$ ng/mL or 125 μ g/mL). These conflicting observations could be explained by the different viability detection mechanisms as well as interpretation of viability of the two different viability assays. As mentioned in **Section 3.1.3**, the propidium iodide viability assay is unable to detect cytostatic effect and therefore, cells that have lost their cellular functionalities, apart from an intact cell membrane, would still be perceived as “live cells”. As PACA nanoparticles have been reported to inhibit cell growth (Tseng *et al.*, 1990), it is possible that the propidium iodide viability assay could have overestimated the viability compared to the MTS assay.

To ensure that the nanoparticles did not affect cellular functions, concentrations of nanoparticles that resulted in cell viability greater than 80% as determined by the MTS viability assay were used for subsequent uptake studies. Concentrations of nanoparticles of 12.5 μ g/mL and 125 μ g/mL were used for uptake studies in undifferentiated Caco-2 cells and fully differentiated Caco-2 cell monolayers, respectively.

3.4.4. Cellular association of oligoarginine-associated nanoparticles determined by FACS analysis

3.4.4.1. Undifferentiated Caco-2 cells

As the FACS technique was unable to differentiate between the cells that had internalized the nanoparticles from the cells that were only associated with the nanoparticles on the cell surface (Madani *et al.*, 2011), all FACS results were interpreted as cellular association rather than uptake. The addition of RRH to a solution of FITC-dextran did not improve cellular association of FITC-dextran with 2 day old Caco-2 cells (**Figure 3-8** and **Figure 3-9**). All nanoparticle formulations enhanced the cellular uptake of FITC-dextran ($P < 0.01$) (**Figure 3-8**). Entrapment of FITC-dextran in unmodified

PECA nanoparticles increased the cellular association to approximately 16%. Physically mixing the unmodified PECA nanoparticles with RRH solution, or tagging the unmodified PECA nanoparticles with 10 μmol RRH did not further improve the cellular association (**Figure 3-8**). However, associating the nanoparticles with a higher concentration of oligoarginine either through entrapment or tagging further increased the cellular association to 30%, 45%, and 80% for RR (100 μmol)-associated, RRH (100 μmol)-tagged, R4acaH (34 μmol)-associated nanoparticles, respectively (**Figure 3-8**). Given the positive zeta potential of RRH (100 μmol)-tagged and R4acaH (34 μmol)-associated nanoparticles (**Section 2.4.2**), it is postulated that the oligoarginine was present on the surface of the nanoparticles and this resulted in higher cellular association of nanoparticles compared to anionic PECA nanoparticles (unmodified and RR (100 μmol)-associated), eventually leading to increased cell uptake.

The variable release profiles of FITC-dextran (**Section 3.4.2**) from the types of nanoparticles should also be taken into account in the interpretation of the FACS data. As the oligoarginine-associated nanoparticles have fast FITC-dextran release, determination of the cellular association via FACS analysis may be biased. For example, there would be a high possibility of the Caco-2 cells associating with empty RRH-tagged nanoparticles after 1 h incubation, which could not be detected by FACS. Therefore, the FACS analysis may potentially give an underestimate in the cellular association. As free FITC-dextran is not readily taken up by the cells (**Figure 3-8**), the free FITC-dextran released from the nanoparticles is unlikely to affect the FACS analysis.

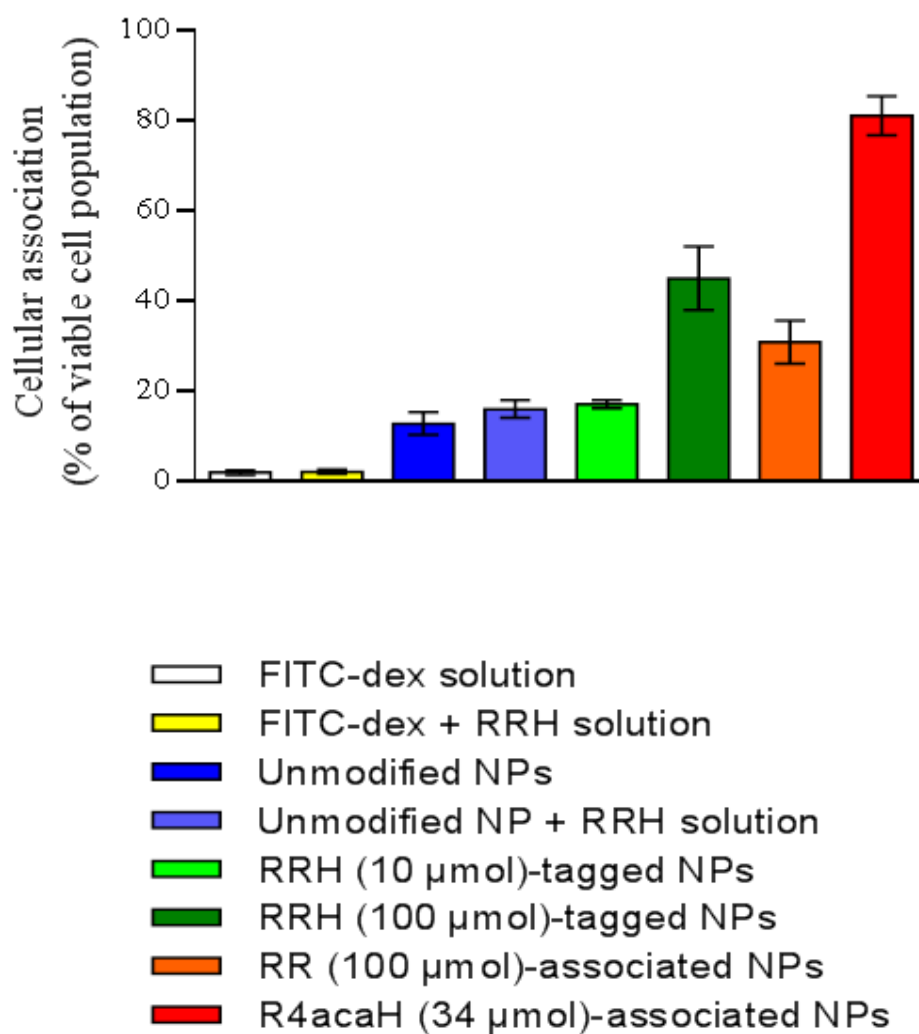


Figure 3-8. Cellular association of different nanoparticle formulations (12.5 µg/mL) in Caco-2 cells (seeded for 2 days) at 37°C. Data are means ± SD ($n = 6$).

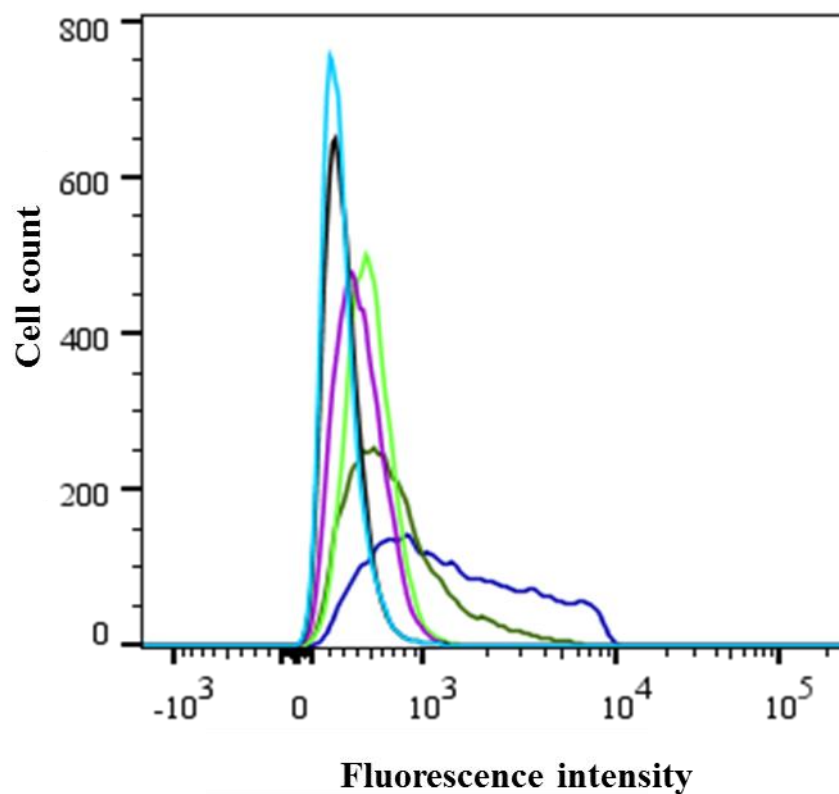


Figure 3-9. Population of cells associated with different FITC-dextran formulations based on fluorescence intensity; Blank (■); FITC-dextran solution (■); Unmodified nanoparticles (■); RR (100 μmol)-associated nanoparticles (■); RRH (100 μmol)-tagged nanoparticles (■); and R4acaH (34 μmol)-associated nanoparticles (■).

Incubating the undifferentiated Caco-2 cells with FITC-dextran loaded PECA nanoparticles associated with different oligoarginine also resulted in a higher cell population with stronger intensity of FITC fluorescence (**Figure 3-9**). The stronger FITC fluorescence intensity is indicative that a higher amount of FITC-dextran was being associated or taken up by the Caco-2 cells. However, this observation could not be directly interpreted as increased cellular association or uptake of nanoparticles because different nanoparticle formulations had different FITC-dextran release rates (**Figure 3-5**). For instance, more cells were seen associated with stronger intensity of FITC-dextran entrapped in R4acaH (34 μmol)-associated nanoparticles compared to RRH (100 μmol)-tagged (**Figure 3-9**). This could be due to the higher FITC-dextran load in R4acaH (34 μmol)-associated nanoparticles rather than more R4acaH (34 μmol)-associated nanoparticles associating with the cells. Therefore, distinguishing between cellular association and uptake of nanoparticles could not be concluded based on only FACS (Madani *et al.*, 2011) that detects the fluorescent probe that is non-covalently associated in the nanoparticles.

In the present experiment, it has been shown that the formulation containing two arginine residues, RRH (100 μmol)-tagged nanoparticles, can increase cellular association. This is contrary to the finding that at least hexa-arginine (R6) is required for effective penetration (Wender *et al.*, 2008; Wender *et al.*, 2000). The presence of multiple arginine molecules on the surface of the nanoparticles may have allowed the shorter arginine residues to act like a single oligoarginine when interacting with cells. Rothbard *et al.* (2002) investigated the spacing between the arginine residues in oligoarginine via molecular modelling. An uptake study showed a significant increased mean fluorescence in the cells incubated with fluorescent probe conjugated to hepta-arginine with aminocaproic acid spacers (RacaRRacaRRacaRR) compared to a hepta-arginine (R7) fluorescent conjugate (Rothbard *et al.*, 2002). This suggests that the spacing between the arginine residues plays a role in enhancing cellular uptake. Although faster rates of cell uptake were observed with increased aminocaproic acid spacers in the oligoarginine, the pattern of the spacing in the oligoarginine did not influence the uptake (Rothbard *et al.*, 2002). It was speculated that the increased number of spacers in the oligoarginine increases the flexibility of the arginines to adopt different conformations to interact with the cell surface (Rothbard *et al.*, 2002). A polymer backbone has also been used to space out the arginine residues within the oligoarginine to improve the intranasal absorption of

insulin (Sakuma *et al.*, 2010). Significant blood glucose reduction in mice was observed after nasal administration of insulin physically mixed with octa-arginine (R8) conjugated to a polymer backbone compared to insulin alone, while the physical insulin mixture with R8 had comparable result to insulin alone (Sakuma *et al.*, 2010). Using fluorescent microscopy, Sakuma *et al.* (2010) also demonstrated successful penetration of fluorescent probe into Caco-2 cells and Calu-3 cells when the fluorescent probe was physically mixed with R8-polymer conjugate, while the R8 mixture did not. Therefore, having spacing between arginine residues may be beneficial in enhancing cellular uptake. In the case of oligoarginine-associated PECA nanoparticles, the surface of the nanoparticles could potentially be used as a polymeric backbone for the conjugation of multiple oligoarginine to enhance the uptake of polymeric nanoparticles.

It was also observed that the cellular association enhancement of PECA nanoparticles may not require covalent association of arginine to PECA nanoparticles provided the oligoarginine is on the surface of the nanoparticles as entrapment of R4acaH (34 μmol) also showed significant enhanced cellular association. RR (100 μmol) entrapment, which resulted in anionic nanoparticles, also increased the uptake of PECA nanoparticles although to a lesser extent than RRH (100 μmol)-tagged and R4acaH (34 μmol)-associated nanoparticles. Although it has not been possible to investigate the mechanism by which RR entrapment increased uptake, a tentative hypothesis is that as RR (100 μmol)-associated PECA nanoparticles approach the cell surface, RR is constantly released thus generating a RR concentration gradient on the surface of the cell. The free RR is then able to interact and disrupt the cell membrane to aid with particle penetration into the cell. It is possible that RRH (100 μmol)-tagged and R4acaH (34 μmol)-associated nanoparticles could utilize similar mechanism as well to improve cellular uptake.

To investigate the cellular internalization of the unmodified nanoparticles and RRH-tagged nanoparticles, confocal microscopy was used to study the location of the nanoparticles in the undifferentiated Caco-2 cells following 2 h incubation with the nanoparticle formulations. Confocal imaging is able to give information on the location of the nanoparticles as the technique captures cross-sectional images in consecutive sequences, through the cell (from the apical to basolateral). The intensity of the green fluorescence (unmodified nanoparticles loaded with FITC-dextran) observed was stronger in the images closer to the basolateral, as opposed to the weak fluorescence intensity on

the surface of the cell. This observation suggested the unmodified nanoparticles were internalized into the cell, rather than associated with the cell surface (**Figure 3-10**). As the cells were cultured on a coverslip, the membrane stain, CellMask[®] (red) was unable to label the bottom or the basolateral side of the cell. Therefore, the red fluorescence was not observed in the images showing the cross sections of the cell at deeper depth, 4.38 to 4.92 μm (**Figure 3-10**).

In **Figure 3-11**, the presence of RRH (100 μmol)-tagged nanoparticles loaded with FITC-dextran (green) was seen to be associated on the surface of the cell (apical) as well as in the middle of a Caco-2 cell as the fluorescence intensity of the RRH (100 μmol)-tagged nanoparticles was stronger in the images closer to the apical or cell surface compared to the images closer to the basolateral side. As this was a common observation with most other cells treated RRH (100 μmol)-tagged nanoparticles, it is postulated that the RRH (100 μmol)-tagged nanoparticles were associated very strongly to the cell membrane and subsequent internalization does not readily occur during the 2 h incubation time period investigated. It has been reported that the translocation of oligoarginine across the enterocytes is low and the majority of the CPPs remained associated with the enterocytes (Kamei *et al.*, 2008b). Therefore, although the RRH tagging of the PECA nanoparticles increased the adherence of the nanoparticles to the cell membrane, it may not translate to increased internalization of the nanoparticles.

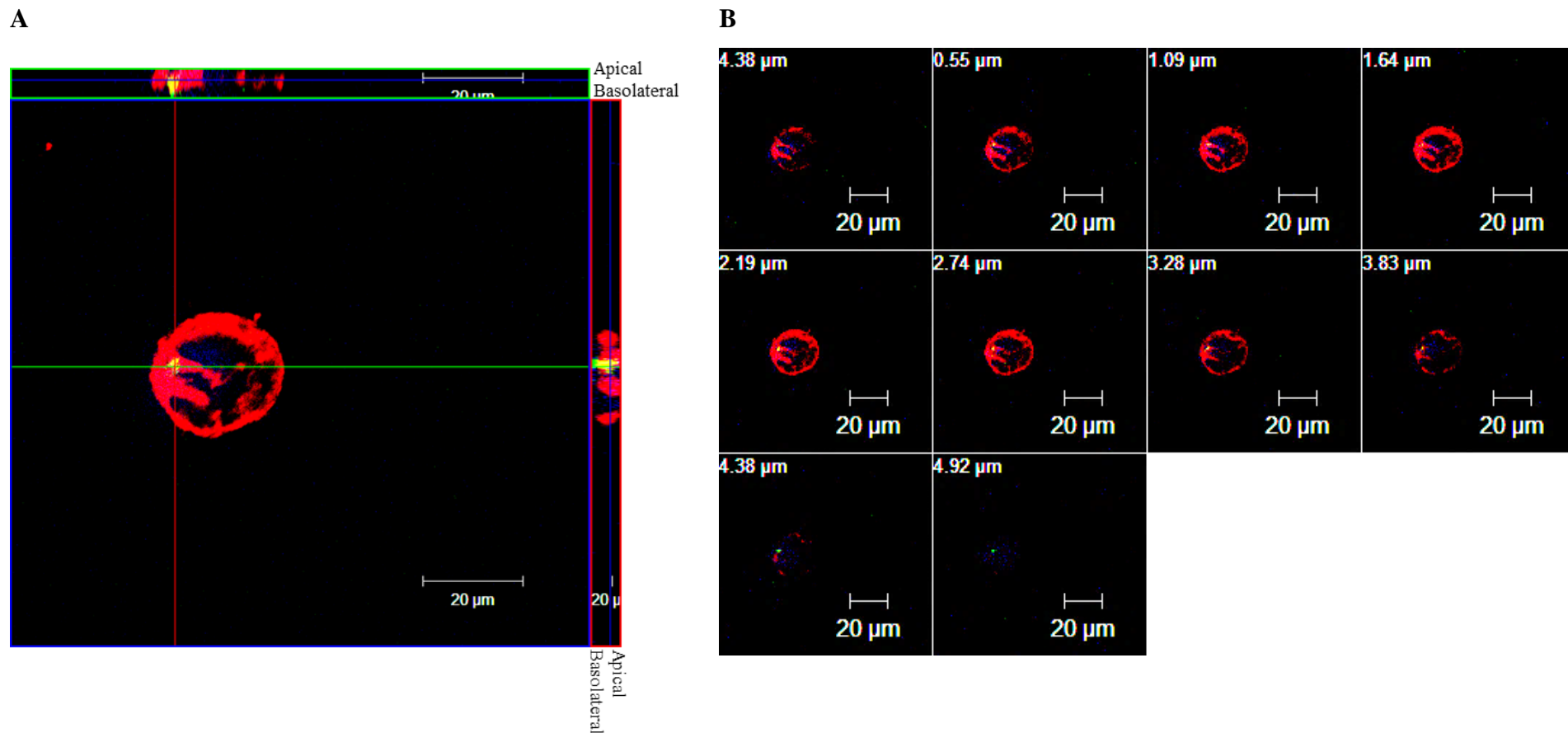


Figure 3-10. Confocal images of an undifferentiated Caco-2 cell. Cells were treated with unmodified nanoparticles (12.5 $\mu\text{g}/\text{mL}$) loaded with FITC-dextran for 2 h at 37°C. **A** shows the orthogonal sections of the cell and **B** shows the cross-sections of the cell in descending order (from the apical to the basolateral). The unmodified nanoparticles (Green) in the Caco-2 cell labeled with membrane stain, CellMask[®] (red) and nucleus stain, DAPI (blue).

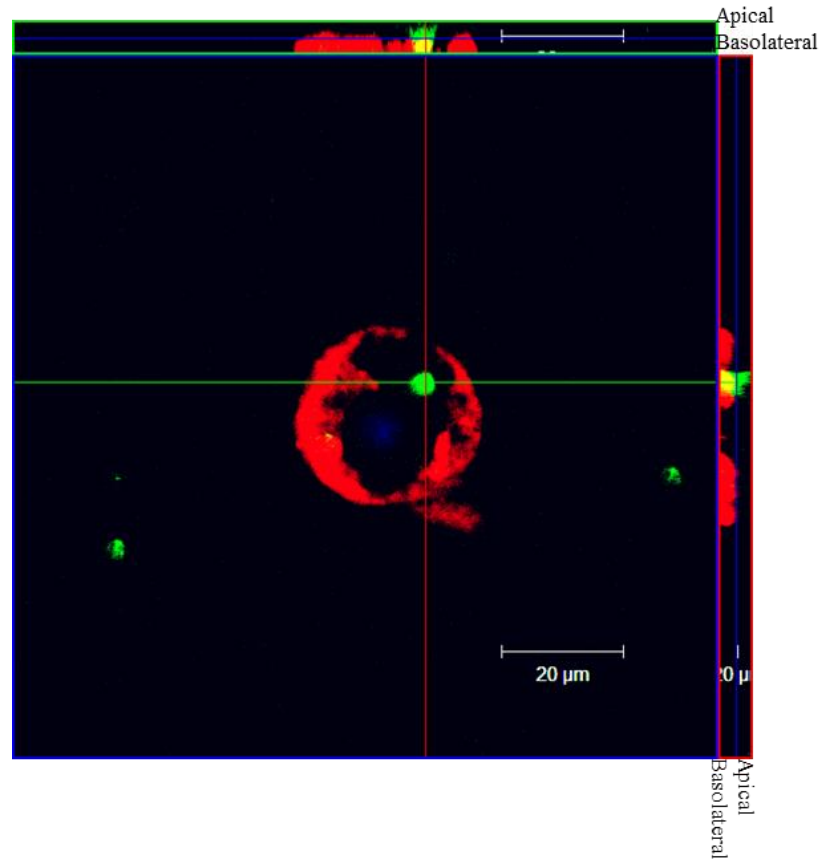
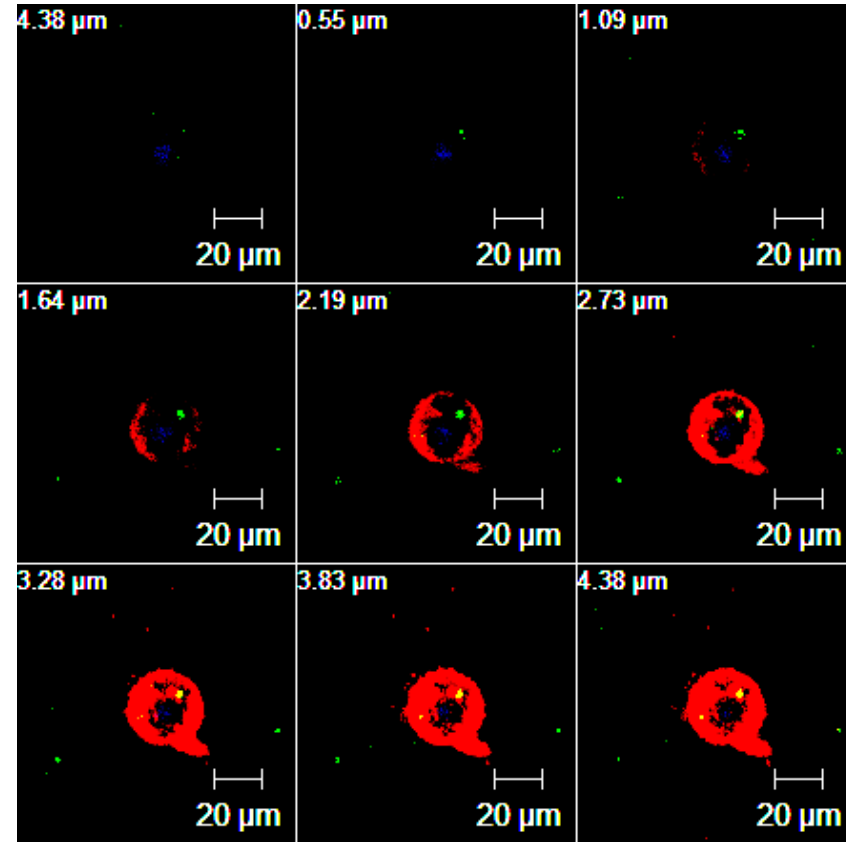
A**B**

Figure 3-11. Confocal images of an undifferentiated Caco-2 cell. Cells were treated with RRH (100 μmol)-tagged nanoparticles loaded with FITC-dextran (12.5 $\mu\text{g}/\text{mL}$) for 2 h at 37°C. **A** shows the orthogonal sections of the cell and **B** shows the cross-sections of the cell in ascending order (from the basolateral to the apical). The RRH (100 μmol)-tagged nanoparticles (Green) in the Caco-2 cell labeled with membrane stain, CellMask[®] (red) and nucleus stain, DAPI (blue).

When incubated at 4°C, the cellular association of the unmodified, RRH (100 µmol)-tagged and R4acaH (34 µmol)-associated nanoparticles were not significantly different ($P > 0.05$) to the uptake performed at 37°C (**Figure 3-12**) with undifferentiated cells. This finding is suggestive that the cellular association of the particles to undifferentiated cells was not significantly influenced by temperature. The cellular association of FITC-dextran in solution was reduced at 4°C. This could be due to the slower diffusion of the fluorescent probe in the solution to the cells. Although the nanoparticles too would be expected to diffuse slower to the cells, the nanoparticles would also have a slower dissociation rate from the cells once adhered due to their lower kinetic energy at 4°C. Although insignificant, both unmodified and RRH (100 µmol)-tagged nanoparticles showed a slight increase in cellular association. However, the increase in cellular association was not observed with R4acaH (34 µmol)-associated nanoparticles and could be because the majority of the R4acaH (34 µmol)-associated nanoparticles were already associated with the majority of the cells (approximately 80%) at 37°C.

As there was no internalization of the unmodified nanoparticles observed at 4°C (**Figure 3-13**), it was postulated that the internalization of the PECA nanoparticles into undifferentiated Caco-2 cells was energy-dependent. The uptake of both anionic and cationic polymeric PLGA nanoparticles into fully differentiated Caco-2 cell monolayers has been reported to be both energy-dependent and energy-independent, though the energy-independent uptake occurred to a lesser extent (He *et al.*, 2013). Although these researchers showed cellular internalization of the polymeric nanoparticles into the cytoplasm at 37°C using confocal imaging, the internalization at 4°C was questionable as most particles, if not all, co-localized with tight junction regions. It is possible that the nanoparticles were crossing the Caco-2 monolayer using the paracellular route as the size of the PLGA nanoparticles was 80 nm, which would be in agreement with the findings of Mathiowitz *et al.* (1997). Others have also reported both anionic nanoparticles and cationic nanoparticles enter cells through energy-dependent pathways, such as macropinocytosis (Harush-Frenkel *et al.*, 2008) and caveolae-dependent endocytosis (Perumal *et al.*, 2008). This finding demonstrated the importance of confocal imaging to verify the uptake result obtained by FACS that is unable to distinguish between the cellular uptake and cellular association.

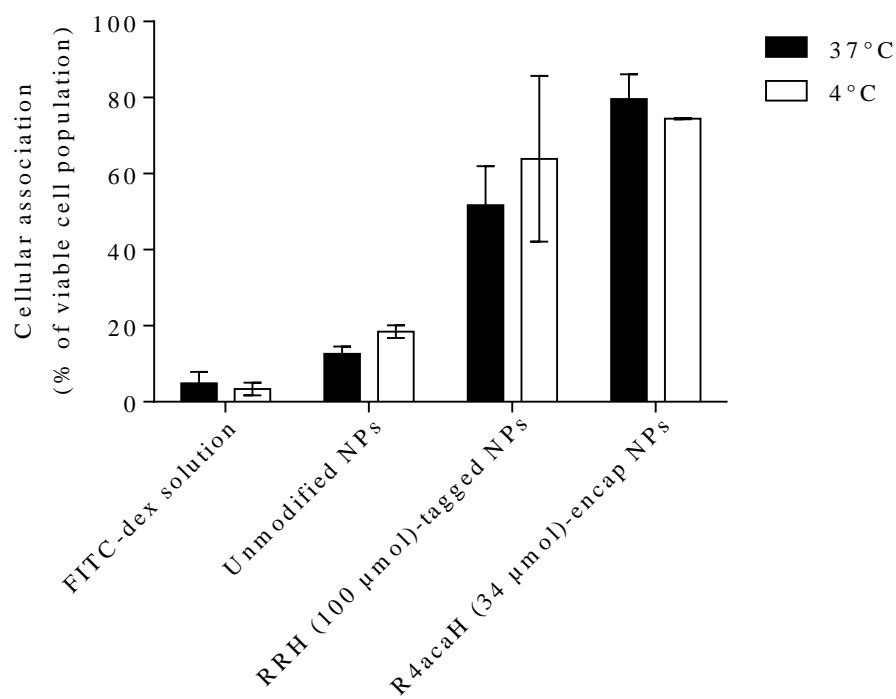


Figure 3-12. Cellular association of different nanoparticle formulations (12.5 μg/mL) in Caco-2 cells (grown for 2 days) at 37°C and 4°C. Data are means ± SD ($n = 2$).

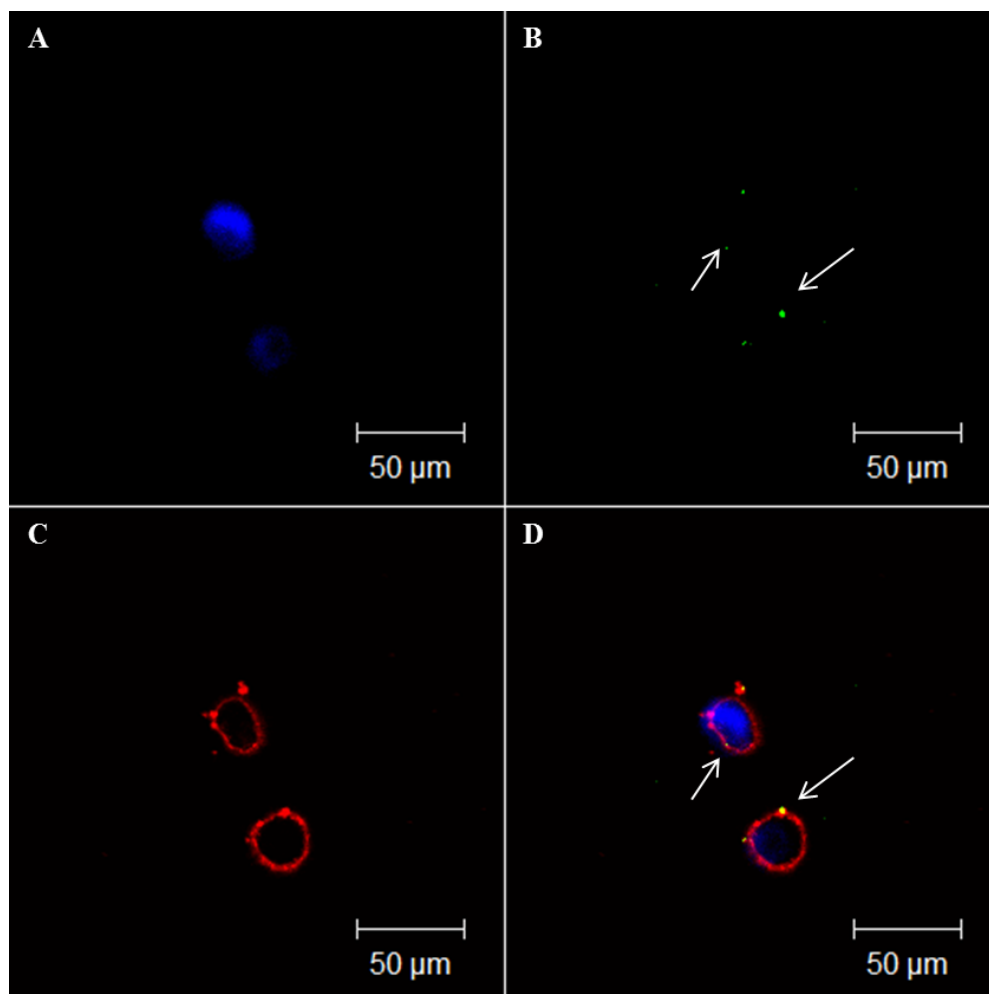


Figure 3-13. Confocal images of an undifferentiated Caco-2 cell. Cells were treated with unmodified nanoparticles loaded with FITC-dextran ($12.5 \mu\text{g/mL}$) for 2 h at 4°C . The images show **A**. The nucleus stain, DAPI (blue); **B**. The unmodified nanoparticles loaded with FITC-dextran (green); **C**. The membrane stain, CellMask[®] (red); **D**. Merged fluorescence.

As RRH ($100 \mu\text{mol}$)-tagged and R4acaH ($34 \mu\text{mol}$)-associated nanoparticles showed higher association with the undifferentiated Caco-2 cells, these formulations were selected for further uptake investigation with fully differentiated Caco-2 cell monolayer.

3.4.4.2. Fully differentiated Caco-2 cell monolayer

The cellular association enhancement with oligoarginine-associated nanoparticles was not observed with fully differentiated Caco-2 cell monolayers (**Figure 3-14**). All nanoparticle formulations were associated with approximately 9% of the viable cellular population at 37°C. A similar result was observed when the ATP pathway was disrupted by the addition of sodium azide and removal of glucose from the incubation medium. At 37°C, the cellular association of the nanoparticle formulations did not differ significantly to the respective cellular association of FITC-dextran solution, with or without ATP-depletion ($P > 0.05$). However, lower incubation temperatures (4°C) resulted in a significantly higher cellular association than at 37°C ($P < 0.001$) for RRH (100 µmol)-tagged and R4acaH (34 µmol)-associated nanoparticles with $20\% \pm 1$ and $28\% \pm 4$ of the cell population, respectively, associated with the nanoparticles (**Figure 3-14**). These differing results at 4°C for RRH (100 µmol)-tagged and R4acaH (34 µmol)-associated nanoparticles could be due to a couple of possibilities. As explained in **Section 3.4.4.1**, although fewer nanoparticles were expected to come in contact to the cell surface due to slower diffusion, the nanoparticles would also have less chance of dissociating from the cells once adhered. Therefore, cationic nanoparticles such as RRH (100 µmol)-tagged and R4acaH (34 µmol)-associated nanoparticles, would be expected to associate with a higher proportion of the cell population.

It is also postulated that the increased cellular association of the cationic, oligoarginine-associated nanoparticles observed at 4°C could be due to the inactivation of efflux pumps, such as MRP1/P-gp that removes cationic nanoparticles from the cells (Bhattacharjee *et al.*, 2013). To confirm that the reduced cellular association was indeed due to the presence of the efflux pumps, the cellular association study was repeated in an ATP-depleted model, where the efflux pumps would be inhibited. However, the increased cellular association of the cationic, oligoarginine-associated nanoparticles (as shown by the cellular association study conducted at 4°C) were not observed in the ATP-depleted model. Therefore, inhibition of efflux pumps could not explain for the increased cellular association of the cationic nanoparticles.

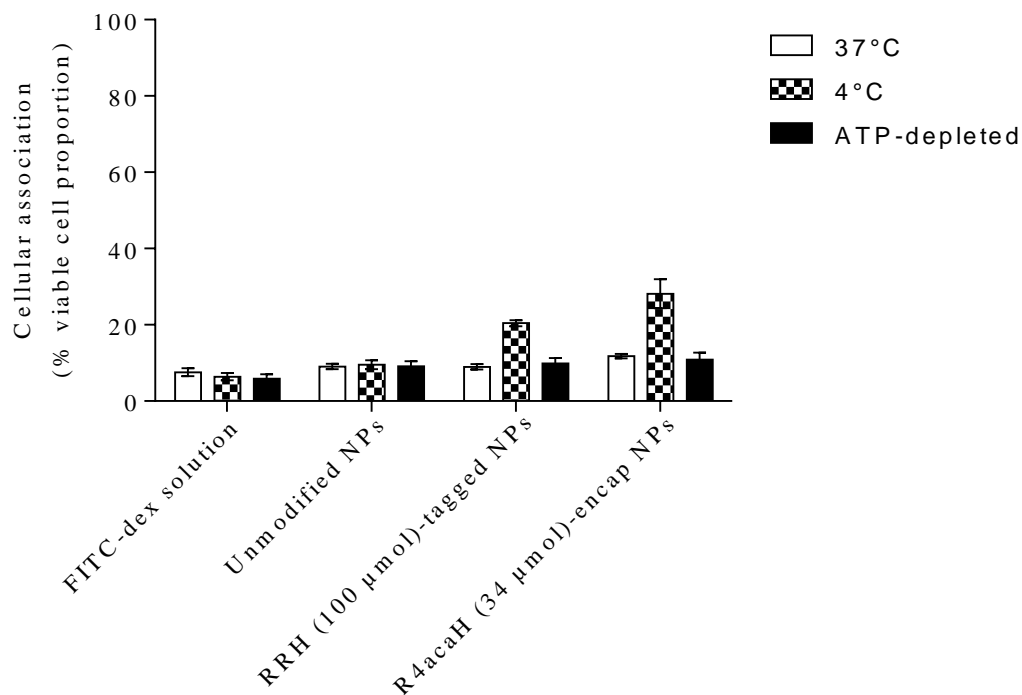


Figure 3-14. Cellular association of fully differentiated Caco-2 cell monolayer (grown for 21 to 28 days) incubated with different nanoparticle formulations at different conditions. Data are means \pm SD ($n = 4$, all 3 conditions were performed together).

Although undifferentiated cells showed higher cellular association with cationic nanoparticles as with other studies (He *et al.*, 2013; Liu *et al.*, 2013; Yin Win and Feng, 2005), this result was not reproduced with fully differentiated Caco-2 cell monolayer model, which is a better representation of the human gut. These differing results could be due to different cellular characteristics between undifferentiated Caco-2 cells and fully differentiated Caco-2 cell monolayers. Hu *et al.* (2009) posed a valid question on the fate of accumulated particles in cells during active cell division. In a normal dividing cell, the subcellular organelles are split and divided into two daughter cells. Therefore, it is also possible for a portion of the absorbed nanoparticles in the parent cell to be inherited by the two daughter cells. Åberg *et al.* (2013) demonstrated that daughter cells can be associated with nanoparticles from the extracellular environment as well as through the inheritance from parent cells during cell division. As the FACS technique detects the fluorescent probe (FITC-dextran) entrapped in the nanoparticles instead of the nanoparticles

themselves, the accumulated fluorescent probe (not the nanoparticles) in the parent cells could be acquired by daughter cells in rapidly dividing undifferentiated Caco-2 cells, provided the cells are initially associated with at least one or more fluorescent-loaded nanoparticles. Therefore, this phenomenon may lead to a larger proportion of the cell population being associated with FITC-dextran fluorescence. However, the magnitude of the bias in the cellular association study due to the cellular division was unable to be determined. Although the time it takes for the Caco-2 cells to double its population is approximately 32 h, the cell population would be composed of cells in various stages of the cell cycle (Visanji *et al.*, 2004). Therefore, it is still possible for cellular division to influence the cellular association even in a 2 h study.

Another possible explanation for fewer particles being associated with fully differentiated Caco-2 cell monolayers is the presence of active efflux transporters that decrease particle accumulation in the cells (Bhattacharjee *et al.*, 2013). However, this hypothesis of the presence of efflux pumps in fully differentiated Caco-2 cell monolayer reduces the cellular association of cationic, oligoarginine nanoparticles was rejected as cellular association of oligoarginine-associated nanoparticles was not enhanced in an ATP-depleted model. Nevertheless, these results showed that cellular association determined from undifferentiated cells should not be extrapolated to fully differentiated Caco-2 cell monolayers. The difference between undifferentiated Caco-2 cells and fully differentiated Caco-2 cell monolayers is further investigated and discussed in **Chapter 4**.

3.5. Conclusion

PECA nanoparticles were able to increase the proportion of cells associated with FITC-dextran in individual Caco-2 cells cultured for 2 days. Associating the nanoparticles with a high amount of oligoarginine (100 μmol for RRH tagging, 100 μmol RR entrapment and 34 μmol for R4acaH entrapment) further enhanced the cellular association. However, confocal imaging revealed that RRH (100 μmol)-tagged nanoparticles, which showed association with a higher proportion of cells compared to the unmodified nanoparticles, were not readily internalized by the cells. Confocal imaging also demonstrated that the unmodified nanoparticles were internalized via energy-dependent pathways as no internalization was observed at 4°C (where all active processes are inactivated (Langel, 2006) even though the cellular association of the unmodified nanoparticles was similar at 37°C and 4°C.

It has been reported that oligoarginine having at least 6 arginine residues is a prerequisite to gain enhanced cellular penetration (Wender *et al.*, 2000). However, the arginine residues can be spaced out within the peptide with lipophilic spacers, such as aminocaproic acid (Rothbard *et al.*, 2002). Therefore, having multiple short chained arginine residues, distributed within certain proximity of each other on the surface of the nanoparticles, can potentially aid with the cellular association and uptake of nanoparticles. Covalent association of arginine to PECA nanoparticles may not be necessary provided the oligoarginine is on the surface of the nanoparticles as the non-covalent entrapment of R4acaH also enhanced cellular association of PECA nanoparticles.

Although the FACS results can be indicative of cellular uptake, the term uptake has to be used cautiously. It is important to point out that the term cellular association in this chapter has been used to indicate strong association of fluorescent material with the cells, either internally or externally. The FACS results were obtained from cells that have been through multiple washes (4 washes in total) and trypsinization prior to analysis, therefore any residual fluorescence left on the cellular surface is expected to be minimal. The result of the FACS analysis was also reinforced with confocal imaging. However, the exact location of the fluorescent particles in the cell would require further confocal imaging with multiple organelle stains, such as the LysoTracker[®] that labels the lysosomes. It is also important to note that the propidium iodide cell staining assay (used in flow cytometry to differentiate live and dead cells) is a poor indicator of cell viability and therefore should be validated with a second viability assay (detecting a different aspect of the cells, such as mitochondria activity).

It is also crucial to re-emphasize that the cellular uptake result obtained with undifferentiated Caco-2 cells should not be extrapolated to fully differentiated Caco-2 cell monolayer. The cellular association enhancement of nanoparticles with oligoarginine association was not able to be replicated in fully differentiated Caco-2 cell monolayer at 37°C. It is possible that the reduced cellular association of nanoparticles is due to the change in characteristics of Caco-2 cells upon differentiation, such as lack of dividing cells, as well as reduced effective absorption area in a monolayer.

One major limitation of using the FACS technique to investigate cellular association is that the results are quantified based on the non-covalently entrapped fluorescent probe (FITC-dextran) in the nanoparticles. As the release rates of the

fluorescent probe from the nanoparticles were different between different nanoparticle formulations, the intensity of fluorescence in the cells measured by the flow cytometer could not be directly interpreted as the number of nanoparticles associated with the cells. Although the FACS data does show the proportion of the cell population that was associated with the fluorescent particles, the number of nanoparticles associated with the cells remained unknown. The next chapter will aim to investigate cellular association based on the nanoparticles associated with the cells.

CHAPTER FOUR

Re-evaluation of cellular association and uptake of oligoarginine-associated PECA nanoparticles

4.1. Introduction

Using the FACS technique to quantify cellular uptake of nanoparticles have several limitations. One of the major limitations is the inability to distinguish cellular internalization from cellular association. Although confocal imaging can be employed to resolve whether particle internalization does occur, neither confocal imaging nor FACS techniques are able to quantify internalization. Therefore, the result from FACS analysis should not be associated with the term “cellular uptake” as with most published literature, which can be misleading. Another issue with quantification of cellular association based on the fluorescent probe, non-covalently entrapped in the nanoparticles is the release of the probe from the nanoparticles. It was shown in **Section 3.5** that fluorescent probe was released at different rates from different types of nanoparticles and this makes the comparison of cellular association between different nanoparticle formulations difficult. The FACS data (**Section 3.4.4**) gave information on the cellular association based on the proportion of the cells that were associated with the nanoparticles, but not on the amount of the nanoparticles associated with the cells. This chapter sets out to covalently tag the PECA nanoparticles with a radionuclide in order to investigate the number of nanoparticles that would associate with the Caco-2 cells over time.

4.1.1. Quantifying delivery based on the bioactive entrapped in nanoparticles compared to nanoparticles

Xu *et al.* (2009) demonstrated using coherent anti-Stokes Raman scattering (CARS) microscopy that PLGA nanoparticles were not readily taken up by KB cells (cross-contaminated cervical cancer (HeLa) cells), contradicting the high particulate uptake result obtained using FACS technique in the same study. CARS imaging is able to distinguish the unlabeled nanoparticles from the intracellular lipid bodies because the vibration peaks of the intracellular lipid bodies (CH_2 stretch at 2840 cm^{-1}) and PLGA nanoparticles (CH_3 stretch at 2940 cm^{-1}) are different. A direct comparison between a confocal image and a CARS image of a sample of KB cells incubated with Nile red-loaded PLGA nanoparticles revealed that the Nile red released from the nanoparticles was co-localized with the lipid bodies, but not the nanoparticles themselves (Xu *et al.*, 2009). Nanoparticles were also not present in the KB cells, indicating that the nanoparticles were not readily internalized by the cells. Therefore, quantifying cellular uptake of

nanoparticles based on non-covalently entrapped fluorescent probe may be misleading and should not be used to represent the uptake of nanoparticles.

4.1.2. Cellular uptake of nanoparticles tagged with fluorescent probe

Apart from CARS imaging, there are alternative methods currently employed to study the uptake of nanoparticles. One of these methods utilizes quantum dots to assess and characterize cellular uptake (Michalet *et al.*, 2005; Wang *et al.*, 2012). Quantum dots are fluorescent semiconductor nanocrystals and their fluorescent properties are dependent on size (Michalet *et al.*, 2005; Wang *et al.*, 2012). These nanocrystals are usually less than 10 nm and their emission wavelengths are proportional to the particle size (Michalet *et al.*, 2005; Wang *et al.*, 2012). Decreasing the size of a quantum dot shifts its emission from red colour (long wavelength) to blue colour (short wavelength). Although quantum dots can be used to study cellular uptake, the uptake result should not be extrapolated to the cellular uptake of polymeric nanoparticles as polymeric nanoparticles are generally bigger than 10 nm and have very different characteristics, such as a lower density compared to quantum dots.

Alternatively, polymeric nanoparticles can be covalently tagged with a fluorescent probe to quantify uptake. Brambilla *et al.* (2010) synthesized rhodamine B cyanoacetate (RCA), which was then added to hexadecylcyanoacetate (HDCA) and methoxypoly(ethylene glycol) cyanoacetate (MePECA) to form P(HDCA-co-RCA-co-MePEGCA) nanoparticles via polymerization in an aqueous medium. These fluorescent PACA nanoparticles were claimed to be able to penetrate into hCMEC/D3 cells (a model for blood brain barrier) via endocytosis, with the majority of the particles accumulating around the nucleus (Brambilla *et al.*, 2010). However, the claim of intracellular penetration of the nanoparticles may be premature because the confocal images were performed without cellular staining, such as the nucleus or the membrane stains, to distinguish the location of the particles. Therefore, it is possible that the confocal images were misinterpreted by the authors, where the fluorescently-tagged particles associated with the cell surface were interpreted as being internalized into the cells. To provide more robust evidence of internalization, the cells should be stained to identify cellular architecture (Fenyvesi *et al.*, 2014). This confocal imaging technique with appropriate cellular staining would provide valuable information on the location of the fluorescent-labeled nanoparticles within the Caco-2 cells.

4.1.3. Cellular uptake of nanoparticles tagged with radiolabels

In addition to tagging a fluorescent marker to nanoparticles, radioactive labels can also be conjugated to polymeric nanoparticles. Conjugation of radioactive labels to the nanoparticles can be achieved either via covalent linkage (i.e. using radioiodine) or via a bifunctional chelator (i.e. using radiometals, such as 1,4,7,10-tetra-azacyclododecane-1,4,7,10-tetraacetic acid (DOTA) and deferoxamine (DFO)) (Snehalatha *et al.*, 2008; Stockhofe *et al.*, 2014). It is also possible to synthesize radiolabeled monomers, such as methyl(cyanoacrylate) (Cary, 2001) or poly(lactic acid) (PLA) (Gref *et al.*, 2003) to be used in the polymerization reactions to form radiolabeled nanoparticles.

Due to the low dose of PECA nanoparticles that can be applied to the Caco-2 cells without any signs of cytotoxicity (up to 12.5 $\mu\text{g}/\text{mL}$ for Caco-2 cells and 125 $\mu\text{g}/\text{mL}$ for fully differentiated Caco-2 cell monolayers as shown in **Section 3.4.3**) and rapid release of FITC-dextran (**Section 3.3.2**), it is difficult to detect and quantify the nanoparticles associated with the cells via fluorescence detection. However, the quantification of nanoparticles may be possible with nanoparticles covalently tagged with a radionuclide via scintillation counting. As the PECA nanoparticles used in the present study were shown to covalently associate with RRH via histidine anchoring (**Section 2.4.1**), it may be possible to covalently tag the PECA nanoparticles with radiolabeled histidine, which is commercially available, in a single step polymerization.

4.1.4. Accumulation of nanoparticles on cell surface

Another important issue with the current published *in vitro* studies of nanoparticle uptake is the common expression of particle dosing unit, which is based on the concentration of particles in the incubating medium as discussed by Hinderliter *et al.* (2010). Though this dosing unit correctly represents the total amount of particles present in the suspension, it does not represent the total amount of particles that the cells anchored on the bottom of the culture plate are exposed to. In fact, the surface of the cell would be only exposed to a fraction of the total particles present in the particle suspension. Therefore the use of this common dosing unit, which does not reflect the amount of nanoparticles on the cells surface, would result in poor correlations between particle dosing and cellular responses (Sayes *et al.*, 2006; Warheit *et al.*, 2009). It is important to appreciate that particle dosing is more complex compared to soluble chemicals (Hinderliter *et al.*, 2010) as the particles in the suspension could undergo aggregation. And although

the characteristics of nanoparticles (such as size, shape, density and zeta potential) determine the subsequent cellular responses (**Section 1.5**), these differences in particle characteristics can also affect the transport processes that deposit the particles on the cell surface (**Figure 4-1**). For example, 30 nm mesoporous silica nanoparticles, which formed 130 nm aggregates in cell incubating medium, showed similar cellular uptake to 110 nm mesoporous silica nanoparticles (Lu *et al.*, 2009).

To help understand and predict the behaviour of *in vitro* drug delivery systems (Baeumer *et al.*, 2009; Buchla *et al.*, 2014) as well as the cellular responses (De Pillis and Radunskaya, 2001; Villasana and Radunskaya, 2003), mathematical models and simulations have been employed. Hinderliter *et al.* (2010) developed a computational model of particokinetics based on sedimentation, diffusion and densimetry for non-interacting spherical particles and their agglomerates in a common cell culture system called *In vitro* Sedimentation, Diffusion and Dosimetry (ISDD) to improve the accuracy and prediction of the accumulation of particulates on the cell surface over time.

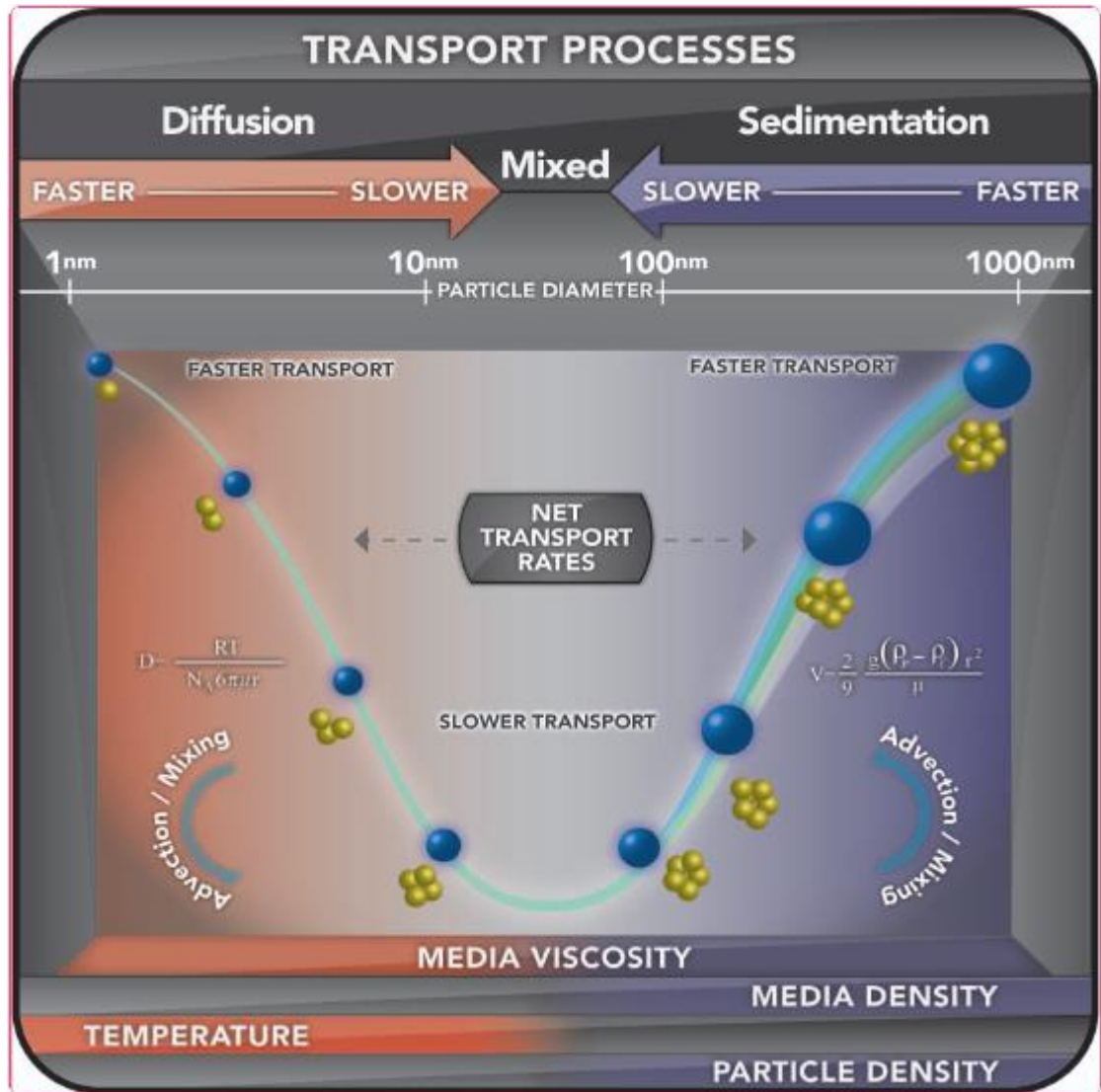


Figure 4-1. Important particle transport processes influencing the accumulation of nanoparticles on the cell surface in *in vitro* systems containing a liquid medium (Hinderliter *et al.*, 2010).

In the ISDD model, contact of particles with the cells is determined by three primary particle transport processes. These processes are diffusion, sedimentation and advection (Hinderliter *et al.*, 2010). In the ISSD model, advection is assumed to be minimal in an undisturbed cell culture medium at a constant temperature. The two remaining factors, sedimentation and diffusion, can be defined by Stokes' Law (**Equation 2**) and Stokes-Einstein equation (**Equation 3**), respectively.

Equation 2. Stokes' Law.

$$V_s = \frac{d^2(\rho_{np} - \rho_{med})\alpha}{18\eta}$$

where V_s = sedimentation rate, ms^{-1} , d = diameter of particle, m ; ρ_{np} = particle density, $\text{kg}\cdot\text{m}^{-3}$; ρ_{med} = medium density, $\text{kg}\cdot\text{m}^{-3}$; α = gravitational acceleration, $\text{m}\cdot\text{s}^{-2}$; η = medium viscosity, $\text{kg}\cdot\text{m}^{-1}\text{s}^{-1}$

Stokes' Law describes the sedimentation rate (V_s) of the nanoparticles in the incubation medium driven by the gravitational force. Sedimentation generally plays a more important role than diffusion in particle transport for particles greater than 200 nm and for particles of high density such as metal particles (Hinderliter *et al.*, 2010).

Equation 3. Stokes-Einstein equation.

$$D = \frac{RT}{3N_A\pi\eta d}$$

where D = diffusion coefficient, m^2s^{-1} , R = gas constant, $\text{L}\cdot\text{kPa}\cdot\text{K}^{-1}\text{mol}^{-1}$, T = temperature, K , N_A = Avogadro's number, η = medium viscosity, $\text{kg}\cdot\text{m}^{-1}\text{s}^{-1}$, d = diameter of particle, m

Stokes-Einstein equation describes the diffusion coefficient (D) of the nanoparticles driven by random collisions between nanoparticles themselves and between nanoparticles and solvent molecules. Transport of particles of 10 nm or less is primarily controlled by diffusion (Hinderliter *et al.*, 2010). Although both sedimentation and diffusion control the particle transport for nanoparticles ranging from 10 to 100 nm, the transport is expected to be slow as neither process predominates (Hinderliter *et al.*, 2010).

The ISDD model (**Equation 4**) is based on a mathematical solution to the laminar convection-diffusion equation, a parabolic partial differential equation derived by Mason and Weaver (1924). Using Matlab[®] simulations of the ISDD model, the accumulation of nanoparticles on the cell surface over time can be predicted.

Equation 4. The *In vitro* Sedimentation, Diffusion and Dosimetry (ISDD) model.

$$\frac{\partial n}{\partial t} = D \frac{\partial^2 n}{\partial x^2} - V \frac{\partial n}{\partial x}$$

where n = particle concentration, g.L^{-1} , t = time, s, x = distance from bottom, m, D = Stokes-Einstein equation, V = Stokes' Law

For the initial conditions, it was assumed that a uniform particle distribution at initiation of the experiment ($n_0 = \text{constant}$ for all x , $t = 0$) and the boundary conditions are; i) no particle flux across the top of the media ($D \frac{\partial n}{\partial x} = Vn$ at $X = L$, total media height (top)) and; b) zero concentration at the bottom, where particles adhering to the cells at the bottom no longer affect particle flux ($n = 0$ at $x = 0$ (bottom)).

4.1.5. Uptake kinetics

In the light of the concept of the accumulation of nanoparticles on cell surface (**Section 4.1.4**), the cellular uptake kinetics of nanoparticles has to be critically re-evaluated. Several nanoparticle uptake kinetic studies have demonstrated that particle uptake increases linearly with longer incubation time (Blechinger *et al.*, 2013; Derakhshandeh *et al.*, 2011; Fernando *et al.*, 2011). Not only does longer incubation time give more time for the cells to take up the nanoparticles, it also causes more nanoparticles to come in contact with the cells due to diffusion and/or sedimentation. Therefore, the dose accumulation of nanoparticles on the cell surface should also be taken into account when correlating the association between the incubation time and measured cellular uptake.

Fernando *et al.* (2011) also showed that fluorescent-tagged poly [(9,9-dioctylfluorenyl-2,7-diyl)-co-(1,4-benzo-(2,1',3)-thiadazole)] (PFBT) nanoparticles were taken up by J774A.1 cells in a dose dependent manner, based on fluorescent intensity using FACS. Although it is not surprising that more nanoparticles would be taken up in cells due to a higher particle concentration, the increased in nanoparticle uptake may not necessarily reflect increased cellular activities (i.e. uptake) but rather be due to more nanoparticles being available to be taken up.

4.1.6. Chapter aims

To aid in understanding the interaction between the nanoparticles and the cell surface at the bio-interface, it is important to take the accumulation of the nanoparticles on the cellular surface into consideration. As the FACS technique is limited to determining the proportion of cells associated with the nanoparticles, radiolabeled PECA nanoparticles can potentially be used to determine the number of nanoparticles associated with the cells via a scintillation assay.

In this chapter, PECA nanoparticles are tagged with radiolabeled, L-Histidine via histidine anchoring to investigate the cellular association of oligoarginine-associated nanoparticles with Caco-2 cells. The ISDD model simulation is also employed to predict the accumulation of the PECA nanoparticles on cell surface to help in understanding the interaction at the bio-interface.

As RRH was the only oligoarginine that could be covalently tagged to PECA nanoparticles and resulted in a positive zeta potential in 1 mM NaCl, RRH-tagged nanoparticles were also used to study the effect of surface charge of PECA nanoparticles on cellular association.

4.2. Materials

L-Histidine (L-His) ($\geq 99\%$ purity) was sourced from Sigma Aldrich (St Louis, MO, USA), while L-Histidine [^{14}C], uniformly labeled (0.1 mCi/mL; 322 mCi/mmol, $> 99\%$ purity) was bought from American Radiolabeled Chemicals (St Louis, MO, USA). Optiphase 'Hisafe' 2 and miniature 6 mL polyethylene vials were purchased from PerkinElmer (Waltham, MA, USA). BCATM Protein assay kit and albumin standard was obtained from Thermo Scientific (Rockford, IL, USA). All other materials used in the following experiments can be found in **Section 2.2**.

4.3. Methods

4.3.1. Determination of the density of PECA nanoparticles

The density (required for the mathematical model) of the nanoparticles was determined by a novel sedimentation method carried out in a centrifuge. Unmodified PECA nanoparticles were isolated and washed from the microemulsion (10 g) (**Section 2.3.3**). Then the nanoparticles were re-suspended in 0.12% (w/v) poloxamer-407 (50 mL). The particle suspension (3 mL) was added to a polyallomer centrifuge tube (25 mm x 89 mm) (Beckman Coulter, Palo Alto, CA, USA) and an equal amount of HBSS (2X) was added to the particle suspension and vortexed to mix. The tube was centrifuged at 3038 *g* at 4°C for various times using a Beckman Optima™ L-80 Ultracentrifuge with Type 60 Ti rotor (Beckman Coulter, Palo Alto, CA, USA). The supernatant was discarded and the nanoparticle pellet was weighed before being vacuum-dried. Samples were weighed daily until a constant weight was reached.

To determine the sedimentation rate, the longest sedimentation distance (*h*) can be calculated based on the angle of the centrifuge tube in the rotor (**Figure 4-2**), $h = \frac{25 \text{ mm}}{\sin(66.5^\circ)}$ = 27.3 mm. During the centrifugation process, the nanoparticles will sediment in the direction of the purple arrow in **Figure 4-2**. The particles located the furthest away from the site of deposition will have the longest sedimentation distance (*h*) and so will take the longest time to sediment. The time when all the nanoparticles have sedimented (that is the time when the pellet mass reaches equilibrium) can then be used to calculate the sedimentation rate. The relative centrifuge force (rcf) of 3038 *g* used to calculate the density of the nanoparticles was based on maximum radial distance (*r*_{max}), 89.9 mm and the rotation speed of the centrifuge. The sedimentation rate can then be used to determine the density of the nanoparticles (detailed density calculations are presented in **Appendix II**).

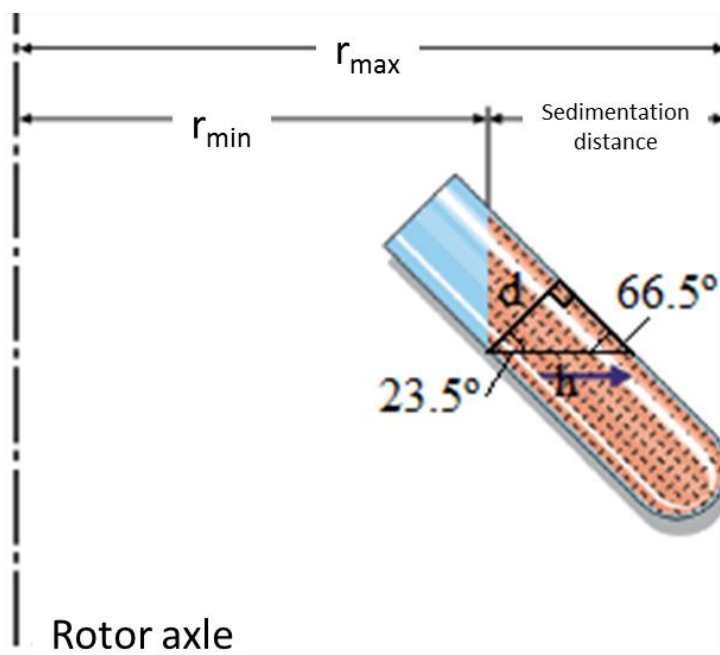


Figure 4-2. The dimension and angle of centrifuge tube in type 60-Ti rotor.

4.3.2. Mathematical simulation based on the ISDD model

The accumulation of nanoparticles on the cell surface *in vitro* was predicted based on the physical characteristics of the experimental system and the nanoparticles, using the ISDD model (Hinderliter *et al.*, 2010). The nanoparticle dose accumulation simulations were carried out with Matlab[®] R2013a (ver. 8.1.0.604, MathWorks[®]) software.

The simulations were run with using parameters values of the incubating HBSS medium shown in **Table 4-1**. The parameters for the density and the size of PECA nanoparticles were determined experimentally via the centrifugation method (see above) and photon correlation spectroscopy, respectively. The density of RRH (100 μmol)-tagged PECA nanoparticles was assumed to be similar to the density of unmodified PECA nanoparticles.

Table 4-1. Parameters of HBSS medium in a 24-well cell culture dish.

Temperature	310.15 K or 37°C
Height	0.00523 m
Volume	$1.0 \times 10^{-6} \text{ m}^{-3}$
Viscosity	$6.904 \times 10^{-4} \text{ Pa.s}$
Density	$998.7 \pm 2.1 \text{ kgm}^{-3}$ ($n = 10$)

4.3.3. Radiolabeling PECA nanoparticles

Microemulsion template (1 g) was prepared (**Section 2.3.1**) with 7.5 nmol L-Histidine (ratio of 2 hot (radioactive) : 1 cold) dissolved in the aqueous phase (0.1 mL), prior to addition of ECA monomer. For RRH (100 μmol)-tagging, the oligoarginine was dissolved together with the L-Histidine in the aqueous phase prior to ECA monomer addition. ECA monomer (20 μL ECA dissolved in 60 μL of chloroform) was added dropwise to the microemulsion template under constant stirring at 700 rpm at 4°C. The polymerization process was allowed to progress for a minimum of 4 h.

Either 0.1 or 0.2 g microemulsion containing the nanoparticles was gently mixed with 605 μL of dilute HCl (pH 2.5) and 605 μL of methanol 80% (v/v). A sample (10 μL) was then drawn for scintillation counting. Then the sample was centrifuged at 20,800 g (Eppendorf Centrifuge 5417C) for 30 min to isolate the nanoparticles from the microemulsion. A sample (200 μL) was drawn from the supernatant for scintillation counting. The pellet of nanoparticles was re-suspended via brief sonication in absolute ethanol to wash the isolated nanoparticles and then spun at 20,800 g for 30 min. This washing procedure was repeated twice. A sample (250 μL) was pooled from each washing for scintillation counting. The nanoparticles were then re-suspended in 0.5 mL 0.12% (w/v) polaxamer-407 prior to re-suspension in equal amount of 2X-concentrated HBSS (pH 7.1). An aliquot of the particle suspension (10 μL) was taken for scintillation counting.

The radiolabeling efficiency (RE) was then determined as the percentage L-His [¹⁴C] recovered in the isolated nanoparticles (based on radioactivity) as a proportion of the total L-His [¹⁴C] added to the microemulsion (**Equation 5**).

Equation 5. Radiolabeling efficiency (RE).

$$\text{RE (\%)} = \frac{[L\text{-His}]_{\text{nanoparticles}}}{[L\text{-His}]_{\text{microemulsion}}} \times 100$$

The nanoparticles were also characterized for both size and zeta potential using dynamic light scattering (Zetasizer ZEN3600, Malvern instruments Ltd, UK) (**Section 2.1.2**).

4.3.4. Release of L-Histidine [¹⁴C] radiolabel in HBSS

Oligoarginine-associated PECA nanoparticles were isolated from 2 g microemulsions and then first re-suspended in 0.5 mL 0.12% (w/v) poloxamer-407 prior to re-suspension in 2X-concentrated HBSS (pH 7.1). The suspension was incubated at 300 rpm at 37°C and samples (100 µL) were drawn at 10, 40, 70, 120, 180 and 240 min. Samples were spun at 20,800 g for 30 min and the supernatant (80 µL) was measured for radioactive L-His by scintillation counting.

4.3.5. Culturing Caco-2 cells and cellular association study

Caco-2 cells were cultured as described in **Section 3.3.3**. Upon 70% cell confluency, cells were trypsinized and seeded on 24-well plate at 25,000 cells/well for 2 days or 21 to 28 days (to obtain fully differentiated monolayer).

Cells were washed twice with HBSS before replacing with 1 mL of radiolabeled nanoparticle formulations (12.5 µg or 100 µg dry weight/mL for undifferentiated cells and fully differentiated cells, respectively; all dispersed in HBSS (1X) with 0.06% poloxamer-407) for incubation at 37°C. After 2 h incubation, the supernatants were discarded and cells were washed twice with ice-cold HBSS. Then the cells were trypsinized and FACS buffer was added to stop the trypsinization process. The cells were centrifuged at 210 g for 5 min and washed again with FACS buffer, before re-suspending each sample in 200 µL 0.1 N NaOH with 0.1% sodium dodecyl sulfate (SDS). The samples were then incubated at 60°C for 1 h to lyse the cells (Le Blay *et al.*, 2004). The lysed samples (100

μL) were used for liquid scintillation counting, while the remaining volume (100 μL) was used to determine the protein content.

Adherence of the nanoparticles to the cells was determined by the number of particles recovered in each of the washing steps after incubation and also after the cells were lysed. Nanoparticles recovered from the medium after the incubation period was defined as *unassociated* with the cells. Nanoparticles removed during 2 washes with HBSS was defined as *recovery after the HBSS wash*, while nanoparticles removed following a further 2 washes of FACS buffer after trypsinization was defined as *recovery after the trypsinization wash*. Nanoparticles recovered after cell lysis was defined as *recovery after cell lysis*. A portion of the nanoparticles recovered after cell lysis were assumed to have been internalized into the cells.

To account for the nanoparticles potentially sticking to the sides of the plastic wells of the cell culture plate, a control incubation experiment (without Caco-2 cells) was conducted. Majority (> 90%) of the unmodified and RRH-tagged nanoparticles were recovered from the supernatant and only a minute amount (< 0.3%) was detected *after the trypsinization wash* and *after cell lysis* procedure (**Appendix III**). Therefore, the experimental results for the recovery of nanoparticles after *the trypsinization wash* and *after cell lysis* would not be affected by the nanoparticles stuck on the sides on the well of the cell culture plate.

4.3.6. Liquid scintillation counting

All samples were made up to 500 μL with ultra-pure water and 5 mL of scintillation liquid (Optiphase 'Hisafe' 2) was added to the samples and mixed prior to scintillation counting with Tricarb[®] 2910TR Liquid Scintillation Analyzer (PerkinElmer, Waltham, MA, USA). Each sample was counted for 5 min and the result was obtained in disintegration-per-minute (dpm) with QuantaSmart[™] (PerkinElmer, ver. 4.00, build #5) software. A standard curve of L-His (25 – 5000 pCi) was prepared; Radioactivity (dpm), $y = 2.3379 \times [\text{L-His (pCi)}] + 57.245$, $R^2 = 1$. The accuracy and the lower limit of quantitation of the L-His was determined based on the lowest concentration of L-His (Pluim *et al.*, 1999). The CV of the lowest concentration of L-His was 4.9% ($n = 3$), which was well within the acceptable range of 20% (Pluim *et al.*, 1999). The accuracy of

the lowest concentration of L-His (25 pCi) was calculated using **Equation 6** to be $92\% \pm 4.5$ ($n = 3$).

Equation 6. Accuracy of scintillation assay.

$$\text{Accuracy (\%)} = \frac{\text{Mean measured concentration}}{\text{Theoretical concentration}} \times 100$$

4.3.7. Protein content determination

Cell samples (100 μL) were analyzed for protein content using a BCATM Protein Assay Kit (Thermo Fisher ScientificTM, Rockford, IL, USA). The method was used as according to the manufacturer's instructions. Briefly, BCA Reagent A and Reagent B were mixed in a 50 to 1 ratio to make the working reagent. Then 25 μL of each sample and 25 μL of the albumin diluted standards (for standard curve) were loaded onto a 96-well plate, prior to adding 200 μL of the working reagent. The plate was then incubated for 30 min at 37°C and cooled to room temperature (25°C) for 2 min before being read in the spectrophotometer (Molecular Devices Spectramax 340 microplate reader, CA, USA) at 562 nm.

4.3.8. Statistics

Comparisons of cellular association between the different nanoparticle formulations were analyzed with General Linear Model ANOVA using Minitab® ver. 16.1.0.0. Post ANOVA pair wise comparisons were assessed using the Bonferroni method. $P < 0.05$ was considered to be significantly different.

4.4. Results and discussion

4.4.1. Determining the density of PECA nanoparticles

The centrifugation method determines the density of the PECA nanoparticles based on the centrifugation time required by the nanoparticles located furthest away to sediment based on Stokes Law. **Figure 4-3** shows the total mass of nanoparticles recovered at different centrifugation times. The different symbols represent the total mass of nanoparticles after drying the nanoparticles that were recovered from centrifugation. The PECA nanoparticles reached a constant mass after 4 days of vacuum drying (**Figure 4-3**). The drying time was longer compared to the previous experiment (**Section 3.4.1**) due to the suspending medium being HBSS, instead of absolute ethanol in the previous experiment. The total mass of nanoparticles recovered increases with longer centrifugation time, which was expected due to sedimentation. After 70 min of centrifugation, the total mass of nanoparticles recovered reached a plateau and this is because all the nanoparticles in the suspension had sedimented (**Figure 4-3**). The time it took for the furthest nanoparticle to sediment can be calculated based on the linear model (total mass recovered, $y = 0.0456x + 5.4548$, $R^2 = 0.864$) and the density of the PECA nanoparticles was calculated to be 1103 kgm^{-3} (detailed calculation and explanation in **Appendix II**).

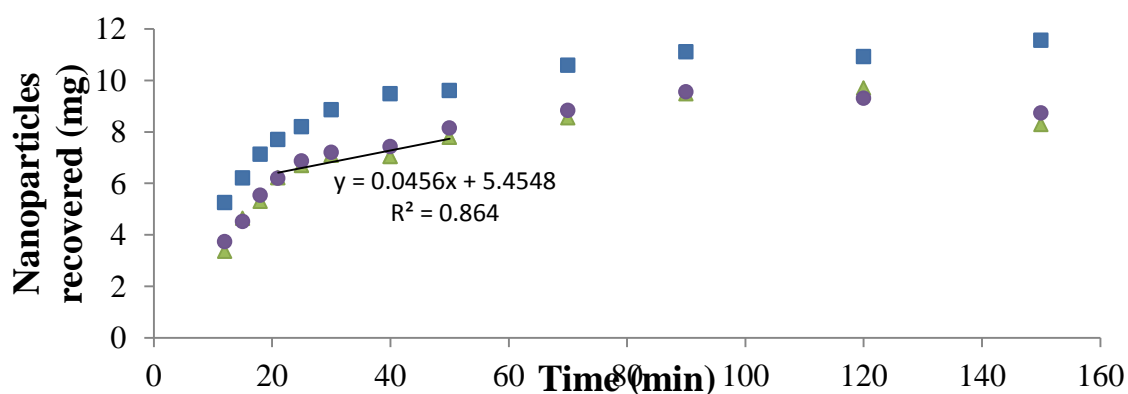


Figure 4-3. Mass of unmodified nanoparticles recovered after centrifugation for different times and changes in the mass of nanoparticles after oven-drying for 3 days (■), 4 days (●) and 5 days (▲). Each data point is a single measurement and data has been adjusted for the mass of salts and poloxamer-407 content.

4.4.2. Characterization of radiolabeled PECA nanoparticles

Radiolabeling the PECA nanoparticles produced mono-dispersed nanoparticles of approximately 200 nm. The unmodified nanoparticles and RRH (100 μmol)-tagged nanoparticles had zeta potentials of -26 mV and +17 mV, respectively (**Table 4-2**). Radiolabeling the PECA nanoparticles with L-His produced more negatively charged PECA nanoparticles compared to unlabeled nanoparticles (-12.6 mV and +35.0 mV for unmodified and RRH (100 μmol)-tagged nanoparticles, respectively) (**Section 2.4.2**). This could be due to the presence of histidine, covalently bound to the PECA wall, on the particle surface that may increase the negative charge of the particle due to the carboxylic groups on histidine. The presence of histidine as a competitive nucleophile may have reduced the amount of RRH covalently associated with the particle surface, thus lowering the cationic charge of RRH-tagged nanoparticles. Although both types of PECA nanoparticles remained individually dispersed upon re-dispersion in HBSS with 0.06% (w/v) poloxamer-407, the zeta potential of both types of particles was effectively neutralized.

Table 4-2. Characterization of the PECA nanoparticles radiolabeled with L-His, with or without RRH tagging. Data are means \pm SD ($n = 2$).

Solvent \ Nanoparticles	Absolute Ethanol with 0.2% Tween 80		0.1 mM NaCl	HBSS with 0.06% (w/v) poloxamer-407		
	Size (d.nm)	PDI	Zeta potential (mV)	Size (d.nm)	PDI	Zeta potential (mV)
Unmodified	222 \pm 19	0.18 \pm 0.06	-26.2 \pm 0.9	220 \pm 16	0.21 \pm 0.02	-0.7 \pm 0.9
RRH (100 μmol)-tagged	186 \pm 4	0.19 \pm 0.10	+17.0 \pm 0.8	190 \pm 2	0.24 \pm 0.05	-1.6 \pm 0.4

Unmodified PECA nanoparticles had a significantly higher association ($P < 0.001$) with radioactive L-His compared to RRH (100 μmol)-tagged nanoparticles, with radiolabeling efficiencies of 77% and 35%, respectively (**Table 4-3**). The lower radiolabeling efficiency for the RRH (100 μmol)-tagged nanoparticles could be explained

by the presence of a competitive nucleophile (RRH) during the polymerization process. Although the L-His was expected to bind more readily to PECA than RRH due to the arginine residues reducing the ability of histidine to act as a nucleophile (**Section 2.4.1**), the molar concentration of RRH present in the aqueous phase was much higher than L-His (a molar ratio of 4000 : 3). Therefore, it was expected that less L-His would be bound to the PECA wall in the presence of RRH.

Table 4-3. Mass balance of radiolabel (L-His) and radiolabeling efficiency of PECA nanoparticles.

Nanoparticles	Radioactivity (L-His) recovered (%)			
	Supernatant of microemulsion	EtOH washes	Isolated nanoparticle (Radiolabeling efficiency)	Total
Unmodified (<i>n</i> = 8)	7.3 ± 1.6	8.4 ± 2.0	77.0 ± 9.4	92.7 ± 7.1
RRH (100 µmol)-tagged (<i>n</i> = 4)	29.1 ± 10.2	27.1 ± 3.0	35.1 ± 17.1	91.2 ± 9.3

4.4.3. L-His [¹⁴C] radiolabel release in HBSS

RRH (100 µmol)-tagged nanoparticles had a slightly higher release of L-His compared to unmodified nanoparticles ($P < 0.05$), with 4% of the L-His associated with RRH (100 µmol)-tagged nanoparticles and 2% of the L-His associated with unmodified PECA nanoparticles released over 3 h (**Figure 4-4**). The higher release of L-His in RRH-tagged nanoparticles could be explained by a lower amount of the L-His being covalently bound to PECA wall as L-His would need to compete with RRH for binding sites during the polymerization process. The physically entrapped L-His would be released faster compared to covalently associated RRH. However, as both particles showed minimal L-His release (less than 5% release over 3 h), L-His radiolabel was considered suitable for tagging the PECA nanoparticles for particle quantification in subsequent uptake studies.

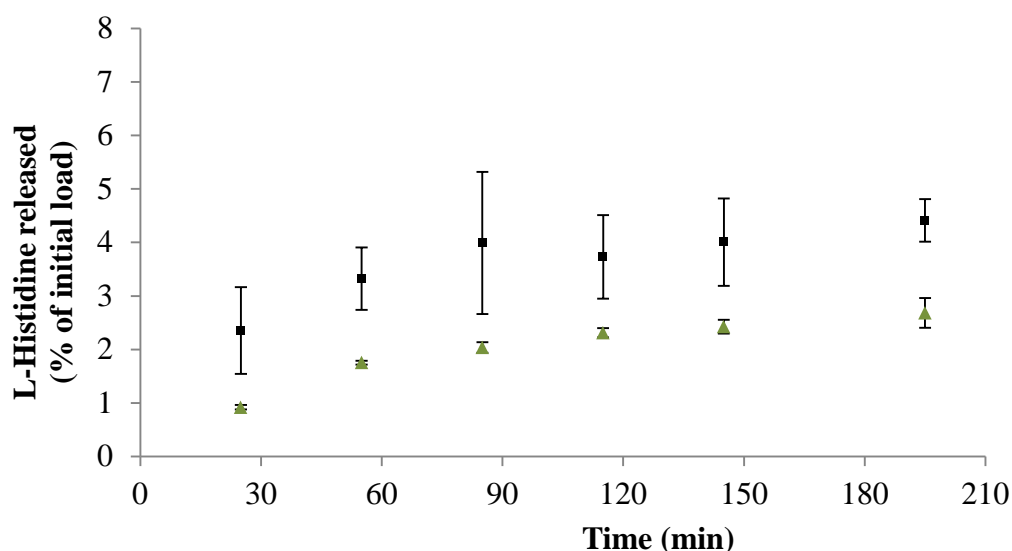


Figure 4-4. Release of L-His radiolabel from unmodified PECA nanoparticles (▲) and RRH (100µmol)-tagged nanoparticles (■) in HBSS over 3 h at 37°C. Data are means \pm SD ($n = 2$).

4.4.4. Dose accumulation on cell surface

According to Matlab[®] simulations based on the ISDD model (**Figure 4-5**), Caco-2 cells were predicted to be exposed to a similar amount of RRH (100 µmol)-tagged PECA nanoparticles (5.3% of loading particle dose) and unmodified PECA nanoparticles (5.0% of loading particle dose) after 4 h. As both types of nanoparticles were greater than 200 nm in diameter (**Table 4-2**), sedimentation was hypothesized to play a greater role than diffusion, in driving the nanoparticles to the cell surface (Hinderliter *et al.*, 2010). Therefore, more unmodified nanoparticles, which were slightly bigger in size than RRH (100 µmol)-tagged PECA nanoparticles (**Table 4-2**), would be expected to accumulate on the cell surface compared to RRH (100 µmol)-tagged PECA nanoparticles (**Equation 2**). However, the simulation model predicted the RRH (100 µmol)-tagged PECA nanoparticles to have slightly greater accumulation than the unmodified nanoparticles. This prediction suggested that diffusion would play a greater role than sedimentation in the particle transport to the cell surface.

In addition to the size of the nanoparticles, the particle density is also an important factor in determining the influence of sedimentation in the transport of

nanoparticles to the cell surface (**Equation 2**). Therefore, diffusion would have a greater influence on particle transport than sedimentation for polymeric nanoparticles, such as PECA, with low particle density. This may be an alternate explanation to why the uptake of particles is inversely proportional to size as shown by Kulkarni and Feng (2013), where 100 nm polystyrene nanoparticles had the highest uptake by the Caco-2 cells (80% confluency) at 37°C, followed by 200 nm and 500 nm nanoparticles with approximately 10%, 7% and 4% of the loading dose taken up, respectively. These uptake results could be due to higher accumulation of smaller particles, driven mainly by diffusion, on the cell surface rather than increased penetration of smaller nanoparticles. Although it is likely that the RRH (100 μmol)-tagged PECA nanoparticles would be slightly denser than the unmodified PECA nanoparticles, the difference in density is considered too small to have an impact on the particle transport in the incubating medium. Therefore, same density for both types of nanoparticles was assumed in the simulation model.

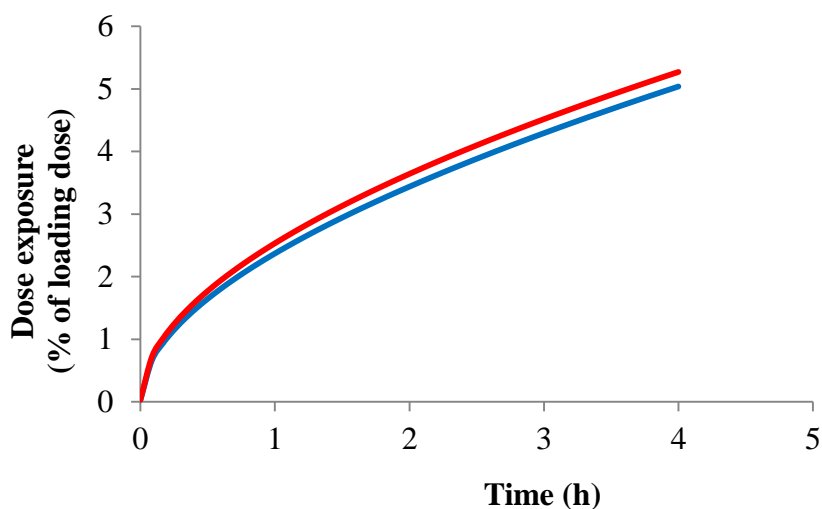


Figure 4-5. Predicted accumulation of nanoparticles on the cell surface for unmodified nanoparticles (blue) and RRH (100 μmol)-tagged nanoparticles (red) over 4 h, simulated based on the ISDD model using Matlab[®].

The simulation model used in this thesis (**Equation 4**) only accounts for sedimentation and diffusion. The model neglects a potentially important factor which is the electrostatic forces between the nanoparticles and cell surface. The distance from the nanoparticles under the electrostatic effect can be estimated by the Debye length of the nanoparticles (**Equation 7**), which is a measure of the net electrostatic effect of colloids in solution and the distance where the electrostatic force is expected to persist. Therefore, the Debye length can give an estimated proximity to the cell surface for electrostatic force to act.

The Debye length is determined mainly by the incubation medium (Jing and Bhushan, 2013). In HBSS, the Debye length of unmodified and RRH (100 μmol)-tagged PECA nanoparticles was calculated to be 0.74 nm (**Equation 7** and **Table 4-4**). Therefore, the electrostatic interaction between the particles and cell surface is only expected to be observed when the PECA nanoparticles are within 0.74 nm of the cell surface. It is also important to note that the Debye length only estimates the proximity of where the electrostatic force would be in effect, but it does not determine whether the force would be attractive or repulsive. As the nanoparticles are required to be very close proximity (0.74 nm) to the cell surface for the electrostatic force to act, it is reasonable to assume that this force plays a negligible role in the transport of nanoparticles in the incubating medium.

Equation 7. Debye length.

$$DL = \frac{\varepsilon_r \varepsilon_0 k_b T}{(2N_a C V^2 E^2)^{0.5}}$$

where DL = Debye length (m), ε_r = dielectric constant, ε_0 = permittivity of vacuum (F/m), k_b = Boltzmann constant (J/K), T = absolute temperature (K), N_a = Avogadro's number, C = buffer concentration (mol/m^3), E = Elementary charge; the electric charge carried by a single proton/electron (C), V = VChemical valence of ions

Table 4-4. Parameters of HBSS medium used to calculate the Debye length of PECA nanoparticles.

Absolute temperature (T)	310.15 K
Buffer concentration (C)	172.20 mol/m ³
Permittivity of Vacuum (ϵ_0)	8.85e ⁻¹² F/m
Dielectric constant (ϵ_r)	78
Boltzmann constant (k_b)	1.38e ⁻²³ J/K
Avogadro's number (N_a)	6.02e ²³
Chemical valence of ions (V)	1
Elementary charge (E)	1.6e ⁻¹⁹

4.4.5. Cellular association of PECA nanoparticles

4.4.5.1. Cellular association with fully differentiated Caco-2 cell monolayers

The kinetics of the association of PECA nanoparticles with the Caco-2 cell monolayer was investigated over 3 h. The majority of the unmodified nanoparticles and RRH (100 μ mol)-tagged nanoparticles (greater than 70%) were unassociated with the cells and were recovered from the supernatant (**Figure 4-6 A**). This finding is in agreement with the simulation model and will be discussed in **Section 4.4.4**. Both unmodified and RRH (100 μ mol)-tagged nanoparticles had a similar amount of nanoparticles recovered after the HBSS wash, which was approximately 2%, for all time points (**Figure 4-6 B**). After the trypsinization wash, there was an increasing amount of particles recovered over 60 min incubation with the unmodified nanoparticles and RRH (100 μ mol)-tagged nanoparticles, (**Figure 4-6 C**). For the unmodified nanoparticles, there was a decrease in nanoparticles recovered after 60 min and for the RRH (100 μ mol)-tagged nanoparticles, there was a decrease after 120 min. The amount of RRH (100 μ mol)-tagged nanoparticles

recovered after the trypsinization wash was significantly higher than the unmodified nanoparticles ($P < 0.01$). After cell lysis, there was no difference in the amount of unmodified nanoparticles recovered compared to RRH (100 μmol)-tagged nanoparticles (**Figure 4-6 D**).

To account for the possibility of different cell populations between all the monolayers used in the study, the nanoparticles recovered after cell lysis were adjusted for protein content (**Appendix IV**). No significant difference between the unmodified and RRH (100 μmol)-tagged nanoparticles in the nanoparticles recovered after cell lysis, adjusted for protein content, were observed (**Figure 4-7**).

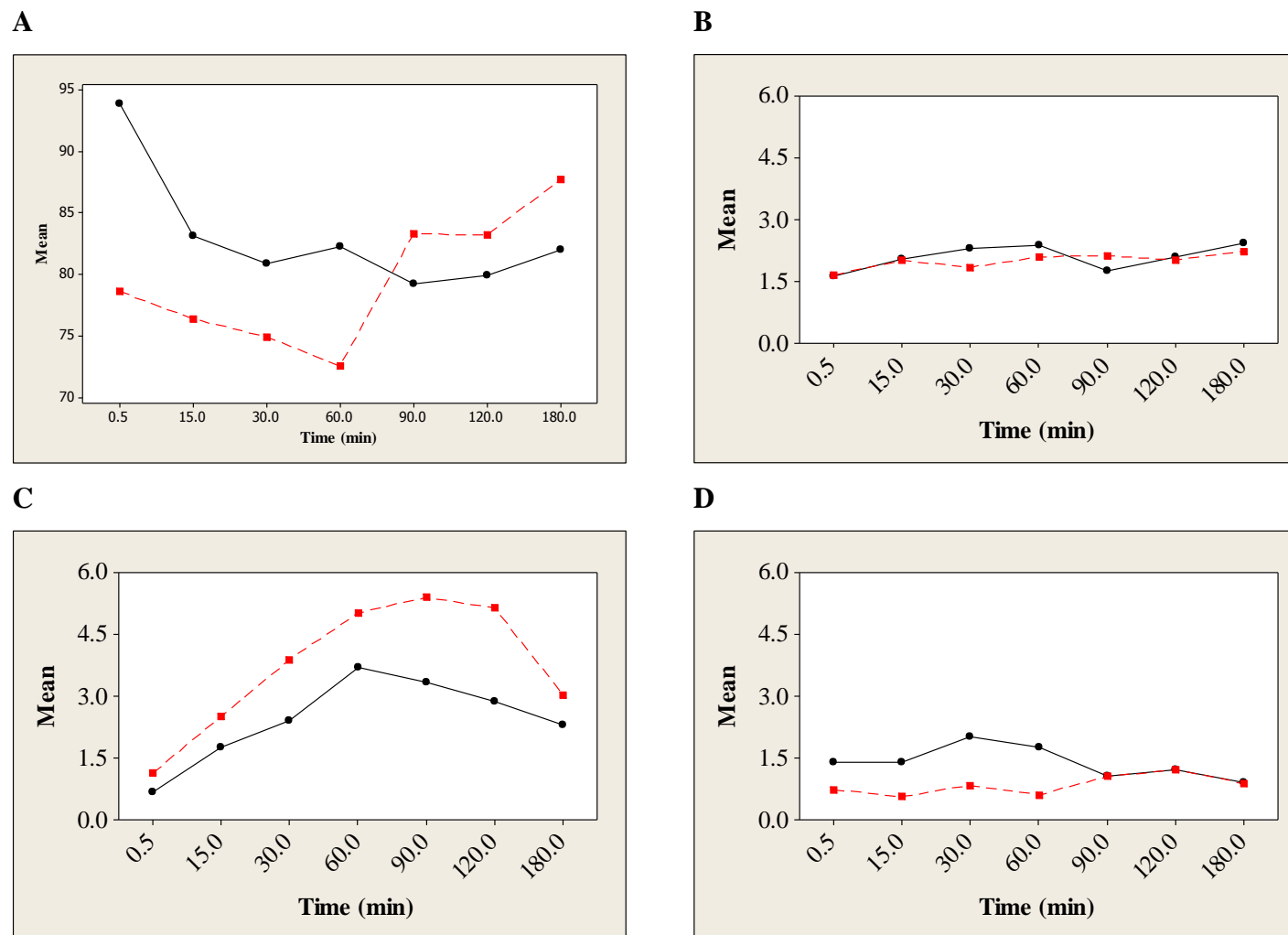


Figure 4-6. Interaction plots of mean recovery (%) of unmodified PECA nanoparticles (●) and RRH (100 μ mol)-tagged PECA nanoparticles (■) **A.** from supernatant, **B.** after HBSS wash, **C.** after trypsinization wash and **D.** after cell lysis, over a 3 h incubation uptake study (fully differentiated Caco-2 cell monolayers) at 37°C. Data are means ($n = 8 - 9$).

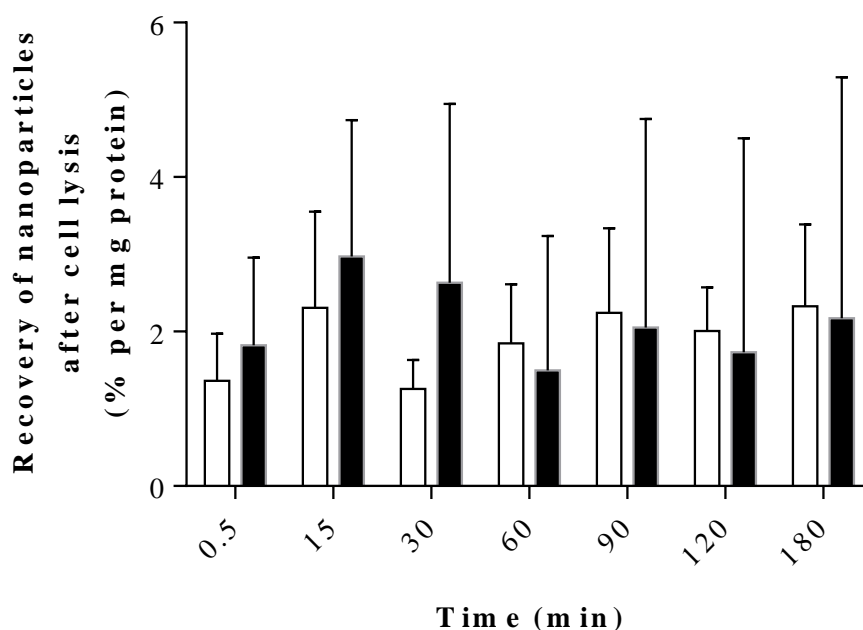


Figure 4-7. Recovery of nanoparticles after cell lysis, adjusted for protein content, for unmodified PECA nanoparticles (unfilled) and RRH (100 μmol)-tagged PECA nanoparticles (filled). The cellular association study was carried out with fully differentiated Caco-2 cells over 3 h incubation at 37°C . Data are means \pm SD ($n = 6$).

There are a number of reasons that could explain why there were different amounts of nanoparticles recovered after the HBSS wash and after the trypsinization wash. A possible explanation could be the nanoparticles associated with the cellular membrane in a layered manner. This would mean that each washing step would remove a layer of the nanoparticles associated to the surface of the nanoparticles, starting with the particles located furthest away from the cell surface. Alternatively, the nanoparticles were associated with the cellular membrane at different strengths. The nanoparticles associated strongly with the cell surface would require more washes to dissociate from the cell surface compared to the nanoparticles associated weakly. Finally, adsorbed nanoparticles on the cellular membrane could be released over time and so contribute to the nanoparticles measured in the washes.

To determine if the nanoparticles were able to associate with the cells in a layered manner, the total number of nanoparticles present in the suspension can be estimated using

the density of the PECA nanoparticles (1103 kgm^{-3}), the amount of PECA nanoparticles suspended in the HBSS ($12.5 \text{ }\mu\text{g}$ or $100 \text{ }\mu\text{g}$ dry weight/mL for undifferentiated and fully differentiated cells, respectively) and the volume of each nanoparticle ($5.58 \times 10^{-21} \text{ m}^3$ for a nanoparticle of 220 nm diameter). Therefore, the number of PECA nanoparticles in a 1 mL suspension was estimated to be 2,032,410,958 for $12.5 \text{ }\mu\text{g/mL}$ and 16,259,287,663 for $100 \text{ }\mu\text{g/mL}$. As determined by the simulation model (**Figure 4-5**), approximately 5% of the unmodified nanoparticles (101,620,548 nanoparticles for $12.5 \text{ }\mu\text{g/mL}$ or 812,964,383 nanoparticles for $100 \text{ }\mu\text{g/mL}$) would have deposited on the surface of the cells in 4 h. Assuming that the nanoparticles were evenly distributed, a 220 nm diameter particle would give an effective contact area (projected circular area of a sphere) of $3.8 \times 10^{-14} \text{ m}^2$. Thus, 4,997,606,410 nanoparticles are required to be deposited on the surface to fully cover the bottom of a well in a 24-well plate with a total surface area of $1.9 \times 10^{-4} \text{ m}^2$. The number of nanoparticles at both concentrations (101,620,548 nanoparticles for $12.5 \text{ }\mu\text{g/mL}$ or 812,964,383 nanoparticles for $100 \text{ }\mu\text{g/mL}$) would not have been sufficient to fully cover the entire bottom surface after 4 h. Therefore, it is unlikely for the particles to associate with the cells in a layered manner.

It is possible that the recovery of the nanoparticles after different washes reflects differences in the strength of the association. The trypsinization wash was performed to detach the cells from the surface of the cell culture dish as well as to digest the arginine and remove the any nanoparticles from the cell surface. Richard *et al.* (2003) demonstrated that the uptake of nona-arginine (R9) tagged with a fluorescent probe (fluorescence intensity as measured by flow cytometry) was significantly reduced with trypsinization. The authors then suggested that the trypsinization is vital in removing CPPs associated with the cell surface, to prevent overestimation of the uptake. Therefore, the recovery of nanoparticles after the trypsinization wash may reflect the nanoparticles with a higher association with the cellular membrane compared to the nanoparticles recovered after the initial HBSS wash.

Alternatively, the different recovery of nanoparticles from the HBSS wash and trypsinization wash could be due to the release of nanoparticles from the cell membrane over time as the trypsinization wash was carried out over at least 20 min while the HBSS wash was carried out over 3 min. Regardless of whether the particle release from the membrane in the trypsinization wash was due to the difference in association strength or

adsorption release over time, the trypsinization wash was still reflective of the tendency of the nanoparticles to adhere to the cellular membrane. This is because more of nanoparticles with a higher adherence tendency to associate with the cells instantaneously upon the introduction of the formulation. Thus, resulting in a higher amount of nanoparticles recovered in the trypsinization wash compared to less adherent particles.

As more RRH (100 μmol)-tagged nanoparticles were recovered after the trypsinization wash, RRH (100 μmol)-tagged nanoparticles were assumed to adhere more to the cell surface compared to unmodified nanoparticles (**Figure 4-6 C**). Therefore, it was expected that RRH (100 μmol)-tagged nanoparticles would have a greater cellular uptake or association with the cells due to increased adherence. However, the recovery of nanoparticles after cell lysis (**Figure 4-6 D** and **Figure 4-7**) showed that although increased adherence was observed with RRH (100 μmol)-tagged nanoparticles compared to unmodified nanoparticles (**Figure 4-6 C**), the RRH (100 μmol)-tagged nanoparticles had similar cellular uptake/very strong cellular association as the unmodified nanoparticles. The decrease in amount of nanoparticles recovered after the trypsinization wash over time (after 60 min for unmodified nanoparticles and after 120 min for RRH (100 μmol)-tagged nanoparticles) was possibly due to dissociation of the particles from the cell membrane back into the surrounding supernatant as no corresponding increase in nanoparticles recovered after cell lysis was observed.

To help understand the movement of nanoparticles on the cell surface, an association ratio over time was plotted (**Figure 4-8**). The association ratio was defined as the sum of nanoparticles recovered after the trypsinization wash and after cell lysis (RATL) over the sum of total nanoparticles recovered from both HBSS and trypsinization washes and cell lysis (TA). The nanoparticles recovered after the trypsinization wash were assumed to have strong association or adherence with cells, while nanoparticles recovered after cell lysis were assumed to have very strong association and/or uptake with the cells. Upon introduction of the nanoparticle formulation (0.5 min), approximately 50% of the cell-associated nanoparticles for both types of nanoparticles were recovered after the trypsinization wash and after cell lysis (**Figure 4-8**). The proportion of nanoparticles recovered after trypsinization wash and cell lysis increased with increasing incubation time, followed by a slight decrease after 60 min for unmodified nanoparticles and 120 min for RRH (100 μmol)-tagged nanoparticles (**Figure 4-8**). Overall, at least 60% of the

associated nanoparticles for both types of nanoparticles were recovered after the trypsinization wash and cell lysis for both the nanoparticles after 15 min of incubation. Although the RRH (100 μmol)-tagged nanoparticles showed a general trend of stronger tendency to adhere to the cells (**Figure 4-6 C**), the proportion of nanoparticles recovered after trypsinization wash and cell lysis to total associated nanoparticles was not significantly different when compared with the unmodified nanoparticles ($P > 0.05$) (**Figure 4-8**). This finding suggested that the RRH (100 μmol)-tagged nanoparticles do not adhere more strongly or are not taken up compared to unmodified nanoparticles even though more RRH (100 μmol)-tagged nanoparticles were found to adhere to the cells upon contact.

Although both types of nanoparticles showed a decrease in the proportion of nanoparticles recovered after the trypsinization wash and after cell lysis at 180 min, the decrease was only significant for unmodified nanoparticles. This observation could be due to exocytosis and efflux of the nanoparticles from the cells as previously discussed in **Section 3.1.1** (Bhattacharjee *et al.*, 2013; He *et al.*, 2013; Hu *et al.*, 2011). However, the decrease was less obvious with the RRH (100 μmol)-tagged nanoparticles and could be due to the effluxed or exocytosed cationic nanoparticles remaining on the surface after removal from the cells.

It is also possible that the decreasing trend of nanoparticle uptake with time is due to cell death caused by the accumulated nanoparticles on the cell surface over time. From the simulation model (**Figure 4-5**), 3.5% and 4.3% of the unmodified nanoparticles are expected to come in contact with the cells after 2 and 3 h of incubation, respectively. The numbers of accumulated unmodified nanoparticles on the cell surface were calculated to be 711,343,835 particles after 2 h for 125 $\mu\text{g}/\text{mL}$ dose and 699,149,370 particles after 3 h for 100 $\mu\text{g}/\text{mL}$ dose, which was comparable between the two experiments. As no cytotoxicity was observed with 125 $\mu\text{g}/\text{mL}$ of nanoparticles up to 2 h (**Section 3.4.3**), it is reasonable to assume no cytotoxicity in the kinetic experiment even though the exposure time is an hour longer here in the kinetic experiment than the cytotoxicity experiment.

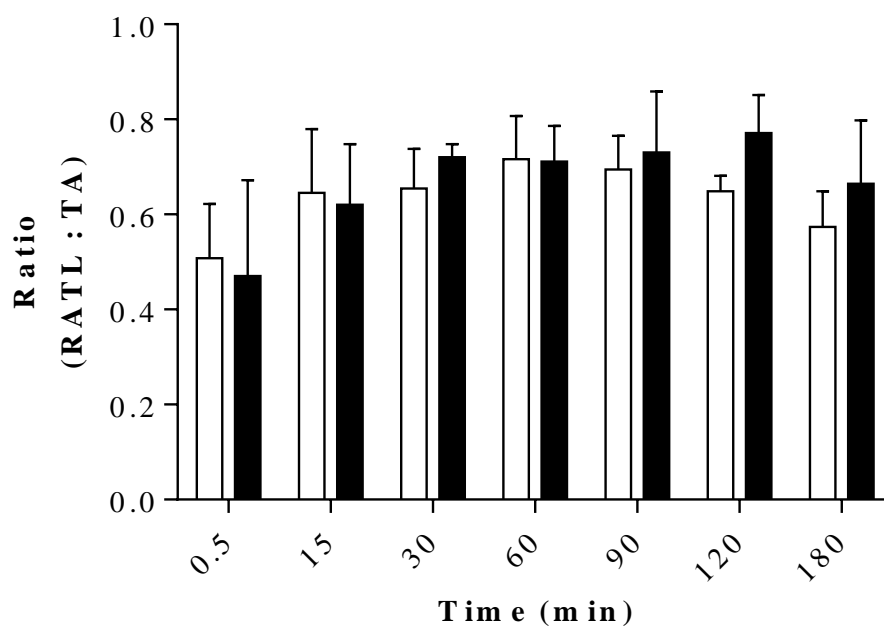


Figure 4-8. Association ratio between the nanoparticles recovered after the trypsinization wash and cell lysis (RATL) over the total nanoparticles associated (TA) over 3 h for unmodified nanoparticles (open bar) and RRH (100 μmol)-tagged nanoparticles (black bar). Data are means \pm SD ($n = 8 - 9$).

4.4.5.2. Comparison between simulation model and experimental uptake

The experimental data showed an increasing amount of total nanoparticles associated (TA) with the monolayer with longer incubation time, with the highest association occurring at 60 min for unmodified nanoparticles (6.8%) and at 90 min for RRH (100 μmol)-tagged nanoparticles (8.6%) (**Figure 4-9 C**). Although the simulation model failed to match exactly with experimental data, a similar accumulation trend of nanoparticles on the surface for both types of nanoparticles was still observed with the simulation model (**Figure 4-9 A and B**).

The simulation model used to predict the accumulated nanoparticles on the cell surface was determined by three primary particle transport processes, which are diffusion, sedimentation and advection. In the model, the advective forces were assumed to be

minimal in an undisturbed cell culture medium at a constant temperature (Hinderliter *et al.*, 2010). Therefore, the simulation model (**Equation 4**) did not account for the initial advection mixing during the initial phase of the formulation introduction to the *in vitro* system. In other words, the model made no allowance for the initial contact the cells might have with the nanoparticles when the nanoparticles were first added into the well with the cells. As shown in **Figure 4-9 A and B**, the immediate particle association at 0.5 min was neglected by the model. Assuming that any nanoparticles within 2 nm (2x Debye length = 1.5 nm) in a homogenous suspension would immediately adhere to the cells, only 0.000038% of the nanoparticles would be expected to be in immediate contact. However, the particle transport during the initial introduction of the formulation would also depend on the velocity of the addition of the formulation as well as the height of the formulation added from to the cells. As these mentioned parameters were not determined in the experiments the degree of accountability due to the initial convective mixing remains unknown.

The particle association with cell monolayer determined experimentally also showed an insignificant decrease ($P > 0.05$) in association after 60 min for unmodified nanoparticles and 120 min for RRH (100 μmol)-tagged nanoparticles. It has been suggested that polymeric nanoparticles can be exocytosed by the cells (He *et al.*, 2013; Hu *et al.*, 2011). A time dependent exocytosis of anionic silica nanoparticles (196 nm, -10 mV) had been postulated, with 50% of the nanoparticles taken up by HepG2 cells being exocytosed back into the incubating medium within 6 h (Hu *et al.*, 2011). However, this observation of “exocytosis” could also be likely due to the release of adhered nanoparticles on the cell surface back into the environment over time. Efflux transporters, such as MDR1/P-gp and MRP1, which can aid in transporting nanoparticles out of the intracellular compartment, have also been hypothesized to be present in fully differentiated Caco-2 monolayers (Bhattacharjee *et al.*, 2013) (**Section 3.1.1**). Although there is a possibility of the efflux transporters and exocytosis reducing the accumulation of nanoparticles in the cells, there is no sufficient evidence in the current experiments in this thesis to confirm this phenomenon.

In summary, significantly more RRH (100 μmol)-tagged nanoparticles were associated to the cells compared to unmodified nanoparticles ($P < 0.001$, analysed with generalized linear ANOVA) (**Figure 4-9 C**) due to higher adherence tendency, but the

difference is low (less than 3%). Although the surface charge of the nanoparticles was not expected to play a crucial role in particle transport, it is still important in determining the adherence of the particles to the cellular membrane (Agarwal and Roy, 2013; Artursson *et al.*, 1994; Bhattacharjee *et al.*, 2013; Gan *et al.*, 2005; Luessen *et al.*, 1996). Therefore, it was expected that the cationic RRH (100 μmol)-tagged nanoparticles would have greater cell association compared to anionic unmodified PECA nanoparticles dispersed in the incubation medium HBSS (pH 7.1).

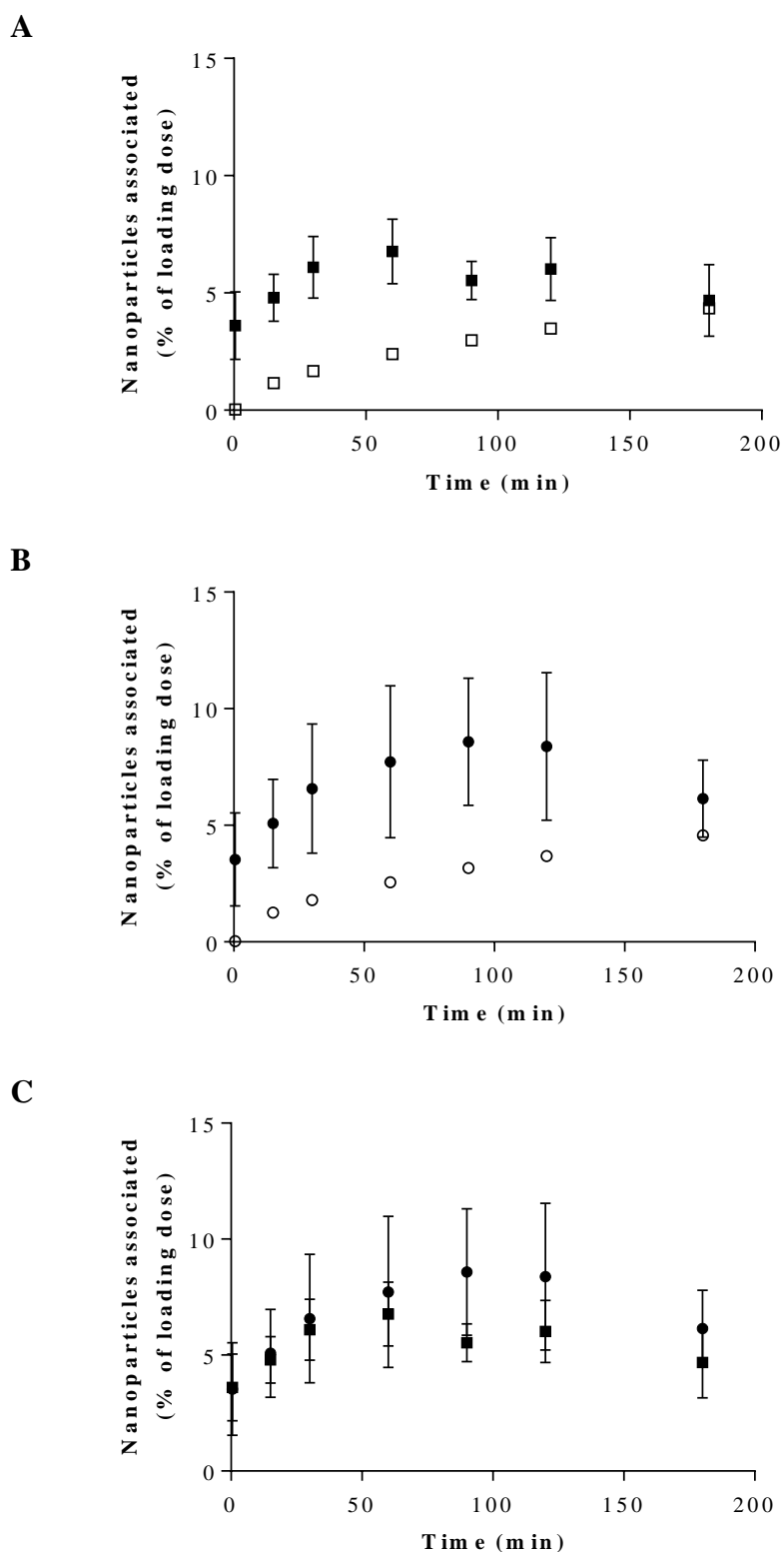


Figure 4-9. Comparison between experimental data (filled) and predicted data using Matlab[®] simulations (unfilled) of cellular association of PECA nanoparticles for **A.** unmodified nanoparticles (■) and **B.** RRH (100 μmol)-tagged PECA nanoparticles (●). **C.** Cellular association of unmodified nanoparticles and RRH (100 μmol)-tagged PECA determined experimentally. Experimental data are means \pm SD ($n = 8 - 9$).

4.4.5.3. Effects of poloxamer-407 on cellular association

It has been reported that the use of poloxamers to prevent aggregation of nanoparticles may interfere or reduce particle internalization into the cells (Müller, 1991). Therefore, the effect of poloxamer-407 concentration on the association of the particles with fully differentiated Caco-2 cell monolayers was investigated. The interaction plots from ANOVA analysis (**Figure 4-10**) showed the general effect of the poloxamer concentrations on the mean recovery (%) of the nanoparticles in the different stages of recovering the nanoparticles. Further ANOVA analysis using general linear model confirmed that the poloxamer-407 concentration between 0.005% (w/v) to 0.112% (w/v) does not affect the cellular association of both unmodified PECA nanoparticles and RRH (100 µmol)-tagged nanoparticles with the Caco-2 cell monolayers ($P > 0.05$) (**Figure 4-10**), even after adjusting for protein content ($P > 0.05$) (**Figure 4-11**). This is contrary to the findings of Müller (1991) where reduced particle internalization by the cells was observed. The authors attributed the reduced cellular internalization to the addition of poloxamer in the nanoparticle formulation, which may cause an increase in particle size as well as a reduction in hydrophobicity. However, it is important to point out that all the PECA nanoparticles in the experiments here in the thesis were re-suspended in a poloxamer-407 solution rather than a direct association with the poloxamer during polymerization of the nanoparticles. Therefore, the poloxamer-407 was expected to be adsorbed on the particle surface, possibly forming a micelle around the nanoparticle as previously mentioned in **Chapter 2** for concentrations greater than 8 µM (0.1 % (w/v)) (Cafaggi *et al.*, 2008). The concentration of poloxamer-407 used was kept to a minimal - only sufficient to prevent aggregation. Therefore, the poloxamer-407 adsorbed on the surface may be displaced upon the nanoparticle contact with the cell surface and would not interfere with cellular internalization. As the poloxamer-407 negated the zeta potential of the nanoparticles, the charge of the nanoparticles did not play a role in the particle transport but the charge may still cause an increased adherence tendency upon contact with the cell surface.

In addition to showing that the poloxamer-407 did not affect the cellular association of the nanoparticles, the interaction plots (**Figure 4-10**) also showed that significantly more RRH (100 µmol)-tagged nanoparticles were associated with the Caco-2 cell monolayers compared to unmodified nanoparticles ($P < 0.05$). This result re-confirms

the observation in **Section 4.4.5.1** that cationic RRH (100 μmol)-tagged nanoparticles have higher cellular adherence tendency compared to anionic unmodified nanoparticles.

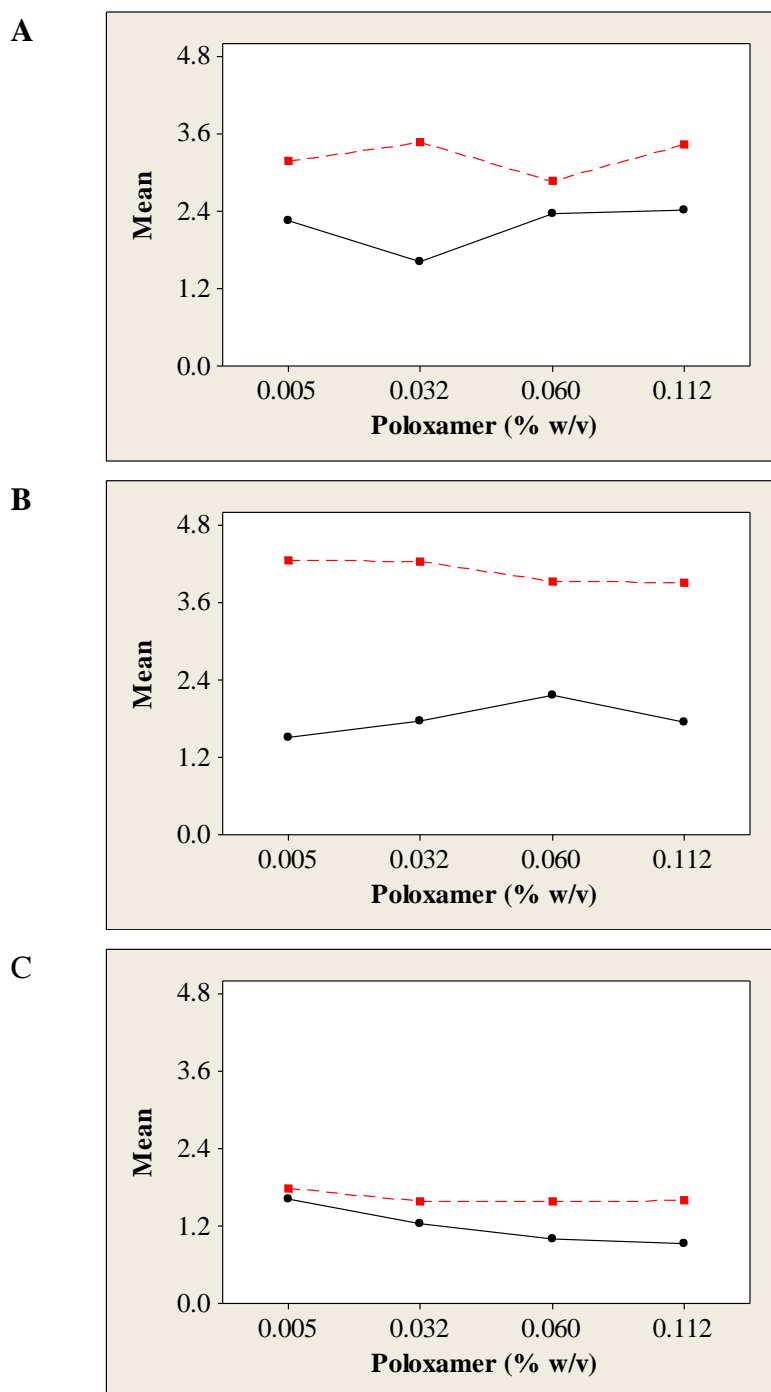


Figure 4-10. Interaction plots of mean recovery (%) of unmodified PECA nanoparticles (●) and RRH (100 μ mol)-tagged PECA nanoparticles (■), **A.** after HBSS wash, **B.** after trypsinization wash and **C.** after cell lysis. Incubation was carried out for 1 h with fully differentiated Caco-2 cell monolayers and with different concentrations of poloxamer-407 (w/v) at 37°C. Data are means ($n = 3$).

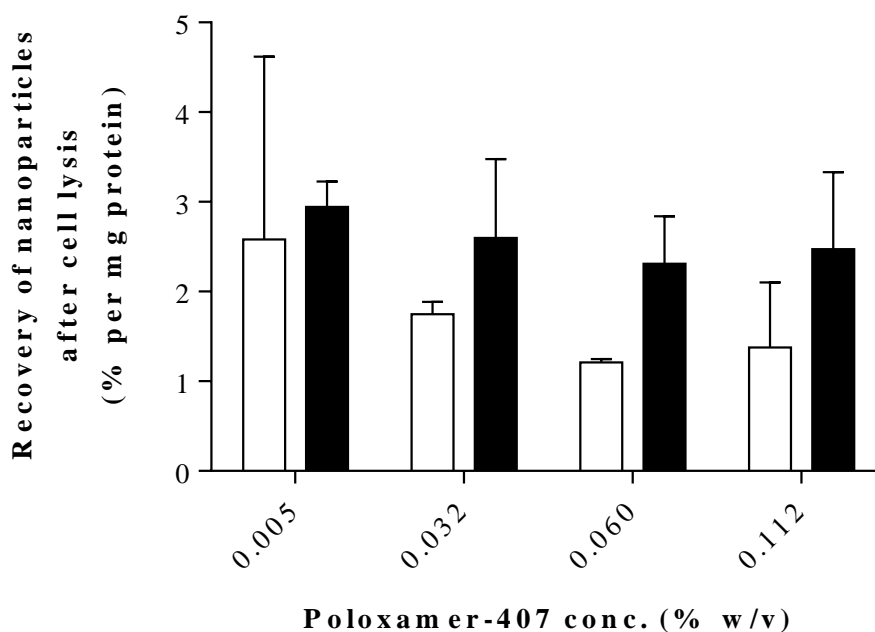


Figure 4-11. Recovery of unmodified PECA nanoparticles (unfilled) and RRH (100 µmol)-tagged PECA nanoparticles (filled) after cell lysis with fully differentiated Caco-2 cell monolayer, adjusted for protein content. Incubation was carried out for 1 h with different concentrations of poloxamer-407 (w/v) at 37°C. Data are means \pm SD ($n = 3$).

4.4.5.4. Cellular association in undifferentiated Caco-2 cells

The cellular association of nanoparticles with undifferentiated Caco-2 cells was also investigated. The majority of unmodified and RRH (100 µmol)-tagged PECA nanoparticles were not associated with the cells, with 90% and 93% of the respective nanoparticles recovered from the incubation medium after 2 h (**Figure 4-12**), which was in agreement with the simulation model where 3.5% of the total nanoparticles was predicted to accumulate on the cell surface in 2 h. Although some of the unmodified nanoparticles were recovered after the HBSS wash (3%) and after the trypsinization wash (0.6%), no detectable amount of RRH (100 µmol)-tagged nanoparticles were recovered after these washes (**Figure 4-12**). However, a significantly higher amount of RRH (100 µmol)-tagged nanoparticles were recovered after cell lysis, compared to unmodified nanoparticles ($P < 0.05$), with 4.7% and 0.7% of the respective nanoparticles recovered (**Figure 4-12**).

As the number of cells in the culture dish may vary, the nanoparticles recovered after cell lysis was adjusted for protein content. The recovery of RRH (100 μmol)-tagged nanoparticles after cell lysis, adjusted for protein content, was still significantly more than unmodified nanoparticles ($P < 0.05$) (**Figure 4-13**). These findings suggest that RRH (100 μmol)-tagged nanoparticles adhered strongly with the cellular membrane or internalized by the undifferentiated Caco-2 cells upon contact, while the majority of the unmodified PECA nanoparticles in contact with cells were less adherent compared to RRH (100 μmol)-tagged nanoparticles.

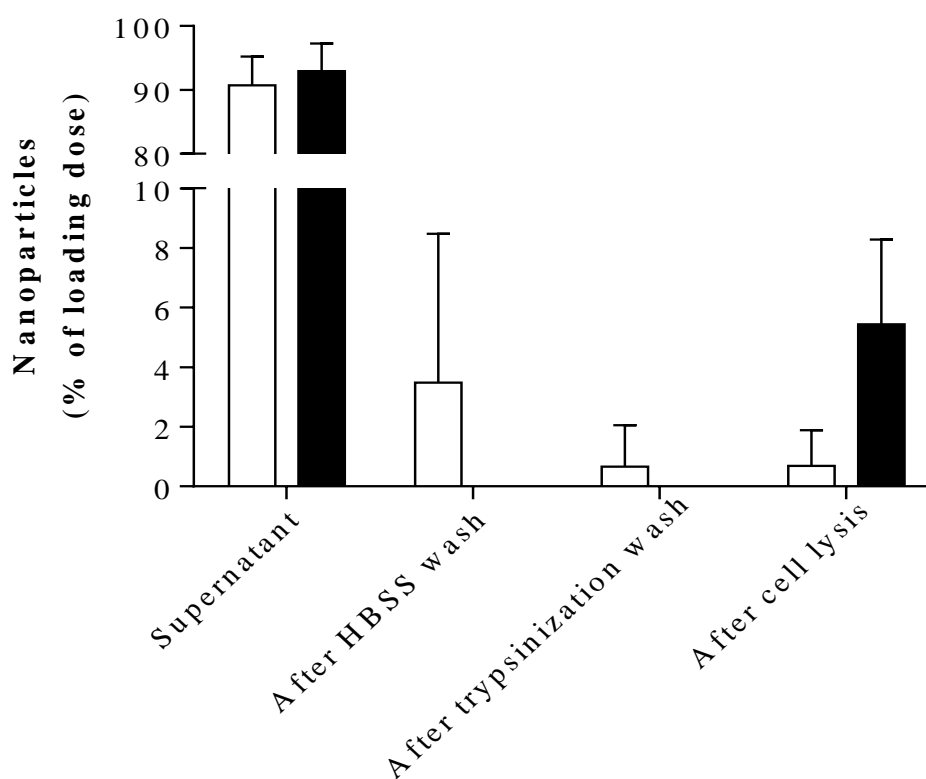


Figure 4-12. Unmodified PECA nanoparticles (unfilled) and RRH (100 μmol)-tagged PECA nanoparticles (filled) recovered from the supernatant, after HBSS wash, after trypsinization wash and after cell lysis. The cellular association was carried out with undifferentiated Caco-2 cells over 2 h at 37°C. Data are means \pm SD ($n = 6$).

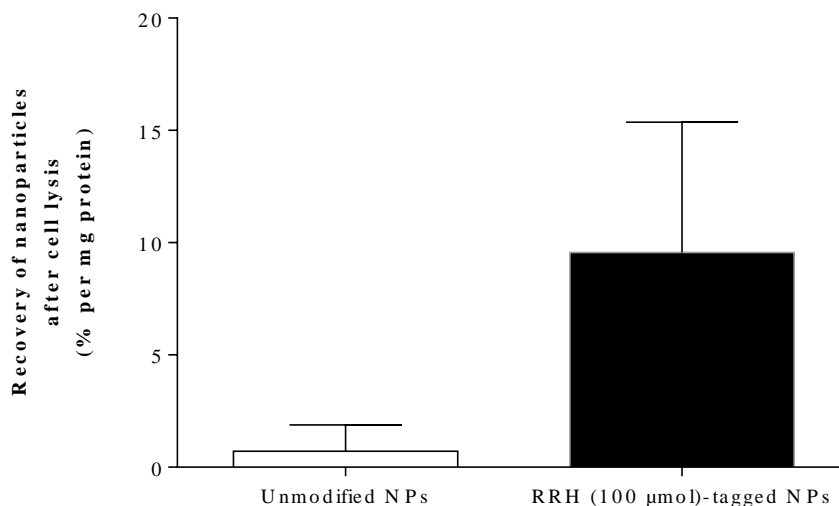


Figure 4-13. Recovery of nanoparticles after cell lysis, adjusted for protein content, for unmodified PECA nanoparticles (unfilled) and RRH (100 µmol)-tagged PECA nanoparticles (filled). The cellular association was carried out with undifferentiated Caco-2 cells over 2 h at 37°C. Data are means \pm SD ($n = 6$).

Although significantly more RRH (100 µmol)-tagged nanoparticles compared to unmodified nanoparticles were recovered after the lysis of the Caco-2 cells, the uptake or association was only a very small fraction (4.7%) of the loading dose (**Figure 4-12**). The minimal association of either unmodified or RRH (100 µmol)-tagged nanoparticles with the Caco-2 cells could be explained by the accumulated nanoparticles on the cell surface. After 2 h, the simulation model predicted approximately 3.5% of the unmodified nanoparticles and 3.7% of the RRH (100 µmol)-tagged nanoparticles were expected to have come in contact (regardless of the strength of association or adherence tendency) with the cell surface. The predicted accumulation of nanoparticles by the simulation model was in a good agreement with the experimental data (4.3% of loading dose for unmodified nanoparticles and 4.7% for RRH (100 µmol)-tagged nanoparticles were associated with the cells after 2 h).

Although the result obtained from FACS showed 45% of the Caco-2 cell population taking up or associating with RRH (100 µmol)-tagged nanoparticles (**Section 3.4.4.1**), the scintillation result suggested that only a small fraction of the nanoparticles were taken up or associated very strongly with the undifferentiated Caco-2 cells. These

results, from both scintillation counting and FACS, also suggest that the RRH (100 μmol)-tagged nanoparticles were taken up or adhered with more cells upon contact compared to unmodified PECA nanoparticles. Although the electrostatic force plays a negligible role in the transport of nanoparticles in the medium, the cationic surface charge on the arginine residues of the RRH (100 μmol)-tagged nanoparticles is still a factor in establishing a very strong association with the cells as all the RRH (100 μmol)-tagged nanoparticles in contact with the cellular membrane were very strongly associated with the cells or taken up by the cells. The importance of cationic surface charge was also shown with positively charged 100 nm wheat germ agglutinin coated-PLA nanoparticles, with 8.5% strongly associated with Caco-2 cells (undifferentiated monolayer) after 2 washes with phosphate buffered saline, as compared to 1.5% of the unmodified anionic PLA nanoparticles after 2 h incubation (Gref *et al.*, 2003). In the present experiment, the electrostatic interactions between the negatively charged cell surface and the positively charge RRH (100 μmol)-tagged nanoparticles, was expected to occur within the Debye length of the particles (Section 4.4.4), which was calculated to be 0.74 nm.

4.4.6. Comparing cellular association of nanoparticles in undifferentiated Caco-2 cells and fully differentiated Caco-2 cell monolayers

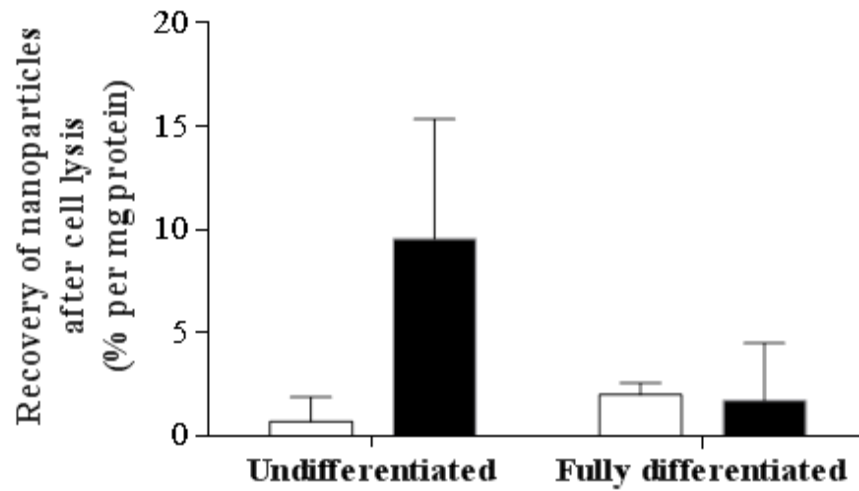
The majority of RRH (100 μmol)-tagged nanoparticles associated with cells were recovered after cell lysis in undifferentiated Caco-2 cells (Figure 4-12), whereas the majority of RRH (100 μmol)-tagged nanoparticles associated with cells were recovered after the trypsinization wash in fully differentiated Caco-2 cell monolayer (Figure 4-6 B). The amount of RRH (100 μmol)-tagged nanoparticles recovered after cell lysis, adjusted for protein content, was significantly higher ($P < 0.05$) compared to unmodified nanoparticles in undifferentiated cells (Figure 4-14 A), but this significant difference was not observed in fully differentiated Caco-2 cell monolayers. From the interaction plot (Figure 4-14 B), the amounts of unmodified nanoparticles recovered after cell lysis were similar in undifferentiated Caco-2 cells and fully differentiated Caco-2 cell monolayers, while the recovery of RRH (100 μmol)-tagged nanoparticles after cell lysis was significantly lower ($P < 0.05$) uptake in fully differentiated Caco-2 cell monolayers compared to undifferentiated Caco-2 cells. This finding concurs with the FACS results, where the RRH (100 μmol)-tagged nanoparticles were associated with a significantly

higher proportion of the undifferentiated Caco-2 cells compared with unmodified nanoparticles (**Section 3.4.4.1**), but no significant difference was observed between the two types of nanoparticles when the experiment was repeated with fully differentiated Caco-2 monolayer (**Section 3.4.4.22**). It was speculated (**Section 4.4.5.4**) that the majority of the RRH (100 μmol)-tagged nanoparticles were taken up or adhered with the cells upon contact with undifferentiated Caco-2 cells. However, this phenomenon was not observed in fully differentiated Caco-2 cell monolayers. This result demonstrated the difference in uptake between undifferentiated and differentiated Caco-2 cells. It is a possibility that as undifferentiated cells could not exocytose or efflux nanoparticles out of the cells, so more cationic RRH (100 μmol)-tagged nanoparticles were able to accumulate inside the cells, leading to a higher cellular association with undifferentiated cells compared with fully differentiated Caco-2 cell monolayers. However, current experiments did not confirm the presence of these efflux mechanisms.

It is also important to note that the undifferentiated cells (2 day old) were not confluent. An individual cell would be able to associate the nanoparticles at all sides of its membrane, except from the basolateral side as the cells are adhered to the bottom of the cell culture dish. However, a confluent cell monolayer would only be able to associate with the nanoparticles presented on the apical side. As the particles would move randomly due to diffusion, the absorptive area of individual, undifferentiated cells would be greater than a fully differentiated monolayer. This would not be adjusted for by normalizing with respect to protein content.

Although it is also possible for dividing cells to acquire nanoparticles from parent cells during active replication phase (discussed in **Section 3.4.4.2**), which could affect the results obtained from FACS, this phenomenon would not skew the scintillation results as scintillation counting only accounts for the nanoparticles associated with the cells, regardless of the number of cells present. Therefore, even in the case where daughter cells inherited the nanoparticles from the parent cells, the total amount of nanoparticles associated with the cells remains the same. The normalization for protein content may reduce the amount of nanoparticles associated “per cell”, however the scintillation result is still comparable between different formulations, provided the cells used between formulations were similar in characteristics, such as still actively dividing.

A



B

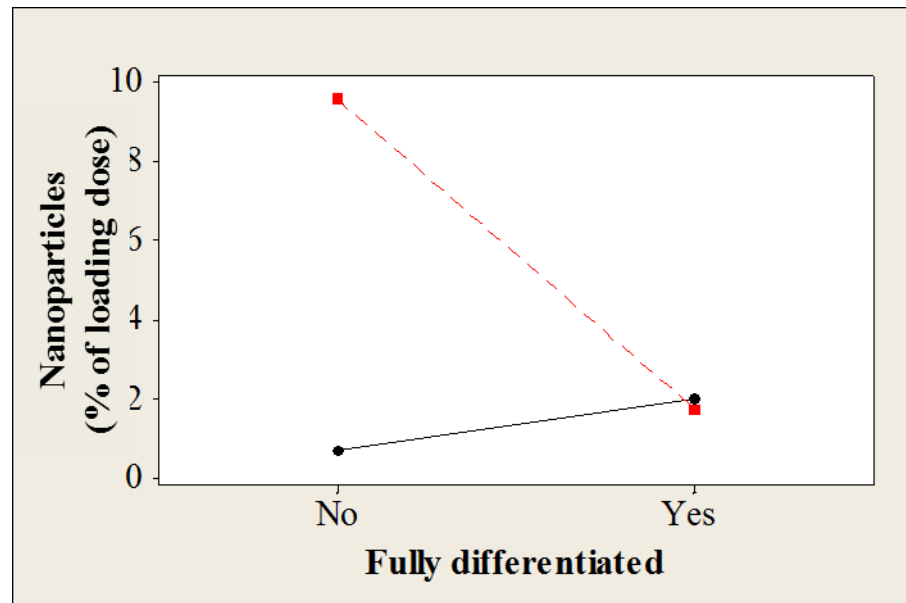


Figure 4-14. **A.** Recovery of unmodified PECA nanoparticles (unfilled) and RRH (100 μmol)-tagged PECA nanoparticles (filled) after cell lysis with undifferentiated and fully differentiated Caco-2 cells after 2 h, adjusted for protein content. **B.** Interaction plot showing the cellular association (very strong association) of unmodified PECA nanoparticles (●) and RRH (100 μmol)-tagged PECA nanoparticles (■) in either undifferentiated or fully differentiated Caco-2 cells. Data are means ($n = 6$).

4.5. Conclusion

PECA nanoparticles could be stably tagged with radioactive L-His, via histidine anchoring, to investigate the cell association and cellular uptake of the nanoparticles into Caco-2 cells. The simulation model was helpful in understanding the transport of the nanoparticles in the incubating medium and explained the low cellular association and uptake of the nanoparticles over time. Although the trend in experimental accumulation of the nanoparticles on the cell surface based on cellular association was in good agreement with the simulation model, the model needs to be improved to account for the initial advective mixing during the introduction of the nanoparticle formulations, especially for cationic nanoparticles with a high tendency to adhere to the cells. The immediate association of the nanoparticles with the cells (within 0.5 min) was observed upon introduction of the nanoparticle formulations, which the simulation model did not account for. Although the electrostatic interaction was not expected to play a significant role in the nanoparticles transport in the medium due to the extremely short Debye length, the surface charge could still play an important role in determining the adherence of the particles to the cellular membrane once the nanoparticles have made contact with the cell surface.

Although the cationic RRH (100 μmol)-tagged nanoparticles showed a higher tendency to adhere to cells compared to the unmodified nanoparticles, the increased cellular adherence did not result in more RRH (100 μmol)-tagged nanoparticles being internalized or adhered very strongly to cell membrane. The use of poloxamer-407 at low concentrations did not affect the association of the PECA nanoparticles with the Caco-2 cell monolayer.

Employing multiple methodologies in assessing nanoparticle uptake, such as flow cytometry and scintillation counting, are essential in understanding true cellular uptake. Scintillation counting of radiolabeled nanoparticles was able to provide information on the amount of nanoparticles that were associated with the Caco-2 cells as well as the strength of association, while the proportion of the cells associated with the nanoparticles could be obtained via the FACS technique (**Section 3.4.4**). In undifferentiated Caco-2 cells, it was shown that more cationic RRH (100 μmol)-tagged nanoparticles was associated with the cells (**Section 4.4.5.4**) and with a higher proportion of the cells (**Section 3.4.4.1**) compared to unmodified PECA nanoparticles.

The improved association of the RRH (100 μmol)-tagged nanoparticles seen in undifferentiated cells was not reflected in fully differentiated Caco-2 cell monolayer. Therefore, it is important to emphasize that the uptake study performed on undifferentiated Caco-2 cells should not be extrapolated to fully differentiated Caco-2 monolayer. Many current uptake studies are performed with undifferentiated Caco-2 cell models, which may not be suitable for predicting gut absorption *in vivo*.

CHAPTER FIVE

General discussion
and future directions

Despite the fact that some studies have shown the possibility of utilizing CPP-conjugated nanoparticles to increase drug delivery into cells as well as across the enterocytes to increase oral bioavailability (Liu *et al.*, 2013; Yan *et al.*, 2013), the scientific understanding of such a delivery system is still lacking. In order to design an effective colloidal carrier for oral drug delivery, it is important to gain fundamental understanding of the interaction of nanoparticles with the cell surface at the bio-interface as the processes and interactions occurring at the bio-interface will dictate the subsequent fate of the nanoparticles (Doherty and McMahon, 2009; Nel *et al.*, 2009). The work in this thesis was directed towards designing oligoarginine-associated PECA nanoparticles for the investigation of cellular association. Therefore, the contribution of this thesis to the field of understanding the bio-interface and the future directions will be discussed in this final chapter.

To obtain accurate information on the processes and interactions occurring at the bio-interface, nanoparticles should be characterized in the conditions that represent the study environment. This is a major issue with the majority of cellular uptake studies published to-date that characterized nanoparticles in a contaminant-free medium, rather than in the incubating medium. This thesis (**Chapter 3**) as well as other studies (Loh *et al.*, 2010; Lu *et al.*, 2009; Schulze *et al.*, 2008) demonstrated that the size and zeta potential of nanoparticles changes in different incubating media, with particle aggregations occurring in most cases. As these altered properties of the nanoparticles would determine the subsequent cellular interactions and activities at the bio-interface (Nel *et al.*, 2009), the characterization carried out only in an uncontaminated system provides very little useful information for understanding the interactions at the bio-interface.

As the surface characteristics of the nanoparticles are paramount in determining cellular responses (Nel *et al.*, 2009), it is also important to determine the amount of oligoarginine present on the surface of the nanoparticles. Using MALDI-TOF and i-TRAQ labeling, the amount of oligoarginine that covalently associated with PECA nanoparticles could be semi-quantified (**Chapter 2**). However, this technique does not give any information regarding the distribution of the oligoarginine on the surface of the nanoparticles. A possible technique that could aid in the visualization of the surface of the nanoparticles is atomic force microscopy (Moribe *et al.*, 2008). Atomic force microscopy measures the interactions (force) between a probe and the sample surface at the single-

molecule level (Ong and Sokolov, 2007). This technique could characterize the distribution of the cationic oligoarginine on the surface of the nanoparticles, via electrostatic interaction with the probe or via binding with a ligand coated probe that targets oligoarginine (Lee *et al.*, 2007). In addition to the characterization of the surface of nanoparticles, atomic force microscopy can also be used to study the interactions of the nanoparticles with other surfaces, such as the cell surface (Ong and Sokolov, 2007). A nanoparticle could be attached to the probe via epoxy conjugation and the atomic force microscopy is then performed on cells to determine the interactions.

To determine cellular association, FACS analysis and scintillation assay were used. Although most published uptake studies associate cellular uptake with FACS results, the term “cellular association” is the appropriate terminology because the FACS technique does not distinguish between cells that have internalized the fluorescent nanoparticles and cells that are associated with the fluorescent nanoparticles on the surface. Distinguishing between cellular uptake and adhesion would require confocal imaging with appropriate cell staining, which is able to determine the location of the nanoparticles (**Chapter 3**). In this thesis, the majority of the RRH-tagged PECA nanoparticles were observed to be adhering to the cell surface and were not internalized by the undifferentiated cells despite the FACS analysis showing a marked association of the RRH-tagged PECA nanoparticles with the undifferentiated cells. The cellular association of the RRH-tagged PECA nanoparticles was also verified with a scintillation assay. Using radioactive histidine-tagged PECA nanoparticles (**Chapter 4**), the association of the nanoparticles (instead of the payload) with the cells could be determined. Although the FACS result showed a marked association of the RRH-tagged PECA nanoparticles with the cells, only a small portion of the nanoparticles in the suspension was associated with the cells. Therefore, the results obtained based on detection of the non-covalently entrapped fluorescent probe should only be associated with payload delivery instead of nanoparticles delivery.

To help further understand the reason for the low association, a simulated mathematical model was used to predict accumulated nanoparticles on the cell surface. (Hinderliter *et al.*, 2010). The particle transport, influenced mainly by particle size and density, in the suspension should be taken into account in determining the dose exposure at each time point. Although the simulation model did not account for the initial advective

mixing during the introduction of the nanoparticle formulations, where immediate association of the nanoparticles with the cells (within 0.5 min) was observed upon introduction of the nanoparticle formulation, the trend in experimental accumulation of the nanoparticles on the cell surface based on cellular association was in good agreement with the simulation model. This result highlights the need to consider the different particle doses accumulated on the cell surface at each time point, rather than the common particle dosing based on the total amount of nanoparticles in the medium, in order to understand the interactions occurring at bio-interface. The increase in cellular association with longer incubation time is likely due to the increased particle accumulation on cellular surface available for absorption.

The effects of the charge of nanoparticles at the bio-interface were also investigated with RRH-tagged PECA nanoparticles (**Chapter 3** and **4**). Cationic, RRH-tagged nanoparticles were observed to have higher cellular adherence tendency and adhered to more cells compared to anionic, unmodified PECA nanoparticles (**Chapter 3** and **4**). However, RRH-tagged nanoparticles were not readily internalized by the Caco-2 cells (**Chapter 3**) or adhered very strongly to the fully differentiated Caco-2 cell monolayers (**Chapter 4**). The adherence tendency may also explain the immediate association of the nanoparticles with the cells upon introduction of the nanoparticle formulation, which the simulation model did not account for. Therefore, the simulation model should be modified in the future to include other factors such as initial convective mixing and adherence tendency based on charge of nanoparticles to be able to predict the accumulation of the nanoparticles on the cell surface more accurately.

This thesis also highlights the important aspects that need to be considered when assessing the cellular uptake of nanoparticles. In this thesis, PECA nanoparticles were covalently associated with oligoarginine with 2 arginine residues (RRH) to assess the effect of oligoarginine association on cellular uptake. These cationic, RRH-tagged nanoparticles showed significantly greater association compared to anionic, unmodified PECA nanoparticles in undifferentiated Caco-2 cells (**Chapter 3** and **4**). However, the marked improvement in cellular association was not reproduced in fully differentiated Caco-2 cell monolayers grown for 21 to 28 days. Therefore, the result of the cellular uptake or association investigated with undifferentiated cells could not be extrapolated to fully differentiated Caco-2 cells, which is a more suitable model in predicting gut

absorption *in vivo*. Although many published studies claimed enhanced cellular uptake with nanoparticles, the majority of these study were carried out with undifferentiated Caco-2 cells (He *et al.*, 2013; Liu *et al.*, 2013; Yin Win and Feng, 2005). It has also been postulated that fully differentiated Caco-2 cell monolayers can efflux nanoparticles from the cells via transporters (Bhattacharjee *et al.*, 2013; He *et al.*, 2013; Hu *et al.*, 2011). However, the ATP-depletion study in this thesis (**Chapter 3**) did not show evidence of such a transporter. The ATP-depletion study should be repeated with the scintillation assay in the future to confirm that the presence of these nanoparticles efflux transporters as the result in **Chapter 3** was based on a fluorescent probe, entrapped non-covalently in the nanoparticles. As discussed previously, the results obtained based on detection of the non-covalently entrapped fluorescent probe should only be associated with payload delivery instead of nanoparticle delivery. It is possible that these efflux transporters remove nanoparticles, but not FITC-dextran (entrapped in the nanoparticles). Therefore, the FACS result in **Chapter 3** only indicates that the FITC-dextran (not the nanoparticles) was not effluxed out of the nanoparticles. In addition to the possibility of efflux transporters being present, the cellular association experiment set up may play an important role in influencing the conflicting result between undifferentiated cells and fully differentiated Caco-2 monolayers. For example, individual, undifferentiated Caco-2 cells would have a greater contact area for nanoparticles compared to a monolayer (**Chapter 4**) and actively dividing, undifferentiated Caco-2 cells may also affect the FACS result (**Chapter 3**).

Another important factor not considered in the *in vitro* cellular uptake model in this thesis is the presence of the mucous layer. The mucous layer has been shown to hinder absorption of nanoparticulates (Norris *et al.*, 1998). Therefore, it would also be appropriate to investigate the impact of mucous on the absorption of nanoparticles associated with oligoarginine. It has been shown that cationic nanoparticles, such as chitosan nanoparticles, have mucoadhesive properties that can prolong contact time with the mucosal surface for increased absorption (Ye *et al.*, 2013). The cellular uptake of oligoarginine associated PECA nanoparticles could be investigated in a Calu-3 cell-line, which produces a mucous layer. Such a study could provide important insights to understand the impact of mucous on cellular uptake and the importance of the surface charge of the nanoparticles in mucoadhesion.

In this thesis, the PECA nanoparticles were shown to be able to only covalently associate with RRH to produce cationic nanoparticles, while oligoarginine with more than two arginine residues failed to achieve covalent association. Wender *et al.* (2008) hypothesized that at least hexa-arginine (R6) is required for enhanced cellular penetration and the penetration efficiency was increased with longer arginine residues up to 15 arginines. Although the enhanced cellular association was still shown with PECA nanoparticles covalently associated di-arginine (R2) peptides, it would of great interest to study the uptake of the nanoparticles covalently associated with oligoarginine comprising more than two arginine residues as a longer arginine chain may lead to greater cellular association. A potential method to covalently associate the PECA nanoparticles with longer arginine residues is to use a stronger nucleophile such as vinyl nucleophile as the linker molecule, instead of histidine.

As PECA nanoparticles are biocompatible and biodegradable, they are perceived to as a promising colloidal carrier candidate for drug formulation (Vauthier *et al.*, 2003; Watnasirichaikul *et al.*, 2000). However, a major setback of using the PECA nanoparticles as a drug delivery system is that the particles are leaky and the issue worsens with oligoarginine association (**Chapter 3**). A possible remedy is to increase the concentration of monomer used to produce a thicker wall (Watnasirichaikul *et al.*, 2002a). However, the introduction of this variable may also alter the resultant particle size and the amount of oligoarginine associated to the particle surface, thus affecting the surface charge (Graf *et al.*, 2009b). PLGA may be an alternative polymer to be utilized in the particulate formulation for oral drug delivery, especially for sustained release formulation. Pegylated PLGA nanoparticles have been demonstrated to have a sustained release of Nile red over 10 days (Vij *et al.*, 2010). Compared to these pegylated PLGA nanoparticles, unmodified PECA nanoparticles released 20% of the load (FITC-dextran 2,000 kDa) within 3 h (**Chapter 3**). The release from the PECA nanoparticles is markedly faster and greater than the pegylated PLGA nanoparticles, considering the fact that the Nile red (318 g/mol) is of similar size of a FITC molecule (389 g/mol) without the dextran conjugate. It is also possible to co-formulate PLGA nanoparticles with CPPs as oligoarginine (R8) has been covalently associated to PLGA nanoparticles (Liu *et al.*, 2013). Therefore, PLGA may be an alternative polymer to PACA, to produce oligoarginine-tagged polymeric nanoparticles that would be able to deliver a higher payload.

This thesis shows the value of PECA nanoparticles in studying the effects of oligoarginine association on cellular uptake. In summary, this thesis has shown the importance of characterization of nanoparticles in the appropriate medium, as well as predicting the accumulation of nanoparticles on cellular surface to aid in understanding the interactions at the bio-interface. This thesis has also demonstrated that oligoarginine can be coupled to a PECA nanoparticulate system to enhance cellular adherence and potentially leading to subsequent enhanced uptake. However, interpretation of cellular uptake has to be made with caution and with critical assessments. Further surface characterization of these oligoarginine PECA nanoparticles is required to enhance our fundamental understanding of the interactions occurring at the bio-interface.

References

- Åberg, C., Kim, J.A., Salvati, A., Dawson, K.A., 2013. Theoretical framework for nanoparticle uptake and accumulation kinetics in dividing cell populations. *Europhysics Letters* 101, 1-6.
- Aderem, A., Underhill, D.M., 1999. Mechanisms of phagocytosis in macrophages. *Annual Review of Immunology* 17, 593-623.
- Agarwal, R., Roy, K., 2013. Intracellular delivery of polymeric nanocarriers: A matter of size, shape, charge, elasticity and surface composition. *Therapeutic Delivery* 4, 705-723.
- Al Khouri Fallouh, N., Roblot-Treupel, L., Fessi, H., Devissauguet, J.P., Puisieux, F., 1986. Development of a new process for the manufacture of polyisobutylcyanoacrylate nanocapsules. *International Journal of Pharmaceutics* 28, 125-132.
- Allison, S.A., Xin, Y., Pei, H., 2007. Electrophoresis of spheres with uniform zeta potential in a gel modeled as an effective medium. *Journal of Colloid and Interface Science* 313, 328-337.
- Andrews, P.C., 1988. Ion-exchange HPLC for peptide purification. *Journal of Peptide Research* 1, 93-99.
- Aprahamian, M., Michel, C., Humbert, W., Devissauguet, J.P., Damgé, C., 1987. Transmucosal passage of polyalkylcyanoacrylate nanocapsules as a new drug carrier in the small intestine. *Biology of the Cell* 61, 69-76.
- Artursson, P., Lindmark, T., Davis, S.S., Illum, L., 1994. Effect of chitosan on the permeability of monolayers of intestinal epithelial cells (Caco-2). *Pharmaceutical Research* 11, 1358-1361.
- Aulenta, F., Hayes, W., Rannard, S., 2003. Dendrimers: A new class of nanoscopic containers and delivery devices. *European Polymer Journal* 39, 1741-1771.
- Aungst, B.J., 2000. Intestinal permeation enhancers. *Journal of Pharmaceutical Sciences* 89, 429-442.
- Aungst, B.J., Saitoh, H., Burcham, D.L., Huang, S.M., Mousa, S.A., Hussain, M.A., 1996. Enhancement of the intestinal absorption of peptides and nonpeptides. *Journal of Controlled Release* 41, 19-31.
- Baeumer, B., Chatterjee, L., Hinow, P., Rades, T., Radunskaya, A., Tucker, I., 2009. Predicting the drug release kinetics of matrix tablets. *Discrete and Continuous Dynamical Systems - Series B* 12, 261-277.
- Bala, I., Hariharan, S., Kumar, M.N.V.R., 2004. PLGA nanoparticles in drug delivery: The state of the art. *Critical Reviews in Therapeutic Drug Carrier Systems* 21, 387-422.
- Bhattacharjee, S., Opstal, E., Alink, G., Marcelis, A.M., Zuilhof, H., Rietjens, I.C.M., 2013. Surface charge-specific interactions between polymer nanoparticles and ABC transporters in Caco-2 cells. *Journal of Nanoparticle Research* 15, 1-14.
- Biemann, K., 1990. Nomenclature for peptide fragment ions (positive-ions). *Methods in Enzymology* 193, 886-887.
- Bilati, U., Allemann, E., Doelker, E., 2005a. Strategic approaches for overcoming peptide and protein instability within biodegradable nano- and microparticles. *European Journal of Pharmaceutics and Biopharmaceutics* 59, 375-388.
- Bilati, U., Pasquarello, C., Corthals, G.L., Hochstrasser, D.F., Allemann, E., Doelker, E., 2005b. Matrix-assisted laser desorption/ionization time-of-flight mass spectrometry for quantitation and molecular stability assessment of insulin entrapped within PLGA nanoparticles. *Journal of Pharmaceutical Sciences* 94, 688-694.

- Blanchfield, J.T., Lew, R.A., Smith, A.I., Toth, I., 2005. The stability of lipidic analogues of GnRH in plasma and kidney preparations: The stereoselective release of the parent peptide. *Bioorganic & Medicinal Chemistry Letters* 15, 1609-1612.
- Blechinger, J., Bauer, A.T., Torrano, A.A., Gorzelanny, C., Bräuchle, C., Schneider, S.W., 2013. Uptake kinetics and nanotoxicity of silica nanoparticles are cell type dependent. *Small* 9, 3970-3980.
- Bonduelle, C.V., Gillies, E.R., 2010. Dendritic guanidines as efficient analogues of cell penetrating peptides. *Pharmaceuticals* 3, 636-666.
- Bootz, A., Vogel, V., Schubert, D., Kreuter, J., 2004. Comparison of scanning electron microscopy, dynamic light scattering and analytical ultracentrifugation for the sizing of poly(butyl cyanoacrylate) nanoparticles. *European Journal of Pharmaceutics and Biopharmaceutics* 57, 369-375.
- Brader, M.L., Sukumar, M., Pekar, A.H., McClellan, D.S., Chance, R.E., Flora, D.B., Cox, A.L., Irwin, L., Myers, S.R., 2002. Hybrid insulin cocrystals for controlled release delivery. *Nature Biotechnology* 20, 800-804.
- Brambilla, D., Nicolas, J., Le Droumaguet, B., Andrieux, K., Marsaud, V., Couraud, P.-O., Couvreur, P., 2010. Design of fluorescently tagged poly(alkyl cyanoacrylate) nanoparticles for human brain endothelial cell imaging. *Chemical Communications* 46, 2602-2604.
- Brewis, I.A., Brennan, P., 2010. Chapter 1 - Proteomics technologies for the global identification and quantification of proteins, *Advances in Protein Chemistry and Structural Biology*, in: Rossen, D.(Ed.). *Academic Press*, pp. 1-44.
- Buchla, E., Hinow, P., Najera, A., Radunskaya, A., 2014. Swallowing a cellular automation pill: Predicting drug release from a matrix tablet. *Simulation* 90, 227-237.
- Buda, A., Sands, C., Jepson, M.A., 2005. Use of fluorescence imaging to investigate the structure and function of intestinal M cells. *Advanced Drug Delivery Reviews* 57, 123-134.
- Butowt, R., Von Bartheld, C.S., 2001. Sorting of internalized neurotrophins into an endocytic transcytosis pathway via the Golgi system: Ultrastructural analysis in retinal ganglion cells. *Journal of Neuroscience* 21, 8915-8930.
- Cafaggi, S., Russo, E., Caviglioli, G., Parodi, B., Stefani, R., Sillo, G., Leardi, R., Bignardi, G., 2008. Poloxamer 407 as a solubilising agent for tolfenamic acid and as a base for a gel formulation. *European Journal of Pharmaceutical Sciences* 35, 19-29.
- Camenisch, G., Alsenz, J., van de Waterbeemd, H., Folkers, G., 1998. Estimation of permeability by passive diffusion through Caco-2 cell monolayers using the drugs' lipophilicity and molecular weight. *European Journal of Pharmaceutical Sciences* 6, 313-319.
- Cameron, A., Appel, J., Houghten, R.A., Lindberg, I., 2000. Polyarginines are potent furin inhibitors. *Journal of Biological Chemistry* 275, 36741-36749.
- Caminade, A., Laurent, R., Majoral, J., 2005. Characterization of dendrimers. *Advanced Drug Delivery Reviews* 57, 2130-2146.
- Cardozo, A.K., Buchillier, V., Mathieu, M., Chen, J., Ortis, F., Ladriere, L., Allaman-Pillet, N., Poirot, O., Kellenberger, S., Beckmann, J.S., Eizirik, D.L., Bonny, C., Maurer, F., 2007. Cell-permeable peptides induce dose- and length-dependent cytotoxic effects. *Biochimica et Biophysica Acta* 1768, 2222-2234.
- Carino, G.P., Mathiowitz, E., 1999. Oral insulin delivery. *Advanced Drug Delivery Reviews* 35, 249-257.

- Carneiro-da-Cunha, M.G., Cerqueira, M.A., Souza, B.W.S., Teixeira, J.A., Vicente, A.A., 2011. Influence of concentration, ionic strength and pH on zeta potential and mean hydrodynamic diameter of edible polysaccharide solutions envisaged for multilayered films production. *Carbohydrate Polymers* 85, 522-528.
- Cartiera, M., Johnson, K., Rajendran, V., Caplan, M., Saltzman, W., 2009. The uptake and intracellular fate of PLGA nanoparticles in epithelial cells. *Biomaterials* 30, 2790 - 2798.
- Cary, R., 2001. Methyl cyanoacrylate and ethyl cyanoacrylate, in: Inter-Organizational Programme for the Sound Management of Chemicals, U.I.W. (Ed.). *World Health Organization*, Geneva, p. Concise International Chemical Assessment Document 36.
- Cheng, Y., Xu, T., 2008. The effect of dendrimers on the pharmacodynamic and pharmacokinetic behaviors of non-covalently or covalently attached drugs. *European Journal of Medicinal Chemistry* 43, 2291-2297.
- Chiu, Y.L., Ali, A., Cao, H., Rana, T.M., 2004. Visualizing a correlation between siRNA localization, cellular uptake and RNAi in living cells. *Chemistry & Biology* 11, 1165-1175.
- Cho, E.C., Xie, J., Wurm, P.A., Xia, Y., 2009. Understanding the role of surface charges in cellular adsorption versus internalization by selectively removing gold nanoparticles on the cell surface with a I2/KI etchant. *Nano Letters* 9, 1080-1084.
- Christiaens, B., Grooten, J., Reusens, M., Joliot, A., Goethals, M., Vandekerckhove, J., Prochiantz, A., Rosseneu, M., 2004. Membrane interaction and cellular internalization of penetratin peptides. *European Journal of Biochemistry* 271, 1187-1197.
- Cicek, H., Tuncel, A., Tuncel, M., Piskin, E., 1994. Degradation and drug release characteristics of monosize polyethylcyanoacrylate microspheres. *Journal of Bioaterials Science, Polymer Edition* 6, 845-856.
- Conner, S.D., Schmid, S.L., 2003. Regulated portals of entry into the cell. *Nature* 422, 37-44.
- Constantinides, P.P., Lancaster, C.M., Marcello, J., Chiossone, D.C., Orner, D., Hidalgo, L., Smith, P.L., Sarkahian, A.B., Yib, S.H., Owen, A.J., 1995. Enhanced intestinal absorption of an RGD peptide from water-in-oil microemulsions of different composition and particle size. *Journal of Controlled Release* 34, 109-116.
- Couvreur, P., Kante, B., Roland, M., Guiot, P., Bauduin, P., Speiser, P., 1979. Polycyanoacrylate nanocapsules as potential lysosomotropic carriers - preparations, morphological and sorptive properties. *Journal of Pharmacy and Pharmacology* 31, 333-332.
- Cowan, P.E., 1996. Possum biocontrol: Prospects for fertility regulation. *Reproduction, Fertility, and Development* 8, 655-660.
- Damgé, C., Aprahamian, M., Couvreur, P., 1988. New approach for oral administration of insulin with polyalkylcyanoacrylate nanocapsules as drug carrier. *Diabetes* 37, 246-251.
- Damgé, C., Vranckx, H., Balschmidt, P., Couvreur, P., 1997. Poly(alkylcyanoacrylate) nanospheres for oral administration of insulin. *Journal of Pharmaceutical Sciences* 86, 1403-1409.
- Daugherty, A.L., Mersny, R.J., 1999. Transcellular uptake mechanisms of intestinal epithelial barrier: Part I. *Pharmaceutical Science and Technology Today* 4, 144-151.
- De Pillis, L.G., Radunskaya, A., 2001. A mathematical tumor model with immune resistance and drug therapy: An optimal control approach. *Journal of Theoretical Medicine* 3, 79-100.

- Derakhshandeh, K., Hochhaus, G., Dadashzadeh, S., 2011. *In vitro* cellular uptake and transport study of 9-Nitrocamptothecin PLGA nanoparticles across Caco-2 cell monolayer model. *Iranian Journal of Pharmaceutical Research* 10, 425-434.
- Derossi, D., Calvet, S., Trembleau, A., Brunissen, A., Chassaing, G., Prochiantz, A., 1996. Cell internalization of the third helix of the antennapedia homeodomain is receptor-independent. *Journal of Biological Chemistry* 271, 18188-18193.
- des Rieux, A., Fievez, V., Garinot, M., Schneider, Y.-J., Preat, V., 2006. Nanoparticles as potential oral delivery systems of proteins and vaccines: A mechanistic approach. *Journal of Controlled Release* 116, 1-27.
- Di Fiore, P.P., De Camilli, P., 2001. Endocytosis and signaling: An inseparable partnership. *Cell* 106, 1-4.
- Doherty, G.J., McMahon, H.T., 2009. Mechanisms of endocytosis. *Annual Review of Biochemistry* 78, 857-902.
- Drasar, B., Hill, M., 1974. Bacterial glycosidase, Human intestinal flora. *Academic Press*, London, pp. 154-171.
- Duchardt, F., Fotin-Mleczek, M., Schwarz, H., Fischer, R., Brock, R., 2007. A comprehensive model for the cellular uptake of cationic cell-penetrating peptides. *Traffic* 8, 848-866.
- Dutta, R.C., 2007. Drug carriers in pharmaceutical design: Promises and progress. *Current Pharmaceutical Design* 13, 761-769.
- El-Andaloussi, S., Järver, P., Johansson, H.J., Langel, Ü., 2007. Cargo-dependent cytotoxicity and delivery efficacy of cell-penetrating peptides: A comparative study. *Biochemical Journal* 40, 285-292.
- El-Aneed, A., Cohen, A., Banoub, J., 2009. Mass spectrometry, Review of the basics: Electrospray, MALDI and commonly used mass analyzers. *Applied Spectroscopy Reviews* 44, 210-230.
- Eldridge, J.H., Hammond, C.J., Meulbroek, J.A., Staas, J.K., Gilley, R.M., Tice, T.R., 1990. Controlled vaccine release in the gut-associated lymphoid tissues: I. Orally administered biodegradable microspheres target the Peyer's patches. *Journal of Controlled Release* 11, 205-214.
- Ermak, T.H., Giannasca, P.J., 1998. Microparticle targeting to M cells. *Advanced Drug Delivery Reviews* 34, 261-283.
- Fasano, A., 1998. Innovative strategies for the oral delivery of drugs and peptides. *Trends in Biotechnology* 16, 152-157.
- Fawell, S., Seery, J., Daikh, Y., Moore, C., Chen, L.L., Pepinsky, B., Barsoum, J., 1994. TAT-mediated delivery of heterologous proteins into cells. *Proceedings of the National Academy Sciences of the United States of America* 91, 664-668.
- Fenyvesi, F., Réti-Nagy, K., Bacsó, Z., Gutay-Tóth, Z., Malanga, M., Fenyvesi, É., Szente, L., Váradi, J., Ujhelyi, Z., Fehér, P., Szabó, G., Vecsernyés, M., Bácskay, I., 2014. Fluorescently labeled methyl-beta-cyclodextrin enters intestinal epithelial Caco-2 cells by fluid-phase endocytosis. *PLoS ONE* 9, e84856.
- Fernando, L.P., Kandel, P.K., Yu, J., McNeill, J., Ackroyd, P.C., Christensen, K.A., 2011. Mechanism of cellular uptake of highly fluorescent conjugated polymer nanoparticles. *Biomacromolecules* 11, 2675-2682.
- Ferrari, A., Pellegrini, V., Arcangeli, C., Fittipaldi, A., Giacca, M., Beltram, F., 2003. Caveolae-mediated internalization of extracellular HIV-1 TAT fusion proteins visualized in real time. *Molecular Therapy* 8, 284-294.
- Filipe, V., Hawe, A., Jiskoot, W., 2010. Critical evaluation of nanoparticle tracking analysis (NTA) by NanoSight for the measurement of nanoparticles and protein aggregates. *Pharmaceutical Research* 27, 796-810.

- Fischer, D., Li, Y., Ahlemeyer, B., Krieglstein, J., Kissel, T., 2003. *In vitro* cytotoxicity testing of polycations: Influence of polymer structure on cell viability and hemolysis. *Biomaterials* 24, 1121-1131.
- Fischer, R., Fotin-Mieczek, M., Hufnagel, H., Brock, R., 2005. Break on through to the other side-biophysics and cell biology shed light on cell-penetrating peptides. *Chembiochem* 6, 2126-2142.
- Fittipaldi, A., Ferrari, A., Zoppe, M., Arcangeli, C., Pellegrini, V., Beltram, F., Giacca, M., 2003. Cell membrane lipid rafts mediate caveolar endocytosis of HIV-1 TAT fusion proteins. *Journal of Biological Chemistry* 278, 34141-34149.
- Foged, C., Nielsen, H.M., 2008. Cell-penetrating peptides for drug delivery across membrane barriers. *Expert Opinion on Drug Delivery* 5, 105-117.
- Fonseca, S.B., Pereira, M.P., Kelley, S.O., 2009. Recent advances in the use of cell-penetrating peptides for medical and biological applications. *Advanced Drug Delivery Reviews* 61, 953-964.
- Frankel, A.D., Pabo, C.O., 1988. Cellular uptake of the TAT protein from human immunodeficiency virus. *Cell* 55.
- Galindo-Rodriguez, S.A., Allemann, E., Fessi, H., Doelker, E., 2005. Polymeric nanoparticles for oral delivery of drugs and vaccines: A critical evaluation of *in vivo* studies. *Critical Reviews in Therapeutic Drug Carrier Systems* 22, 419-464.
- Gan, Q., Wang, T., Cochrane, C., McCarron, P., 2005. Modulation of surface charge, particle size and morphological properties of chitosan-TPP nanoparticles intended for gene delivery. *Colloids and Surfaces B: Biointerfaces* 44, 65-73.
- Gao, J.N., Hugger, E.H., Beck-Westermeyer, M.S., Borchardt, R.T., 2000. Estimating intestinal mucosal permeation of compounds using Caco-2 cell monolayers. *Current Protocols in Pharmacology* Supplement 8, 7.2.1-7.2.23.
- Ghilzai, N.M.K., 2003. New developments in insulin delivery. *Drug Development and Industrial Pharmacy* 29, 253-265.
- Gipps, E., Groscurt, P., Kreuter, J., Speiser, P., 1987. The effects of poly(alkylcyanoacrylate) nanoparticles on human normal and malignant mesenchymal cells *in vitro*. *International Journal of Pharmaceutics* 40, 23-31.
- Goldberg, M., Gomez-Orellana, I., 2003. Challenges for the oral delivery of macromolecules. *Nature Reviews Drug Discovery* 2, 289-295.
- Graf, A., Jack, K.S., Whittaker, A.K., Hook, S., Rades, T., 2008. Protein delivery using nanoparticles based on microemulsions with different structure-types. *European Journal of Pharmaceutical Sciences* 33, 434-444.
- Graf, A., McDowell, A., Rades, T., 2009a. Poly(alkylcyanoacrylate) nanoparticles for enhanced delivery of therapeutics - Is there real potential? *Expert Opinion on Drug Delivery* 6, 371-387.
- Graf, A., Rades, T., Hook, S., 2009b. Oral insulin delivery using nanoparticles based on microemulsions with different structure-types: Optimisation and *in vivo* evaluation. *European Journal of Pharmaceutical Sciences* 37, 53-61.
- Green, M., Loewenstein, P.M., 1988. Autonomous functional domains of chemically synthesized human immunodeficiency virus tat trans-activator protein. *Cell* 55.
- Gref, R., Couvreur, P., Barratt, G., Mysiakine, E., 2003. Surface-engineered nanoparticles for multiple ligand coupling. *Biomaterials* 24, 4529-4537.
- Griffith, D.A., Jarvis, S.M., 1996. Nucleoside and nucleobase transport systems of mammalian cells. *Biochimica et Biophysica Acta* 1286, 153-181.
- Grislain, L., Couvreur, P., Lenaerts, V., Roland, M., Deprez-Decampeneere, D., Speiser, P., 1983. Pharmacokinetics and distribution of a biodegradable drug carrier. *International Journal of Pharmaceutics* 15, 335-345.

- Gruber, P., Rubinstein, A., Li, V.H., Bass, P., Robinson, J.R., 1987. Gastric emptying of nondigestible solids in the fasted dog. *Journal of Pharmaceutical Sciences* 76, 117-122.
- Gullberg, E., 2005. Particle transcytosis across the human intestinal epithelium: Model development and target identification for improved drug delivery, Faculty of Pharmacy. *Uppsala University*, Sweden, pp. 1-62.
- Gundogdu, E., Yurdasiper, A., 2014. Drug transport mechanism of oral antidiabetic nanomedicines. *International Journal of Endocrinology and Metabolism* 12, e8984.
- Hamman, J.H., Enslin, G.M., Kotzé, A.F., 2005. Oral delivery of peptide drugs: Barriers and developments. *Biodrugs* 19, 165-177.
- Harush-Frenkel, O., Debotton, N., Benita, S., Altschuler, Y., 2007. Targeting of nanoparticles to the clathrin-mediated endocytic pathway. *Biochemical and Biophysical Research Communications* 353, 26 - 32.
- Harush-Frenkel, O., Rozentur, E., Benita, S., Altschuler, Y., 2008. Surface charge of nanoparticles determines their endocytic and transcytotic pathway in polarized MDCK cells. *Biomacromolecules* 9, 435 - 443.
- Harvey, R.A., Clark, M.A., Finkel, R., Rev, J.A., Whalen, K., 2011. II. Routes of drug administration, Lippincott's illustrated reviews: Pharmacology, 5th, North America ed. *Lippincott Williams & Wilkins*.
- He, B., Lin, P., Jia, Z., Du, W., Qu, W., Yuan, L., Dai, W., Zhang, H., Wang, X., Wang, J., Zhang, X., Zhang, Q., 2013. The transport mechanisms of polymer nanoparticles in Caco-2 epithelial cells. *Biomaterials* 34, 6082-6098.
- He, C., Hu, Y., Yin, L., Tang, C., Yin, C., 2010. Effects of particle size and surface charge on cellular uptake and biodistribution of polymeric nanoparticles. *Biomaterials* 31, 3657-3666.
- Hilgendorf, C., Hildegard Spahn-Langguth, Regardh, C.G., Lipika, E., Amidon, G.L., Langguth, P., 2000. Caco-2 versus Caco-2/HT29-MTX co-cultured cell lines: Permeabilities via diffusion, inside- and outside-directed carrier-mediated transport. *Journal of Pharmaceutical Sciences* 89, 63-75.
- Hinderliter, P., Minard, K., Orr, G., Chrisler, W., Thrall, B., Pounds, J., Teeguarden, J., 2010. ISDD: A computational model of particle sedimentation, diffusion and target cell dosimetry for *in vitro* toxicity studies. *Particle and Fibre Toxicology* 7, 36.
- Hoffmann, H., 2000. Analytical methods and stability testing of biopharmaceuticals, in: McNally, E.J. (Ed.), *Drugs and the Pharmaceutical Science: Protein Formulation and Delivery*. *Marcel Dekker Incorporation*, New York, pp. 71-110.
- Hong, S., Bielinska, A.U., Mecke, A., Keszler, B., Beals, J.L., Shi, X., Balogh, L., Orr, B.G., Baker, J.R., Banaszak-Holl, M.M., 2004. Synthetic and natural polycationic polymer nanoparticles interact selectively with fluid-phase domains of DMPC lipid bilayers. *Bioconjugate Chemistry* 15, 774-782.
- Hong, S., Leroueil, P.R., Janus, E.K., Peters, J.L., Kore, M.M., Islam, M.T., Orr, B.G., Baker, J.R., Banaszak-Holl, M.M., 2006. Interaction of polycationic polymers with supported lipid bilayers and cells: Nanoscale hole formation and enhanced membrane permeability. *Bioconjugate Chemistry* 17, 728-734.
- Hu, L., Mao, Z., Gao, C., 2009. Colloidal particles for cellular uptake and delivery. *Journal of Materials Chemistry* 19, 3108-3115.
- Hu, L., Mao, Z., Zhang, Y., Gao, C., 2011. Influences of size of silica particles on the cellular endocytosis, exocytosis and cell activity of HepG2 cells. *Journal of Nanoscience Letters* 1, 1-16.

- Hubatsch, I., Ragnarsson, E.G., Artursson, P., 2007. Determination of drug permeability and prediction of drug absorption in Caco-2 monolayers. *Nature Protocols* 2, 2111-2119.
- Hulme, E.C., Trevethick, M.A., 2010. Ligand binding assays at equilibrium: Validation and interpretation. *British Journal of Pharmacology* 161, 1219-1237.
- Husain, A., Hamielec, A.E., Vlachopoulos, J., 1980. Particle size analysis using size exclusion chromatography. Size exclusion chromatography (GPC). *Journal of the American Chemical Society* 138, 47-75.
- ICH, 1996. Guidance for industry - Q2B Validation of analytical procedures: Methodology. *Food and Drug Administration (FDA)*.
- Irvine, G.B., 2003. High-performance size-exclusion chromatography of peptides. *Journal of Biochemical and Biophysical Methods* 56, 233-242.
- Jiang, X., Musyanovych, A., Rocker, C., Landfester, K., Mailander, V., Nienhaus, G.U., 2011. Specific effects of surface carboxyl groups on anionic polystyrene particles in their interactions with mesenchymal stem cells. *Nanoscale* 3, 2028-2035.
- Jing, D., Bhushan, B., 2013. Quantification of surface charge density and its effect on boundary slip. *Langmuir* 29, 6953-6963.
- Jones, A.T., 2007. Micropinocytosis: Searching for an endocytic identity and role in the uptake of cell penetrating peptides. *Journal of Cellular and Molecular Medicine* 11, 670-684.
- Jones, S.W., Christison, R., Bundell, K., Voyce, C.J., Brockbank, S.M.V., Newham, P., Lindsay, M.A., 2005. Characterisation of cell-penetrating peptide-mediated peptide delivery. *British Journal of Pharmacology* 145, 1093-1102.
- Jung, T., Kamm, W., Breitenbach, A., Kaiserling, E., Xiao, J.X., Kissel, T., 2000. Biodegradable nanoparticles for oral delivery of peptides: Is there a role for polymers to affect mucosal uptake? *European Journal of Pharmaceutics and Biopharmaceutics* 50, 147-160.
- Kafka, A.P., Kleffmann, T., Rades, T., McDowell, A., 2009. Histidine residues in the peptide D-Lys⁶-GnRH: Potential for copolymerization in polymeric nanoparticles. *Molecular Pharmaceutics* 6, 1483-1491.
- Kafka, A.P., Kleffmann, T., Rades, T., McDowell, A., 2010a. Characterization of peptide polymer interactions in poly(alkylcyanoacrylate) nanoparticles: A mass spectrometric approach. *Current Drug Delivery* 7, 208-215.
- Kafka, A.P., Kleffmann, T., Rades, T., McDowell, A., 2010b. *In vitro* evaluation of PACA nanoparticles for peroral delivery of the neuropeptide D-Lys₆-GnRH, Proceedings of the 12th Conference of the Formulation and Delivery of Bioactives Conference, Dunedin, New Zealand.
- Kafka, A.P., McLeod, B.J., Rades, T., McDowell, A., 2011. Release and bioactivity of PACA nanoparticles containing D-Lys⁶-GnRH for brushtail possum fertility control. *Journal of Controlled Release* 149, 307-313.
- Kalantzi, L., Goumas, K., Kalioras, V., Abrahamsson, B., Dressman, J., Reppas, C., 2006. Characterization of the human upper gastrointestinal contents under conditions simulating bioavailability/bioequivalence studies. *Pharmaceutical Research* 23, 165 - 176.
- Kamei, N., Morishita, M., Eda, Y., Ida, N., Nishio, R., Takayama, K., 2008a. Usefulness of cell-penetrating peptides to improve intestinal insulin absorption. *Journal of Controlled Release* 132, 21-25.
- Kamei, N., Morishita, M., Ehara, J., Takayama, K., 2008b. Permeation characteristics of oligoarginine through intestinal epithelium and its usefulness for intestinal peptide drug delivery. *Journal of Controlled Release* 131, 94-99.

- Kamei, N., Onuki, Y., Takayama, K., Takeda-Morishita, M., 2013. Mechanistic study of the uptake/permeation of cell-penetrating peptides across a Caco-2 monolayer and their stimulatory effect on epithelial insulin transport. *Journal of Pharmaceutical Sciences* 102, 3998-4008.
- Kante, B., Couvreur, P., Dubois-Krack, G., De Meester, C., Guiot, P., Roland, M., Mercier, M., Speiser, P., 1982. Toxicity of polyalkylcyanoacrylate nanoparticles. I. Free nanoparticles. *Journal of Pharmaceutical Sciences* 71, 786-790.
- Kaplan, I.M., Wadia, J.S., Dowdy, S.F., 2005. Cationic TAT peptide transduction domain enters cells by macropinocytosis. *Journal of Controlled Release* 102, 247-253.
- Kar, M., Tiwari, N., Tiwari, M., Lahiri, M., Gupta, S.S., 2013. Poly-L-arginine grafted silica mesoporous nanoparticles for enhanced cellular uptake and their application in DNA delivery and controlled drug release. *Particle & Particle Systems Characterization* 30, 166-179.
- Karn, P.R., Vanić, Z., Pepić, I., Škalko-Basnet, N., 2011. Mucoadhesive liposomal delivery systems: the choice of coating material. *Drug Development and Industrial Pharmacy* 37, 482-488.
- Kaznessis, Y.N., Kim, S., Larson, R.G., 2002. Specific mode of interaction between components of model pulmonary surfactants using computer simulations. *Journal of Molecular Biology* 322, 569-582.
- Kerseman, V., Kerseman, K., Cornelissen, B., 2008. Cell penetrating peptides for *in vivo* molecular imaging applications. *Current Pharmaceutical Design* 14, 2415-2427.
- Khafagy, E.-S., Morishita, M., Onuki, Y., Takayama, K., 2007. Current challenges in non-invasive insulin delivery systems: A comparative review. *Advanced Drug Delivery Reviews* 59, 1521-1546.
- Koschek, K., Dathe, M., Rademann, J., 2013. Effects of charge and charge distribution on the cellular uptake of multivalent arginine-containing peptide-polymer conjugates. *Chembiochem* 14, 1982-1990.
- Kraehenbuhl, J.P., Neutra, M.R., 2000. Epithelial M cells: Differentiation and function. *Annual Review of Cell and Developmental Biology* 16, 301-332.
- Krael, K., Davies, N.M., Hook, S., Rades, T., 2005. Using different structure types of microemulsions for the preparation of poly(alkylcyanoacrylate) nanoparticles by interfacial polymerization. *Journal of Controlled Release* 106, 76-87.
- Krael, K., Girvan, L., Hook, S., Rades, T., 2007. Characterisation of colloidal drug delivery systems from the naked eye to Cryo-FESEM. *Micron* 38, 796-803.
- Krael, K., Pitaksuteepong, T., Davies, N.M., Rades, T., 2004. Entrapment of bioactive molecules in poly(alkylcyanoacrylate) nanoparticles. *American Journal of Drug Delivery* 2, 251-259.
- Kulkarni, S., Feng, S.-S., 2013. Effects of particle size and surface modification on cellular uptake and biodistribution of polymeric nanoparticles for drug delivery. *Pharmaceutical Research* 30, 2512-2522.
- Kumar, R., Korideck, H., Ngwa, W., Berbeco, R.I., Makrigiorgos, G.M., Sridhar, S., 2014. Third generation gold nanoplatfrom optimized for radiation therapy. *Translational Cancer Research* 2, 1-18.
- Langel, U., 2006. Handbook of Cell-Penetrating Peptides, Second Edition. *Taylor & Francis*.
- Langguth, P., Bohner, V., J., H., Merkle, H.P., Wolffram, S., Amidon, G.L., Yamashita, S., 1997. The challenge of proteolytic enzymes in intestinal peptide delivery. *Journal of Controlled Release* 46, 39-57.

- Le Blay, G., Fliss, I., Lacroix, C., 2004. Comparative detection of bacterial adhesion to Caco-2 cells with ELISA, radioactivity and plate count methods. *Journal of Microbiological Methods* 59, 211-221.
- Lee, C.-K., Wang, Y.-M., Huang, L.-S., Lin, S., 2007. Atomic force microscopy: Determination of unbinding force, off rate and energy barrier for protein–ligand interaction. *Micron* 38, 446-461.
- Lee, H.L., Dubikovskaya, E.A., Hwang, H., Semyonov, A.N., Wang, H., Jones, L.R., Twieg, R.J., Moerner, W.E., Wender, P.A., 2008. Single-molecule motions of oligoarginine transporter conjugates on the plasma membrane of Chinese Hamster Ovary cells. *Journal of the American Chemical Society* 130, 9364-9370.
- Lee, M.T., Hung, W.C., Chen, F.Y., Huang, H.W., 2005. Many-body effect of antimicrobial peptides: On the correlation between lipid's spontaneous curvature and pore formation. *Biophysical Journal* 89, 4006-4016.
- Lemmer, H.J., Hamman, J.H., 2013. Paracellular drug absorption enhancement through tight junction modulation. *Expert Opinion on Drug Delivery* 10, 103-114.
- Leonard, F., Kulkarni, R.K., Brandes, G., Nelson, J., Cameron, J.J., 1966. Synthesis and degradation of poly(alkyl α -cyanoacrylates). *Journal of Applied Polymer Science* 10, 259-272.
- Leroueil, P.R., Berry, S.A., Duthie, K., Han, G., Rotello, V.M., McNerny, D.Q., Baker, J.R., Orr, B.G., Banaszak-Holl, M.M., 2008. Wide varieties of cationic nanoparticles induce defects in supported lipid bilayers. *Nano Letters* 8, 420-424.
- Leroueil, P.R., Hong, S., Mecke, A., Baker, J.R., Orr, B.G., Banaszak-Holl, M.M., 2007. Nanoparticle interaction with biological membranes: Does nanotechnology present a Janus face? *Accounts of Chemical Research* 40, 335-342.
- Lewin, M., Carlesso, N., Tung, C.H., Tang, X.W., Cory, D., Scadden, D.T., Weissleder, R., 2000. Tat peptide-derivatized magnetic nanoparticles allow *in vivo* tracking and recovery of progenitor cells. *Nature Biotechnology* 18, 410-414.
- Lherm, C., Muller, F., Puisieux, F., Couvreur, P., 1992. II. Cytotoxicity of cyanoacrylate nanoparticles with different alkyl chain length. *International Journal of Pharmaceutics* 84, 13-22.
- Li, Y., Chen, X., Gu, N., 2008. Computational investigation of interaction between nanoparticles and membranes: Hydrophobic/hydrophilic effect. *The Journal of Physical Chemistry B* 112, 16647-16653.
- Li, Y.P., Pei, Y.Y., Zhou, Z.H., Zhang, H., Gu, Z.H., Ding, J., Zhou, J.J., Gao, X.J., 2001a. PEGylated polycyanoacrylate nanoparticles as tumor necrosis factor- α carrier. *Journal of Controlled Release* 71, 287-296.
- Li, Y.P., Pei, Y.Y., Zhou, Z.H., Zhang, X.Y., Gu, Z.H., Ding, J., Gao, X.J., Zhu, J.H., 2001b. Stealth polycyanoacrylate nanoparticles as tumor necrosis factor- α carriers: Pharmacokinetics and antitumor effects. *Biological and Pharmaceutical Bulletin* 24, 662-665.
- Li, Z.-l., Ding, H.-m., Ma, Y.-q., 2013. Translocation of polyarginines and conjugated nanoparticles across asymmetric membranes. *Soft Matter* 9, 1281-1286.
- Liang, J.F., Yang, V.C., 2005. Insulin-cell penetrating peptide hybrids with improved intestinal absorption efficiency. *Biochemical and Biophysical Research Communications* 335, 734-738.
- Lipinski, C.A., Lombardo, F., Dominy, B.W., Feeney, P.J., 2001. Experimental and computational approaches to estimate solubility and permeability in drug discovery and development settings. *Advanced Drug Delivery Reviews* 46, 3-26.

- Liu, L., 2009. Application of ultrasound spectroscopy for nanoparticle sizing in high concentration suspensions: A factor analysis on the effects of concentration and frequency. *Chemical Engineering Science* 64, 5036-5042.
- Liu, X., Liu, C., Zhang, W., Xie, C., Wei, G., Lu, W., 2013. Oligoarginine-modified biodegradable nanoparticles improve the intestinal absorption of insulin. *International Journal of Pharmaceutics* 448, 159-167.
- Loh, J.W., Yeoh, G., Saunders, M., Lim, L.-Y., 2010. Uptake and cytotoxicity of chitosan nanoparticles in human liver cells. *Toxicology and Applied Pharmacology* 249, 148-157.
- Lowe, P.J., Temple, C.S., 1994. Calcitonin and insulin in isobutylcyanoacrylate nanocapsules: protection against proteases and effect on intestinal absorption in rats. *Journal of Pharmacy and Pharmacology* 46, 547-552.
- Lu, F., Wu, S.-H., Hung, Y., Mou, C.-Y., 2009. Size effect on cell uptake in well-suspended, uniform mesoporous silica nanoparticles. *Small* 5, 1408-1413.
- Luessen, H.L., Bde Leeuw, B.J., Langemeijer, M.W.E., de Boer, A.G., Verhoef, J.C., Junginger, H.E., 1996. Mucoadhesive polymers in peroral peptide drug delivery. IV. Carbomer and chitosan improve the intestinal absorption of the peptide drug buserelin *in vivo*. *Pharmaceutical Research* 13, 1668-1672.
- Maassen, S., Couvreur, P., Dubois-Krack, G., Speiser, P., 1993. Cell cultures for the assessment of toxicity and polymeric drug carriers. *STP Pharmaceutical Science* 3, 11-22.
- Madani, F., Lindberg, S., Langel, Ü., Futaki, S., Gräslund, A., 2011. Mechanisms of cellular uptake of cell-penetrating peptides. *Journal of Biophysics* 2011, 1-10.
- Mahato, R.I., Narang, A.S., Thoma, L., Miller, D.D., 2003. Emerging trends in oral delivery of peptide and protein drugs. *Critical Reviews in Therapeutic Drug Carrier Systems* 20, 153-214.
- Malik, N., Wiwattanapatapee, R., Klopsch, R., Lorenz, K., Frey, H., Weener, J.W., Meijer, E.W., Paulus, W., Duncan, R., 2000. Dendrimers: Relationship between structure and biocompatibility *in vitro* and preliminary studies on the biodistribution of 125I-labelled PAMAM dendrimers *in vivo*. *Journal of Controlled Release* 65, 133-148.
- Maniak, M., 2001. Macropinocytosis Endocytosis, in: Marsh, M.(Ed.). *Oxford University Press*, Oxford.
- Mason, M., Weaver, W., 1924. The settling of small particles in a fluid. *Physical Review* 23, 412-426.
- Mathiowitz, E., Jacob, J.S., Jong, Y.S., Carino, G.P., Chickering, D.E., Chaturvedi, P., Santos, C.A., Vijayaraghavan, K., Montgomery, S., Bassett, M., Morrell, C., 1997. Biologically erodable microspheres as potential oral drug delivery systems. *Nature* 386, 410-414.
- Matsuzaki, K., Yoneyama, S., Miyajima, K., 1997. Pore formation and translocation of melittin. *Biophysical Journal* 73, 831-838.
- Medina, S.H., El-Sayed, M.E.H., 2009. Dendrimers as carriers for delivery of chemotherapeutic agents. *Chemical Reviews* 109, 3141-3157.
- Michalet, X., Pinaud, F.F., Bentolila, L.A., Tsay, J.M., Doose, S., Li, J.J., Sundaresan, G., Wu, A.M., Gambhir, S.S., Weiss, S., 2005. Quantum dots for live cells, *in vivo* imaging and diagnostics. *Science* 307, 538-544.
- Michel, C., Aprahamian, M., Defontaine, L., Damgé, C., 1991. The effect of site of administration in the gastrointestinal tract on the absorption of insulin from nanocapsules in diabetic rats. *Journal of Pharmacy and Pharmacology* 43, 1-5.

- Mitchell, D.J., Steinman, L., Kim, D.T., Fathman, C.G., Rothbard, J.B., 2000. Polyarginine enters cells more efficiently than other polycationic homopolymers. *The Journal of Peptide Research* 56, 318-325.
- Monza da Silveira, A., Duchene, D., Ponchel, G., 2004. Drug release characteristics from combined poly(isobutylcyanoacrylate) and cyclodextrin nanoparticles loaded with progesterone. *Polymer Science Series A* 46, 1-8.
- Moribe, K., Wanawongthai, C., Shudo, J., Higashi, K., Yamamoto, K., 2008. Morphology and surface states of colloidal probucol nanoparticles evaluated by atomic force microscopy. *Chemical and Pharmaceutical Bulletin* 56, 878-880.
- Morille, M., Passirani, C., Vonarbourg, A., Clavreul, A., Benoit, J.-P., 2008. Progress in developing cationic vectors for non-viral systemic gene therapy against cancer. *Biomaterials* 29, 3477-3496.
- Morishita, M., Kamei, N., Ehara, J., Isowa, K., Takayama, K., 2007. A novel approach using functional peptides for efficient intestinal absorption of insulin. *Journal of Controlled Release* 118, 177-184.
- Morishita, M., Peppas, N.A., 2006. Is the oral route possible for peptide and protein drug delivery? *Drug Discovery Today* 11, 905-910.
- Müller, R.H., 1991. Colloidal carriers for controlled drug delivery and targeting - Modification, characterization and *in vivo* distribution. *Wissenschaftliche Verlagsgesellschaft Stuttgart*, CRC Press Boca Raton.
- Müller, R.H., Lherm, C., Herbort, J., Blunk, T., Couvreur, P., 1992. Alkylcyanoacrylate drug carriers: I. Physicochemical characterization of nanoparticles with different alkyl chain length. *International Journal of Pharmaceutics* 84, 1-11.
- Na, D.H., DeLuca, P.P., Lee, K.C., 2004. Direct determination of the peptide content in microspheres by matrix-assisted laser desorption/ionization time-of-flight mass spectrometry. *Analytical Chemistry* 76, 2669-2673.
- Nagahara, H., Vocero-Akbani, A.M., Snyder, E.L., Ho, A., Latham, D.G., Lissy, N.A., Becker-Hapak, M., Ezhevsky, S.A., Dowdy, S.F., 1998. Transduction of full-length TAT fusion proteins into mammalian cells: TAT-p27Kip1 induces cell migration. *Nature Medicine* 4, 1449-1452.
- Nam, H.Y., Hahn, H.J., Nam, K., Choi, W., Jeong, Y., Kim, D., Park, J.S., 2008. Evaluation of generations 2, 3 and 4 Arginine modified PAMAM dendrimers for gene delivery. *International Journal of Pharmaceutics* 363, 199-205.
- Nel, A.E., Madler, L., Velegol, D., Xia, T., Hoek, E.M.V., Somasundaran, P., Klaessig, F., Castranova, V., Thompson, M., 2009. Understanding biophysicochemical interactions at the nano-bio interface. *Nature Materials* 8, 543-557.
- Norris, D.A., Puri, N., Sinko, P.J., 1998. The effect of physical barriers and properties on the oral absorption of particulates. *Advanced Drug Delivery Reviews* 34, 135-154.
- Nyberg, F., Pernow, C., Moberg, U., Eriksson, R.B., 1986. High-performance liquid chromatography and diode-array detection for the identification of peptides containing aromatic amino acids in studies of endorphin-degrading activity in human cerebrospinal fluid. *Journal of Chromatography* 359, 541-551.
- Ong, Q.K., Sokolov, I., 2007. Attachment of nanoparticles to the AFM tips for direct measurements of interaction between a single nanoparticle and surfaces. *Journal of Colloid and Interface Science* 310, 385-390.
- Owens, D.R., Zinman, B., Bolli, G., 2003. Alternative routes of insulin delivery. *Diabetic Medicine* 20, 886-898.
- Pan, L., He, Q., Liu, J., Chen, Y., Ma, M., Zhang, L., Shi, J., 2012. Nuclear-Targeted Drug Delivery of TAT Peptide-Conjugated Monodisperse Mesoporous Silica Nanoparticles. *Journal of the American Chemical Society* 134, 5722-5725.

- Pantos, A., Tsogas, I., Paleos, C.M., 2008. Guanidinium group: A versatile moiety inducing transport and multicompartmentalization in complementary membranes. *Biochimica et Biophysica Acta* 1778, 811-823.
- Parton, R.G., Simons, K., 2007. The multiple faces of caveolae. *Nature Reviews Molecular Cell Biology* 8, 185-194.
- Pauletti, G.M., Okumu, F.W., Borchardt, R.T., 1997. Effect of size and charge on the passive diffusion of peptides across Caco-2 cell monolayers via the paracellular pathway. *Pharmaceutical Research* 14, 164-168.
- Perumal, O.P., Inapagolla, R., Kannan, S., Kannan, R.M., 2008. The effect of surface functionality on cellular trafficking of dendrimers. *Biomaterials* 29, 3469-3476.
- Pini, A., Falciani, C., Bracci, L., 2008. Branched peptides as therapeutics. *Current Protein Peptide Science* 9, 468-477.
- Pinto, M., Robine-Leon, S., Appay, M.D., Kedinger, M., Triadou, N., Dussaulx, E., Lacoroix, B., Simon-Assmann, P., Haffen, K., Fogh, J., Zwelbaum, A., 1983. Enterocyte-like differentiation and polarization of the human colon carcinoma cell line Caco-2 in culture. *Biology of the Cell* 47, 323-330.
- Pisal, D.S., Kosloski, M.P., Balu-iyer, S.V., 2009. Delivery of therapeutic proteins. *Journal of Pharmaceutical Sciences* 99, 2557-2575.
- Pitaksuteepong, T., Davies, N.M., Tucker, I.G., Rades, T., 2002. Factors influencing the entrapment of hydrophilic compounds in nanocapsules prepared by interfacial polymerisation of water-in-oil microemulsions. *European Journal of Pharmaceutics and Biopharmaceutics* 53, 335-342.
- Pluim, D., Maliapaard, M., van Waardenburg, R.C.A.M., Beijnen, J.H., Schellens, J.H.M., 1999. 32P-Postlabeling assay for the quantification of the major platinum-DNA adducts. *Analytical Biochemistry* 275, 30-38.
- Pooga, M., Kut, C., Kihlmark, M., Hallbrink, M., Fernaeus, S., Raid, R., Land, T., Hallberg, E., Bartfai, T., Langel, U., 2001. Cellular translocation of proteins by transportan. *The Journal of the Federation of American Societies for Experimental Biology* 15, 1451-1453.
- Pooga, M., Soomets, U., Hallbrink, M., Valkna, A., Saar, K., Rezaei, K., Kahl, U., Hao, J.X., Xu, X.J., Wiesenfeld-Hallin, Z., Hukfeld, T., Bartfai, T., Langel, U., 1998. Cell penetrating PNA constructs regulate galanin receptor levels and modify pain transmission *in vivo*. *Nature Biotechnology* 16, 857-861.
- Pouny, Y., Rapaport, D., Mor, A., Nicolas, P., Shai, Y., 1992. Interaction of antimicrobial dermaseptin and its fluorescently labeled analogues with phospholipid membranes. *Biochemistry* 31, 12416-12423.
- Pujals, S., Fernandez-Carneado, J., Lopez-Iglesias, C., Kogan, M.J., Giralt, E., 2006. Mechanistic aspects of CPP-mediated intracellular drug delivery: Relevance of CPP self-assembly. *Biochimica et Biophysica Acta* 1758, 264-279.
- Rabanel, J.M., Aoun, V., Elkin, I., Mokhtar, M., Hildgen, P., 2012. Drug-loaded nanocarriers: Passive targeting and crossing of biological barriers. *Current Medicinal Chemistry* 19, 3070-3102.
- Raimondi, F., Santoro, P., Barone, M.V., Pappacoda, S., Barretta, M.L., Nanayakkara, M., Apicella, C., Capasso, L., Paludetto, R., 2008. Bile acids modulate tight junction structure and barrier function of Caco-2 monolayers via EGFR activation. *American Journal of Physiology - Gastrointestinal and Liver Physiology* 294, G906-G913.
- Rao, A., Schoenenberger, M., Gnecco, E., Glatzel, T., Meyer, E., Brändlin, D., Scandella, L., 2007. Characterization of nanoparticles using atomic force microscopy. *Journal of Physics: Conference Series* 61, 971-976.

- Rao, K.S., Reddy, M.K., Horning, J.L., Labhasetwar, V., 2008. TAT-conjugated nanoparticles for the CNS delivery of anti-HIV drugs. *Biomaterials* 29, 4429-4438.
- Reis, C.P., Neufeld, R.J., Ribeiro, A.J., Veiga, F., 2006. Nanoencapsulation II. Biomedical applications and current status of peptide and protein nanoparticulate delivery systems. *Nanomedicine* 2, 53-65.
- Reix, N., Parat, A., Seyfritz, E., Van Der Werf, R., Epure, V., Ebel, N., Danicher, L., Marchioni, E., Jeandidier, N., Pinget, M., Frère, Y., Sigrist, S., 2012. *In vitro* uptake evaluation in Caco-2 cells and in vivo results in diabetic rats of insulin-loaded PLGA nanoparticles. *International Journal of Pharmaceutics* 437, 213-220.
- Rejman, J., Oberle, V., Zuhorn, I.S., Hoekstra, D., 2004. Size-dependent internalization of particles via the pathways of clathrin- and caveolae-mediated endocytosis. *Biochemical Journal* 377, 159-169.
- Richard, J.P., Melikov, K., Brooks, H., Prevot, P., Lebleu, B., Chernomordik, L.V., 2005. Cellular uptake of unconjugated TAT peptide involves clathrin-dependent endocytosis and heparan sulfate receptors. *Journal of Biological Chemistry* 280, 15300-15306.
- Richard, J.P., Melikove, K., Vives, E., Ramos, C., Verbeure, B., Gait, M.J., Chernomordik, L.V., Lebleu, B., 2003. Cell-penetration peptides: A reevaluation of the mechanism of cellular uptake. *Journal of Biological Chemistry* 278, 585-590.
- Riss, T.L., Moravec, R.A., 2004. Use of multiple assay endpoints to investigate the effects of incubation time, dose of toxin and plating density in cell-based cytotoxicity assays. *Assay and Drug Development Technologies* 2, 51-62.
- Ritschel, W.A., 1991. Microemulsions for improved peptide absorption from the gastrointestinal tract. *Methods and Findings in Experimental and Clinical Pharmacology* 13, 205-220.
- Rothbard, J.B., Garlington, S., Lin, Q., Kirschberg, T., Kreider, E., McGrane, P.L., Wender, P.A., Khavari, P.A., 2000. Conjugation of arginine oligomers to cyclosporin A facilitates topical delivery and inhibition of inflammation. *Nature Medicine* 6, 1253-1257.
- Rothbard, J.B., Kreider, E., VanDeusen, C.L., Wright, L., Wylie, B.L., Wender, P.A., 2002. Arginine-rich molecular transporters for drug delivery: Role of backbone spacing in cellular uptake. *Journal of Medicinal Chemistry* 45, 3612-3618.
- Rothmann, J.E., 1994. Mechanisms of intracellular protein transport. *Nature* 372, 55-63.
- Säälik, P., Elmquist, A., Hansen, M., Padari, K., Saar, K., Viht, K., Langel, U., Pooga, M., 2004. Protein cargo delivery properties of cell-penetrating peptides: A comparative study. *Bioconjugate Chemistry* 15, 1246-1253.
- Saar, K., Lindgren, M., Hansena, M., Eiríksdóttir, E., Jiang, Y., Rosenthal-Aizmana, K., Sassiana, M., Langel, Ü., 2005. Cell-penetrating peptides: A comparative membrane toxicity study. *2005* 345, 55-65.
- Sakuma, S., Suita, M., Masaoka, Y., Kataoka, M., Nakajima, N., Shinkai, N., Yamauchi, H., Hiwatari, K.-i., Tachikawa, H., Kimura, R., Yamashita, S., 2010. Oligoarginine-linked polymers as a new class of penetration enhancers. *Journal of Controlled Release* 148, 187-196.
- Salama, N.N., Eddington, N.D., Fasano, A., 2006. Tight junction modulation and its relationship to drug delivery. *Advanced Drug Delivery Reviews* 58, 15-28.
- Sambuy, Y., Angelis, I., Ranaldi, G., Scarino, M.L., Stamatii, A., Zucco, F., 2005. The Caco-2 cell line as a model of the intestinal barrier: influence of cell and culture-related factors on Caco-2 cell functional characteristics. *Cell Biology and Toxicology* 21, 1-26.

- Sandvig, K., Pust, S., Skotland, T., van Deurs, B., 2011. Clathrin-independent endocytosis: mechanisms and function. *Current Opinion in Cell Biology* 23, 413-420.
- Santra, S., Yang, H., Stanley, J.T., Holloway, P.H., Moudgil, B.M., Walter, G., Mericle, R.A., 2005. Rapid and effective labeling of brain tissue using TAT-conjugated Cds:Mn/Zns quantum dots. *Chemical Communications* 25, 3144-3146.
- Sardan, M., Kilinc, M., Genc, R., Tekinay, A.B., Guler, M.O., 2013. Cell penetrating peptide amphiphile integrated liposomal systems for enhanced delivery of anticancer drugs to tumor cells. *Faraday Discussions* 166, 269-283.
- Sawant, R.R., Sawant, R.M., Kale, A.A., Torchilin, V.P., 2008. The architecture of ligand attachment to nanocarriers controls their specific interaction with target cells. *Journal of Drug Targeting* 16, 596-600.
- Sayes, C., Wahi, R., Kurian, P., Liu, Y., West, J., Ausman, K., Warheit, D., Colvin, V., 2006. Correlating nanoscale titania structure with toxicity: A cytotoxicity and inflammatory response study with human dermal fibroblasts and human lung epithelial cells. *Toxicological Sciences* 92, 174 - 185.
- Schere, D., Robinson, J.R., Kreuter, J., 1994. Influence of enzymes on the stability of poly(butylcyanoacrylate) nanoparticles. *International Journal of Pharmaceutics* 101, 165-168.
- Schilling, R.J., Mitra, A.K., 1991. Degradation of insulin by trypsin and alpha-chymotrypsin. *Pharmaceutical Research* 8, 721-727.
- Schulze, C., Kroll, A., Lehr, C.-M., Schäfer, U.F., Becker, K., Schnekenburger, J., Isfort, C.S., Landsiedel, R., Wohlleben, W., 2008. Not ready to use - overcoming pitfalls when dispersing nanoparticles in physiological media. *Nanotoxicology* 2, 51-61.
- Seto, E.S., Bellen, H.J., Lloyd, T.E., 2002. When cell biology meets development : Endocytic regulation of signaling pathways. *Genes and Development* 16, 1314-1336.
- Sharma, G., Modgil, A., Layek, B., Arora, K., Sun, C., Law, B., Singh, J., 2013. Cell penetrating peptide tethered bi-ligand liposomes for delivery to brain *in vivo*: Biodistribution and transfection. *Journal of Controlled Release* 167, 1-10.
- Simons, A.L., Renouf, M., Hendrich, S., Murphy, P.A., 2005. Human gut microbial degradation of flavonoids: Structure–function relationships. *Journal of Agricultural and Food Chemistry* 53, 4258-4263.
- Snehalatha, M., Venugopal, K., Saha, R.N., Babbar, A.K., Sharma, R.K., 2008. Etoposide loaded PLGA and PCL Nanoparticles II: Biodistribution and pharmacokinetics after radiolabeling with Tc-99m. *Drug Delivery* 15, 277-287.
- Sorensen, J.S., Dearing, M.D., 2006. Efflux transporters as a novel herbivore counter-mechanism to plant chemical defenses. *Journal of Chemical Ecology* 32, 1181-1196.
- Stockhofe, K., Postema, J., Schieferstein, H., Ross, T., 2014. Radiolabeling of Nanoparticles and Polymers for PET Imaging. *Pharmaceutics* 7, 392-418.
- Swaan, P.W., 1998. Recent advances in intestinal macromolecular drug delivery via receptor-mediated transport pathways. *Pharmaceutical Research* 15, 826-834.
- Taberner, A., Velasco, A., Granda, B., Lavado, E.M., Medina, J.M., 2002. Transcytosis of albumin in astrocytes activates the streol regulatory element-binding protein-1, which promotes the synthesis of the neurotrophic factor oleic acid. *Journal of Biological Chemistry* 277.
- Tenhoor, C., Dressman, J., 1992. Oral absorption of peptides and proteins. *STP Pharmaceutical Sciences* 2, 301-312.

- Thapa, R.K., Baskaran, R., Madheswaran, T., Rhyu, J.Y., Kim, J.O., Yong, C.S., Yoo, B.K., 2013. Effect of saturated fatty acids on tacrolimus-loaded liquid crystalline nanoparticles. *Journal of Drug Delivery Science and Technology* 23, 137-141.
- Thompson, C.M., Fedorov, Y., Brown, D.D., Suh, M., Proctor, D.M., Kuriakose, L., Haws, L.C., Harris, M.A., 2012. Assessment of Cr(VI)-induced cytotoxicity and genotoxicity using high content analysis. *PLoS ONE* 7, e42720.
- Thorek, D.L., Tsourkas, A., 2008. Size, charge and concentration dependent uptake of iron oxide particles by non-phagocytic cells. *Biomaterials* 29, 3583-3590.
- Thorén, P.E.G., Persson, D., Isakson, P., Goksör, M., Önfelt, A., Nordén, B., 2003. Uptake of analogs of penetratin, Tat(48–60) and oligoarginine in live cells. *Biochemical and Biophysical Research Communications* 307, 100-107.
- Tobio, M., Gref, R., Sanchez, A., Langer, R., Alonso, M.J., 1998. Stealth PLA-PEG nanoparticles as protein carriers for nasal administration. *Pharmaceutical Research* 15, 270-275.
- Tomalia, D.A., 2005. Birth of a new macromolecular architecture: Dendrimers as quantized building blocks for nanoscale synthetic polymer chemistry. *Progress in Polymer Science* 30, 294-324.
- Torchilin, V.P., 2007. TAT peptide-mediated intracellular delivery of pharmaceutical nanocarriers. *Advanced Drug Delivery Reviews* 60, 548-558.
- Torgersen, M.L., Skretting, G., van Deurs, B., Sandvig, K., 2001. Internalization of cholera toxin by different endocytic mechanisms. *Journal of Cell Science* 114, 3737-3747.
- Tseng, Y.C., Hyon, S.H., Ikada, Y., 1990. Modification of the synthesis and investigation of properties for 2-cyanoacrylates. *Biomaterials* 11, 73-79.
- Tsuji, A., Tamai, I., 1996. Carrier-mediated intestinal transport of drugs. *Pharmaceutical Research* 13, 963-977.
- Tünnemann, G., Martin, R.M., Haupt, S., Patsch, C., Edenhofer, F., Cardoso, M.C., 2006. Cargo-dependent mode of uptake and bioavailability of TAT-containing proteins and peptides in living cells. *The Journal of the Federation of American Societies for Experimental Biology* 20, 1775-1784.
- Van Itallie, C.M., Fanning, A.S., Anderson, J.M., 2003. Reversal of charge selectivity in cation or anion-selective epithelial lines by expression of different claudins. *American Journal of Physiology - Renal Physiology* 285, F1078-F1084.
- Vauthier, C., Dubernet, C., Fattal, E., Pinto-Alphandary, H., Couvreur, P., 2003. Poly(alkylcyanoacrylates) as biodegradable materials for biomedical applications. *Advanced Drug Delivery Reviews* 55, 519-548.
- Verma, A., Stellacci, F., 2010. Effect of Surface Properties on Nanoparticle–Cell Interactions. *Small* 6, 12-21.
- Vij, N., Min, T., Marasigan, R., Belcher, C., Mazur, S., Ding, H., Yong, K.-T., Roy, I., 2010. Development of PEGylated PLGA nanoparticle for controlled and sustained drug delivery in cystic fibrosis. *Journal of Nanobiotechnology* 8, 22.
- Villanueva, A., Cañete, M., Roca, A.G., Calero, M., Veintemillas-Verdaguer, S., Serna, C.J., Morales, M.d.P., Miranda, R., 2009. The influence of surface functionalization on the enhanced internalization of magnetic nanoparticles in cancer cells. *Nanotechnology* 20, 115103.
- Villasana, M., Radunskaya, A., 2003. A delay differential equation model for tumor growth. *Journal of Mathematical Biology* 47, 270-294.
- Visanji, J.M., Duthie, S.J., Pirie, L., Thompson, D.G., Padfield, P.J., 2004. Dietary isothiocyanates inhibit Caco-2 cell proliferation and induce G2/M phase cell cycle

- arrest, DNA damage, and G2/M checkpoint activation. *The Journal of Nutrition* 134, 3121-3126.
- Vives, E., Brodin, P., Lebleu, B., 1997. A truncated HIV-1 Tat protein basic domain rapidly translocates through the plasma membrane and accumulates in the cell nucleus. *Journal of Biological Chemistry* 272, 16010-16017.
- Vlachou, M., Naseef, H., Efentakis, M., Tarantili, P.A., Andreopoulos, A.G., 2001. Swelling properties of various polymers used in controlled release systems. *Journal of Biomaterials Applications* 16, 125-138.
- Wadia, J., Stan, R., Dowdy, S.F., 2004. Transducible TAT-HA fusogenic peptide enhances escape of TAT-fusion proteins after lipid raft macropinocytosis. *Nature Medicine* 10, 310-315.
- Wagstaff, K.M., Jans, D.A., 2006. Protein transduction: Cell penetrating peptides and their therapeutic applications. *Current Medicinal Chemistry* 13, 1371-1387.
- Wang, Q.Z., Chen, X.G., Liu, N., Wang, S.X., Liu, C.S., Meng, X.H., Liu, C.G., 2006. Protonation constants of chitosan with different molecular weight and degree of deacetylation. *Carbohydrate Polymers* 65, 194-201.
- Wang, T., Bai, J., Jiang, X., Nienhaus, U., 2012. Cellular uptake of nanoparticles by membrane penetration: A study combining confocal microscopy with FTIR spectroelectrochemistry. *ACS Nano* 6, 1251 - 1259.
- Wang, W., 1999. Instability, stabilization and formulation of liquid protein pharmaceuticals. *International Journal of Pharmaceutics* 185, 129-188.
- Wang, X.-Q., Zhang, Q., 2012. pH-sensitive polymeric nanoparticles to improve oral bioavailability of peptide/protein drugs and poorly water-soluble drugs. *European Journal of Pharmaceutics and Biopharmaceutics* 82, 219-229.
- Warheit, D., Sayes, C., Reed, K., 2009. Nanoscale and fine zinc oxide particles: can in vitro assays accurately forecast lung hazards following inhalation exposures? *Environmental Science & Technology* 43, 7939 - 7945.
- Watanasirichaikul, S., Davies, N.M., Rades, T., Tucker, I.G., 2000. Preparation of biodegradable insulin nanocapsules from biocompatible microemulsions. *Pharmaceutical Research* 17, 684-689.
- Watanasirichaikul, S., Rades, T., Tucker, I.G., Davies, N.M., 2002a. Effects of formulation variables on characteristics of poly(ethylcyanoacrylate) nanocapsules prepared from w/o microemulsions. *International Journal of Pharmaceutics* 235, 237-246.
- Watanasirichaikul, S., Rades, T., Tucker, I.G., Davies, N.M., 2002b. *In vitro* release and oral bioactivity of insulin in diabetic rats using nanocapsules dispersed in biocompatible microemulsion. *Journal of Pharmacy and Pharmacology* 54, 473-480.
- Weatherall, E., Willmott, G.R., Glossop, B., 2013. Individual nanoparticle zeta potential measurements using tunable resistive pulse sensing, Proceedings of the International Conference on Sensing Technology, ICST, pp. 874-878.
- Weiss, C.K., Ziener, U., Landfester, K., 2007. A route to nonfunctionalized and functionalized poly(n-butylcyanoacrylate) nanoparticles: Preparation in miniemulsion. *Macromolecules* 40, 928-938.
- Wen, J.Y., Ledger, R., Butt, A.G., McLeod, B.J., Davies, N.M., Tucker, I.G., 2002a. Inhibition of proteolysis in luminal extracts from the intestine of the brushtail possums. *Journal of Pharmacy and Pharmacology* 54, 1365-1372.
- Wen, J.Y., Ledger, R., McLeod, B.J., Davies, N.M., Butt, A.G., Tucker, I.G., 2002b. Enzymatic degradation of luteinizing hormone releasing hormone (LHRH) by mucosal homogenates from the intestine of the common brushtail possum (*Trichosurus vulpecula*). *Life Sciences* 71, 3019-3030.

- Wender, P.A., Galliher, W.C., Goun, E.A., Jones, L.R., Pillow, T.H., 2008. The design of guanidium-rich transporters and their internalization mechanisms. *Advanced Drug Delivery Reviews* 60, 452-472.
- Wender, P.A., Mitchell, D.J., Pattabiraman, K., Pelkey, E.T., Steinman, L., Rothbard, J.B., 2000. The design, synthesis and evaluation of molecules that enable or enhance cellular uptake: Peptoid molecular transporters. *Proceedings of the National Academy Sciences of the United States of America* 97, 13003-13008.
- White, P.J., Hickey, P., Sze Tu, L., Headey, S.J., Scanlon, M.J., Boyd, B.J., Pouton, C.W., 2012. Colloidal characteristics and formulation of pure protein particulate vaccines. *Journal of Pharmacy and Pharmacology* 64, 1386-1393.
- Woitiski, C.B., Carvalho, R.A., Ribeiro, A.J., Neufeld, R.J., Veiga, F., 2008. Strategies toward the improved oral delivery of insulin nanoparticles via gastrointestinal uptake and translocation. *Biodrugs* 22, 223-237.
- Xu, P., Gullotti, E., Tong, L., Highley, C.B., Errabelli, D.R., Hasan, T., Cheng, J.-X., Kohane, D.S., Yeo, Y., 2009. Intracellular drug delivery by poly(lactic-co-glycolic acid) nanoparticles, revisited. *Molecular Pharmaceutics* 6, 190-201.
- Xu, X., Caswell, K.K., Tucker, E., Kabisatpathy, S., Brodhacker, K.L., Scrivens, W.A., 2007. Size and shape separation of gold nanoparticles with preparative gel electrophoresis. *Journal of Chromatography A* 1167, 35-41.
- Yan, L., Wang, H., Jiang, Y., Liu, J., Wang, Z., Yang, Y., Huang, S., Huang, Y., 2013. Cell-penetrating peptide-modified PLGA nanoparticles for enhanced nose-to-brain macromolecular delivery. *Macromolecular Research* 21, 435-441.
- Yang, L., Broom, M.F., Tucker, I.G., 2012. Characterization of a nanoparticulate drug delivery system using scanning ion occlusion sensing. *Pharmaceutical Research* 29, 2578-2586.
- Ye, Y., Xu, Y., Liang, W., Leung, G.P.H., Cheung, K.-H., Zheng, C., Chen, F., Lam, J.K.W., 2013. DNA-loaded chitosan oligosaccharide nanoparticles with enhanced permeability across Calu-3 cells. *Journal of Drug Targeting* 21, 474-486.
- Yin Win, K., Feng, S.-S., 2005. Effects of particle size and surface coating on cellular uptake of polymeric nanoparticles for oral delivery of anticancer drugs. *Biomaterials* 26, 2713-2722.
- Yoshida, T., 1997. Peptide separation in normal phase liquid chromatography. *Analytical Chemistry* 69, 3038-3043.
- Zhang, Q., Tang, J., Fu, L., Ran, R., Liu, Y., Yuan, M., He, Q., 2013. A pH-responsive α -helical cell penetrating peptide-mediated liposomal delivery system. *Biomaterials* 34, 7980-7993.
- Zhou, J., Moya, S., Ma, L., Gao, C., Shen, J., 2009. Polyelectrolyte coated PLGA nanoparticles: Templatation and release behaviour. *Macromolecular Bioscience* 9, 326-335.
- Zhou, X.H., 1994. Overcoming enzymatic and absorption barriers to nonparenterally administered protein and peptide drugs. *European Journal of Pharmaceutical Sciences* 29, 239-252.
- Zorko, M., Langel, U., 2005. Cell-penetrating peptides: Mechanism and kinetics of cargo delivery. *Advanced Drug Delivery Reviews* 57, 529-545.

Appendix I.

Size, polydispersity index and zeta potential of PECA nanoparticles in HBSS, with the addition of poloxamer-407 (0.06%). Data are means \pm SD ($n \geq 2$).

Nanoparticles	Size (d.nm)	Polydispersity index	Zeta potential (mV)
Unmodified	235.4 \pm 39.5	0.23 \pm 0.03	-0.63 \pm 0.51
RRH (100 μ mol)-tagged	194.1 \pm 10.1	0.24 \pm 0.03	-1.11 \pm 0.87
R4acaH (34 μ mol)- entrapped	164.7 \pm 13.1	0.23 \pm 0.01	-0.76 \pm 0.62

Appendix II.

The sedimentation rate of the nanoparticles can be calculated based on the maximum sedimentation distance ($h = 27.3$ mm). The linear correlation between the mass of nanoparticles recovered after centrifugation and the centrifugation time can be used to estimate the centrifugation time required for the nanoparticle located furthest away from the site of deposition. However, as the centrifuge tube was placed on an angle in the rotor, the distance travelled by the nanoparticles to sediment would vary depending on the location of the particles in the tube (**Figure A**). After a short centrifugation time, the total mass of nanoparticles recovered would include the nanoparticles located outside the area of interest (**Figure A**). Therefore, the first few centrifugation time points ($t = 12, 15$ and 18 min) were excluded from the linear correlation to account only for the nanoparticles located within the path with the longest sedimentation distance ($h = 27.3$ mm) and travelling in a straight path to sediment (**Figure A**). The nanoparticle mass recovered from centrifugation at time points 21, 25, 30, 40 and 50 min was used to plot a linear correlation. Data from these time points were chosen based on a deviation of 1 mg or greater from data prior to 21 min. This deviation signifies a new sedimentation rate trend that accounts only for the nanoparticles with the longest sedimentation distance ($h = 27.3$ mm) and travelling on a straight line to sediment (**Figure A**).

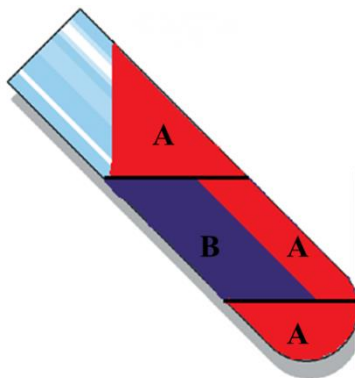


Figure A. Location of nanoparticles in a centrifuge tube, placed at an angle in the rotor. Nanoparticles located in the red area **A** of the centrifuge tube are expected to sediment faster than the nanoparticles in the purple area **B**. Nanoparticles in the purple area **B** are the nanoparticles of interest and are located within the longest sedimentation route, h .

The average dry mass of nanoparticles recovered from centrifugation at time points 70, 90, 120 and 150 min was used as the total mass of nanoparticles that had fully sedimented (total mass of nanoparticles recovered, $y = 9.0059 \pm 0.6947$ mg). Data from these time points were chosen based on a deviation of lesser than 1 mg from data obtained from time points after 70 min. The small deviation indicates that the maximum mass of nanoparticles recoverable from the suspension has reached a constant and all the nanoparticles, including the nanoparticles with the longest sedimentation distance, have sedimented.

Using the straight line model (Total mass of nanoparticles recovered, $y = 0.0456 x$ (centrifugation time) + 5.4548, $r^2 = 0.864$) and the maximum mass of recoverable nanoparticles, y-intercept ($y = 9.0059$ mg), the time it took for the furthest nanoparticle to sediment was calculated to be 77.88 min.

The sedimentation rate of nanoparticles can be found in **Equation 2** as defined by Stokes' Law. However, the sedimentation rate of the nanoparticles can also be calculated from **Equation 8**. Therefore, the equation can be re-written as **Equation 9** and the nanoparticle density can be calculated.

Equation 8. Sedimentation rate of nanoparticles.

$$V_s = \frac{h}{t}$$

where V_s = sedimentation rate, ms^{-1} , h = distance travelled to sediment, m; t = time taken to sediment, s

Equation 9. Sedimentation rate based on maximum sedimentation distance, h and Stokes' Law.

$$\frac{h}{t} = \frac{d^2(\rho_{np} - \rho_{med})\alpha}{18\eta}$$

where V_s = sedimentation rate, ms^{-1} , d = diameter of particle, m; ρ_{np} = particle density, $\text{kg}\cdot\text{m}^{-3}$; ρ_{med} = medium density, $\text{kg}\cdot\text{m}^{-3}$; α = gravitational acceleration, $\text{m}\cdot\text{s}^{-2}$; η = medium viscosity, $\text{kg}\cdot\text{m}^{-1}\text{s}^{-1}$

Appendix III

Recovery of radiolabeled PECA nanoparticles from wells without cells (control) after 2 h incubation at 37°C. Data are mean \pm SD ($n = 3$).

Nanoparticles	Nanoparticles recovered (% of loading dose)			
	Supernatant	After HBSS wash	After trypsinization wash	After cell lysis
Unmodified	93.5 \pm 3.2	1.0 \pm 0.1	0.2 \pm 0.1	0.1 \pm 0.1
RRH (100 μ mol)-tagged	111 \pm 1.0	0.5 \pm 0.3	0 \pm 0	0 \pm 0

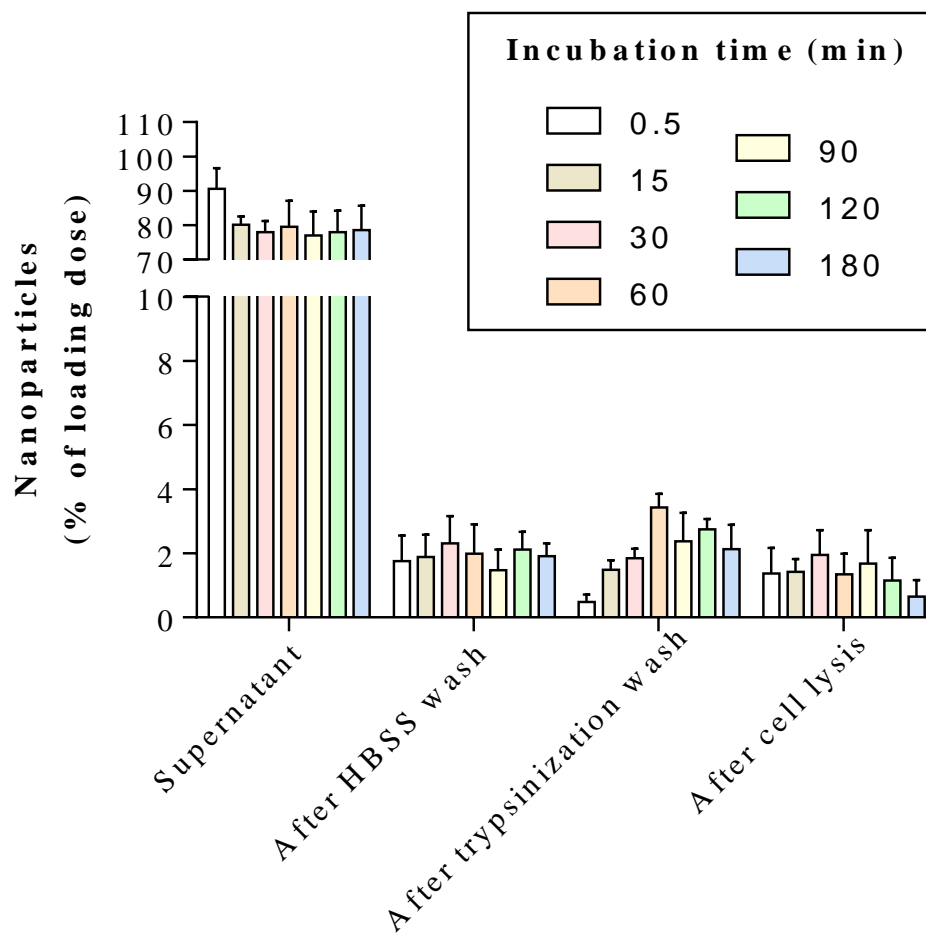
Appendix IV

Protein content of Caco-2 cells. Data are means \pm SD.

Caco-2 cells	Protein content (μ g/mL)
Undifferentiated cells ($n = 16$)	2016 \pm 288
Fully differentiated monolayers ($n = 48$)	20851 \pm 3950

Appendix V

Recovery of radiolabeled, unmodified PECA nanoparticles in the cellular association study with different incubation time. The nanoparticle formulation was incubated with fully differentiated Caco-2 monolayers at 37°C. Data are means \pm SD ($n = 8 - 9$).



Appendix VI

Recovery of radiolabeled, RRH (100 μ mol)-tagged PECA nanoparticles in the cellular association study with different incubation time. The nanoparticle formulation was incubated with fully differentiated Caco-2 monolayers at 37°C. Data are means \pm SD ($n = 8 - 9$).

